In vitro study of gas embolism formation in microfluidic vascular networks

Karine Baassiri

Department of Bioengineering

McGill University, Montreal

December 2024

A thesis submitted to McGill University in partial fulfillment of the requirements of the degree of Ph.D. in Biological and Biomedical Engineering.

Preface

This thesis is dedicated to my parents, Mohammad and Mirvat, who poured their hearts into making my life as rich and as meaningful as possible. The pride I feel in being your daughter is immeasurable, and I will always strive to honor the impact of your support and dedication. You not only gave me a beautiful childhood but also ensured that its warmth and strength continue to guide me into adulthood.

I would also like to dedicate this work to every Ph.D. candidate who invested years of effort into having their hard work recognized. The physical and mental struggles you endure may not be acknowledged immediately, but they are never in vain. Stay resilient, keep your chin up, and push forward.

Karine Baassiri

Table of Content

List of Figures

List of Tables

Abstract

Vascular gas embolism is a potentially life-threatening medical condition caused by the presence of gas bubbles in the vascular network, leading to reduced blood flow and possible disruptions in the transport of oxygen to tissues and vital organs. Despite its significant implications for patient health, particularly in iatrogenic contexts, the origins and underlying mechanisms remain poorly understood. Since the onset of this condition is physical in nature, the purpose of this study is to investigate the genesis of gas embolism and its varied manifestations by employing a series of abiotic microfluidic devices designed to simulate the human vascular system with different hematological and anatomical configurations, subjected to pressure-related scenarios.

The characteristics of bubble formation were first correlated with increasing levels of pressure applied to different geometries of artificial blood vessels, modeled by the first set of microfluidic platforms. Vascular channels with larger widths and 'intact' thin walls produced the greatest bubble volumes, especially at high pressures, while smaller channel widths exhibited earlier onset of bubble generation at lower pressure thresholds. The origins of gas embolism were directly related to the presence of excess gases by varying the storage conditions of these vascular systems on a chip and monitoring the impact of pressured gases in the local material network. A second set of microfluidic platforms was then introduced to determine patterns of bubble formation in the presence of local damages and critical areas in the vascular walls. As the integrity of the wall was compromised, the application of pressure quickly generated intravascular bubbles, with greater volumes and increased chaotic behavior appearing in larger channels with wider perforations, respectively. This reveals greater risks associated with gas embolism for patients who have weakened blood vessels, whether due to genetic factors or medical histories.

The research also explores the impact of different anatomical and hematological factors on bubble behavior by varying the equivalent hematocrit concentrations of a synthetic blood solution in another designed series of microfluidic devices, comprising two channel widths and three wall thicknesses. These biological factors were correlated with the nucleation density, the generation frequency, the maximum volume, and the mean velocity of generated bubbles. The risks of bubble immobilization and vascular wall damage were determined as well, particularly in smaller channel widths, which were more susceptible to ruptures at lower pressure thresholds.

Finally, a novel microscale hyperbaric system was created to model decompression sickness, using compressed air and nitrogen at different pressure thresholds and periods of compression. Rapid decompression from higher pressures and longer compression durations led to the formation of larger and more numerous bubbles, most of which appeared 10 minutes and even 30 minutes post-return to atmospheric conditions. This emphasizes the need for improved safety measures in scenarios involving pressure changes, especially since the symptoms of decompression sickness continue manifesting even 30 minutes post-decompression.

These findings reveal the complex interplay of physical, biological, and environmental factors in gas embolism, highlighting the importance of personalized approaches in its management and prevention, as well as the development of stringent safety protocols for medical procedures involving gas introduction.

Résumé

L'embolie gazeuse vasculaire est une condition médicale potentiellement mortelle causée par la présence de bulles de gaz dans le réseau vasculaire, entraînant une réduction du flux sanguin et d'éventuelles perturbations du transport de l'oxygène vers les tissus et les organes vitaux. Malgré ses implications significatives pour la santé des patients, en particulier dans les contextes iatrogéniques, ses origines et ses mécanismes sous-jacents restent mal compris. Étant donné que l'apparition de cette condition est de nature physique, cette étude vise à explorer la genèse de l'embolie gazeuse et ses diverses manifestations en utilisant une série de dispositifs microfluidiques abiotiques conçus pour simuler le système vasculaire humain avec différentes configurations hématologiques et anatomiques, soumises à des scénarios liés à la pression.

Les caractéristiques de la formation des bulles ont d'abord été corrélées avec des niveaux croissants de pression appliqués à différentes géométries de vaisseaux sanguins artificiels, modélisées par le premier ensemble de plateformes microfluidiques. Les canaux vasculaires de plus grande largeur et aux parois minces et intactes ont produit les plus grands volumes de bulles, en particulier à des pressions élevées, tandis que les canaux plus étroits ont présenté une apparition plus précoce de la formation de bulles à des seuils de pression plus bas. Les origines de l'embolie gazeuse ont été directement reliées à la présence d'un excès de gaz en faisant varier les conditions de stockage de ces systèmes vasculaires sur puce et en surveillant l'impact des gaz sous pression dans le réseau matériel local. Un second ensemble de plateformes microfluidiques a ensuite été introduit pour déterminer les schémas de formation des bulles en présence de dommages locaux et de zones critiques dans les parois vasculaires. À mesure que l'intégrité de la paroi était compromise, l'application de pression générait rapidement des bulles intravasculaires, avec des volumes plus importants et un comportement plus chaotique apparaissant dans les canaux plus larges avec des perforations plus étendues, respectivement. Cela révèle des risques accrus d'embolie gazeuse pour les patients ayant des vaisseaux sanguins affaiblis, que ce soit en raison de facteurs génétiques ou d'antécédents médicaux.

L'étude explore également l'impact de divers facteurs anatomiques et hématologiques sur le comportement des bulles en faisant varier les concentrations équivalentes en hématocrite d'une solution sanguine synthétique dans une autre série de dispositifs microfluidiques, comprenant deux

largeurs de canal et trois épaisseurs de paroi. Ces facteurs biologiques ont été corrélés avec la densité de nucléation, la fréquence de génération, le volume maximal et la vitesse moyenne des bulles générées. Les risques d'immobilisation des bulles et de dommages aux parois vasculaires ont également été déterminés, en particulier dans les canaux plus étroits, qui se sont révélés plus susceptibles aux ruptures à des seuils de pression plus bas.

Enfin, un nouveau système hyperbare à l'échelle microscopique a été créé pour modéliser le mal de décompression, en utilisant de l'air comprimé et de l'azote à différents seuils de pression et en augmentant les périodes de compression. Une décompression rapide à partir de pressions plus élevées et de périodes de compression plus longues a conduit à la formation de bulles plus grandes et plus nombreuses, dont la majorité est apparue 10 minutes et même 30 minutes après le retour aux conditions atmosphériques. Cela souligne la nécessité d'améliorer les mesures de sécurité dans les scénarios impliquant des variations de pression, d'autant plus que les symptômes du mal de décompression semblent continuer à se manifester jusqu'à 30 minutes après la décompression.

Ces résultats révèlent l'interaction complexe des facteurs physiques, biologiques et environnementaux dans l'embolie gazeuse, soulignant l'importance d'approches personnalisées en matière de gestion et de prévention, ainsi que le développement de protocoles de sécurité stricts pour les procédures médicales impliquant l'introduction de gaz.

Acknowledgments

First, I want to extend my deepest appreciation to my supervisor, Prof. Dan V. Nicolau, whose mentorship has been a cornerstone of my development. His guidance transcended academic instruction, as he taught me the virtues of patience, tolerance, and the importance of character. He continuously challenged me to broaden my horizons, to step outside my comfort zone, and to look beyond the narrow confines of my research with a broader, more holistic perspective.

I would also like to acknowledge McGill University for creating an environment that thrives on collaboration and mutual support. The university's commitment to fostering an atmosphere of learning, growth, and shared achievement provided me with the resources and community necessary to excel.

To my people, those who have guided, encouraged, and sustained me, both academically and personally, it would have been impossible to complete this journey without you.

To my partner, you have been my constant source of strength. I am endlessly grateful to you.

Lastly, mom and dad — this PhD belongs to you as much as it does to me, if not more.

Contribution to Original Knowledge

This thesis offers several distinct contributions to original knowledge and scholarship in the study of vascular gas embolism. A novel microfluidic framework was introduced, encompassing a controllable physiological environment, to provide real-time imaging and experimental-based correlations between the origins of gas emboli and different geometrical, anatomical, and pressure-related parameters.

First and foremost, the use of microfluidic devices to model human blood vessels is still a developing field with considerable untapped potential. Vascular systems on a chip hold promise for the study of sudden, rare, and complex medical conditions that pose challenges in their *in vivo* investigation, such as gas embolism. The work outlined below validates the possibility of this research avenue by introducing four innovative 'abiotic' microfluidic designs, simulating different microvascular geometric features, for a better understanding of the origins and manifestations of intravascular bubbles in a controlled and reproducible experimental setting. This approach presents significant advancement in the application of microfluidic technology for the exploration of pathological phenomena in general, and the fundamentals of gas embolism in particular (Articles 1 to 3).

Second, these microfluidic platforms enable real-time imaging and recording of the onset of intravascular bubble formation, a phenomenon that had not been observed before. The integration of a confocal microscope in all experimental setups provided the ability to monitor how bubbles originate in different physiological conditions and maintain all acquired data for further processing using ImageJ and Matlab, amongst other software for data analysis. This enables a better understanding of the susceptibility of key input parameters to develop gas emboli, which is substantial for the preventive measures that must be adopted to ensure patients' safety based on their predisposition to this medical condition (Articles 1 and 2).

Third, the complex and multifactorial nature of gas embolism poses significant challenges in understanding the conditions that contribute to its formation, development, and eventual dissipation. The development of a comprehensive and controllable framework allows a fundamental-based approach to isolate each input parameter and systemically assess its role in the initiation of this disease. The characteristics of bubble formation were correlated with variations

in microchannel geometry (channel width and wall thickness), biological factors (equivalent hematocrit concentration in the synthetic blood solution), and environmental conditions (gas type, pressure threshold and compression duration), revealing all critical factors in the generation of bubbles with the most prominent patterns (Articles 1 to 3).

Finally, the microscale hyperbaric system offers an innovative platform that combines artificial blood vessels, synthetic blood solutions, pulsatile blood circulation, and global pressure variations to model numerous decompression scenarios. This experimental setup is crucial as it not only replicates conditions related to diving and high-altitude activities that would typically lead to gas embolism, but it also enables the monitoring and assessment of bubble progression during standard treatment protocols from Hyperbaric Oxygen Therapy—where the use of phones, microscopes, cameras, and electrical devices is strictly prohibited. The efficiency of these established protocols had never been tested, therefore extensive optimization is both required and made possible with the use of this system (Article 3).

Contribution of Authors

I confirm that I am the primary author and main contributor to each of the chapters outlined below. I established and executed the overall research plan, which included the design of microfluidic devices, the fabrication of master wafers, the replication of devices, the preparation of working fluids, the testing of different rheological and mechanical properties, the procurement of safety equipment from external suppliers, and the setup of the experimental procedure. I was solely responsible for conducting all the experiments, performing data and image analysis, and drafting the initial manuscripts as first author.

The contributions of all secondary authors and collaborators are detailed below for each chapter.

Chapter 1:

- Mohammad Mahdi Mardanpour: collected and compiled data for Table 1.2, Figure 1.3, and Figure 1.7.
- Kenneth M. LeDez: contributed to writing the final draft of the review.
- Neal W. Pollock: contributed to writing the final draft of the review.
- Dan Popa: contributed to writing the final form of the review.
- Dan V. Nicolau: initiated the project, coordinated the workflow, adjusted the table of content, and provided final approval for publication.

Chapter 2:

- Thomas Allen: developed a custom Matlab code and contributed to data analysis.
- Dan V. Nicolau: contributed to data analysis and interpretation, edited the manuscript, and provided final approval for publication.

Chapter 3:

- Dan V. Nicolau: edited the figures and contributed to data analysis.

Chapter 4:

- Thomas Allen: fabricated the portable power source and developed a Matlab code for data analysis.
- Dan V. Nicolau: contributed to conceptualization and data interpretation.

Introduction

Vascular gas embolism is a rare but potentially life-threatening medical condition that occurs due to the presence of gas emboli in the venous or arterial system. These emboli can become lodged and immobilized in blood vessels, leading to vascular obstructions with subsequent complications. The disease can progress via two primary mechanisms: a physical route, characterized by the partial or complete obstruction of blood flow due to gas bubbles mechanically blocking the transport of oxygen-carrying red blood cells, and a biochemical route, where the presence of emboli triggers inflammatory responses by promoting the aggregation of white and red blood cells. This immune activation can exacerbate vascular damage, compounding the severity of the condition.

There are multiple categories associated with gas embolism. The first of which depends on the bubble location, classifying it as either venous gas embolism or arterial gas embolism. It is important to note that gas emboli may not have formed where they are found, as they can migrate through the bloodstream due to continuous circulation. The second category is associated with the mechanism of gas entry, leading to two types of gas embolism. The more extensively studied type is known as global gas embolism, which results from the *in situ* creation of bubbles following sudden exposure to pressure variations that affect large organs or the entire body. This is commonly observed in individuals engaged in pressure-related activities such as diving, aviation, and space exploration. The subsets of global gas embolism are decompression sickness, which occurs when nitrogen gas comes out of solution due to heterogeneous nucleation and tissue supersaturation, and arterial gas embolism resulting from pulmonary barotrauma due to lung over-expansion injuries. Conversely, local gas embolism occurs when gas is introduced into the vascular system via external sources, accidentally or intentionally, either from trauma to gas-containing organs or invasive medical procedures. The latter leads to iatrogenic gas embolism, which can arise from improper use of intravenous catheters, cardiopulmonary bypass procedure, wound irrigation, or laparoscopic surgery. These mechanisms highlight the complex nature of vascular gas embolism, as its clinical manifestations are highly dependent on the location, size, and distribution of gas bubbles within the circulatory system.

Figure 0.1 provides a comprehensive overview of the different types of gas embolism.

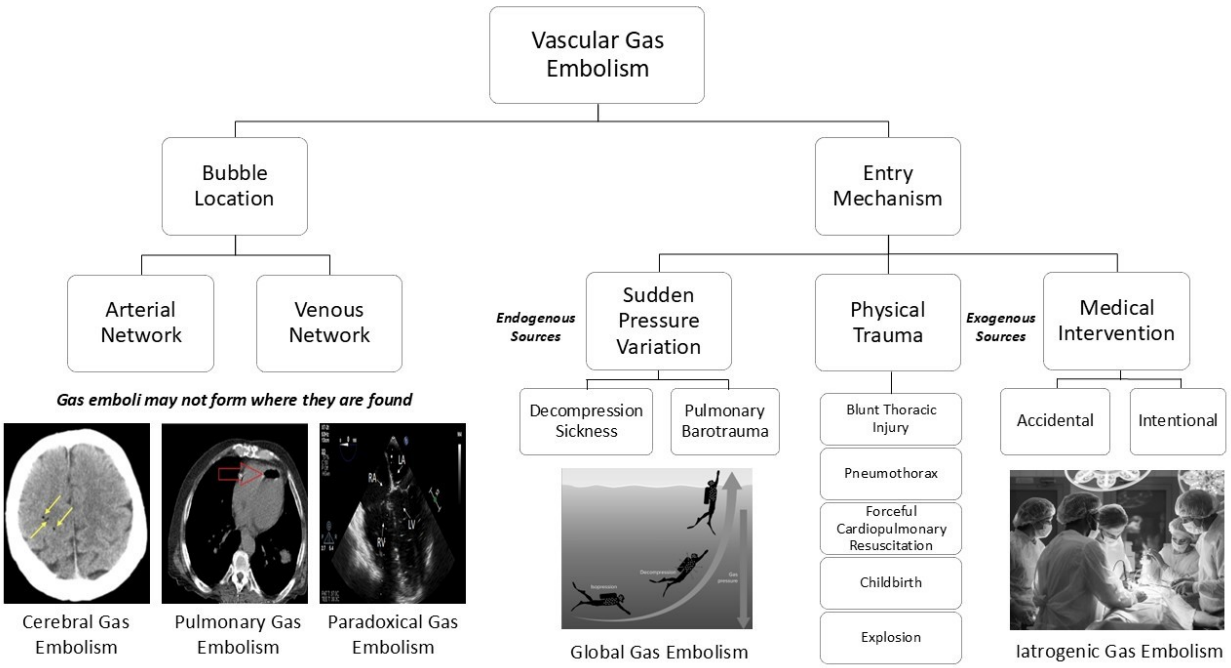

Figure 0.1. Categories of gas embolism based on the bubble location and entry mechanism.

Regardless of their origins, the sudden and unpredictable nature of gas embolism makes it nearly impossible to detect the bubbles at the onset of their formation. In the absence of a timely diagnosis, these emboli pose significant risks, as they can lead to partial and even complete obstruction of blood flow to tissues and vital organs, ultimately disrupting the mechanism of oxygen transfer within the human body. Although there are instances when microbubbles are intentionally introduced into the bloodstream, such as in the use of microscopic oxygen-carrying bubbles to enhance radiation therapy for cancer treatment, they can still lead to adverse secondary effects. They can even cause damages on the vascular endothelium due to friction between the gas bubble and the intravascular routes, increasing the likelihood of neurological and cardiovascular complications.

In recent decades, microfluidic technology helped revolutionize various fields, from diagnostics to biological research, by providing precise control and real-time observation of experimental parameters in reproducible conditions. These advancements allow researchers to investigate complex pathological phenomena that are difficult or nearly impossible to observe *in vivo*. In the context of gas embolism, microfluidic platforms can be designed as artificial blood vessels that

replicate the geometric, biological, and environmental factors influencing bubble formation and evolution.

The main objective of this research is to harness the potential of microfluidic devices to advance the understanding of gas embolism through *in vitro* disease simulation within a controlled microenvironment. This allows scientists and medical doctors to bridge the gap between theoretical knowledge and clinical practice by simulating gas embolism within engineered vascular systems on a chip, enabling a detailed assessment of bubble formation, movement, and interactions with vascular walls under varying conditions. To this end, four distinct microfluidic systems were designed to examine the genesis of vascular gas embolism, with a specific focus on the interplay between intravascular bubble formation and three key factors: (i) geometric characteristics of biomimetic vascular channels, (ii) rheological properties of synthetic blood solutions, and (iii) pressure variations that replicate real-life conditions within the microenvironment. By assessing the contribution of each of these parameters, the multifactorial nature of vascular gas embolism can be unravelled to ultimately derive the optimum diagnostic tools, preventive measures, and therapeutic strategies, leading to better patient outcomes.

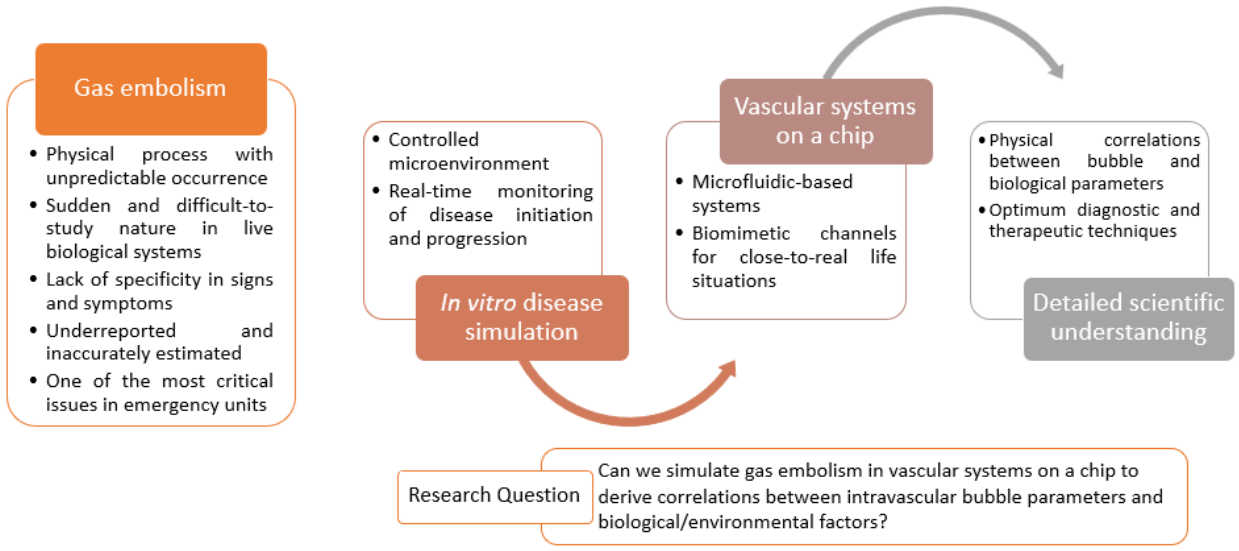

Figure 0.2. The research framework for the *in vitro* study of gas embolism formation in microfluidic vascular networks.

The thesis is structured around three main objectives, each contributing to a deeper understanding of gas embolism through experimental investigations and quantitative analysis.

1. Developing Abiotic Microfluidic Vascular Models

The first objective is to design and fabricate abiotic microfluidic platforms that closely replicate the human vascular system for the *in vitro* investigation of gas embolism.

1.1. Designing vascular channels that resemble arterioles and venules, allowing the analysis of bubble behavior in both simple blood vessels and bifurcated networks.

1.2. Fabrication of biomimetic microfluidic devices using photolithography followed by soft lithography to create channels with high dimensional accuracy.

1.3. Integration of real-time monitoring techniques, including high-speed microscopy and pressure sensors, to capture bubble formation and movement under physiologically relevant conditions.

2. Replicating Gas Embolism in Artificial Vascular Networks

The second objective focuses on mimicking the formation, growth, and movement of gas bubbles in vascular systems on a chip under varying pressure conditions.

2.1. Determination of pressure thresholds required for bubble nucleation and expansion in microfluidic vascular models of different widths and wall thicknesses.

2.2. Analysis of bubble mobility and interaction with vascular walls in both low- and high-pressure environments to assess the risk of embolization and vascular occlusion.

2.3. Examination of chaotic bubble behavior in dynamic flow conditions to understand how bubble behavior changes based on vessel size, wall integrity and pressure fluctuations.

3. Determining the Multifactorial Nature of Gas Embolism

The third and final objective isolates different input parameters to determine the impact of hematological factors, i.e., synthetic blood composition, and geometric features, i.e., channel width, wall thickness, generation of bifurcation, and perforation size on the likelihood and severity of gas embolism.

3.1. Investigation of the relationship between hematocrit concentration and bubble nucleation, including correlations between blood viscosity and bubble stability.

3.2. Evaluation of gas embolism risks in weakened vessels, simulating clinical conditions such as vascular injury, or disease-related wall weakness.

3.3. Modeling of decompression sickness using a microscale hyperbaric system to analyze how sudden pressure variations using different types of gases influence bubble formation and distribution.

By systematically addressing these three research objectives, the study provides a comprehensive understanding of the mechanisms underlying vascular gas embolism. The controlled microfluidic environment allows for precise experimentation, eliminating confounding variables commonly encountered in *in vivo* studies. These findings also contribute to the development of targeted interventions and preventative measures, ultimately improving patient safety in clinical and high-pressure environments, all the while supporting advancements in biomimetic modeling, diagnostics, and treatment strategies for gas embolism.

Chapter 1. Comprehensive Review of Literature

1.1. Background of Review Chapter

The first chapter, currently in print, presents a comprehensive review of vascular gas embolism, examining its key concepts and definitions from both scientific and medical perspectives. It explores the implications of gas embolism, detailing its signs, associated risks, and potential consequences. Additionally, it highlights strategies for optimum prevention, diagnosis, and treatment, emphasizing the importance of improving patient outcomes and minimizing long-term complications.

Recent research efforts have advanced the generation of bubbles at the microscale within microfluidic channels, primarily relying on hydrodynamic techniques. These *in vitro* studies determined the impact of bubble formation on fluid dynamics and biological cells. More importantly, the review establishes the foundation for the three subsequent chapters of this thesis by addressing critical factors necessary for the biomimicry of microvasculature in artificial environments. These factors include the selection of suitable materials, the design of microfluidic geometries, the surface characteristics of synthetic blood vessels, and the choice of blood analogues. Such elements are essential for creating realistic simulations of blood flow and gas embolism, contributing to both experimental and clinical applications. The role of surfactants is also highlighted, as these compounds can significantly affect the behavior of gas bubbles and their interaction with biological compounds.

Although there is significant progress made in the physical simulation of gas bubbles, microfluidic devices offer unique opportunities to enhance our understanding of gas embolism, shedding light on previously unexplored aspects of its behavior and mechanisms. The ability to replicate gas embolism in a controlled environment paves the way for the development of novel therapeutic interventions, ultimately enhancing treatment strategies for this critical medical condition.

This work is the result of the collaborative efforts by six contributors, who have helped shape this review as a book chapter (Chapter 17) in the upcoming Elsevier publication, *Recent Advances in Hemodynamics and Blood Mimetics*.

1.2. Review Chapter:

CHAPTER 17

In Vitro Studies of Gas Embolism

Karine Baassiri[a], Mohammad Mahdi Mardanpour[a], Kenneth M. LeDez[b], Neal W. Pollock[c], Dan Popa[d], Dan V. Nicolau[a]

[a]Department of Bioengineering, Faculty of Engineering, McGill University, Montreal, Quebec, H3A 0E9, Canada

[b]Faculty of Medicine, Memorial University, Health Sciences Centre, St. John's, Newfoundland and Labrador, A1C 5S7, Canada

[c]Department of Kinesiology, School of Medicine, Université Laval, Quebec City, Quebec, G1V 0A6, Canada

[d]Department of Emergency Medicine, Hennepin County Medical Center and University of Minnesota School of Medicine, Minneapolis, MN, USA

1.2.1. Abstract

Vascular gas embolism is a medical condition resulting from the existence of gas bubbles in the venous or arterial system. Gas embolism has been associated with a wide range of circulatory, cardiovascular, and neurological outcomes, including severe neurological sequelae and death. The origins of intravascular bubbles are attributed to multiple factors, stemming from (i) endogenous sources, as in the cases of decompression sickness and pulmonary barotrauma, which lead in-situ generation of bubbles or (ii) exogenous sources, such as accidental or intentional introduction of gas during medical procedures. Despite being one of the most critical complications in acute and critical care units, the genesis and pathophysiology of gas embolism remains poorly understood. The reportedly rare occurrence of gas embolism, coupled with its potentially devastating effects, makes large scale clinical trials logistically and ethically impossible. Recent efforts have attempted to replicate gas embolism *in vitro*, benefiting from the development of microfluidics technology. The present review describes the fundamentals of gas embolism, the preconditions for the mimicking of gas embolism in artificial micro-environments, and the recent state of the art in the physical simulation of gas embolism in microfluidics devices.

1.2.2. Introduction

Gas embolism, first reported in the 19th century as a potentially fatal medical condition[1], occurs when gas bubbles are present in blood vessels, which if large can lead to limited, or blocked blood flow, and thus decrease O_2 supply to the brain and other vital organs[2]. The presence of gas emboli in the circulatory system can also trigger a cascade of adverse effects, such as damage to vascular endothelium and blood components, leading to the formation of microparticles with active cell membrane fragments, which may escalate to complications in the vascular, cardiac, and neurological systems[3].

The basic causes leading to gas embolism are known: either intentional or accidental introduction of gases, or the creation *in situ* of gas emboli due to the rapid decrease of pressure, which leads to the desorption of gases in the blood stream or from the surrounding tissues. Despite this basic, widely accepted knowledge, the fundamentals-based link between cause and effect is poorly understood, particularly regarding the mechanisms of gas bubble generation and evolution, leading to difficulties in risk assessment.

Perhaps the most obvious expression of the poor understanding of gas embolism is the variability of statistical data related to its incidence and its outcomes. For instance, a large-scale review of scientific diving, described incidence rates of decompression illness, including both decompression sickness (DCS) and arterial gas embolism (AGE), ranging from 0.32 per 10,000 person-dives up to 35.3 per 10,000 person-dives in different diving communities[4]. In comparison, the occurrence rate of iatrogenic bubbles in clinical settings was estimated at 0.03/1000 hospitalizations[5], while another study reported approximately 50 times higher rates, at about 1.3/1000[6]. More recent works report varied, *and* higher incidence of gas embolism, especially due to iatrogenic causes, such as from 0.005% for the more serious systemic AGE [7], 10-50% for the often less serious venous gas embolism (VGE) during hysteroscopy[8] , and up to 50% for cases of pediatric laparoscopic appendectomy[9].

Large variability also exists regarding the outcomes of gas embolism. Clinical cases with delayed therapeutic interventions were associated with mortality of up to 33% and severe neurological sequelae of up to 35%[10]. While the frequency of gas embolism in initially non-problematic exposures was not quantified, existing studies[11] suggest that these can evolve in situations with

difficult outcomes. These figures were claimed to increase significantly, potentially reaching as high as 23% for venous cases[12]. Moreover, recent investigations asserted that incidence rates can range between 10 to 80% of all neurosurgeries, and 57% of all orthopedic surgeries, with patients exhibiting either clear or ambiguous clinical effects[13]. Examples of medical procedures that carry the greatest risks of iatrogenic (medically caused) gas bubble formation are caesarean section, hip replacement surgery, craniotomy performed on the patient in the sitting position, and cardiac surgery with cardiopulmonary bypass[1]. A study on cerebral gas embolism attributed its causes to central venous catheterization (22%), cardiopulmonary bypass (19%), lung biopsy (10%), angiography/contrast injection (5%), endoscopic retrograde cholangial-pancreatography (6%), hemodialysis (6%), and mechanical ventilation (6%)[14]. Additionally, the medical history of a patient has been shown to have an impact on disease progression; those who experienced cardiac arrest exhibited a mortality rate of 54%, compared to those who did not suffer cardiac arrest who had a mortality rate of 14%[10]. One problem with all these studies is that they report outcomes post-gas embolism event, and very rarely report on systematic studies, such as a recent experimental study using CO_2 laparoscopy on pigs[15], which reports 60% mortality.

Despite acknowledgements[16-18] that gas embolism is one of the most critical and pressing issues in acute and critical care units, the related scientific interest is low and decreasing in relative terms, and stagnant in absolute terms (in the context of an exponential yearly increase in medical reports in the literature). Figure 1.1 presents the comparative evolution of the ratio of the reports regarding gas embolism, and that of thromboembolism, per 1000 medical reports. It can be easily observed that after the 1950s the interest in gas embolism started to decline whereas the interest in thromboembolism is steadily increasing (consistently after the 1980s). Several sets of problems, many ‘Catch 22’ style, some fundamental, some technological, and some socio-cultural, synergistically conspire to this low intensity of research, especially for a medical condition with unpredictable outcomes, and one increasingly triggered by invasive medical procedures. The attention thromboembolism receives in published studies is likely related to the better understanding of the mechanisms and the availability of effective treatments, but unfortunately, the opposite is true about gas embolism.

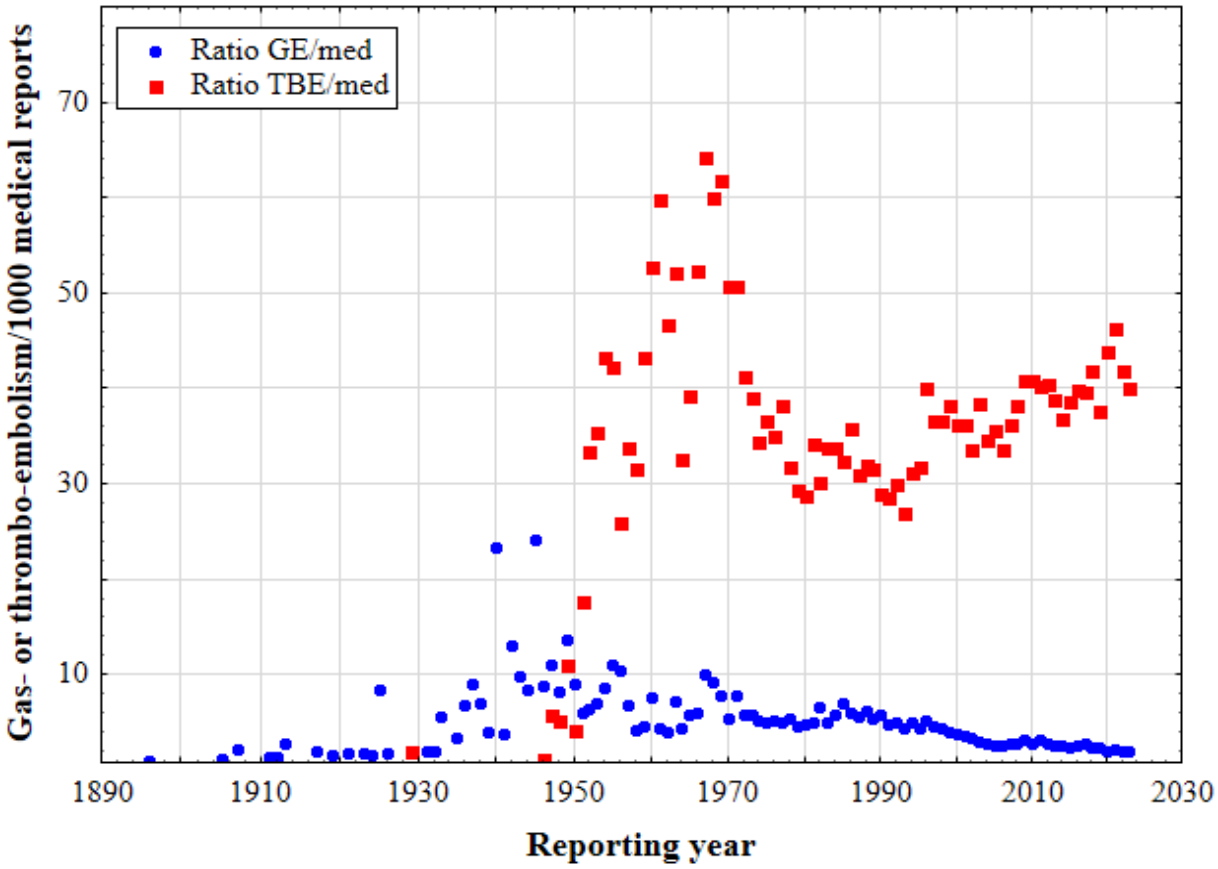

Figure 1.1. Evolution of the ratio of reports of gas- (GE) and thrombo-embolism (TBE) per 1,000 medical (med) reports obtained from literature.

First, fundamentally, because the genesis of gas emboli is near instantaneous, their size is relatively small, and their location is difficult to pinpoint (other than, obviously, with localized insertion of gas), the imaging of gas emboli is very difficult. Indeed, presently there are no reports of imaging of the genesis of gas emboli in humans, compared with the imaging post-event, in many cases on dead patients. It is generally accepted that severe cases of gas embolism represent a small proportion of the total cases, many of which are unnoticed, especially due to being removed by the pulmonary bubble filter (an exception is if the patient is undergoing general anesthesia when neurologic effects may be detected only after emergence from anesthesia). However, the mere recognition of high mortality and devastating neurological sequelae, even for a small proportion of cases, makes it impossible to justify clinical trials, or even animal trials, as a large population would be expected to find the allegedly small percentage of severe cases. An example of this conundrum is exemplified by a recent report[9], which methodically used ultrasound imaging to

detect cases of gas embolism after pediatric laparoscopic appendectomy. While this work reported a much higher incidence of gas embolism, i.e., 50%, this represents half of the small population of only 10 patients. Similarly, another study[15], which reported 60% mortality in pigs exposed to experimental CO_2 laparoscopy, used a very small statistical population (10 pigs).

Second, from the technological point of view, no biochemical diagnostics currently exists to quickly identify gas embolism, especially when symptoms can be easily attributed to other medical conditions. Worse, the only available treatment is hyperbaric oxygen therapy (HBOT), which requires access to limited resources. Furthermore, the lack of diagnostics does not encourage the study of easily accessible treatment, and the lack of (easily accessible) treatment does not encourage the development of diagnostics.

Third, there are additional clinical problems in the healthcare setting. The effects of AGE may be so catastrophic and require such intensive resuscitation that the true diagnosis may not be considered in a timely manner. Also, the patient may be so unstable that it is challenging to investigate, for example, by computed tomography (CT) scans of the brain. And finally, even if the diagnosis is suspected or confirmed by CT scan, there may be concerns about the practicality and safety of transfer to a hyperbaric chamber facility, especially if this is distant or involves air transportation where, if sea level pressure is not maintained, bubbles will grow with altitude. The situation in diving is different. The diagnosis is likely to be suspected quickly. However, many victims will develop pain, paralysis, and/or loss of consciousness after inadequate decompression during surfacing. This is much more challenging than when cerebral gas embolism occurs in a hospital and often drowning will occur. If initial interventions succeed, the focus will be on transfer to a hyperbaric chamber. In all cases, where neurologic symptoms or signs are present, and the circumstances suggest cerebral AGE, imaging cannot be justified if it will lead to a delay in transfer to HBO therapy.

The present work will review the basics of gas embolism, and using this background, progress to report recent advancements in the studies of gas embolism *in vitro*, using microfluidics networks mimicking microvasculature and the conditions leading to gas embolism.

1.2.3. Gas Embolism

Vascular gas embolism occurs when one or more gas bubbles are introduced or generated within the venous or arterial networks. The gas sources can be mainly attributed to (i) intravascular bubble formation following a rapid reduction in ambient pressure experienced in diving or aerospace, due to expansion of existing gas and rupture of pulmonary tissue or de novo in supersaturated tissues that are overburdened with gas content[19], (ii) accidental or intentional introduction of gases into the circulatory system during medical or surgical procedures[20], (iii) accidental injection of gas through non-medical means, e.g., industrial equipment, or (iv) penetrating trauma to gas-containing organs[21]. Any of these factors can not only disrupt blood and oxygen delivery to vital organs but also initiate a cascade of adverse biological effects[22].

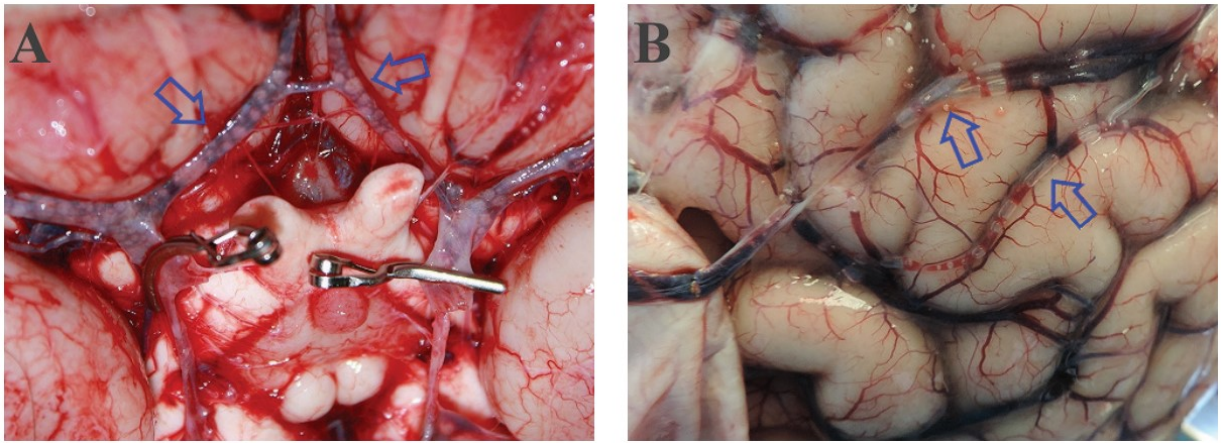

Figure 1.2. A. Cerebral AGE in diving fatality, with spherical air bubbles in the circulus arteriosus cerebri (arrows). **B.** Iatrogenic cerebral arterial air embolism due to forceful cardiopulmonary resuscitation with over-pressure lung damage. Cylindrical gas bubbles with semi-spherical end caps in the dural vessels (arrows). Reproduced with permission from [23].

A key factor determining the clinical consequences of VGE is the effectiveness of the pulmonary "bubble filter" in preventing gas emboli from crossing from the venous (right heart) to the arterial (left heart) side of the circulation. A further key factor is the presence of any cardiac or pulmonary abnormalities that result in right-to-left shunts that enables some blood to bypass the lung bubble filter.

1.2.3.1.Medical Perspective

Venous gas embolism occurs when gas bubbles are present in the venous system, while arterial gas embolism pertains to bubbles in the arterial network. However, it is important to note that gas emboli may not form where they are found as blood is constantly flowing. For example, venous gas emboli may be arterialized if they are not filtered out in the pulmonary capillary bed or if they cross from right-to-left heart through a patent foramen ovale (PFO). For atmospheric gases to enter an open system, there must be an opening in a vessel that is exposed to the atmosphere or other gas space, and a pressure gradient that favors gas entry[24]. Consequently, exposed blood vessels that have negative pressures in comparison with ambient conditions are at risk of gas embolism. Injury to blood vessels will normally lead to at least some degree of constriction of the vessel due to contraction of smooth muscle fibres in the vessel wall and this is a physiologic response to help reduce or stop bleeding along with the formation of blood clots. However, veins in some locations that are at a negative pressure compared to atmospheric may be held open by surrounding tissues. An example is at the base of the skull where cranial surgery in the sitting position may lead to significant venous gas embolism due to the tendency of bone and fascia to splint veins open resulting in entrainment of air. Another example is the disconnection of a central venous catheter where the catheter itself both splints open the central vein and acts as a pathway to entrain air especially when inspiration creates a negative pressure inside the chest that is transmitted to the central veins which then literally suck in air through the open end of the catheter.

In most cases of venous gas embolism, the pulmonary capillaries act as natural bubble filters that prevent the passage of venous gas bubbles into the arterial circulation. However, severe venous gas embolism may lead to froth formation within the heart, thereby causing inefficient pumping and shortness of breath (“chokes”). Also, venous gas embolism results in increased pressures in the right heart and pulmonary arteries, and reduced cardiac output[25]. When there is a PFO, which is present in approximately 20% of the population[26], or any other defect that can lead to a right-to-left shunt, venous bubbles may cross to the left heart and then enter the arterial system as an arterial gas embolism[1]. Increases in pulmonary artery pressures may contribute to such right-to-left shunting. Straining efforts, such as coughing, or during a Valsalva maneuver[27], may also cause shunting due to opening of a PFO. Transpulmonary shunting can also occur independent of PFO, with the likelihood of crossover increasing with exercise intensity[28]. Shunting can take

place even in the absence of increased pressure on the right side, depending on the size of the PFO or transpulmonary shunt. Serious consequences can occur if the left heart pumps these bubbles to the brain, spinal cord, or coronary arteries[1, 29]. In general, the symptoms of arterial gas embolism depend on the affected vessels and the degree of collateral blood supply, but they could resemble those of a stroke or heart attack[30].

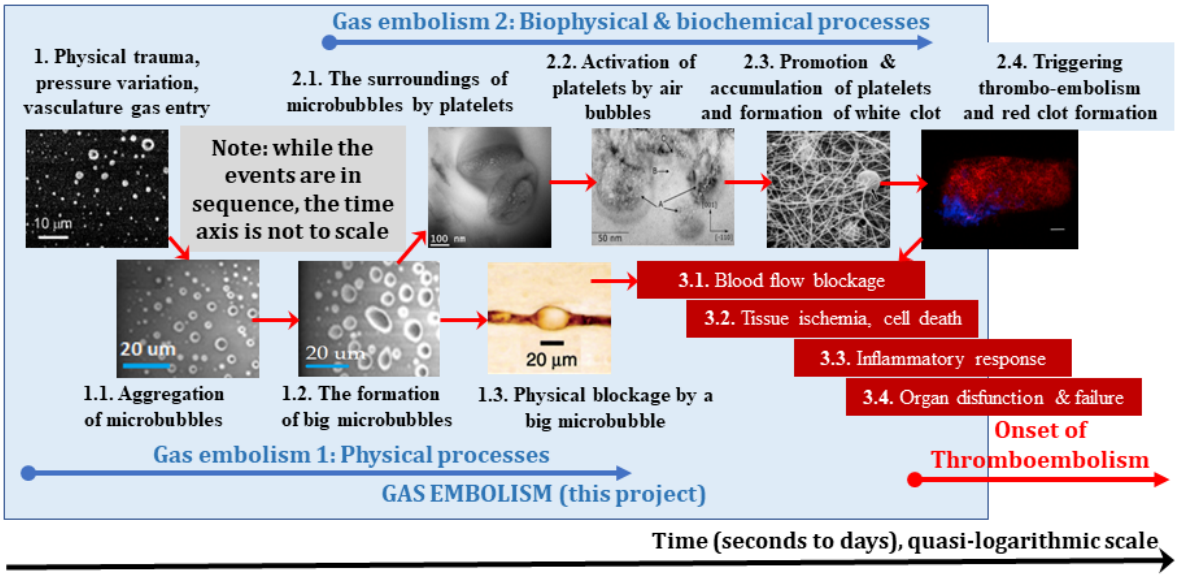

Figure 1.3. Gas embolism: abiotically (bottom) and biophysical/chemical (top) processes. The time until organ failure ranges from < 3 minutes for the brain, to 24-72 hours for muscles. Microscopy images reprinted with permission from [31-36].

Spinal cord embolism is a different yet related phenomenon that typically involves a combination of arterial and venous obstructions with grey matter damage and inflammation[37]. This leads to impaired function, i.e., venous infarction, due to bubbles affecting the venous drainage network of the spinal cord by causing arterial backpressure[37]. Thromboembolism, on the other hand, is the lodging of a solid thrombus, i.e., a blood clot, inside a blood vessel, more able to cause a blockage than can gas embolism due to its highly distortable nature. In some cases, gas embolism can trigger the formation of thromboembolism due to the formation of blood clots on the tail of lodged gas bubbles, leading to the ultimate creation of a solid thrombus. Vascular gas embolism remains significantly less prominent in medical and scientific literature, which could be due to difficulties associated with its imaging, diagnosis, and treatment.

Essentially, there are two paths leading to the limiting blood flow and O_2 transport: the faster physical path, leading to mechanical blockage (bottom path in Figure 1.3); and a slower, parallel (top) cascade of biochemical processes, leading to blockages that are biological in nature, i.e., white clots (containing platelets, fibrin, white, and red blood cells, in this order[38]), and eventually red clots (containing a higher ration of red blood cells, the latter similar to thromboembolism). While the sequence of stages is generally accepted[2], the actual, even approximate timeline is unknown. The activation of platelets by air bubbles was demonstrated *in vitro*, with a timeline of 180 min, but in bulk and in static conditions[39].

1.2.3.2.Global Gas Embolism

Endogenous gas sources refer to gases that are present within the body, either in blood, or within gas-containing organs, such as the lungs, or in saturated tissues. Blood and tissues can become supersaturated with excess gas loads, e.g., nitrogen, helium, and other gases used in diving, upon decompression from elevated ambient pressures. Excessive levels of supersaturation can lead to *global* gas formation, in which the accumulation of gases, primarily the inert gases, during exposure to high pressures, such as in diving[29], is followed by a decrease of ambient pressure during return to the surface. While slow decompression can allow dissolved gas to be released to the lungs without formation of gas phase, rapid decompression can lead to gas phase (bubble) formation. This can occur in any sufficiently supersaturated tissues, causing direct irritation or injury through tissue distortion and/or activation of secondary biochemical effects that may ultimately elicit clinical signs and symptoms. DCS can also arise in high altitude activities, such as with acute loss of cabin pressure in aviation or during astronaut decompression in preparation for or conduct of extravehicular activity[40]. Bubbles may create insults as autochthonous agents in the tissues where they form, or in other tissues to which they migrate, with the vascular path as the primary avenue for migration. The incidence of DCS varies, with reported rates ranging from 0.3 to 35 cases per 10,000 dives, varying substantially with the type of diving[4].

Gas may also be introduced from the pulmonary alveoli through the rupture of pulmonary tissue. Gas phase under the skin is known a subcutaneous emphysema, and gas phase entering the vascular path as AGE.

Decompression illness (DCI) is a collective term that encompasses DCS and AGE. The blanket term acknowledges that differentiation is sometimes difficult, and that the two events can

sometimes be seen together. DCS is an insult due to inadequate decompression, and some period of time before a too rapid depressurization. AGE is not dependent on the duration of time at a particular pressure but rather results from overpressure or direct trauma to the lungs and introduction of gas into the circulation.

Decompression stress is facilitated by micronuclei, acting as nucleation sites, that facilitate bubble formation at relatively low levels of supersaturation. Autochthonous bubble formation is likely not a primary instigator for symptoms associated with AGE since it would require considerably larger gas volumes than those expected. The nature and origins of micronuclei remain unknown[19], and ultrasound and direct visualization techniques offer tools for *in vivo* and *in vitro* investigations, respectively[41-45].

1.2.3.3.Local Gas Embolism

Local gas embolism occurs when gas bubbles enter the bloodstream from *exogenous* gas sources, especially in clinical settings, or are created *in situ* by localized variation of pressure, ranging from a particular blood vessel, up to an organ, e.g., lungs. *Exogenous* gases are introduced into the body from external sources of either atmospheric or pressurized (medical or non-medical) gases. One example is when ambient air is drawn into an open vein[1]. Trauma to gas-containing organs can also lead to intravascular bubbles, such as blunt thoracic trauma, forceful cardiopulmonary resuscitation, lung over-expansion injury, air injection through industrial tools, and even childbirth[46-50].

“Iatrogenic” gas embolism refers to the introduction of gas through medical activities, potentially by a wide range of medical procedures and surgical interventions[51], e.g., angiography, hemodialysis, lung biopsy, central venous catheterization, cardiac bypass procedure, laparoscopy, endoscopy, and laser ablation surgery[14, 52, 53]. Clinical reports suggest that injecting more than 100 mL of air into the venous system at rates greater than 100 mL/s can be fatal[54]. The range of symptoms that could manifest in these patients include respiratory distress, lung damage, cardiac arrest, and hypoxia[1]. A recent study investigating the risks of carbon dioxide insufflation, a procedure routinely performed during laparoscopic surgery, found that inadvertent placement of the gas insufflation needle near a blood vessel or organ may not only increase the potential for silent gas injection, but also lead to the formation of gas bubbles[55]. Despite carbon dioxide being

20 times more soluble in blood than oxygen, the mortality rate of pigs with venous carbon dioxide embolism was found to be 60% for a continuous intravenous infusion rate of 1.2 mL/kg/min[55].

Local gas embolism can also result from rupture, tearing, or damage to gas-containing organs, such as the lungs, gastro-intestinal tracts, and sinus cavities[56-58]. This phenomenon is observed in pulmonary barotrauma, which is characterized by the rupture of lung tissue, occurring in multiple scenarios that include rapid depressurization with insufficient ventilation to control pulmonary pressures. It can lead to AGE due to direct gas entry into the pulmonary capillaries and venules. For instance, underwater divers who rapidly ascend while holding their breath can provoke lung rupture[59]. Pressure gradients play a crucial role in this process, driving the expansion of air in the lungs during changes in ambient pressure. With expansion, the pulmonary tissue continues to enlarge until the tensile strength limit is exceeded[60, 61]. This results in alveolar rupture, allowing gas from the lungs to enter the venous pulmonary circulation that travels to the left side of the heart. From there, the gas can circulate throughout the body via the systemic arteries[62]. Remarkably, pulmonary tissue rupture can occur in individuals ascending from depths as shallow as 1.2 meters if starting with a full lung volume[62].

1.2.3.4.Prevention, Diagnostics, and Therapy of Gas Embolism

The clinical effects of AGE are largely determined by the site(s) of bubble introduction, the volume introduced, movement through the vascular system, and subsequent local effects. Accurate diagnosis is typically contingent on recognizing the symptoms of this condition, often manifesting as neurological complications, while evaluating the relevant context and circumstances of the patient. There are multiple instances where patients suddenly exhibit a combination of clinical symptoms, such as dyspnea, coughing, and chest pain, or neurological symptoms that can include seizures, fainting, mental status shifts, and focal neurological deficits, such as hemiparesis, and hemiplegia[24]. For example, disconnection of an upper body central venous catheter without clamping may result in air entrainment when patient inspiration creates a negative pressure in the chest and central veins. While a known risk associated with underwater diving, gas embolism may not be suspected in other circumstances by healthcare professionals who lack familiarity with this medical occurrence. The earliest indicators of gas embolism may be reduced end-tidal carbon dioxide measurements for patients under anesthesia[24], whereas a later sign is clinical cyanosis (blue coloration) or low oxygen saturation on the pulse oximeter monitor levels[63]. By the time

oxygen saturation is dramatically reduced, generated gas bubbles may have already progressed to the point of causing substantial harm. AGE, if affecting the coronary arteries or central nervous system, may exhibit a rapid onset with severe clinical effects. The contribution of bubbles may not be suspected, and treatment may be delayed or insufficient.

The initial management of this condition includes preventing further gas entry in iatrogenic and trauma-related conditions, administering 100% oxygen to facilitate inert gas elimination and improve oxygenation, and providing supportive care (airway, ventilation, hemodynamic). Upright postures of the victim promotes distribution of bubbles to the brain due to buoyancy effects and therefore supine positioning is preferred[13]. Durant's maneuver, (head-down left lateral position) may be considered for large volume venous air embolism but not for cerebral arterial gas embolism (CAGE) as it increases the risks of brain oedema[64, 65]. Additional procedures may also be required, including air aspiration from the central circulation[66], cardiopulmonary resuscitation[67], and chest tube for pneumothorax.

While 100% oxygen may improve symptoms and signs of AGE the only definitive therapy available today is HBOT, where the patient is placed inside a hyperbaric chamber to breathe pure oxygen at elevated pressures. Standard treatment tables exist for different conditions and some for different presentations[68, 69]. The administration of 100% oxygen can reduce the size of bubbles and produce a steep gradient favoring elimination of inert gas. Treatment also provides oxygen to ischemic organs, such as the brain, and decreases cerebral oedema[24]. It can also minimize the inflammation that arises from the action, and that which may persist long after bubbles have been resorbed.

The relatively small number of facilities able to provide HBOT is a problem. There are additional challenges associated with patient transportation, especially since air transport poses a risk of depressurization, and consequently, bubble expansion. Alternatives include ground transportation or transport in aircraft able to maintain low altitude flight or to maintain near-ground level cabin pressure. In cases where gas embolism is suspected, CT imaging may be used to confirm the presence of macro-bubbles in vital organs, such as the heart or brain. It is crucial to emphasize that therapeutic intervention should not be delayed while waiting for such scans, provided that the clinical diagnosis is clear. In these circumstances, prompt treatment with hyperbaric oxygen, if available can be lifesaving and take precedence over diagnostic imaging. Supportive care and 100% oxygen are primary support during transport to a hyperbaric facility and in situations where

definitive care is not possible. In the context of addressing these challenges, exploring microscale structures to assess the efficacy of HBO becomes an intriguing avenue for potential research.

1.2.4. Preconditions for Mimicking Microvasculature

Microfluidics-based devices recently evolved from the now classical lab-on-a-chip devices for diagnostics[70] and for high throughput screening[71], into more complex "organoids-on-a-chip", which mimic physiologically-representative mini-organs, such as lungs[72-77]. Microfluidic platforms have been progressively moving to the forefront of artificial methods for disease modelling due to their ability to not only simulate a controlled microenvironment, most relevant as organs-on-a-chip[78], but also provide real-time monitoring of disease initiation and progression in close-to-real-life situations. This could be particularly useful for gas embolism because (i) the onset is sudden and difficult to examine in live humans, or even in animals; and (ii) gas embolism is initially a physical phenomenon that requires detailed understanding to reduce subsequent biological effects. Microfluidic devices can be designed to mimic blood vessels and biological tissue for the study of gas bubble formation at the onset of different nucleation sites. Vascular geometry and biomimetic fluid circulation play important roles in the genesis, evolution, and resolution of microbubbles. While the topography and hydrophobic heterogeneity of vascular surfaces form potential bubble nucleation sites[79]. Despite its rather mature development, microfluidics methodology has not been widely used to investigate gas embolism, perhaps reflecting the under-reporting of gas embolism in medical literature or the novelty of the approach. In the following sections we shall analyse the opportunities and the challenges of mimicking gas embolism process in microfluidics systems.

1.2.4.1.Material Properties

The first question in considering the mimicking of the microvasculature by microfluidics is if the mechanical and physico-chemical properties, such as surface tension and gas diffusivity, of the materials used match those of vasculature. Poly-di(methyl-di-siloxane), commonly referred to as PDMS, is the most widely used polymer for the fabrication of biomimetic devices due to its biocompatibility, gas permeability, optical transparency, ease of replication, precise microfabrication[80], and inherent properties that are amenable to blood vessel simulation[81, 82]. Material properties pertaining to different sections of vascular channels may be engineered through

the adjustment of mechanical and physiochemical characteristics of PDMS. This involves varying the molecular weights and curing protocols of the elastomer kit, to mimic the properties of blood vessels, according to venous, ~~or~~ arterial or capillary physiological dimensions, biological age, sex, and medical history.

Table 1.1. Comparison of physical and mechanical properties of blood vessels with PDMS.

Material Properties	Biological Vascular Walls	PDMS-Based Vascular Walls
Young's modulus	0.04 MPa – 2 MPa (abdominal aorta)[83] 0.05 MPa – 1.45 MPa (iliac artery) [83]	0.05 MPa – 2 MPa[84] Tunable to 5 MPa[85] by varying the ratio of PDMS base elastomer to curing agent
Oxygen diffusivity	3.4 x 10-5 cm^2/s under atmospheric conditions[86, 87]	~ 10^{-6} cm^2/s for 10:1 PDMS Tunable by varying the ratio of PDMS base elastomer to curing agent[88]
Hydrophilicity and hydrophobicity	75° ± 20° (advancing) 65° ± 20° (receding) arteries and veins	75° ± 15° (advancing) 60° ± 20° (receding)
Nucleation sites	Varies depending on blood type of blood vessels	Beads embedded on PDMS surfaces

More specifically, Young's modulus of PDMS is closely related to the measured values of the mechanical properties of human blood vessels. It has been reported that, depending of the composition of the pre-polymer and curing protocols, PDMS has a Young's modulus within the range of 0.05 to 2 MPa[84, 89], and goes up to 5 MPa[85, 90], in comparison with 0.05 to 2 MPa for human veins[91], 0.04 to 2 MPa for abdominal aorta sections[83], 0.05 to 1.45 MPa for iliac arteries[83, 92], and up to 5 MPa for cerebral arteries[91]. In terms of gas diffusivity, the diffusion coefficients of oxygen and nitrogen are reported as 3.4 x 10^{-5} cm^2/s[93] and 4.1 × 10^{-5} cm^2/s[94] in PDMS, respectively, at 35°C. These values can be modulated by composition and curing

processing to the approximate rate of gas diffusion in blood vessels, i.e., 10^{-6} cm^2/s[95], and human tissues in general, i.e., 1.1 x 10^{-4} to 4 x 10^{-8} cm^2/s[96]. Table 1.1 summarizes these parameters.

1.2.4.2.Microvasculature versus Microfluidics Geometry

The intricacies of vascular network mimicry require a comprehensive understanding of the considerable variability exhibited by blood vessels in the human body in accordance with diverse biological factors. The width of different sections of the vascular system spans, approximately, from 4 mm for arteries, 30 μm for arterioles, 2 μm for capillaries, 10-30 μm for venules, to 0.5 mm for veins[97, 98]. While vascular wall thicknesses are approximately 1 mm for arteries, 20 μm for arterioles, 1 μm for capillaries, 20 μm for venules, and 5 mm for veins[97, 98]. To replicate these intricate networks, microfluidic devices are typically fabricated via the generation of a master mold, which is the negative 3D image of the mimicked blood vessels. These masters can be fabricated using various technologies, the most used being photolithography using SU8 negative resist[99], which is exposed, baked (leading to its crosslinking in the exposed pattern), followed by the dissolution ("development") of unexposed areas. Negative tone photolithography has the advantage of generating the necessary negative relief directly, made of crosslinked SU8 photoresist on a silicon wafer surface[100]. SU8 lithography has severe limitations of printing features around one micron or less, this does not appear as a problem for the mimicking of blood vessels. Alternatively, the master can be fabricated using positive patterning, either deep ultraviolet, or e-beam lithography[101], which generate, upon exposure and development, a 'resist mask' on the surface of a silicon wafer, which is subsequently etched in areas not covered by the resist mask, usually by reactive-ion etching. While these technologies are more expensive, the quality of the masters made of silicon is superior to those made of SU8[102], i.e., there are more precise, near-perfect profiles, and can be used essentially indefinitely. The final step of the fabrication consists in the replication of the negative master by pouring the PDMS pre-polymer, crosslinking by curing, peeling-off, plasma treatment, and then sealing the stamp on a surface (usually a transparent glass microscope slide). The optimization of fabrication conditions is a critical step in the replication of designed structures, involving testing different combinations of spin coating speeds, soft baking conditions, duration, and power of the of exposure, and hard baking conditions to ensure high accuracy.

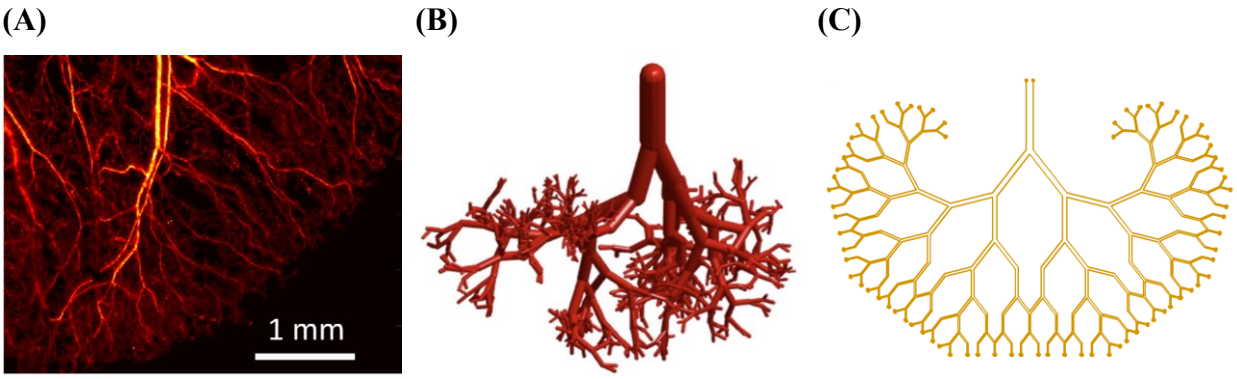

Figure 1.4. Comparison between real and artificial blood vessels. The artificial network is designed according to Murray's law of bifurcation, in accordance with the real network. **A.** The actual microvasculature within the mouse ear[103]. **B.** A three-dimensional rendering of the artificial microvasculature modelled according to Murray's law of bifurcation[104]. **C.** A two-dimensional representation depicting the adherence of artificial blood vessels to Murray's law of bifurcation. Images (A) and (B) reproduced with permission from [103, 104].

The present microfabrication technologies can be used to obtain essentially any desired network mimicking microvasculature, the only limitation being that the networks must have a two-dimensional (2D) geometry, which not only required by planar lithography, but also by the requirement of visualization of the phenomena in the mimicked microvasculature. Although three-dimensional (3D) networks can be fabricated with a resolution of around 30 μm, the inner visualization of these networks is near-impossible.

1.2.4.3.Surfaces of Blood Vessels

The first pre-condition of the artificial structures mimicking blood vessels is to ensure that the overall surface tension of the inner walls of the artificial blood vessels (usually measured by the contact angle made by a water micro-droplet on a surface), is similar to that of the biological models. The surface tension of PDMS, the primary material used in bio-mimicked structures, was compared with the contact angle of animal blood vessels. Contact angles were assessed for six blood vessels obtained from sheep, namely the aorta (AO), pulmonary artery (PA), pulmonary vein (PV), right atrium (RA), left atrium (LA), and superior vena cava (SVC) [105]. Furthermore, contact angle measurements for water, water/glycerol, porcine plasma, and porcine 46% hematocrit on the surface of PDMS (Figure 1.5B) exhibit a strong similarity with those for the real blood vessels.

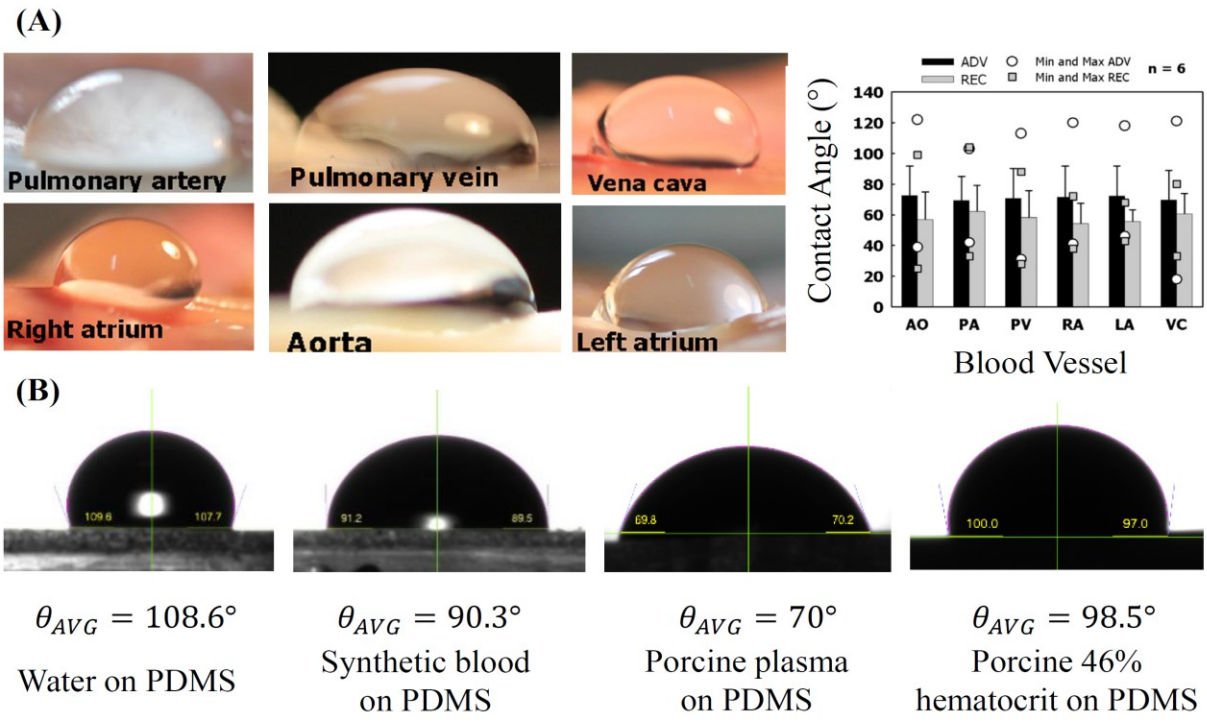

Figure 1.5. A. Contact angles were measured for six blood vessels obtained from sheep, including aorta (AO), pulmonary artery (PA), pulmonary vein (PV), right atrium (RA), left atrium (LA), and superior vena cava (VC)). The graph bars represent the mean ± standard deviation. Circles (ADV) and squares (REC) denote the minimal (Min) and maximal (Max) values, respectively[105]. **B.** Contact angle measurements were performed for water, water/glycerol, porcine plasma, and porcine 46% hematocrit on the surface of PDMS. Images and graph in (A) reproduced with permission from [105].

The second pre-condition of mimicking blood vessels is to achieve a similar biochemical interface between their walls and blood. The walls of blood vessels are 'carpeted' with various proteins, e.g., fibrin, thrombin, collagen, tropoelastin, fibronectin. Consequently, and especially if bio-physico-chemical interactions between the biomolecules and cells in the fluid and the walls are to be studied, the latter must be functionalized with these proteins. Fortunately, a large body of knowledge exists regarding protein adsorption on surfaces, including a comprehensive database[85], as well from knowledge of the impact of the properties of the carrier fluid on adsorbed protein patterns[106]. However, for 'simple' studies regarding the initial stages of gas embolism, which do not involve complicated biomolecular or cell interactions with the walls, the functionalization with a neutral protein, such as bovine serum albumin or casein, or achieving the same surface tension of PDMS walls similar to that of the actual vessels, by tailored plasma treatment, would suffice.

The third pre-condition of mimicking blood vessels is to achieve a similar heterogeneity of the topography, and if needed surface hydrophobicity. While surface topography can be easily achieved using one of the microlithography techniques listed above, the heterogeneity of the surface hydrophobicity, which could be important as it was reported[107] that hydrophobic 'islands' are prime candidates for bubble nucleation is more difficult. Nucleation of gas emboli could be studied on a microfluidic device (Figure 1.6) consisting of a basal optically transparent layer, with patterned hydrophobic islets, i.e., lipid, or lipid-mimicked islets; and a PDMS microfluidic network mimicking microvasculature, functionalized with relevant proteins, capping the basal layer. The patterning of hydrophobic islets can be done by one of the following methods (in Figure 1.6, i-v): (i) a thin layer of hydrophobic PDMS mixed with SiO_2 microbeads is deposited on the basal layer, cured, hydrophilized by plasma treatment, and then let for hydrophobicity to recover strictly on PDMS material, thus resulting in a layer of hydrophilic beads (if high enough concentration) with hydrophobic islands in between[108]; (ii) a thin, still transparent Au layer is patterned by e-beam lithography, resulting in Au islands in a 'glass sea', subsequently functionalized by Au- and glass-specific SAMs, with hydrophobic, and hydrophilic terminal groups, respectively[109]; (iii) patterning hydrophobic islets by microcontact printing with pyramidal PDMS stamps[110]; (iv) mounting hydrophobic beads on top of PDMS micro-pyramids on a flat PDMS layer[84]; and the most straightforward, the surest, but also the most time consuming (v) "negative lithography" consisting of selectively ablating large portions of a lipid layer deposited on a glass surface by laser micro-ablation[111, 112]. The relatively large dimensions of lipid islets, i.e., around 1 mm[107], do not raise patterning difficulties. Furthermore, capitalizing on laser microablation being relatively unconstrained by the nature of the layer to be ablated[112, 113], this methodology will be also used to tentatively generate patterns of artificial blood clots by selective ablation of coagulated blood, for future studies on thromboembolism.

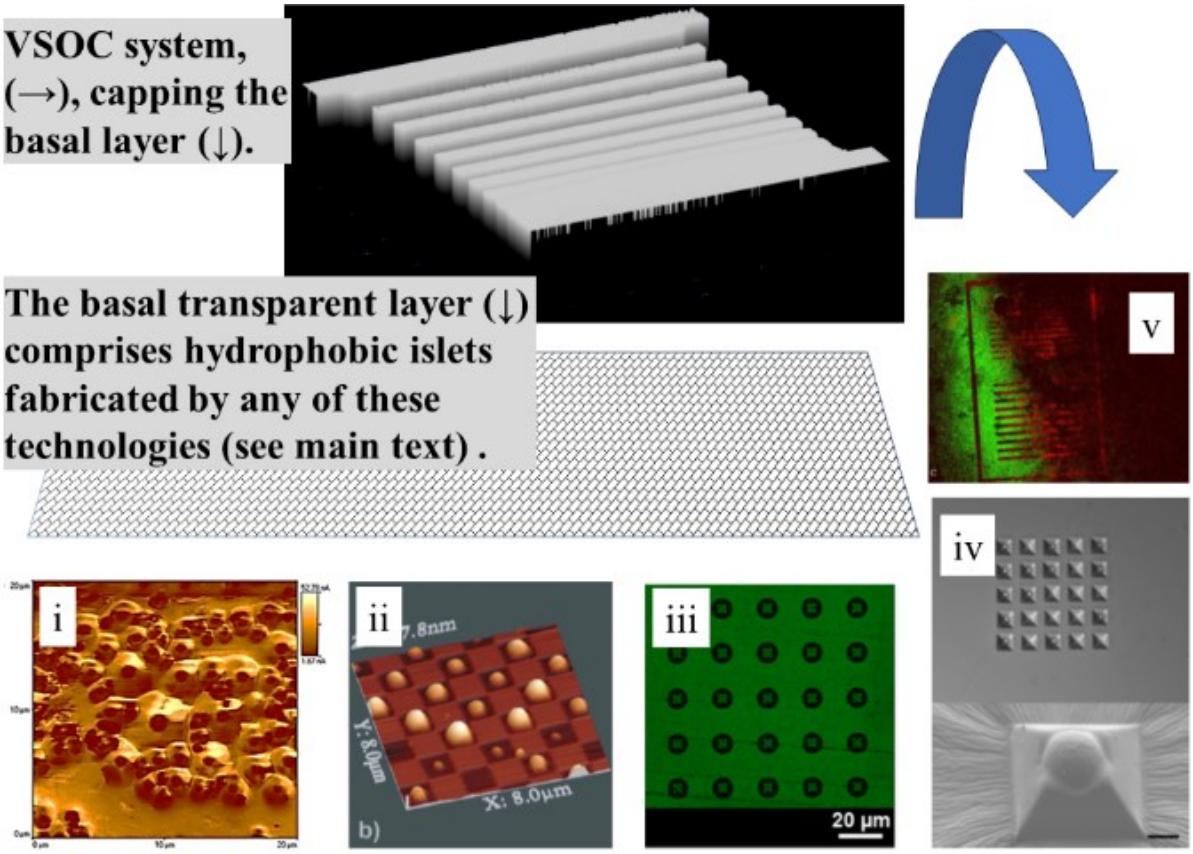

Figure 1.6. Possible device for the study of emboli nucleation on lipid islets printed on a basal layer, capped by a PDMS structure (flipped) mimicking blood vessels. Microscopy images (i) to (v) reproduced with permission from [84, 108, 114-116].

1.2.4.4.Blood Analogues

The practical challenges associated with using real blood in experimental studies, such as cost, accessibility, storage constraints, and ethical concerns, prompted the development of synthetic blood solutions for *in vitro* hemodynamic research. These analogues aim to closely mimic the rheological properties of real blood, including the dynamic viscosity, shear-thinning behavior, and refractive index[83, 117]. To achieve this, aqueous solutions are formulated, starting with a base mixture of distilled water and glycerine. Specific concentrations of xanthan gum are then added to replicate the viscous and elastic features of blood across a broad range of shear rates. This tailored approach allows for matching different hematocrit concentrations, ranging from 20% to 80%[117]. The graph in Figure 1.7 displays the viscosity and interfacial tension of both synthetic hematocrit preparations and animal blood samples.

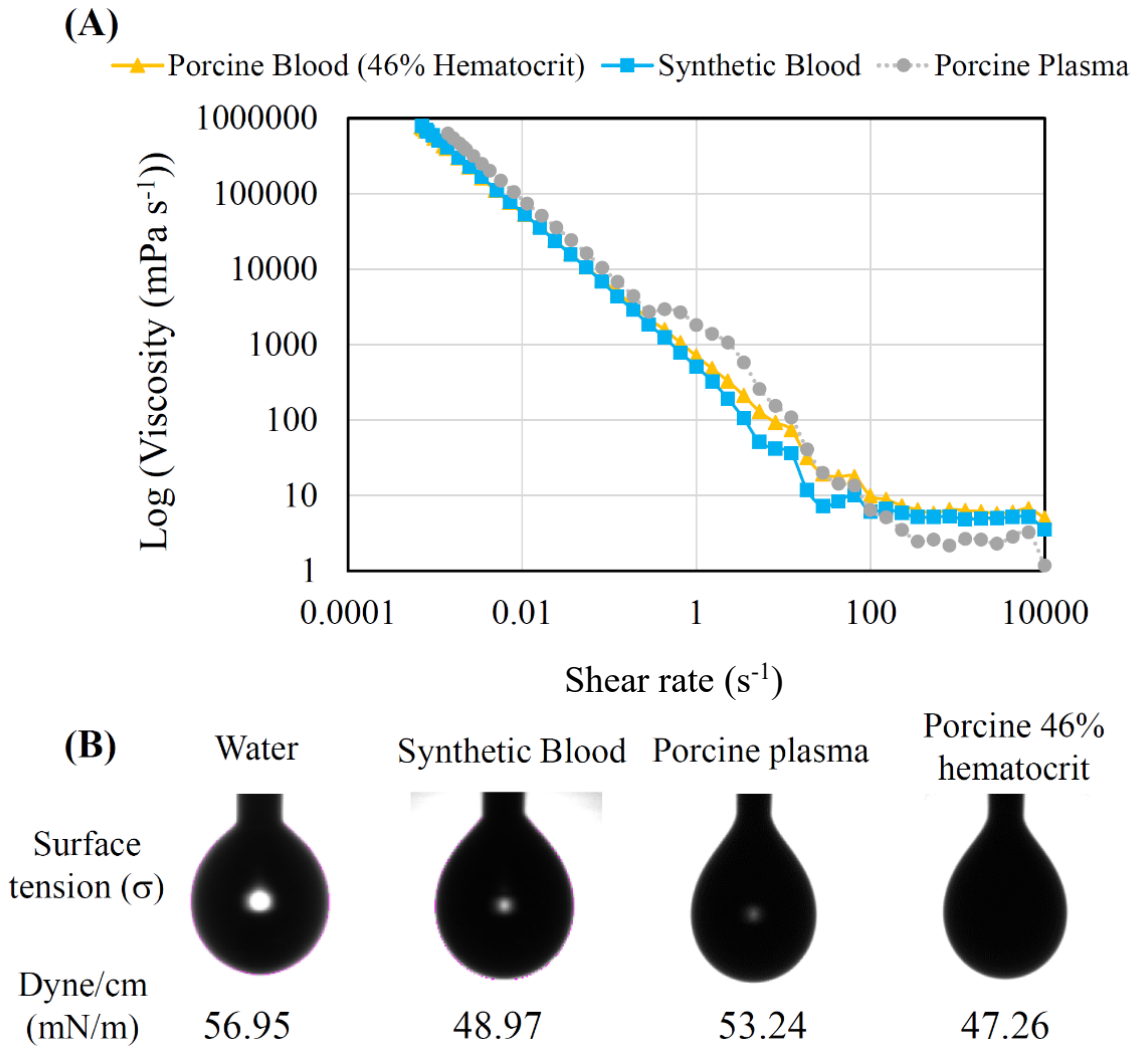

Figure 1.7. A. The graph represents data from viscosity measurements of working fluids and porcine blood (N=3). **B.** The surface tension of the working fluids and porcine blood samples (N=10).

1.2.5. In Vitro Studies of Gas Embolism

Although multiphasic flow in confined channels is a well-studied and understood concept[118, 119], only a limited number of research studies used microfluidic devices to detect, record, and analyze the generation and behavior of gas bubbles, in terms of their evolution, dissipation, and biological effects.

1.2.5.1.Mechanisms of Bubble Generation

The mechanism of bubble formation on a microfluidic chip was reported[120], where a *liquid* droplet generator based on a T-shaped structure consisted of introducing an aqueous solution into a channel filled with an organic fluid. The continuous organic fluid had a stronger affinity for the channel walls, while the water-based fluid was immiscible and repelled by the walls. As a result, when the immiscible, soon-to-be dispersed, fluid entered the main channel, it naturally broke up into small aqueous droplets[120]. The field of microbubble generation within microfluidic channels evolved into three main hydrodynamics-based techniques. The most common method uses a compressed air stream that supersaturates the working liquid with air, before releasing the pressure from the mixture using a specifically designed nozzle system, thereby causing bubble formation based on the principle of cavitation[121-124]. The second approach to creating bubbles in microsystems involves the use of specific geometries where a narrow passage in the main channel constricts the continuous fluid, while the discontinuous fluid is dispensed from a nozzle closely positioned upstream of the constriction at low offset pressures. The converging streamlines of the carrier fluid help in directing and forcing the discontinuous fluid into the orifice[125-128]. A variation of this method can include additional features that substitute the flow focusing geometry to break off the bubbles, such as mechanical vibration or fluidic oscillation[121, 129-132]. The third method induces cavitation using power ultrasound, thereby forming bubbles at points of extreme rarefaction within standing ultrasonic waves[121, 133].

The first microscale system investigating the formation of gas bubbles comprise a Y-junction microchannel designed at biologically relevant length scales to generate bubbles based on a mixture of water and air[134]. The bulk liquid is injected at flow rates between 2 and 3 mL/min to mimic blood circulation in similarly sized vessels, while air is injected at increasingly smaller flow rates than the bulk liquid to produce smaller and fewer bubbles. The bubbles were then classified based on two distinct behaviors as they traverse the bifurcation point to determine the effect of bulk liquid flow rates and bubble sizes on bubble behavior in channels of known widths at Y-shaped branching geometries. The first behavior is determined by complete bubble progression into one of the daughter vessels without division, while the second behavior is the bubble splitting into two smaller bubbles at the bifurcation point.

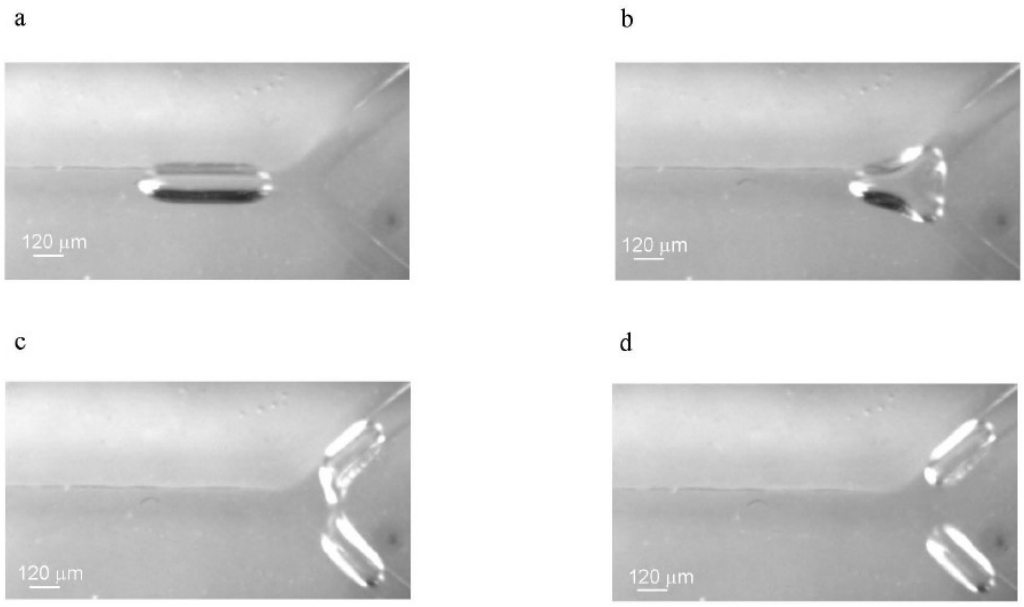

Figure 1.8. Dividing bubble behavior in Y-shaped microfluidic channels. **a.** Large bubbles flowing through the parent channel at the liquid flow rate. **b.** Bubble division as the leading edge of the bubble reaches the bifurcation. **c.** Trailing edge of the bubble continues to reach the bifurcation. **d.** Complete bubble division and flow into both daughter channels. Reproduced with permission from [134].

Another microdevice was used to analyze the origins and evolution mechanisms of bubbles in microchannels fabricated from polymethylmethacrylate (PMMA)[135]. Although this study was not focused on gas embolism mimicry, it succeeded in depicting the importance of liquid flow rate, liquid pressure, and channel surface properties as factors contributing to bubble formation and elimination in microchannels. Since PMMA is impermeable, the bubble sources in the system can be strictly attributed to dissolved gases in the liquid, insoluble gases trapped in the channel cavities, and gases created from the phase change of the liquid[135]. Consequently, the impact of specific free energy and interfacial surface energy changes was investigated in eight microchannels fabricated on a PMMA plate, with a temperature control system for nine individual aluminum heating blocks. It was found that the generation of bubbles is made possible by (i) reducing the fluid pressure, thereby decreasing both the nucleation temperature and the gas solubility within that fluid, (ii) increasing the liquid flow time through the microchannel, which would increase the amount of gained energy at a fixed heating plate temperature, and (iii) modifying the surface properties to increase the hydrophobicity of the channels[135]. These experimental findings

provide a better understanding of gas bubble dynamics, which can be extrapolated to biological systems.

A biomimetic system simulating the geometry of human blood vessels with the circulation of two blood-mimicking solutions at different equivalent hematocrit concentrations was recently reported[136]. The origins of microbubble formation were investigated in a central vascularized channel, surrounded by two pressure chambers undergoing different volumes of air injection. As the amount of injected air increased, intravascular bubbles were generated with more pronounced characteristics due to pressure variations[136]. This study established correlations between input parameters, such as vascular width and equivalent hematocrit concentration, and output parameters, e.g., bubble size, velocity, frequency, and nucleation sites, thereby displaying different patterns based on induced pressures and biological characteristics, including gender and medical history.

The generation of bubbles inside tissues was also made possible through exposure to laser radiation. The ability of laser treatment to produce an intraocular pressure regulating effect in glaucomatous eyes was demonstrated[137] through the formation of stabilizing pores. A system of pores with complex configurations, consisting in areas of reduced density and stiffness, was created following exposure to a 1.56 μm laser. Although gas embolism was not formally discussed, the precursor to this process was the generation of small gas bubbles enriched with Ca^{2+} ions at the gas-fluid interface within laser-treated sclera. These bubbles played a crucial role in maintaining pore stability and preventing their collapse. A subsequent study[138] investigated the effects of the same pore formation procedure on cartilage regeneration. Microphotographs of the laser-irradiated cartilage, obtained using transmission electron microscopy (TEM), revealed simultaneous nanobubble generation, identified as transparent spheroids following laser exposure. While the dynamics of gas bubble formation and evolution were not described, their presence and stability in irradiated tissues were extensively demonstrated.

1.2.5.2.Impact of Bubbles on Fluid Dynamics

Using a microfluidic model of small arteriole bifurcations a study[139] reported on the impact of bubbles modulated by the impact of pressure. Individual air bubbles of specific sizes were injected into the parent channel, their movement was subsequently analyzed based on the driving pressure that was induced across the bifurcation by varying the elevations of two reservoirs connected to

the inlet and outlet. The critical pressures for mobilizing and immobilizing the bubble were found to be directly related to the bubble size. Longer bubbles resulted in higher critical pressures for both effects, with the critical pressure for unlodging being higher than that for lodging[139]. These differences could be attributed to contact angle hysteresis and interactive forces at the interface between the gas bubble and the channel walls.

This work was followed by further research on bubble behavior at bifurcation points of Y-shaped microfluidic channels by correlating the size and movement of gas bubbles in a working fluid with different biomimetic flow rates[134]. The bubbles were first introduced into the parent channels where they continued to circulate with water due to the pressure gradient created by the syringe pump. Upon reaching the Y-junction, two distinct bubble behaviors were determined as a function of size and flow rate: dividing and non-dividing bubbles, with few instances of lodging for daughter bubbles. The likelihood of dividing bubbles was found to be higher if (i) their size was relatively large in comparison with the channel length, and (ii) they are flowing in a liquid with a higher Reynolds number[134]. The structure of larger bubbles was adapted from spherical to sausage shaped, to reduce the interfacial surface area between the gas and the liquid. Since spherical bubbles have the lowest amount of free energy, sausage-shaped bubbles were found to be rather unstable with tendencies to lower their energy through bubble division when given enough momentum[134].

A new level of complexity was introduced in the study of sausage-shaped bubbles, also referred to as tubular or Taylor bubbles, in microfluidic devices by incorporating blood flow into the microchannels[140]. The circulation of these bubbles in microvessels was replicated *in vitro* at low capillary numbers, to determine their impact on blood flow at the cellular level. Their presence led to complex changes in the thickness of cell-free layers and the concentration of red blood cells: (i) downstream of the bubble, cell-free layers were observed along the centerline and near the channel walls due to the migration of red blood cells to an intermediate region between the centerline and the wall; while (ii) upstream of the bubble, less distinct cell-free layers and higher cell concentrations were detected with maximum red blood concentrations being near the walls[140]. This means that microbubbles lead to heterogeneous cellular distributions and can have a significant impact on biological transport processes, such as oxygen delivery and nitric oxide

scavenging by red blood cells. Furthermore, spatial, and temporal variations in blood rheology can have a crucial role in mobilizing and immobilizing these bubbles.

Another level of complexity was added to the same line of work by investigating the effect of bifurcations, i.e., geometric variations, on bubble behavior in microchannels with two types of circulating blood solutions[141]. The flow of gas bubbles through the bifurcating network exhibited similar influences as previous studies on local hematocrit levels, with higher red blood concentrations located upstream than downstream of the bubble. Interestingly, the difference between local cell concentrations before and after bubble passage was more prominent for the 10% than for the 5% hematocrit blood solutions. This inspired further analysis by introducing a third level of complexity in 2020, focusing on the effect of gas bubbles on the local hematocrit level of two types of blood solutions (5% and 10%), in a microfluidic device with three bifurcating networks mimicking a small region of the capillary network[142]. The experimental findings were coherent with the authors' earlier work, whereby (i) a higher concentration of red blood cells was found upstream of the bubble than downstream, (ii) these differences in red blood cell concentrations are more prominent for blood solutions with higher hematocrit levels, and (iii) bubble division will occur for tubular bubbles at Y-junctions, leading to uneven distribution of cells between daughter channels[142].

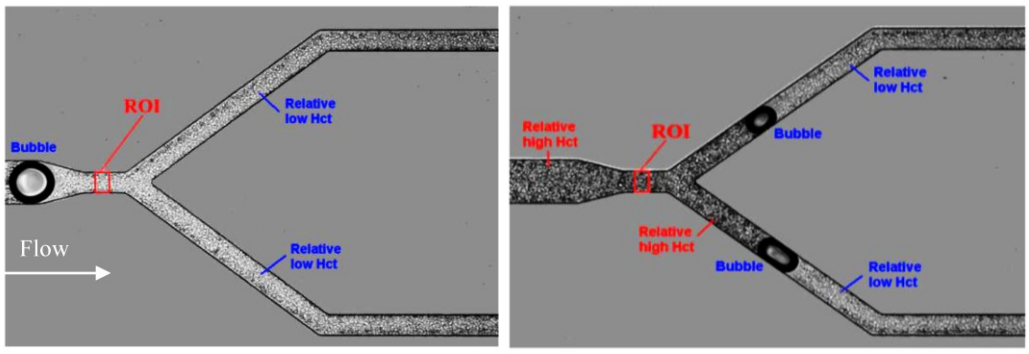

Figure 1.9. Impact of bubble passage on local hematocrit levels, upon air injection in the parent channel and two daughter channels, before and after bubble passage. Reproduced with permission from [142].

The reason behind this non-uniform distribution of red blood cells in the vicinity of gas bubbles was not fully explored until recent research efforts introduced a set of *in vivo* and *in vitro* experiments to investigate the stopping mechanism of Taylor bubbles[143]. Microfluidic devices with T-junctions were fabricated to provide a clear observation of bubble motion in small vessels

and to determine the factors leading to its immobilization. Microchannels were coated with bovine serum albumin to prevent blood coagulation, and fibrinogens contained in the blood solution were labelled to emit red fluorescence upon cross-linking with fibrin. It was determined that flow recirculation was the driving mechanism behind red blood cell aggregation downstream of the bubble; two recirculation zones at the tail of the bubble were bringing blood cells onto the bubble surface, while two recirculation zones on the head of the bubble were pushing blood cells away from the bubble surface[143]. This ultimately leads to the formation of a blood clot downstream of the bubble, which continues to grow until it breaks the lubrication film between the surface of the bubble and the channel walls. The gas bubble eventually stops moving due to increased flow resistance, thereby resulting in the formation of gas embolism. The impact of coagulation on bubble immobilization and disease manifestation was validated in an experimental setup that did not result in bubble lodging upon replacing the blood solution with a glycerol water solution at the same viscosity[143]. This work provides a better understanding of the driving forces that lead to bubble lodging in small vessels and inspires research on optimum preventive measures and therapeutic interventions to reduce the risks associated with this medical phenomenon.

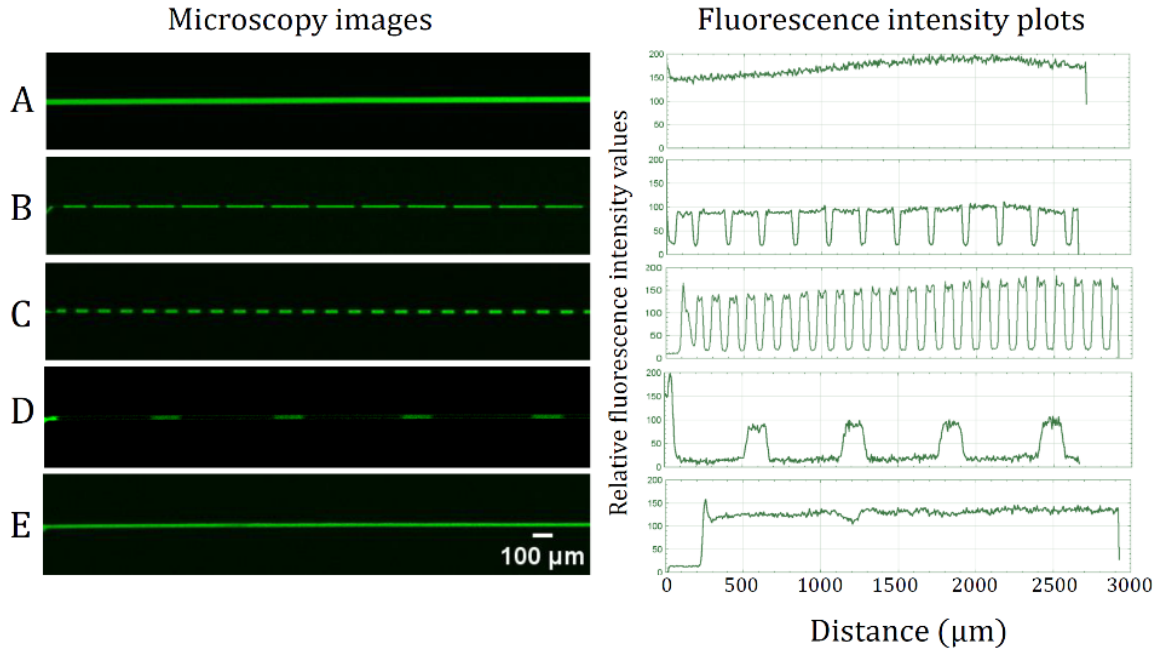

Figure 1.10. Flow patterns and fluorescence intensity profiles of air bubbles versus liquid slugs, in different microfluidic structures, for increasing air to liquid ratios (top to bottom). Reproduced with permission from [144, 145].

Finally, the most recent experiments reported on the introduction of air bubbles into microfluidic channels simulating blood vessels, using a method akin to controlled air injection in medical procedures. Five types of air bubble and liquid patterns were observed in T- and Y-shaped junctions (Figure 1.10), namely quasi-continuous flow; alternation of liquid slugs (green) with either uniform or irregular Taylor bubbles; long air bubbles with favourable movement in the middle of the channel; and continuous and parallel flows of air and liquid[144, 145]. The size distribution of air bubbles was observed to be chaotic for low air: liquid ratios, i.e., for less volumes injected in the microvasculature.

1.2.5.3.In Vitro Studies of Nucleation of Bubbles

Bubble nucleation, an intriguing physical phenomenon with diverse applications, marks the initial stage in bubble formation from either a liquid or solid. Heterogenous nucleation entails the spontaneous emergence of a gas bubble on a surface, which subsequently expanding into a larger one, and ultimately detaching from the surface moving through the surrounding liquid medium.

Focusing on hydrodynamic cavitation in microfluidic devices, one review[146] documented ways of implementing cavitation in a wide array of biomedical applications. Cavitation typically occurred when the liquid static pressure abruptly drops to the critical saturation vapor pressure, leading to bubble formation in low-pressure regions of fluidic systems. The necessary pressure drops for inducing hydrodynamic cavitation can be achieved by passing the fluid through flow restrictive elements like orifice plates and venturi tubes. The impact of geometrical parameters, such as inlet and outlet angles, throat length, and width ratio, was recently investigated on cavitation inception and microbubble generation rate in venturi tubes[147]. It was found that the cavitation number was heavily influenced by geometry, with smaller outlet angles resulting in increased microbubble numbers and decreased cavitation inception numbers. These findings were well aligned with an earlier study[148] that proposed a unified theoretical model for cavitating flows in hydrodynamic cavitation reactors. This study suggested that adjusting the ratio of orifice width to pipe width was optimal for controlling cavitating flow intensity in reactors with orifice configurations. Additionally, increasing the downstream pipe size of the hole intensified cavitating flows.

1.2.5.4.In Vitro Studies on Surfactant Impact of Gas Emboli

Surfactants are essential for minimizing the interfacial tension between different phases, including the interface between a liquid and a gas, and the interface between two immiscible liquids[149]. This reduction occurs as surfactant molecules accumulate at the interface, forming a monolayer that decreases the energy needed to expand the surface area[150]. In the possible treatment of gas embolism, surfactants have the potential to interact with gas bubbles, potentially affecting their stability and absorption dynamics[151]. As a result, the impact of surfactants on decreasing the surface tension to facilitate bubble rupture can lead to various outcomes, such as energy release, shock wave generation, and potential tissue or structural damage, depending on the actual local circumstances[152]. Conversely, surfactants can also be employed to promote the gradual dissolution or reabsorption of gas entrapped within bubbles, thereby averting their sudden collapse[153].

Given the emulsifying properties of surfactants, they can serve as a medium for facilitating the reabsorption of gases by molecules with significant capacity. Perfluorocarbons (PFCs) represent a significant class of these molecules[154, 155]. Their molecular structure provides them with high gas solubility, enabling them to transport significant quantities of nitrogen, oxygen, and carbon dioxide[156]. By combining surfactants with PFCs, emulsions were recommended as an effective treatment for gas embolism[157]. Table 1.2 outlines the inventory of medicinal compounds derived from PFCs, that can be used for treating gas embolism.

The effectiveness of the medical compounds listed in Table 1.2 was evaluated through *in vivo* experiments[151, 158-163]. When exogenously introduced into blood vessels, these compounds did not alter the initial bubble morphology, but they significantly improved their fragmentation and absorption speed. Consequently, this led to an increase in the total surface area of emboli and expedited the bubble reabsorption process[159].

The interventions with surfactants could help to speed elimination and break up of bubbles to help improve the patient while transferring for definitive HBOT. Additionally, such interventions could restore some perfusion and reduce neurologic damage. However, this research avenue would require substantial *in vitro* work before considering clinical trials, and eventually the use in humans.

Table 1.2. Medicinal compounds, sourced from perfluorocarbons (PFCs), combined with the corresponding emulsifier.

Product name	PFC-composition	Surfactant (emulsifier)	Ref.
Fluosol-DA™ (FG)	14% perfluorodecalin, 6% perfluorotripropylamine	Pluronic F-68, egg yolk-phospholipids, potassium oleate	[164]
Perftoran™/Vidaphor™ (FG)	1% perfluorodecalin, 3% perfluoromethylcyclohexyl-piperidin	Proxanol 268, egg yolk-phospholipids	[151]
Oxygent™ (SG)	58% perfluoroctylbromid, 2% perfluorodecylbromide	egg yolk-phospholipids	[163]
Oxycyte™ (SG)	60% perfluoroterbutylcyclohexan	egg yolk-phospholipids	[163]
Oxypherol™/Fluo-sol-43™/ FC 43™ (FG)	20% perfluorotributylamine	Pluronic F-68	[165]
Oxyfluor™ (SG)	78% perfluorodichlorooctane	egg yolk-phospholipids, safflower oil	[166]

1.2.5.5.Effect of Bubbles on Biological Cells

A microfluidic system was introduced to study the mechanism associated with gas embolism and the subsequent cellular responses to mechanical contact with bubbles[167]. This platform was developed to generate and manipulate microbubbles at high levels of precision and control by capitalizing on the gas permeability of PDMS. A single-layer microfluidic chip, consisting of a cell culture chamber with a width of 3 mm and a height of 100 μm, was fabricated through standard photolithography followed by soft lithography techniques. Bubble generators were incorporated into the design with steel needles inserted into 0.7 mm inlet holes, located at the end of these generators, to provide an interface with the external gas supply[167]. The simulation of gas embolism in the microfluidic system was made possible due to the application of external gas

pressure to permit gas permeation between the bubble generators and the cell culture chamber. This PDMS-based membrane was set at a thickness of 50 μm[168] to allow gases to easily pass through. The positioning and widths of the microbubbles were controlled by adjusting the opening times of the valve from the external gas cylinder.

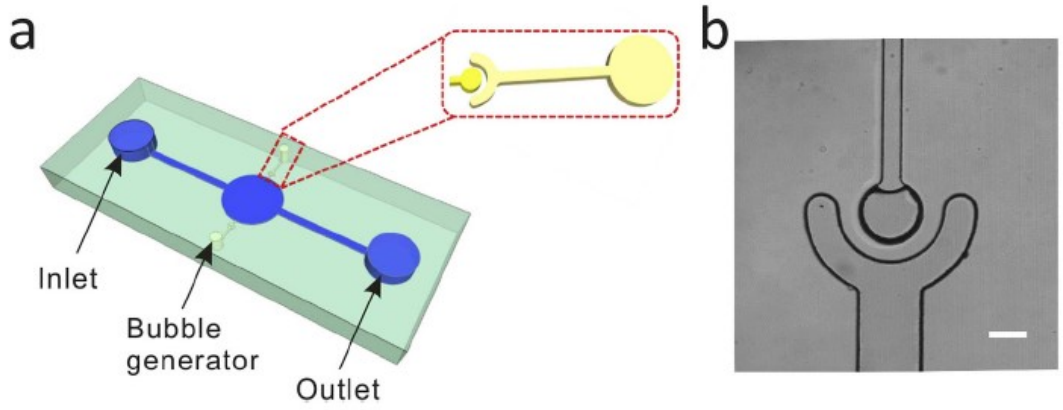

Figure 1.11. Design elements of the microfluidic device. **a.** The system consists of an inlet and an outlet (2.5 mm in width) connected by a cell culture chamber (3 mm in width, 100 μm in height) in the middle. The yellow part of the schematic represents the two bubble generators with 0.7 mm inlets. **b.** An amplified micrograph of the bubble generator at a scale bar of 100 μm. Reproduced with permission from [167].

The sequence of physiological events that could occur following the generation and growth of gas bubbles is yet to be determined. However, the effect of mechanical contact between microbubbles and biological cells was only recently explored by performing cell viability analysis and intracellular calcium imaging in microfluidic platforms[167]. It was demonstrated that (i) short-term contact with bubbles for less than 15 minutes does not typically result in the death of cultured endothelial cells, (ii) bubble contact leads to a significant increase in intracellular calcium levels of contacted cells, and (iii) calcium signals are propagated via small nucleotides and gap junctions between adjacent cells during the process of bubble expansion[167].

1.2.6. Conclusion

The study of gas embolism in microscale systems can be a very effective tool in providing a better understanding of its underlying mechanisms in close-to-real-life circumstances at the micron scale. The complex nature of this medical condition underlines the need for real-time observation of bubble behavior in a controlled environment where various factors can be precisely regulated and

manipulated. The *in vivo* environment is highly dynamic and subject to various physiological factors that can influence bubble behavior, such as i) viscosity, surface tension, flow rate and composition of blood, ii) geometry and mechanical properties of blood vessels, iii) elasticity and gas transport in tissues, and iv) biochemical and biomechanical interactions with vascular endothelium and blood components. These factors introduce different layers of complexity in terms of simulating the conditions related to gas embolism formation and progression, but they are facilitated due to the versatility of microfluidic devices. This review provides an overview of recent publications on physiological bubble production in microfluidic devices, highlighting the current consensus, disagreements, strengths, and limitations. The goal is to emphasize the importance of continued research in this area to advance fundamental knowledge in order develop better diagnostic, preventive and therapeutic strategies.

1.2.7. References

1. Gordy, S. and S. Rowell, *Vascular air embolism.* Int J Crit Illn Inj Sci, 2013. **3**(1): p. 73-6.
2. Goldman, S., J.M. Solano-Altamirano, and K.M. LeDez, *Gas Bubble Dynamics in the Human Body*. Gas Bubble Dynamics in the Human Body. 2017: Academic Press. 1-295.
3. Yu, X., et al., *Bubble-induced endothelial microparticles promote endothelial dysfunction.* PloS one, 2017. **12**(1): p. e0168881.
4. Dardeau, M.R., et al., *The incidence of decompression illness in 10 years of scientific diving.* Diving Hyperb Med, 2012. **42**(4): p. 195-200.
5. Bessereau, J., et al., *Long-term outcome of iatrogenic gas embolism.* Intensive care medicine, 2010. **36**: p. 1180-1187.
6. Freund, M.C., et al., *Systemic air embolism during percutaneous core needle biopsy of the lung: frequency and risk factors.* BMC pulmonary medicine, 2012. **12**(1): p. 1-12.
7. Mandelstam, P., et al., *Complications associated with esophagogastroduodenoscopy and with esophageal dilation.* Gastrointestinal Endoscopy, 1976. **23**(1): p. 16-19.
8. Verma, A. and M.P. Singh, *Venous gas embolism in operative hysteroscopy: A devastating complication in a relatively simple surgery.* Journal of Anaesthesiology Clinical Pharmacology, 2018. **34**(1): p. 103-106.
9. Fuentes, S., et al., *Gas Embolism in Pediatric Minimally Invasive Surgery: Should It Be a Concern?* Journal of Laparoendoscopic & Advanced Surgical Techniques, 2023.

10. van Hulst, R.A., J. Klein, and B. Lachmann, *Gas embolism: pathophysiology and treatment.* Clin Physiol Funct Imaging, 2003. **23**(5): p. 237-46.
11. Moon, R.E., *Hyperbaric oxygen treatment for decompression sickness.* Undersea Hyperb Med, 2014. **41**(2): p. 151-7.
12. Vesely, T.M., *Air embolism during insertion of central venous catheters.* Journal of Vascular and Interventional Radiology, 2001. **12**(11): p. 1291-1295.
13. Shaikh, N. and F. Ummunisa, *Acute management of vascular air embolism.* Journal of Emergencies, Trauma and Shock, 2009. **2**(3): p. 180.
14. Hatling, D., et al., *Iatrogenic cerebral gas embolism–A systematic review of case reports.* Acta Anaesthesiologica Scandinavica, 2019. **63**(2): p. 154-160.
15. Bazin, J., et al., *Haemodynamic conditions enhancing gas embolism after venous injury during laparoscopy: a study in pigs.* British journal of anaesthesia, 1997. **78**(5): p. 570-575.
16. Brull, S.J. and R.C. Prielipp, *Vascular air embolism: A silent hazard to patient safety.* Journal of critical care, 2017. **42**: p. 255-263.
17. Ross, C., et al., *Acute Management of High-Risk and Intermediate-Risk Pulmonary Embolism in Children: A Review.* Chest.
18. Roy, P.-M., D. Douillet, and A. Penaloza, *Contemporary management of acute pulmonary embolism.* Trends in cardiovascular medicine, 2021.
19. Papadopoulou, V., et al., *A critical review of physiological bubble formation in hyperbaric decompression.* Advances in colloid and interface science, 2013. **191**: p. 22-30.
20. Medby, C., A.O. Brubakk, and H.E. Myrvold, *Iatrogen gassemboli.* Tidsskrift for Den norske legeforening, 2001.
21. Walker III, J.R., E.J. Hexdall, and H.M. Murphy-Lavoie, *Diving Gas Embolism*, in *StatPearls [Internet]*. 2022, StatPearls Publishing.
22. Rosengartenis, L., *How much air in an IV line is too much?*
23. Rybárová, V., et al., *GAS EMBOLISM: A REVIEW, INSIGHTS INTO THE ETIOPATHOLOGY, AND FORENSIC IMPLICATIONS.* ROMANIAN JOURNAL OF LEGAL MEDICINE, 2020. **28**(3): p. 229-235.
24. McCarthy, C.J., et al., *Air embolism: practical tips for prevention and treatment.* Journal of Clinical Medicine, 2016. **5**(11): p. 93.

25. Feil, M. and P.P.S. Authority, *Reducing risk of air embolism associated with central venous access devices.* Situations, 2012. **56**(18): p. 24.
26. Irwin, B. and S. Ray, *Patent foramen ovale--assessment and treatment.* Cardiovasc Ther, 2012. **30**(3): p. e128-35.
27. Zhao, E., et al., *Influence of the Valsalva maneuver on cardiac hemodynamics and right to left shunt in patients with patent foramen ovale.* Sci Rep, 2017. **7**: p. 44280.
28. Eldridge, M.W., et al., *Exercise-induced intrapulmonary arteriovenous shunting in healthy humans.* Journal of Applied Physiology, 2004. **97**(3): p. 797-805.
29. Goldman, S., M. Solano-Altamirano, and K. Ledez, *Gas Bubble Dynamics in the Human Body*. 2017: Academic Press.
30. Pearson, E., *Emergency Medical Responder. 3rd Can Ed*. 2010, Pearson.
31. Takahara, K. and S. Suzuki, *In situ water radiolysis in a scanning electron microscope and observation of micro-and nanobubbles formation.* Journal of Applied Physics, 2021. **130**(2).
32. Brown, W.R., et al., *Longer Duration of Cardiopulmonary Bypass Is Associated With Greater Numbers of Cerebral Microemboli.* Stroke, 2000. **31**(3): p. 707-713.
33. Kadri, O.E., et al., *In vivo measurement of blood clot mechanics from computational fluid dynamics based on intravital microscopy images.* Computers in biology and medicine, 2019. **106**: p. 1-11.
34. David, M., et al., *The effect of the substrate temperature on extended defects created by hydrogen implantation in germanium.* Journal of Applied Physics, 2007. **102**(9).
35. Nordmark, H., et al., *Transmission electron microscopy study of hydrogen defect formation at extended defects in hydrogen plasma treated multicrystalline silicon.* Journal of Applied Physics, 2009. **105**(3).
36. Hantgan, R.R., R.G. Taylor, and J.C. Lewis, *Platelets interact with fibrin only after activation.* 1985.
37. Tosi, L., G. Rigoli, and A. Beltramello, *Fibrocartilaginous embolism of the spinal cord: a clinical and pathogenetic reconsideration.* Journal of Neurology, Neurosurgery & Psychiatry, 1996. **60**(1): p. 55-60.
38. Stanton, P.E., et al., *White clot syndrome.* Southern Medical Journal, 1988. **81**(5): p. 616-620.

39. Storm, B.S., et al., *Air Bubbles Activate Complement and Trigger Hemostasis and C3-Dependent Cytokine Release Ex Vivo in Human Whole Blood.* Journal of Immunology, 2021. **207**(11): p. 2828-2840.
40. Eckmann, David M., et al. "Gas Embolism and Surfactant-Based Intervention: Implications for Long-Duration Space-Based Activity." Annals of the New York Academy of Sciences 1077.1 (2006): 256-269.
41. Bollinger, B., et al., *Dual-frequency ultrasound detection of stationary microbubbles in tissue.* Undersea Hyperb Med, 2009. **36**(2): p. 127-36.
42. Newhouse, V. and P.M. Shankar, *Bubble size measurements using the nonlinear mixing of two frequencies.* The Journal of the Acoustical Society of America, 1984. **75**(5): p. 1473-1477.
43. Nishi, R., *The scattering and absorption of sound waves by a gas bubble in a viscous liquid.* Acta Acustica united with Acustica, 1975. **33**(2): p. 65-74.
44. Wilbur, J.C., et al., *Signals consistent with microbubbles detected in legs of normal human subjects after exercise.* Journal of Applied Physiology, 2010. **108**(2): p. 240-244.
45. Pollock, N.W., *Use of ultrasound in decompression research.* Diving and Hyperbaric Medicine, 2007. **37**(2): p. 68-72.
46. LeDez, K.M., *Air embolism and blunt chest trauma.* Canadian Journal of Anesthesia/Journal canadien d'anesthésie, 2011. **58**(12): p. 1140-1141.
47. Ho, A.M.-H. and E. Ling, *Systemic air embolism after lung trauma.* The Journal of the American Society of Anesthesiologists, 1999. **90**(2): p. 564-575.
48. Horrocks, C., *Blast injuries: biophysics, pathophysiology and management principles.* BMJ Military Health, 2001. **147**(1): p. 28-40.
49. Phillips, Y.Y., *Primary blast injuries.* Annals of emergency medicine, 1986. **15**(12): p. 1446-1450.
50. Riley, D., M. Clark, and T. Wong, *World Trade Center Terror: Explosion Trauma—Blast, Burns, and Crush Injury.* Advanced Emergency Nursing Journal, 2002. **24**(2): p. 47-59.
51. Muth, C.M. and E.S. Shank, *Gas embolism.* New England Journal of Medicine, 2000. **342**(7): p. 476-482.

52. Klein, J., et al., *A systematic review of the semi-sitting position in neurosurgical patients with patent foramen ovale: how frequent is paradoxical embolism?* World neurosurgery, 2018. **115**: p. 196-200.
53. Wu, T., et al., *Two cases of fatal iatrogenic air embolism confirmed by autopsies.* Journal of Forensic and Legal Medicine, 2021. **82**: p. 102209.
54. Platz, E., *Tangential gunshot wound to the chest causing venous air embolism: a case report and review.* The Journal of emergency medicine, 2011. **41**(2): p. e25-e29.
55. Orhurhu, V.J., C.C. Gao, and C. Ku, *Carbon dioxide embolism.* 2019.
56. Kennedy-Little, D. and T. Sharman, *Pulmonary barotrauma.* 2020.
57. Cipel, L. and M.T. Gyepes, *"Contrast buttle": a sign indicating perforation of the digestive tract.* American Journal of Roentgenology, 1979. **133**(1): p. 97-101.
58. Vaezeafshar, R., et al., *Barosinusitis: Comprehensive review and proposed new classification system.* Allergy Rhinol (Providence), 2017. **8**(3): p. 109-117.
59. *Divers Alert Network Annual Diving Reports*, in *DAN Annual Diving Report 2018 Edition: A Report on 2016 Diving Fatalities, Injuries, and Incidents*, P. Buzzacott and P.J. Denoble, Editors. 2018, Divers Alert Network

60. Melamed, Y., A. Shupak, and H. Bitterman, *Medical problems associated with underwater diving.* N Engl J Med, 1992. **326**(1): p. 30-5.
61. Bove, A.A., *Diving medicine.* Am J Respir Crit Care Med, 2014. **189**(12): p. 1479-86.
62. Schaffer, K.E., et al., *Mechanisms in development of interstitial emphysema and air embolism on decompression from depth.* J Appl Physiol, 1958. **13**(1): p. 15-29.
63. Mirski, M.A., et al., *Diagnosis and treatment of vascular air embolism.* The Journal of the American Society of Anesthesiologists, 2007. **106**(1): p. 164-177.
64. Durant, T.M., J. Long, and M.J. Oppenheimer, *Pulmonary (venous) air embolism.* American heart journal, 1947. **33**(3): p. 269-281.
65. Feil, M., *Preventing central line air embolism.* AJN The American Journal of Nursing, 2015. **115**(6): p. 64-69.
66. Colley, P.S. and A.A. Artru, *Bunegin-Albin catheter improves air retrieval and resuscitation from lethal venous air embolism in upright dogs.* Anesthesia & Analgesia, 1989. **68**(3): p. 298-301.

67. Ericsson, J.A., J.D. Gottlieb, and R.B. Sweet, *Closed-chest cardiac massage in the treatment of venous air embolism.* New England Journal of Medicine, 1964. **270**(25): p. 1353-1354.
68. Eoh, E.J., B. Derrick, and R. Moon, *Cerebral arterial gas embolism during upper endoscopy.* A&A Practice, 2015. **5**(6): p. 93-94.
69. Moon, R.E., *Bubbles in the brain: what to do for arterial gas embolism?* Critical care medicine, 2005. **33**(4): p. 909-910.
70. Sackmann, E.K., A.L. Fulton, and D.J. Beebe, *The present and future role of microfluidics in biomedical research.* Nature, 2014. **507**(7491): p. 181-189.
71. Dittrich, P.S. and A. Manz, *Lab-on-a-chip: microfluidics in drug discovery.* Nature reviews Drug discovery, 2006. **5**(3): p. 210-218.
72. Kızılkurtlu, A.A., et al., *Lung on a chip for drug screening and design.* Current Pharmaceutical Design, 2018. **24**(45): p. 5386-5396.
73. Shrestha, J., et al., *Lung-on-a-chip: the future of respiratory disease models and pharmacological studies.* Critical Reviews in Biotechnology, 2020. **40**(2): p. 213-230.
74. Leiby, K.L., M.S.B. Raredon, and L.E. Niklason, *Bioengineering the blood-gas barrier.* Comprehensive Physiology, 2020. **10**(2): p. 415-452.
75. Jimenez-Valdes, R.J., et al., *Where We Stand: Lung Organotypic Living Systems That Emulate Human-Relevant Host–Environment/Pathogen Interactions.* Frontiers in Bioengineering and Biotechnology, 2020. **8**.
76. Li, K., et al., *Biomimetic human lung-on-a-chip for modeling disease investigation.* Biomicrofluidics, 2019. **13**(3).
77. Huh, D., et al., *Microfabrication of human organs-on-chips.* Nature Protocols, 2013. **8**(11): p. 2135-2157.
78. Aziz, A.U.R., et al., *The Role of Microfluidics for Organ on Chip Simulations.* Bioengineering (Basel), 2017. **4**(2).
79. Arieli, R., *Nanobubbles form at active hydrophobic spots on the luminal aspect of blood vessels: consequences for decompression illness in diving and possible implications for autoimmune disease—an overview.* Frontiers in Physiology, 2017. **8**: p. 591.
80. Bhattacharjee, N., et al., *The upcoming 3D-printing revolution in microfluidics.* Lab on a Chip, 2016. **16**(10): p. 1720-1742.

81. Fuard, D., et al., *Optimization of poly-di-methyl-siloxane (PDMS) substrates for studying cellular adhesion and motility.* Microelectronic Engineering, 2008. **85**(5-6): p. 1289-1293.
82. Baudoin, R., et al., *Parallelized microfluidic biochips in multi well plate applied to liver tissue engineering.* Sensors and Actuators B: Chemical, 2012. **173**: p. 919-926.
83. Nguyen and, T., et al., *A method for matching the refractive index and kinematic viscosity of a blood analog for flow visualization in hydraulic cardiovascular models.* J. Biomech. Eng., 2004. **126**(4): p. 529-535.
84. Filipponi, L., et al., *Microbeads on microposts: An inverted architecture for bead microarrays.* Biosensors and Bioelectronics, 2009. **24**(7): p. 1850-1857.
85. Vasina, E.N., et al., *The BAD project: data mining, database and prediction of protein adsorption on surfaces.* Lab on a Chip, 2009. **9**(7): p. 891-900.
86. Mongrain, R., et al., *Effects of diffusion coefficients and struts apposition using numerical simulations for drug eluting coronary stents.* 2007.
87. Wagner, C.E., et al., *Quantifying the consistency and rheology of liquid foods using fractional calculus.* Food Hydrocolloids, 2017. **69**: p. 242-254.
88. Wagner, C.E., et al., *A rheological study of the association and dynamics of MUC5AC gels.* Biomacromolecules, 2017. **18**(11): p. 3654-3664.
89. Brown, X.Q., K. Ookawa, and J.Y. Wong, *Evaluation of polydimethylsiloxane scaffolds with physiologically-relevant elastic moduli: interplay of substrate mechanics and surface chemistry effects on vascular smooth muscle cell response.* Biomaterials, 2005. **26**(16): p. 3123-3129.
90. Palchesko, R.N., et al., *Development of polydimethylsiloxane substrates with tunable elastic modulus to study cell mechanobiology in muscle and nerve.* PloS one, 2012. **7**(12): p. e51499.
91. Monson, K.L., et al., *Axial mechanical properties of fresh human cerebral blood vessels.* J. Biomech. Eng., 2003. **125**(2): p. 288-294.
92. Poepping, T.L., et al., *A thin-walled carotid vessel phantom for Doppler ultrasound flow studies.* Ultrasound in medicine & biology, 2004. **30**(8): p. 1067-1078.
93. Held, M., et al., *Intracellular mechanisms of fungal space searching in microenvironments.* Proceedings of the National Academy of Sciences, 2019. **116**(27): p. 13543-13552.

94. Markov, D.A., et al., *Variation in diffusion of gases through PDMS due to plasma surface treatment and storage conditions.* Biomedical microdevices, 2014. **16**(1): p. 91-96.
95. Vadapalli, A., R.N. Pittman, and A.S. Popel, *Estimating oxygen transport resistance of the microvascular wall.* American Journal of Physiology-Heart and Circulatory Physiology, 2000. **279**(2): p. H657-H671.
96. Popel, A.S., *Theory of oxygen transport to tissue.* Critical reviews in biomedical engineering, 1989. **17**(3): p. 257.
97. Müller, B., et al. *High-resolution tomographic imaging of microvessels*. in *Proceedings of SPIE - The International Society for Optical Engineering*. 2008.
98. Popel, A.S. and P.C. Johnson, *Microcirculation and Hemorheology.* Annu Rev Fluid Mech, 2005. **37**: p. 43-69.
99. Chen, Z. and J.B. Lee, *Biocompatibility of SU-8 and Its Biomedical Device Applications.* Micromachines (Basel), 2021. **12**(7).
100. Mack, C.A. and J.E. Connors. *Fundamental differences between positive-and negative-tone imaging*. in *Optical/Laser Microlithography V*. 1992. SPIE.
101. Geissler, M. and Y. Xia, *Patterning: Principles and some new developments.* Advanced Materials, 2004. **16**(15): p. 1249-1269.
102. Chen, Y., *Nanofabrication by electron beam lithography and its applications: A review.* Microelectronic Engineering, 2015. **135**: p. 57-72.
103. Bi, R., et al., *In vivo label-free functional photoacoustic monitoring of ischemic reperfusion.* Journal of biophotonics, 2019. **12**(7): p. e201800454.
104. Yang, J., Y.E. Pak, and T.-R. Lee, *Predicting bifurcation angle effect on blood flow in the microvasculature.* Microvascular research, 2016. **108**: p. 22-28.
105. Arieli, R. and A. Marmur, *Evolution of bubbles from gas micronuclei formed on the luminal aspect of ovine large blood vessels.* Respiratory physiology & neurobiology, 2013. **188**(1): p. 49-55.
106. Clancy, K.F.A., et al., *Protein microarray spots are modulated by patterning method, surface chemistry and processing conditions.* Biosensors and Bioelectronics, 2019. **130**: p. 397-407.

107. Arieli, R., *Nanobubbles form at active hydrophobic spots on the luminal aspect of blood vessels: Consequences for decompression illness in diving and possible implications for autoimmune disease-An overview.* Frontiers in Physiology, 2017. **8**(AUG).
108. Tsuzuki, T., Baassiri, K., Mahmoudi, Z., Nicolau, D.V., *Hydrophobic recovery of PDMS surfaces in contact with hydrophilic entities: relevance to biomedical devices.* Materials, 2022. **in print**.
109. Kašpar, O., et al., *Confinement of water droplets on rectangular micro/nano-arrayed surfaces.* Lab on a Chip, 2016. **16**(13): p. 2487-2493.
110. Filipponi, L., et al., *Protein patterning by microcontact printing using pyramidal PDMS stamps.* Biomedical Microdevices, 2016. **18**(1): p. 1-7.
111. Ivanova, E.P., et al., *Polymer microstructures fabricated via laser ablation used for multianalyte protein microassay.* Langmuir, 2002. **18**(24): p. 9539-9546.
112. Nicolau, D.V., et al., *Protein immobilisation on micro/nanostructures fabricated by laser microablation.* Biosensors and Bioelectronics, 2010. **26**(4): p. 1337-1345.
113. Dobroiu, S., et al., *Laser-assisted structuring of metal-polymer bilayers for protein patterning.* Microelectronic Engineering, 2010. **87**(5-8): p. 1190-1194.
114. Kašpar, O., et al., *Confinement of water droplets on rectangular micro/nano-arrayed surfaces.* Lab on a Chip, 2016. **16**(13): p. 2487-2493.
115. Filipponi, L., et al., *Protein patterning by microcontact printing using pyramidal PDMS stamps.* Biomedical microdevices, 2016. **18**: p. 1-7.
116. Dobroiu, S., et al., *Laser-assisted structuring of metal–polymer bilayers for protein patterning.* Microelectronic engineering, 2010. **87**(5-8): p. 1190-1194.
117. Brookshier, K. and J. Tarbell, *Evaluation of a transparent blood analog fluid: aqueous xanthan gum/glycerin.* Biorheology, 1993. **30**(2): p. 107-116.
118. Sattari, A., P. Hanafizadeh, and M. Hoorfar, *Multiphase flow in microfluidics: From droplets and bubbles to the encapsulated structures.* Advances in Colloid and Interface Science, 2020. **282**: p. 102208.
119. Zhang, W., et al., *Bubble breakup in microchannels: A review.* Chemical Engineering Journal, 2024: p. 149868.
120. Thorsen, T., et al., *Dynamic pattern formation in a vesicle-generating microfluidic device.* Physical review letters, 2001. **86**(18): p. 4163.

121. Zimmerman, W.B., et al., *Microbubble generation.* Recent patents on engineering, 2008. **2**(1): p. 1-8.
122. Burns, S., S. Yiacoumi, and C. Tsouris, *Microbubble generation for environmental and industrial separations.* Separation and purification technology, 1997. **11**(3): p. 221-232.
123. Vion, P., *Pressurised water pressure-reducing nozzle for generating microbubbles in a flotation plant*. 2007, Google Patents.
124. Takahashi, T., T. Okumura, and K. Kubo, *Microbubble generating device and hair washing device utilizing the same*. 2010, Google Patents.
125. Garstecki, P., A. Gańán-Calvo, and G. Whitesides, *Formation of bubbles and droplets in microfluidic systems.* Bulletin of the Polish Academy of Sciences: Technical Sciences, 2005. **53**(4).
126. Zimmerman, W.B., *Microfluidics: history, theory and applications*. Vol. 466. 2006: Springer Science & Business Media.
127. Noguchi, Y. and S. Chuang, *Method and system for generating microbubble-contained liquid and microbubble generator to be assembled in the system*. 2011, Google Patents.
128. Lorenceau, E., et al., *A high rate flow-focusing foam generator.* Physics of fluids, 2006. **18**(9): p. 097103.
129. Tesař, V., C.-H. Hung, and W.B. Zimmerman, *No-moving-part hybrid-synthetic jet actuator.* Sensors and Actuators A: Physical, 2006. **125**(2): p. 159-169.
130. Tesař, V., *Pressure-driven microfluidics*. 2007: Artech House Norwood.
131. Zhang, X., *Novel aerator studies on yeast growth.* University of Sheffield, MSc in Environmental and Energy Engineering dissertation, 2007.
132. Varma, A., *Microbubble generation for the enhanced air lift recovery of oil from oil sands.* University of Sheffield, MSc in Environmental and Energy Engineering dissertation, 2007.
133. Makuta, T., et al., *Generation of micro gas bubbles of uniform width in an ultrasonic field.* Journal of Fluid Mechanics, 2006. **548**: p. 113-131.
134. Jablonski, E.L., et al., *Microfluidics in the Undergraduate Laboratory: Device Fabrication and an Experiment to Mimic Intravascular Gas Embolism.* Chemical Engineering Education, 2010. **44**(1): p. 81-87.
135. Jia, L., Z. Li, and Q. Wei, *Bubble generation and growth mechanism in PMMA microfluidic chip.* AIP Advances, 2022. **12**(5): p. 055106.

136. Baassiri, K. and D. Nicolau, *Investigating the Mechanism of Intravascular Bubble Formation in Designed Arrays of Vascularized Systems on a Chip.*
137. Baum, O., et al., *Laser-assisted formation of micropores and nanobubbles in sclera promote stable normalization of intraocular pressure.* Laser Physics Letters, 2017. **14**(6): p. 065601.
138. Sobol, E., et al., *Laser-induced micropore formation and modification of cartilage structure in osteoarthritis healing.* Journal of Biomedical Optics, 2017. **22**: p. 091515.
139. Bull, J.L., et al. *A microfluidic model of microbubble lodging in small arteriole bifurcations*. in *2005 3rd IEEE/EMBS Special Topic Conference on Microtechnology in Medicine and Biology*. 2005. IEEE.
140. Bento, D., et al., *Microbubble moving in blood flow in microchannels: Effect on the cell-free layer and cell local concentration.* Biomedical microdevices, 2017. **19**(1): p. 1-10.
141. Bento, D., et al. *Blood Flow of Bubbles Moving in Microchannels with Bifurcations*. in *ECCOMAS Thematic Conference on Computational Vision and Medical Image Processing*. 2019. Springer.
142. Bento, D., et al., *Bubbles moving in blood flow in a microchannel network: The effect on the local hematocrit.* Micromachines, 2020. **11**(4): p. 344.
143. Li, Z., et al., *Flow field around bubbles on formation of air embolism in small vessels.* Proceedings of the National Academy of Sciences, 2021. **118**(26): p. e2025406118.
144. Mardanpour, M.M., et al., *Investigation of air bubble behavior after gas embolism events induced in a microfluidic network mimicking microvasculature.* Lab on a Chip, 2024.
145. Mardanpour, M.M., et al., *In Vitro Investigation of Gas Embolism in Microfluidic Networks Mimicking Microvasculature.* 2022.
146. Hosseinpour Shafaghi, A., et al., *On cavitation inception and cavitating flow patterns in a multi-orifice microfluidic device with a functional surface.* Physics of fluids, 2021. **33**(3).
147. Li, M., et al., *Study of Venturi tube geometry on the hydrodynamic cavitation for the generation of microbubbles.* Minerals Engineering, 2019. **132**: p. 268-274.
148. Moholkar, V.S. and A.B. Pandit, *Modeling of hydrodynamic cavitation reactors: a unified approach.* Chemical Engineering Science, 2001. **56**(21): p. 6295-6302.
149. Hanwright, J., et al., *Influence of surfactant on gas bubble stability.* Langmuir, 2005. **21**(11): p. 4912-4920.

150. Vega, E.J. and J.M. Montanero, *Influence of a surfactant on bubble bursting.* Experimental Thermal and Fluid Science, 2024. **151**: p. 111097.
151. Eckmann, D.M., J. Zhang, and P.S. Ayyaswamy, *Hydrodynamics and interfacial surfactant transport in vascular gas embolism.* Journal of Heat Transfer, 2021. **143**(10): p. 100802.
152. Karthikesh, M.S. and X. Yang, *The effect of ultrasound cavitation on endothelial cells.* Experimental Biology and Medicine, 2021. **246**(7): p. 758-770.
153. Eckmann, D.M., S.C. Armstead, and F. Mardini, *Surfactants reduce platelet–bubble and platelet–platelet binding induced by in vitro air embolism.* The Journal of the American Society of Anesthesiologists, 2005. **103**(6): p. 1204-1210.
154. Cabrales, P., *Perfluorocarbon Emulsions.* Alternatives to Blood Transfusion in Transfusion Medicine, 2010: p. 380-388.
155. Krafft, M.P. and J.G. Riess, *Therapeutic oxygen delivery by perfluorocarbon-based colloids.* Advances in colloid and interface science, 2021. **294**: p. 102407.
156. Spiess, B.D., *Perfluorocarbon emulsions as a promising technology: a review of tissue and vascular gas dynamics.* Journal of Applied Physiology, 2009. **106**(4): p. 1444-1452.
157. Mayer, D. and K.B. Ferenz, *Perfluorocarbons for the treatment of decompression illness: how to bridge the gap between theory and practice.* European Journal of Applied Physiology, 2019. **119**(11-12): p. 2421-2433.
158. Branger, A.B. and D.M. Eckmann, *Theoretical and experimental intravascular gas embolism absorption dynamics.* Journal of Applied Physiology, 1999. **87**(4): p. 1287-1295.
159. Branger, A.B. and D.M. Eckmann, *Accelerated arteriolar gas embolism reabsorption by an exogenous surfactant.* The Journal of the American Society of Anesthesiologists, 2002. **96**(4): p. 971-979.
160. Eckmann, D.M. and S.L. Diamond, *Surfactants attenuate gas embolism-induced thrombin production.* The Journal of the American Society of Anesthesiologists, 2004. **100**(1): p. 77-84.
161. Eckmann, D.M., S. Kobayashi, and M. Li, *Microvascular embolization following polidocanol microfoam sclerosant administration.* Dermatologic surgery, 2005. **31**(6): p. 636-643.

162. Eckmann, D.M., et al., *Gas Embolism and Surfactant-Based Intervention: Implications for Long-Duration Space-Based Activity.* Annals of the New York Academy of Sciences, 2006. **1077**(1): p. 256-269.
163. Torres, L.N., B.D. Spiess, and I.P. Torres Filho, *Effects of perfluorocarbon emulsions on microvascular blood flow and oxygen transport in a model of severe arterial gas embolism.* journal of surgical research, 2014. **187**(1): p. 324-333.
164. Ingram, D.A., M.B. Forman, and J.J. Murray, *Activation of complement by Fluosol attributable to the pluronic detergent micelle structure.* Journal of cardiovascular pharmacology, 1993. **22**(3): p. 456-461.
165. Spiess, B.D., et al., *Protection from venous air embolism with fluorocarbon emulsion FC-43.* Journal of Surgical Research, 1986. **41**(4): p. 439-444.
166. Briceno, J.C., et al., *Oxygen transport and consumption during experimental cardiopulmonary bypass using oxyfluor.* ASAIO journal, 1999. **45**(4): p. 322-327.
167. Ma, P., et al., *An integrated microfluidic device for studying controllable gas embolism induced cellular responses.* Talanta, 2020. **208**: p. 120484.
168. Liu, B., et al., *Manipulation of micro-objects using acoustically oscillating bubbles based on the gas permeability of PDMS.* Biomicrofluidics, 2018. **12**(3): p. 034111.

Chapter 2. Genesis of Gas Embolism

2.1. Background of First Article

The first original contribution of this thesis, submitted for publication in the *Lab on a Chip* journal, investigates the mechanisms underlying bubble formation in iatrogenic gas embolism by simulating the pressures exerted during surgical procedures at a microscopic scale. Specifically, the study focuses on gas insufflation, a widely used technique in laparoscopic surgery where air or carbon dioxide is introduced into the abdominal cavity to create an expanded workspace. This procedure is performed using a Veress needle, a device that is blindly inserted into the peritoneal cavity to deliver gas. While effective, this method carries inherent risks, including accidental vascular penetration, which can lead to the unintended introduction of gas into the bloodstream—one of the guaranteed causes of iatrogenic gas embolism.

To explore the origins of gas embolism, microfluidic devices were designed to replicate both intact and damaged vascular walls. In the case of intact, "healthy" vascular structures, intravascular bubble formation was examined by subjecting unilateral pressure chambers to increasing volumes of a fluorescent water solution. This incompressible pressurizing medium allowed for precise detection of structural vulnerabilities, such as ruptures and microleaks in the vascular walls. When no such leaks were present, four different vascular channel widths were subjected to direct mechanical stresses, leading to the formation of distinct microbubble patterns. These patterns were influenced by the magnitude of the applied pressure as well as the biomechanical properties of the surrounding tissue. Experiments were also conducted using microfluidic models with deliberately damaged walls. These models were designed to mimic conditions found in patients with weakened blood vessels or cases where the Veress needle was inadvertently inserted into a vessel. By varying the insufflation rates, different bubble formation patterns were observed, with the geometric configuration of the vascular channel and the size of the perforation playing key roles in determining the distribution and behavior of the bubbles.

The pressure thresholds for intravascular bubble generation were quantified in both intact and damaged systems. These thresholds were first estimated through theoretical calculations and then experimentally validated using manometer measurements. Interestingly, anatomical and geometric variations significantly influenced bubble formation, with distinct bubble behaviors emerging in

response to the presence of excess gas volumes in the local material network. While this relationship had been hypothesized in previous literature, this study provided the first real-time, reproducible observation of the phenomenon, offering crucial insights into the underlying mechanisms of gas embolism.

These findings contribute to a deeper understanding of the interplay between gas insufflation, vascular integrity, and embolism risk, with potential implications for improving surgical protocols and patient safety.

2.2. Article 1:

Lab on a Chip

ROYAL SOCIETY OF CHEMISTRY

PAPER

View Article Online
View Journal | View Issue

In Vitro Generation of Bubbles in Microfluidic Systems Mimicking Iatrogenesis of Gas Embolism

Karine Baassiri[a], Thomas Allen[a], Dan V. Nicolau*[a]

[a]Department of Bioengineering, Faculty of Engineering, McGill University, Montreal, Québec, H3A 0E9, Canada. Email: dan.nicolau@mcgill.ca

2.2.1. Abstract

Gas embolism is a medical condition caused by the presence of gas bubbles in the circulatory system, possibly posing significant health risks due to the blockage of blood to essential organs. Despite its clinical relevance, the mechanisms governing the bubble genesis remain insufficiently understood. This study employs microfluidic systems to investigate the genesis of bubbles modulated by pressures equivalent to those used in laparoscopy. Polydimethylsiloxane-based microfluidic devices mimicking microvasculature were used to simulate gas embolism events at the microscale, in artificial vessels with widths of 30 µm, 50 µm, 80 µm, or 250 µm. Vascular walls with thicknesses of 25 µm often lead to ruptures, those with 50 µm widths generated bubbles, and those with 75 µm widths were resistant to microscale gas embolism. The storage of artificial microvasculature in pressured gas environment led to the generation of bubbles in artificial blood long after it was cleared of excess gas, demonstrating the role of tissues as 'gas reservoirs' prolonging gas embolism. Gas embolism events in artificial vessels with intact walls, or small perforations (16 µm and 32 µm) showed that there is a sizeable population of large emboli created at lower pressures, whereas the emboli created at larger pressures are evenly distributed in smaller ranges, but resulting in larger total volumes of gas introduced in the system. Finally, regardless of their genesis smaller vessels manifest more pronounced propensity of gas embolism, as many bubble lengths are longer than two consecutive bifurcations. These findings suggest that gas

embolism is still problematic for small pressures and small vessels, usually thought as safe in medical practice.

2.2.2. Introduction

Vascular gas embolism is a medical condition caused by the presence of gas bubbles (or in the medical context, gas emboli), in the circulatory system, which can lead to their lodging and immobilization in blood vessels[1]. The subsequent blockage or hindrance of blood flow will decrease the transport of oxygen to critical organs[2]. While gas embolism can be lethal, with high mortality rates[3], or can cause severe neurological outcomes[4, 5], it is rarely detected early[6]. This lack of early detection could be extremely dangerous as critical organs can be severely affected in a matter of minutes. Because gas embolism is, in the first instance, a purely physical process, there is no blood biochemical analysis that can reliably detect it[6]. Moreover, should such a blood analysis exist, the rapid onset of gas emboli would make this hypothetical test inadequate. Conversely, while gas emboli can be visualized easily, either by ultrasound imaging or MRI, their uncertain location in the body, coupled with the rapid onset of this condition, make imaging-based diagnostics challenging[7] prior to the only known remedial intervention – hyperbaric oxygen therapy. Finally, because in most instances, gas embolism is detected only by severe neurological symptoms, indicating a critical condition, its outcomes are often devastating, e.g., high mortality (from 8-12%[8] to 46%[9]), and severe neurological sequelae, e.g., 9-35% of survivors[8].

These difficulties, both fundamental and practical, translated into a relative decrease in studying gas embolism, with a recent review[10] revealing that the present annual reports on gas embolism represent a very small fraction compared with those few decades ago. This relative lack of interest is ill-timed, as it was reported that all medical and surgical specialities can lead to gas embolism[11]. This insufficient understanding translates in reported statistics regarding the occurrence of gas embolism varying wildly, e.g., from 0.005% for arterial[12], to 10-50% for venous gas embolism[13]. For laparoscopic surgery alone, the reported incidence of gas embolism

is 50% in child appendectomy[6], 70% in cholecystectomy[14], and 100% in total hysterectomy[15].

The presence of small gas bubbles in the venous system is not uncommon, but they are usually filtered in the intricate biological microfluidic system of the lungs[2], when blood passes from the ever-decreasing-in-width veins to venules to the ever-increasing-in-width arterioles to arteries[16]. However, if the total volume of gas bubbles is large, the lung filter can be overwhelmed[17, 18]. Alternatively, if the gas bubbles are already present in the arterial system, downstream of the lung filter, they cannot be cleared. In these instances, bubbles that are large enough can block or delay the passage of red blood cells (RBCs) carrying oxygen to irrigated organs, with potential devastating medical effects, especially for the brain[19].

Gas embolism can be 'systemic', when the emboli are the result of the variation of pressure applied to the whole body, as seen in diving[2], and high altitude activities[20]. Conversely, 'local' gas embolism results from accidental or intentional introduction, or *in situ* creation of bubbles in the vascular network, particularly during invasive medical procedures and surgical interventions[11], e.g., laparoscopy, endoscopy, angiography, haemodialysis, coronary artery bypass surgery, central venous catheterization[21], lung biopsy[22], and wound irrigation[23]. Arguably, a 'meso-scale' gas embolism occurs when the pressure variation affects a limited region or organ[24, 25], such as blunt thoracic trauma[26, 27], forceful cardiopulmonary resuscitation[28], lung over-expansion injury[29], explosions[30], and even childbirth[31].

Gas embolism is rapidly emerging as one of the most critical complications in emergency units[29-31]. The rising prevalence of invasive medical procedures involving pressured gases, such as laparoscopy, gastroendoscopy, automated radiological and bubble-containing injections for ultrasound imaging, inevitably contributes to a surge in iatrogenic cases of gas embolism. These risks are further amplified in high-risk patient groups, such as the elderly, obese patients, or those with a medical history of cardiovascular and pulmonary diseases, including atherosclerosis, vascular malformations, or prior surgeries, all of which can compromise the integrity of blood vessels[32]. Because essentially all iatrogenesis of gas emboli is localised, research should replicate these phenomena at microscopic scale. Fortunately, microfluidics can provide a versatile

platform for the study of these cause-effect relationships, at the microscopic level, especially considering that gas embolism is, initially, a purely physical process.

After initial applications in diagnostics, microfluidic devices are progressively moving to the forefront of modelling diseases and medical conditions, e.g., organs-on-a-chip[6, 33-36], due to their ability to create controlled microenvironments providing real-time monitoring of initiation and progression of medically relevant phenomena at the microscopic scale[37, 38]. This approach was extensively applied to biological models such as airway-on-a-chip[39] and alveolus-on-a-chip[40, 41], including a recently developed advanced 3D construct[42] providing high-precision biomimetic alveolar structures. Moreover, several research efforts are using microfluidics to study the evolution, the dissipation, and the biological effects of artificially generated gas bubbles. A series of experimental and computational studies[43-45] focused on the impact of bubble formation on blood flow at the cellular level, i.e., the cell-free layers and concentrations of RBCs, in microchannels with bifurcating networks. Another study[46] observed the impact of mechanical contact with gas bubbles on biological cells. Most recently, the effects of air-to-liquid ratios in microchannels with Y-shaped and T-shaped junctions were investigated for various widths of the artificial vessels and equivalent hematocrit concentrations of blood[47]. Despite this emerging line of research, all these studies used injected bubbles, that is, overlooking the actual origins of bubble formation.

The present work examines the generation of bubbles, by using gas insufflation during laparoscopic surgery as a model process. The origins of gas embolism are investigated *in vitro* by inducing bubble formation through local pressure variations at a mimicked interface between blood vessels and surgical instruments.

2.2.3. Materials and Methods

2.2.3.1.Experimental Setup and Image Processing

The experimental setup consisted of an inverted confocal microscope (Olympus IX83 fluorescence microscope, Olympus Corporation), two programmable syringe pumps (Pump 11 Elite Syringe Pumps, Harvard Apparatus), a polydimethylsiloxane (PDMS) made microfluidic device, a working fluid, a 20 mL air-filled syringe (BD Plastipak™), and a dyed water solution (Figure 1A). The working fluid consisted of a solution of synthetic blood, that replicates human blood for

viscosity (3.5 to 5.5 cP for normal blood[46]) and surface tension (53 to 58 mN/m for normal blood[47]). The solution was prepared from a base mixture of 60% distilled water and 40% glycerine. Xanthan gum was added at 0.04% of the total weight, to match human blood at a hematocrit concentration of 46%[48]. Although PDMS channels allow direct visualization of blood flow, a fluorescent tracer, namely fluorescein sodium salt from Fischer Scientific, was incorporated into the formulation at a volume of 2 mL from a 2% stock solution for 100 mL of the working fluid.

After placing the assembled devices in the microscope stage, the syringe pumps were connected to the corresponding channels for stable and continuous flow. The first syringe pump injected the working fluid into a main artificial vascular channel at flow rates similar to those of blood flow, i.e., 20 µL/h, 50 µL/h, 110 µL/h, and 770 µL/h for 30 µm, 50 µm, 80 µm, and 250 µm channel widths, respectively[49, 50]. The second pump was used to exert various levels of pressure on the main channel, either by injecting 0.05 to 0.3 mL of a dyed water solution (dye: fluorescein sodium salt) into a pressure cavity at 25 mL/h, or by introducing air directly into the cavity at 10 mL/h, 15 mL/h, 25 mL/h, 50 mL/h, 75 mL/h, and 100 mL/h. The dyed water solution was selected as the pressurizing medium for the first type of devices to enable the detection of microscopic ruptures at the interface between the pressure cavity and the vascular channel, leading to uncalibrated injection of gas in the artificial bloodstream.

All visual data, including still images and movies, were acquired at sub-millimetre resolution, using the Olympus PLN 4X and 20X magnifying objectives, at 50 fps, and 20 millisecond exposure time. Subsequent data analysis was conducted using ImageJ, a Java-based image processing program[51], and a custom-developed Matlab script (code presented in SI.1). The sizes of the bubbles in microchannels with various widths and various sizes of wall openings were analysed and correlated with the applied pressure and insufflation rate.

2.2.3.2.Chip Fabrication and Storage

Master structures were fabricated by standard photolithography, using SU8 (StructSure™ Line, Kayaku® Advanced Materials), an epoxy-based negative photoresist. The optimum fabrication parameters were: soft baking conditions of 3 minutes at 65°C followed by 6 minutes at 95°C; ultraviolet exposure for 55 seconds; hard baking for 2 minutes at 65°C, then for 7 minutes at 95°C. Microfluidic chips were subsequently fabricated via polymer replica moulding, using the

Sylgard® 184 silicone elastomer kit (Dow Inc.). The PDMS formulation was prepared at a mixing ratio of 10:1 (base:curing agent), before being poured, degassed, and cured overnight in an oven at 65°C.

The PDMS chips were treated for hydrophilization in oxygen plasma and sealed on top of clean glass slides, with inlets and outlets secured in place to introduce the working fluid, dyed water solution, and air into the respective channels. All prepared devices simulating blood vessels with intact walls were divided into three groups: (i) one group was stored at standard temperature and pressure conditions; (ii) the second group underwent degasification in a vacuum desiccator for 24 hours; and (iii) the third group underwent 48-hour degasification. At the end of the degasification period of the third group, some of the chips were selected for (iv) gas immersion, using compressed nitrogen in a clear pressure tank (from SR-TEK, UK), for 48 hours at pressures of 1500 mmHg, 2063 mmHg and 2625 mmHg.

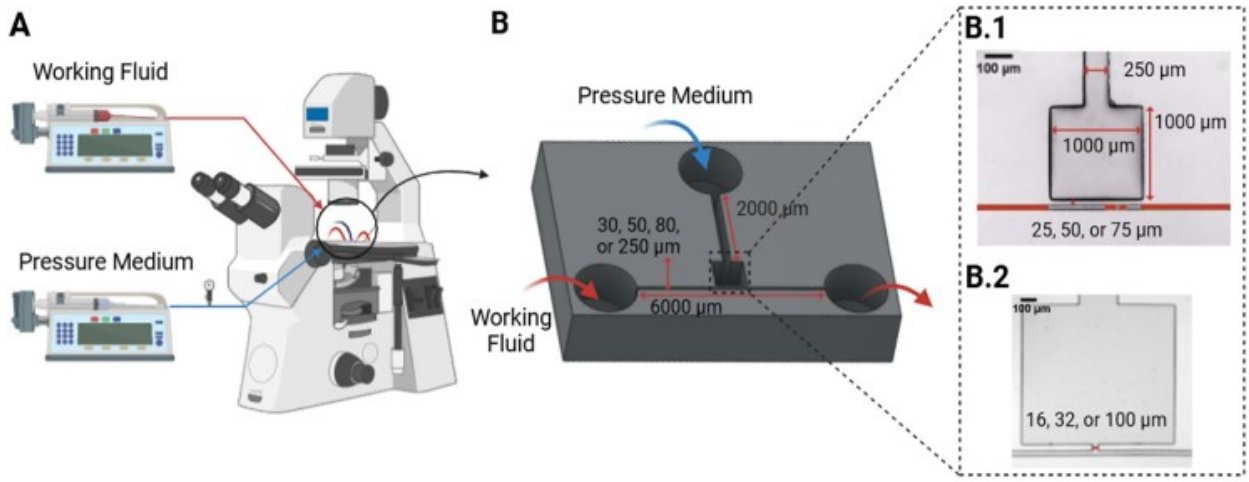

Figure 2. 1. Experimental setup. **A.** The microfluidic device, placed on the microscope stage, had inlets connected to two syringe pumps, one (red inlet) for the working fluid (synthetic blood), and one (blue inlet) for the pressure cavity (dyed water solution, or air). An outlet for draining the circulated synthetic blood working fluid (red outlet) back into atmospheric conditions is also present. **B.** The pressure cavity consisted

of a rectangular 1 mm^2 chamber, with **B.1**. no micro-perforation, or **B.2.** calibrated perforations of 16, 32, or 100 μm.

2.2.3.3.Design of the Vascular Systems on a Chip

The formation of intravascular bubbles was explored using a microfluidic platform, consisting of a vascular channel designed to simulate human arterioles and venules undergoing gas embolism events, upon exposure to local pressures. The width of the channel varied between 30 μm, 50 μm, 80 μm, and 250 μm, all of which were facing a 1 mm^2 square-shaped pressure cavity on one side (Figure 2.1B). The pressure cavity mimicked the tip of a Veress needle, exerting pressure in the near vicinity of a blood vessel, or more generally the pressure exercised on V-shaped tissue with bottom vascularisation. The separation between the main channel and the pressure cavity varied between 25 μm, 50 μm, and 75 μm, to mimic different thicknesses of the blood vessels in the vicinity of the pressure front. To investigate bubble formation in vessels with perforated walls, a second microfluidic platform was developed comprising a 50 μm-long perforation connecting the pressure cavity to the artificial blood vessel. These perforations varied in width between 16 μm, 32 μm, and 100 μm to simulate the effect of damages on the vascular walls. Figure 2.1 outlines the dimensions and geometric features of both microfluidic structures, highlighting the key design elements used to simulate bubble formation in both intact and compromised vascular systems.

2.2.4. Results and Discussion

2.2.4.1.Physical Processes During Medical Procedures Using Insufflation

Apart from the intentional or accidental direct injection of gases into the blood circuit, e.g., for ultrasound imaging[52], laparoscopy appears to be, intuitively, the most likely medical procedure to result in gas embolism[53]. Indeed, the reported incidence of gas embolism in laparoscopic surgeries can reach up to 50% for child appendectomy[6], up to 70% for cholecystectomy[14], and up to 100% for total hysterectomy[15]. While other medical procedures, e.g., colonoscopy, also use higher gas pressures[54], in laparoscopy the gas is almost fully contained in a closed system, i.e., the pneumoperitoneum, thus continuously pressuring the exposed organs (and peritoneum) during surgery.

During laparoscopic surgery, gas (air or carbon dioxide) is insufflated into the peritoneal cavity through a Veress needle (Figure 2.2) at rates of 4,000-6,000 mL/min, to achieve pressures

ranging from 10 to 20 mmHg (above atmospheric pressure)[55-57]. The open volume created by gas pressure is needed to facilitate visualization, and to create more space for handling instruments during surgery. This operational space is sustained by a continuous gas flow of 200 to 400 mL/min throughout the entire surgical procedure, which typically lasts from 30 to 60 minutes[56]. Importantly, in this timeframe, if gas embolism occurs, only its physical aspects can manifest, with biochemical (e.g., inflammatory response, oxidative stress, clotting pathway activation), and biological (e.g., cell damage, cellular hypoxia, organ dysfunction) aspects having a much longer timeframe[58-60]. For instance, the onset of muscle tissue dysfunction due to lack of oxygen is reported to occur within 24 to 72 hours[7]. The pressure exerted by residual postoperative gases, which dissipate within 3 days in 81%, and within 7 days in 96% of patients[61], continues to affect the surfaces of internal tissues.

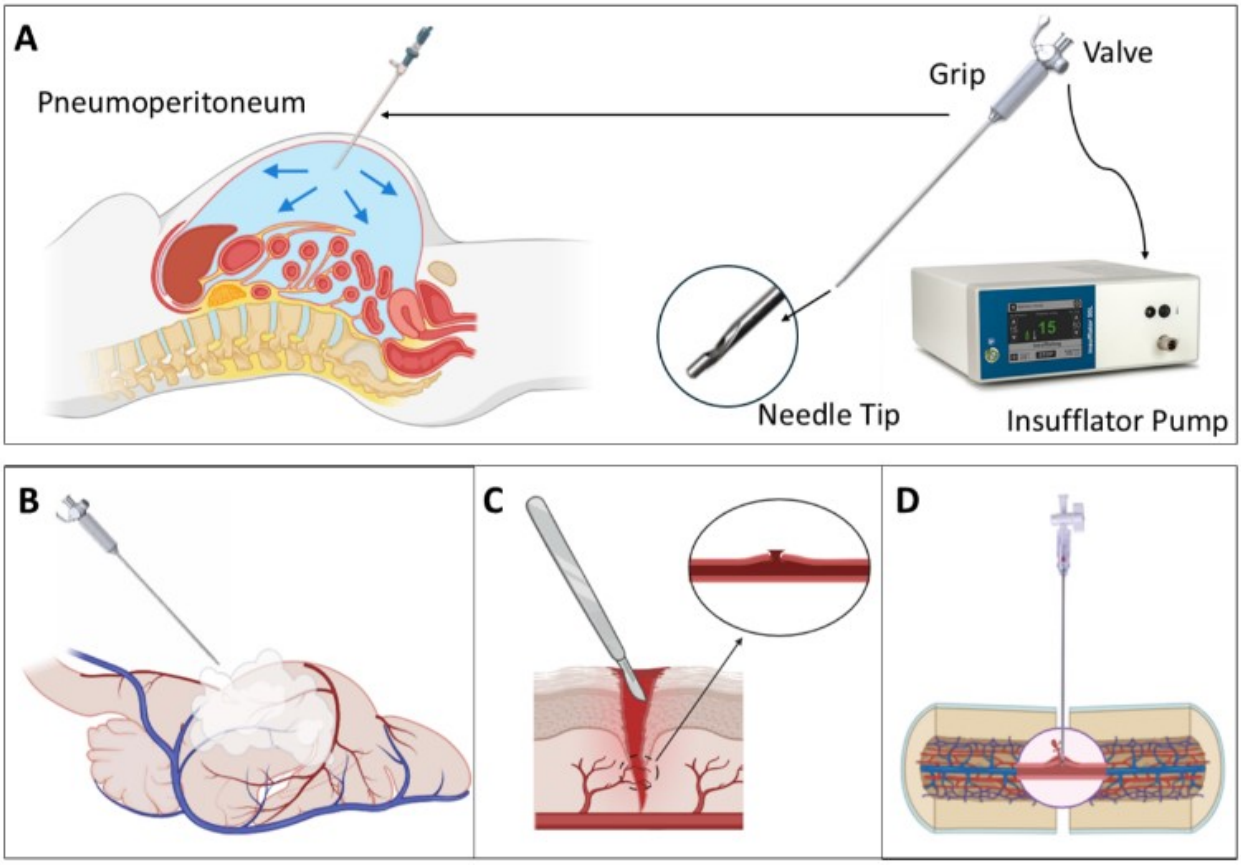

Figure 2.2. A. Illustration of gas insufflation during laparoscopic surgery. Possible scenarios of localized gas embolism: **B.** Percolation of pressured gas through the small vessels with very thin walls; **C.** Direct injection of pressured gas into the bloodstream through perforations in the vascular walls, due to damage

incurred by the scalpel; or **D.** Gas entry through ruptures when the tip of the Veress needle is blocked by a blood vessel.

The exposed sides of the organs are likely to present larger venous and arterial vessels with stronger walls, that are less prone to gas entry into the bloodstream. However, the laparoscopy-assisted surgery will, by necessity, open the inner volume of the operated organ, which is increasingly richer in narrower vessels with ever-thinner walls. Gas embolism can, in principle, also occur during the dissection of highly vascularized tissue or through microscopic injuries caused by tissue manipulation using surgical instruments[34, 62], such as the Veress needle, which benefits from minimal visual guidance[63]. A recent study[6] showed that, while gas embolism events continuously occur at low rates during laparoscopy-assisted appendectomy, these events increase considerably during the operation phase. To put things in context, if blood vessels are accidentally open and if the blood pressure is higher than the gas pressure induced during pneumoperitoneum, then bleeding would become apparent, immediately followed, usually, by corrective wound cauterization, which would stop the bleeding. However, the blood pressure in very narrow venules, e.g., 10 μm[64], can be as low as 3 mmHg[65], thus being considerably below the surrounding laparoscopic pressure. Consequently, in these instances, the bleeding will not occur, with the local breach going unnoticed, and the gas will inexorably get into the bloodstream.

The severe danger of this scenario was demonstrated by an experimental study[66], which simulated the iatrogenesis of arterial gas embolism in pigs by direct injection of carbon dioxide, at pressures and flow rates considerably lower than those used in laparoscopy, i.e., 1.2 mL/kg/min, resulting in mortality rates of 60%. The use of air, which is approximately 20 times less soluble than carbon dioxide[67], will make gas embolism an almost certainty. In this instance, considering the lethal threshold of gas, i.e., 3-5 mL/kg[68], for a 60 kg patient, lethality will take approximately 50 seconds if carbon dioxide is used, and only approximately 3 seconds for air (detailed calculations presented in SI.2).

Another possible scenario leading to gas embolism may occur even in the absence of an opening in the walls of blood vessels. For instance, the accidental close contact between the tip of a Veress needle and the walls of blood vessels will lead to a build-up of pressure on a small footprint. Alternatively, deep surgical incisions would reveal very fine blood vessels, exposed to gas pressure

building up in a geometric V-shaped ‘cul de sac’. Finally, the pressure exerted on the tissue surrounding a fine blood vessel could result in the ex-diffusion of dissolved air in the adjacent tissue, which acts as a ‘gas reservoir’, leading to the *in situ* genesis of gas emboli.

Considering this background, this study selected laparoscopy as the benchmark medical procedure for the *in vitro* assessment of the genesis of gas embolism. The experimental strategy was also helped by the fact that laparoscopy benefits from well-established protocols, which provide precise values and timelines for gas pressures. First, we assessed the scenario involving the mass transfer of gas from the tissues surrounding a vessel, upon exposure to external pressure, into the bloodstream. Second, the *in vitro* genesis of gas embolism was studied in two variants: (i) when small blood vessels are not yet compromised, and the pressured gas enter the bloodstream through mechanically intact walls; and (ii) when the walls of the blood vessels are pierced, and the pressured gas can enter the bloodstream by direct injection through micro-perforations.

2.2.4.2.Physical Processes During Medical Procedures Using Insufflation

The mimicry of the iatrogenesis of gas embolism in laparoscopic-like conditions requires that the microfluidic system replicates *in vitro* the material properties, the dimensions, the fluids, and the operation parameters involved.

Materials. The tissues that form the walls of blood vessels consist of one layer of loose connective tissue, multiple layers of smooth muscle cells, elastin fibres, a thin sheet of endothelial cells lining the lumen, and a basal lamina separating the endothelium from the rest of the outer tissue layers[45]. The endothelial lining is the only component that is present in the entire vascular system, even in the smallest vessels[45]. Despite this complex structure, the properties of PDMS make it an ideal candidate for mimicking biological tissue[69, 70]:

Young’s Modulus. PDMS mechanical properties are similar to human blood vessels and soft tissues, including stress-induced responses[55, 56]. The Young’s modulus of PDMS ranges typically from 0.05 to 2 MPa[71], and it can reach 5 MPa[72]. These values match the observed range for Young’s moduli of human soft tissues (approximately 1MPa)[73, 74], veins (0.05 to 2 MPa)[75], sections of the abdominal aorta (0.04 to 2 MPa), iliac arteries (0.05 to 1.45 MPa)[76], and cerebral arteries (up to 5 MPa)[75], with the lower values of Young’s moduli being associated with smaller blood vessels.

Diffusivity. The diffusion coefficient of air in PDMS ranges between 1.4 x 10^{-5} cm^2/s and 3.7 x 10^{-5} cm^2/s at physiological temperature[77-82], comparable to the gas diffusivity in blood vessels, which ranges from 1 x 10^{-5} cm^2/s[80] to 2.35 x 10^{-5} cm^2/s[79], with higher diffusivities being associated with smaller blood vessels.

In addition, PDMS properties are modulated by pre-polymer composition, curing protocols, presence of additives[83], and plasma treatment[84]. Finally, PDMS is optically transparent, making it highly suitable for visualizing experiments, and it is the material of choice for fabricating microfluidic devices, supported by numerous validated protocols[50]

Fluids. The working fluid can be formulated to closely replicate the rheological properties of human blood within the normal range of hematocrit concentrations[85], ensuring that the flow dynamics within the microchannels accurately simulate the blood flowing through blood vessels.

Geometry of Microvasculature. Among the multitude of blood vessel types, arterioles are the smallest arterial vessels with widths of less than 300 μm, while venules are the smallest venous vessels with widths that range from 10 μm to 100 μm[86]. The wall thicknesses of blood vessels vary between 20 μm and 1,000 μm from arterioles to arteries, and from 2 μm to 500 μm from venules to veins[43, 44]. The channel widths of 30 μm, 50 μm, 80 μm, and 250 μm correspond to a broad spectrum of typical size ranges of arterioles and venules.

The 1 mm^2 square-shaped pressure cavity adjacent to these channels, without any perforation in the space separating the pressure and the bloodstream, emulated the possible role of the tip of the Veress needle during laparoscopic procedures, or the localised pressure applied to a tissue with a ‘cul de sac’ geometry and a vascularized bottom. The second set of devices incorporated calibrated perforations of varying sizes to model punctured blood vessels with differing degrees of damage.

The similarity between human microvasculature and the biomimetic microfluidic system (VSOC) is presented in Table 2.1.

Table 2.1. Microvasculature mimicry using PDMS microfluidic devices.

System	Width (µm)[87, 88]	Wall Thickness (µm)[89]	Flow Rate (µL/h)[90]	Young's Modulus (MPa)[71, 72, 75, 91]	Diffusivity (x10^{-5} cm^2/s)[77-82]
Arterioles	10 – 300	20	3.61 – 1060	0.66 – 3.25	1 – 2.35
Venules	10 – 100	2	3.63 – 159	0.002 – 0.003	1 – 2.35
VSOC	30 – 250	25 – 75	20 – 770	0.05 – 5	1.4 – 3.7

Operation of Microfluidic System. The genesis and characteristics of generated bubbles in the vascular channels, undergoing lateral pressures similar to those used in laparoscopy practice were investigated for intact artificial walls of the blood vessels, and separately for blood vessels with openings, i.e., calibrated perforations. Although both air and carbon dioxide are typically used for gas insufflation in laparoscopy[92], this study used, conservatively, air (explained in detail in SI.3).

The experiments simulating gas embolism in blood vessels with intact walls, used fluorescently dyed water as a liquid piston to compress air in the pressure cavity, which in turn pressured the blood vessel wall. The use of dyed water allowed for the distinction between genuine bubbles formed *in situ* in the artificial blood vessels, and those created through direct injection following accidental (and unquantifiable) ruptures in the walls. As the injected volume of dyed water increased, the gas was pressurized in progressively smaller volumes in the microfluidic cavity. The pressure cavity was visibly and measurably expanding, bringing the wall of the cavity closer to the vascular channel. Since there were no outlets for pressure, the reduced separation between the pressure cavity and the artificial blood vessel resulted, after a certain threshold, in either (i) the generation of bubbles in the microfluidics channel close to the pressure cavity, or if the pressure was too high, (ii) the rupture of the wall and direct injection of air into the fluid stream. The scenarios (i) and (ii) were analysed separately, but the latter was studied in more detail by

fabricating precisely calibrated micro-perforation prior to the application of pressurised gas, by using microfluidics chips with different geometries (Figures 2.1B1 and 2.1B2, respectively).

2.2.4.3. Bubble Generation Modulated by the Separation Between Applied Pressure and Blood Flow

The formation of bubbles modulated by the separation between the applied pressure and the blood flow was first studied for various widths of the wall between the pressure cavity and the microfluidic channel, i.e., 25 µm, 50 µm, and 75 µm, and for two extreme channel widths, i.e., 50 µm and 250 µm, and for different pressures, reaching up to 15.5 mmHg. Depending on the distance between the pressure cavity and the artificial blood vessel, three distinct regime behaviors were observed (Figure *2*.3A):

i. When the separation between the front of the applied pressure and the artificial blood vessel was the narrowest, i.e., 25 µm, the bubbles were always generated, almost immediately after pressure application, However, collapses of the separation wall frequently occurred, leading to the direct injection of gas through ruptured perforations.

ii. For mid-sized separations, i.e., 50 µm, the production of bubbles was constant, after a longer ramping up period. No collapse of the wall was observed.

iii. When the separation was the largest, i.e., 75 µm, the generation of bubbles did not occur, regardless of the pressure being applied.

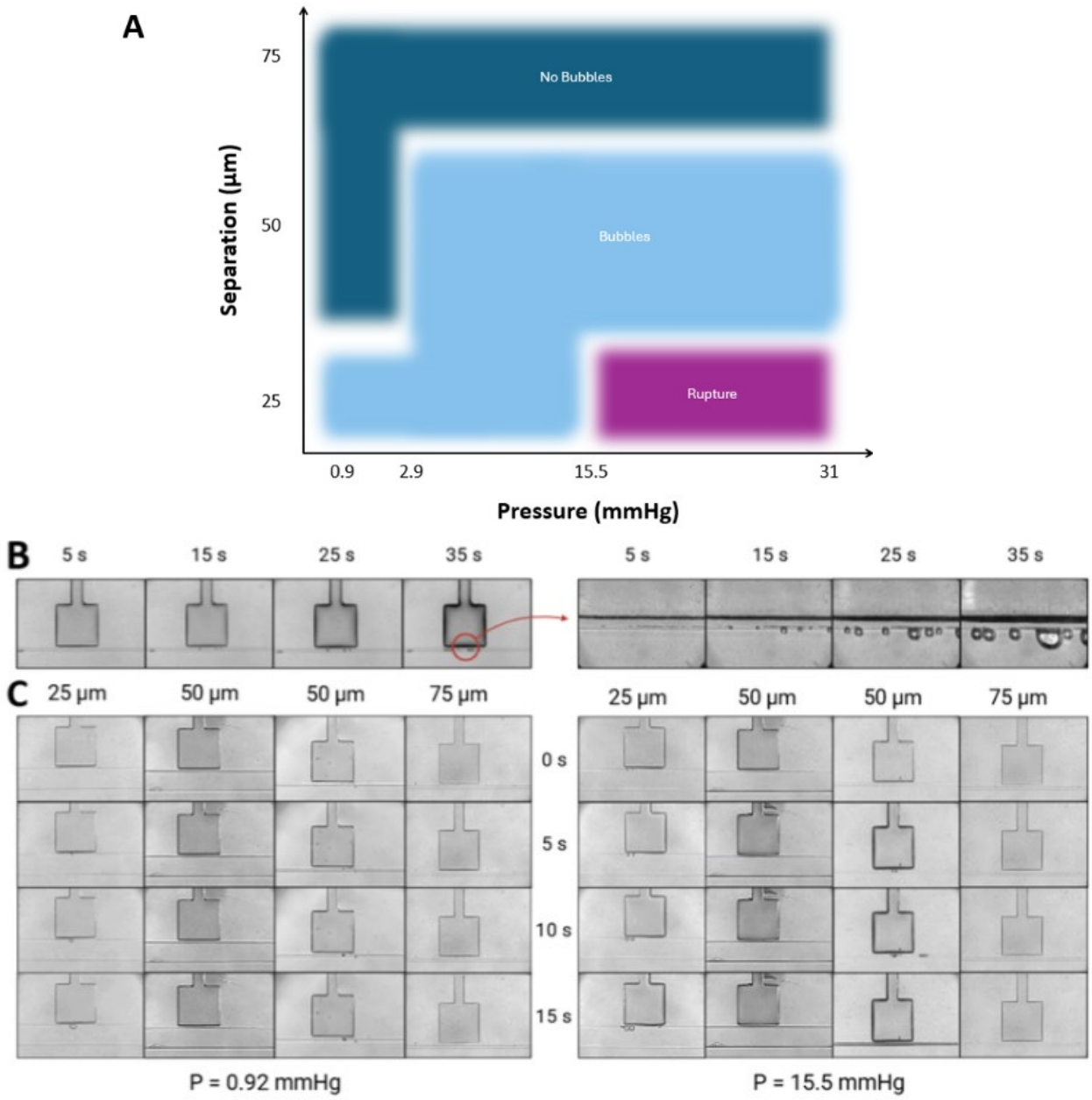

Figure 2.3. A. Regions of operation of the microvasculature-on-a-chip modulated by the separation between the pressure cavity and the artificial blood vessel, and by the applied pressure. **B.** Effect of pressure on the formation of bubbles during insufflation (microscopy images using 4X and 20X objectives, left and right, respectively). **C.** Patterns of bubble formation for volume injections of dyed water solution at 0.05 mL and 0.15 mL, corresponding to pressures of 0.92 mmHg and 15.5 mmHg above atmospheric value, in

channels with widths of 250 μm (two left-hand columns) and 50 μm (two right-hand columns), at separations of 25 μm, 50 μm, and 75 μm as indicated in the columns.

These results correlate well with other studies[93, 94] investigating the gas permeability of PDMS, which showed that, to achieve an efficient mass transfer of gas, the thickness of PDMS membranes should ideally be around 50 μm, with thicker membranes inhibiting pressure-driven mass transfer.

The experiments also assessed the propensity of bubble generation as modulated by the width of the artificial blood vessels. It was found that, for the same applied pressure of 8.62 mmHg, bubbles emerged constantly in the narrowest channels, i.e., with 50 μm width, but they were absent in the widest channels, i.e., with 250 μm widths.

2.2.4.4.Generation of Bubbles Modulated by the Gas Content in Artificial Tissue (PDMS)

To assess the influence of gases dissolved in the surrounding artificial tissue on the process of gas embolism, three scenarios were tested experimentally (results presented in Figure 2.4, and in Movies 1 to 13), using exclusively microfluidic devices without calibrated perforations.

Degasification of Artificial Tissues. No bubble generation was observed when the devices were degassed in vacuum for 48 hours (Movies 2, 3 and 5), or for a shorter 24 hour-period of degasification, even if they were subsequently presented to where similar pressures as those used during laparoscopy (Figure 2.4A).

Saturation of Artificial Tissues with Nitrogen. When the surrounding artificial tissue was saturated, through exposure to higher pressures of a gas with low solubility, i.e., nitrogen, prior to experiments simulating gas embolism, bubbles appeared in the blood vessels immediately after exposure to normal pressure, even if the external pressure was not yet applied (Figure 2.4B, Movies 6 to 11). The use of nitrogen, as opposed to air, was a conservative choice, which resulted in less gas being absorbed in the artificial tissue. The emergence of bubbles persisted even after the devices were stored in atmospheric conditions for 1.5 hours after removal from the gas immersion (Movies 12 and 13).

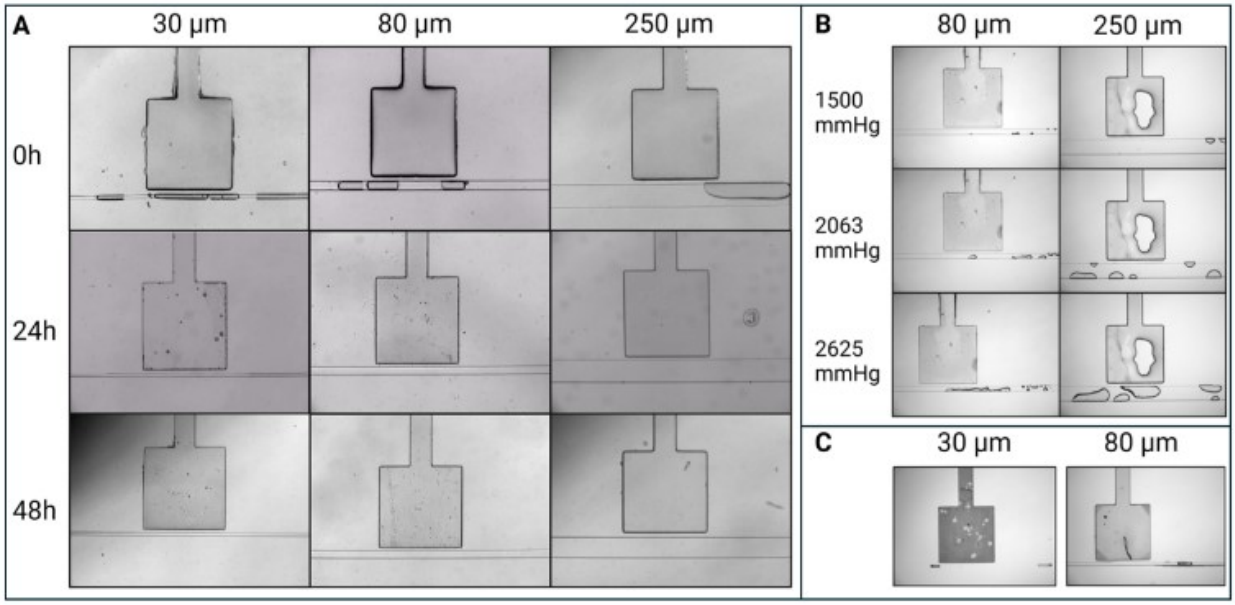

Figure 2.4. Comparison of bubble generation in microfluidic devices presented to various storage conditions. **A.** Absence of bubbles in devices that were degassed for 24 and 48 hours, even if air pressure at 15.5 mmHg was applied in the pressure cavity. **B.** Presence of bubbles in devices first degasified for 48 hours, followed by an immersion in nitrogen for 48 hours at various pressures. **C.** Appearance of bubbles in channels with 30 µm and 80 µm widths, 1.5 hours after the previous immersion in nitrogen, followed by a return to atmospheric conditions.

2.2.4.5.Bubble Generation in Microvasculature Without Perforations

The pressure in the pressure cavity ranged from 0.92 mmHg to 31.24 mmHg above atmospheric pressure, largely overlapping with the pressures used in laparoscopy. More specifically, the intraperitoneal pressures during laparoscopic insufflation typically range from 12 to 15 mmHg[32]. For at-risk patients, these pressures are reduced to 5 to 7 mmHg[95]. The generally recommended range of applied pressures in the peritoneal cavity for insufflation is between 10 mmHg and 20 mmHg[56]. High upper thresholds were considered here to assess extreme scenarios of gas insufflation, such as medical procedures, surgical interventions, and traumatic exposures, where the gas pressure exceeds nominal values.

Smaller channel widths were more prone to bubble formation than larger channels, as evidenced by the 30 µm channels exhibiting bubbles at the lowest pressure thresholds, while the 250 µm channels were the last to start generating bubbles (shown in SI.4). As the pressure increased, average volumes of generated bubbles increased, regardless of the channel width. The increase

of the average volumes followed an approximately logarithmic relationship with the applied pressures, with maximum values appearing in the channel with widths of 250 µm, largely due to bubble coalescence (Figure 2.5A).

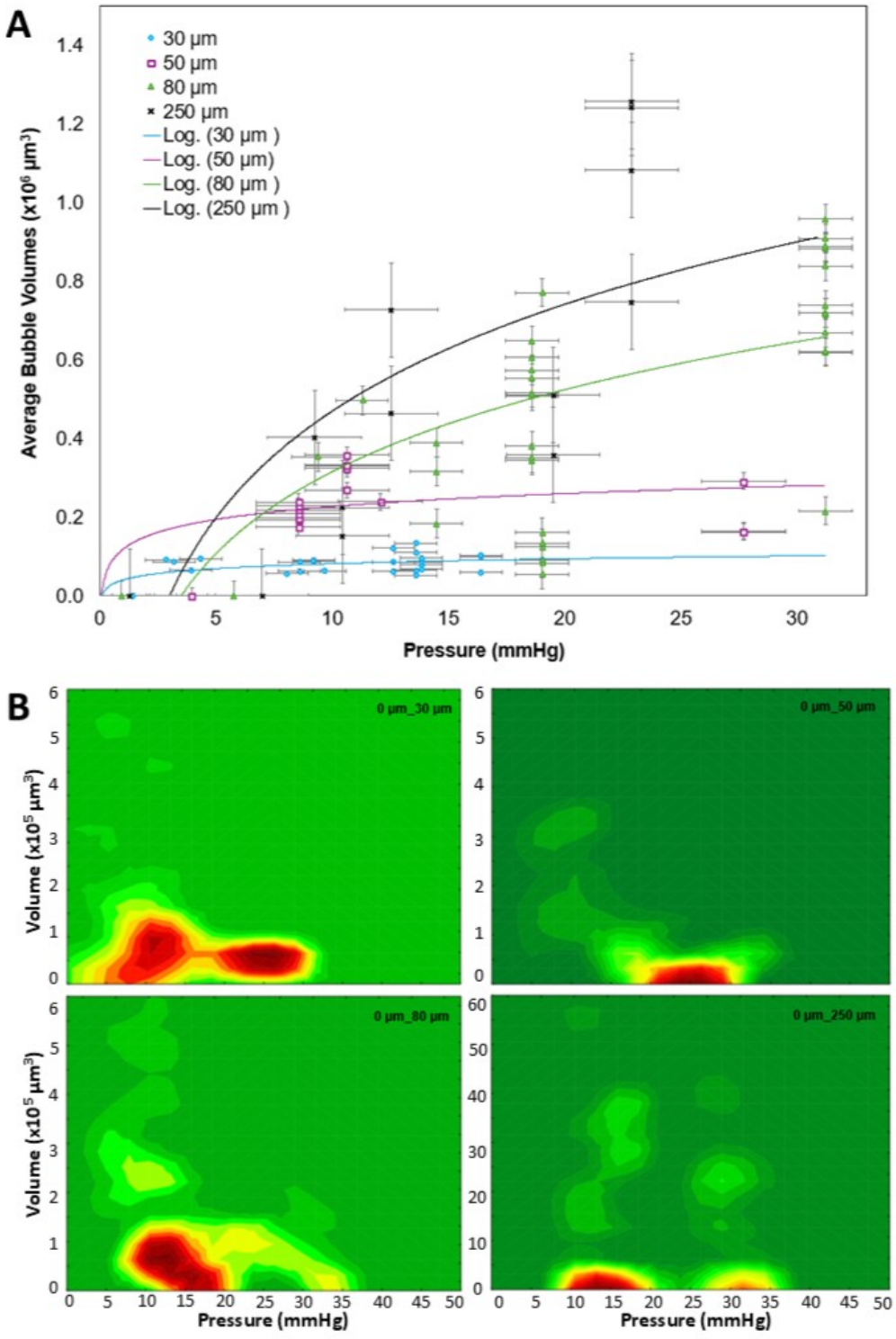

Figure 2.5. A. Effect of the local pressure on bubble formation in microfluidic channels (without

calibrated perforations) located in the vicinity of a pressure cavity. **B.** The distribution of the volumes of individual bubbles versus the applied pressure on channels without perforated walls. The red colour represents the highest number of observations, gradually transitioning to dark green, which represents no observations.

A more detailed analysis was provided by examining the volumes of individual bubbles. Figure 2.5B compares the volumes of individual bubbles versus applied pressures, for channels with widths of 30 μm, 50 μm, 80 μm, and 250 μm. The first, somehow counterintuitive observation is that, regardless of the channel width, the largest proportion of bubbles occurred at small-to-medium pressures, and that this trend is more visible for narrower blood vessels. Even more unexpected was that in channels with widths of 30 μm, 50 μm, and 80 μm, a substantial population of bubbles had larger volumes at low pressures (for channels with widths of 250 μm, the volumes of the bubbles were more evenly distributed versus pressure). Finally, and more visible than the analysis of average volumes, it appears that the bubbles generated in channels with widths of 250 μm were considerably larger (one order of magnitude) than those that appeared in the smaller channels.

This relationship between applied pressures and individual bubble volumes also suggests an initial rapid increase in bubble size, which stabilizes once pressures exceed a critical threshold (further details are presented in SI.5).

2.2.4.6.Bubble Generation in Microvasculature with Calibrated Perforations

The experiments conducted on microfluidic chips featuring calibrated perforations that simulate openings in the walls of blood vessels reveal a translation from the process of gas embolism through membranes without apparent openings (analysed above) to scenarios involving walls with relatively large openings (Figure 2.6). The observed phenomena for applied pressures of 4.54 mmHg to 42.74 mmHg (detailed calculations are provided in the supplementary information, SI.6) include:

i. The artificial blood vessels with thicknesses of 50 μm (the nominal value for all subsequent experiments) and openings of 16 μm (top row in Figure 6) manifest gas embolism events almost exclusively at lower pressures. Larger channel widths result in populations of individual bubbles with larger volumes while preserving the population of smaller bubbles.

ii. Conversely, i.e., artificial blood vessels with larger openings, i.e., 100 µm, the volume of individual bubbles is more evenly distributed against pressures. The blood vessels with 32 µm openings exhibit a transition between the behaviors observed for very small openings (bubbles generated at low pressures only), and for large 100 µm-wide openings.

iii. In all these instances, the volume of individual bubbles in the largest artificial blood vessels, i.e., with widths of 250 µm, is considerably higher than the volumes recorded in blood vessels with the same opening.

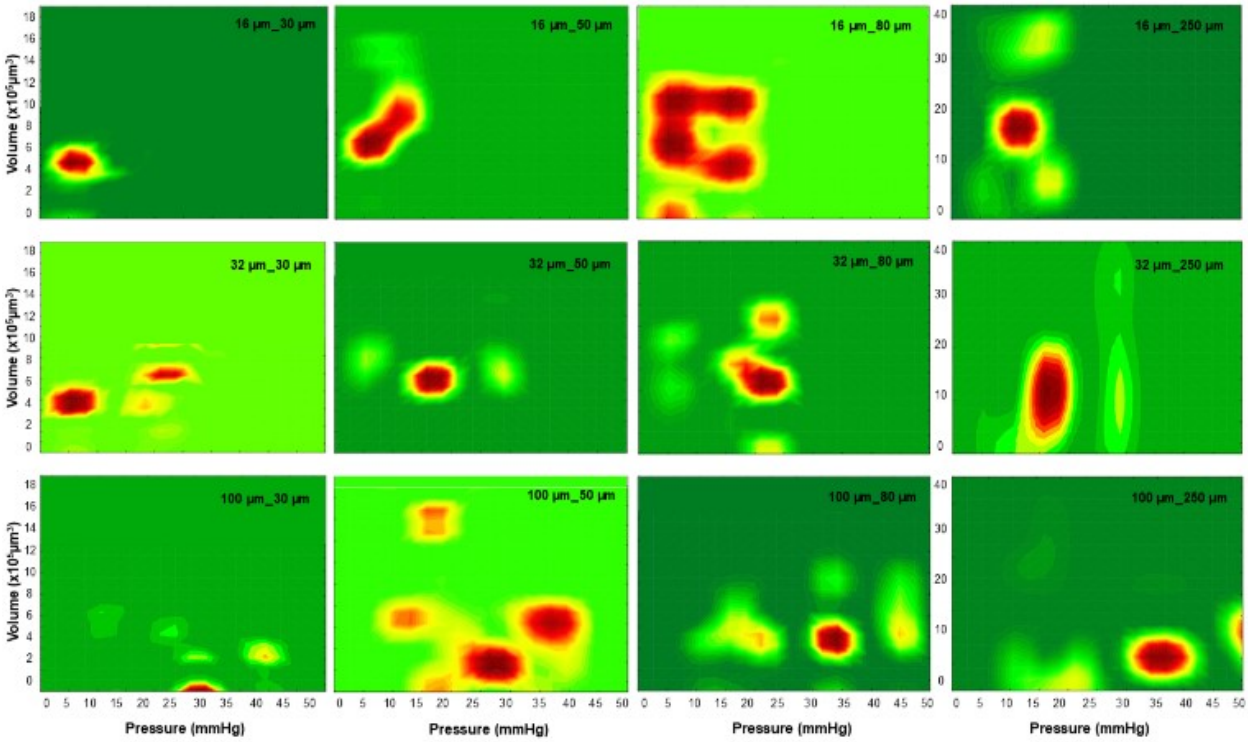

Figure 2.6. The distribution of volumes of individual bubbles versus applied pressures on channels with perforated walls, for openings with 16 µm widths (top row), 32 µm widths (middle row), and 100 µm widths (top row). The red colour represents the highest number of observations, gradually transitioning to dark green, which represents no observations.

2.2.4.7.Medical Relevance

A wide range of invasive medical procedures can lead to iatrogenic gas embolism. Unlike systemic gas embolism, such as decompression sickness (DCS), these procedures often create localized pressure gradients or cause perforations in blood vessels, resulting in the localized formation of gas emboli. Procedures like forceful cardiopulmonary resuscitation and airbag deployment represent intermediate cases between systemic and localized gas embolism. Therefore, research

into the microscopic genesis of gas emboli, as presented here, enhances our understanding of this medical condition.

A second fundamental reason to study gas embolism in abiotic systems stems from the nature of the phenomena involved, and their specific dynamics. Essentially, there are two paths involved in the evolution of gas embolism, both of which run in parallel, but involve different time frames and processes[96]:

i. Faster Physical Path: This path involves the rapid creation of gas emboli and the formation of a membrane around the bubble, delaying its dissolution back into the blood. This leads to mechanical blockage of blood flow and, consequently, reduced oxygen delivery to essential organs.

ii. Slower Biochemical and Biological Path: This slower, parallel path involves a cascade of biochemical processes, leading to biological blockages, such as white and eventually red clots. The activation of platelets by air bubbles was demonstrated in vitro, with a timeline of 180 minutes[97].

Because the physical nature of the early stages of gas embolism justifies its study in abiotic microfluidic systems, the possible medical relevance from the results described above follows.

Impact of Gases Dissolved in Tissues on Gas Embolism. The experiments involving the degasification of artificial tissues before simulating gas embolism may not have immediate medical relevance, as living tissues are typically saturated with surrounding or breathing gases. However, the absence of bubbles when the surrounding material is depleted of gases, even if the artificial microvasculature is subsequently exposed to external pressures for longer periods of time, i.e., 48 hours, demonstrates the "tug-of-war" between the slow mass transfer of gases into gas-depleted artificial tissues and the rapid, thin membrane-mediated transfer in gas-saturated blood.

In contrast, the saturation of tissues with gases of low solubility, such as nitrogen, mirrors the process occurring in divers' bodies after shallow dives at depths of 1 m, 1.7 m, and 2.5 m, due to the ex-diffusion of gases from the tissues. While these depths are quite small, there are reports that gas bubbles can emerge from diving excursions at depths as little as 1 m[98]. When the body is lifted to lower depths or normal atmospheric pressure, emboli are likely to form instantaneously, overlapping with a similar process that occurs due to gas desorption in the blood itself. Importantly, while hyperbaric oxygen therapy (HBOT) aids in clearing emboli from the blood, tissues supersaturated with gases from prolonged dives can serve as gas reservoirs for further, likely

slower, long-term genesis of gas emboli. Therefore, it appears that HBOT should continue for longer periods of time, until these tissue gas reservoirs are depleted.

Gas Embolism Initiated Through a Thin Artificial Tissue Membrane. Experiments probing the generation of gas emboli, as modulated by the thickness of the membrane separating the pressure volume from the bloodstream, provide the first medically relevant insights from the mimicry of gas embolism at the microscopic scale.

i. Blood vessels with undamaged wall thicknesses below 25 μm, such as small venules and arterioles, are prone to local micrometre-sized ruptures if directly exposed to pressured gas, e.g., during surgery. Depending on the balance between pressures in the bloodstream and the pneumoperitoneum, these ruptures can lead to either bleeding (more prevalent for arterioles), or direct injection of the used gas into the bloodstream (more common in venules). Venous pressures, typically between 8 – 12 mmHg[99], are significantly lower than arterial pressures, which range from 110 – 120 mmHg systolic and 70 – 80 mmHg diastolic[100]. Moreover, venules, often operating near 0 mmHg[101, 102], experience smaller fluctuations of pressure fluctuations than arterioles.

ii. Blood vessels with walls around 50 μm thick, when directly exposed to laparoscopic pressures, can experience microscopic gas embolism events.

iii. Blood vessels with walls thicker than 75 μm, if undamaged, are generally resistant to gas embolism events.

A second medically relevant insight arises from analysing the volumes of individual emboli rather than their averages. The size distribution of bubbles in the 30 μm, 50 μm, and 80 μm channels suggests that low laparoscopic pressures pose hidden risks of gas embolism in venules and arterioles. The presence of a small but significant population of larger bubbles generated at lower pressures indicates that more severe gas embolism events could still occur in this pressure regime. These findings challenge the conventional assumption that higher pressures lead to larger bubbles. Indeed, surgeons often recommend operating at lower insufflation pressures, with 10 mmHg generally considered a "safe zone." However, these partial conclusions need to be qualified: in larger blood vessels, such as veins and arteries, individual bubble volumes are considerably larger due to available space for expansion and coalescence but are relatively independent of pressure.

Gas Embolism Initiated Through Calibrated Perforations. The experiments using microfluidic devices with calibrated openings expand upon and confirm the experimental results obtained from mimetic blood vessels with intact walls:

i. In blood vessels that are 30 μm to 80 μm wide (equivalent to venules and arterioles) with no or very small openings, gas embolism events manifest at low pressures. While the total volume of gases transported into the bloodstream is small, there is a notable population of large bubbles. Given the small scale of both blood vessels and wall openings (if present), these events may go unnoticed, potentially leading to the silent accumulation of bubbles in the bloodstream and possible aggregation in larger blood vessels.

ii. The sporadic and unpredictable occurrence of these large bubbles at low pressures suggest a more complex interaction between pressure and bubble dynamics than previously observed. The dynamic nature of large bubble formation at lower pressures can be attributed to the slow buildup of pressure within the system, leading to irregular bubble formation and a random distribution of bubble sizes. A single large bubble, formed at 'safe' pressure thresholds, could obstruct a blood vessel, leading to gas embolism events.

iii. In larger vessels, bubbles tend to be more uniformly distributed in size versus pressure. However, the total volume of gas is considerably higher and more noticeable due to the larger scale of the system, thus posing different, but more manageable challenges.

Analysis of the Lengths of Gas Emboli in Blood Vessels with Various Widths. To gain further medical insights into the risks of gas embolism, the volume distribution of individual bubbles can be translated in lengths of Taylor bubbles, which can be then correlated with the typical distances between bifurcations in blood vessels.

It is generally accepted that the geometry of human (and mammalian) microvasculature system follows Murray's law[103, 104], which governs the relationship between the diameters of parent and daughter vessels. However, the relationship between the distance between bifurcations and the diameter of the blood vessel has received less attention. Fortunately, a comprehensive review of large anatomical data[105] revealed that the mean ratio of the distance between two bifurcations and the diameter of the respective blood vessel is approximately 10.37. Figure 2.7 presents the distribution of Taylor bubble lengths across various applied pressures for all studied cases, indicating the likely distances between bifurcations in the respective vessels. The conclusions of this analysis are as follows:

i. In large vessels, such as those with widths of 80 µm and more notably 250 µm, the ends of the Taylor bubbles fail to reach two consecutive bifurcations.

ii. In smaller vessels, specifically those with widths of 50 µm and more prominently 30 µm, there are numerous instances where Taylor bubbles are long enough to reach two consecutive bifurcation sites. This situation is more pronounced in vessels with larger openings, but not in those with intact walls.

iii. While other parameters play a role in the propensity of bubble coalescence, or conversely their splitting in bifurcations, such as blood flow rate, surface tension, and viscosity[106], it appears that the risk of gas embolism in microvasculature is heightened for smaller vessels with larger openings, particularly in the venous system where blood pressures are lower.

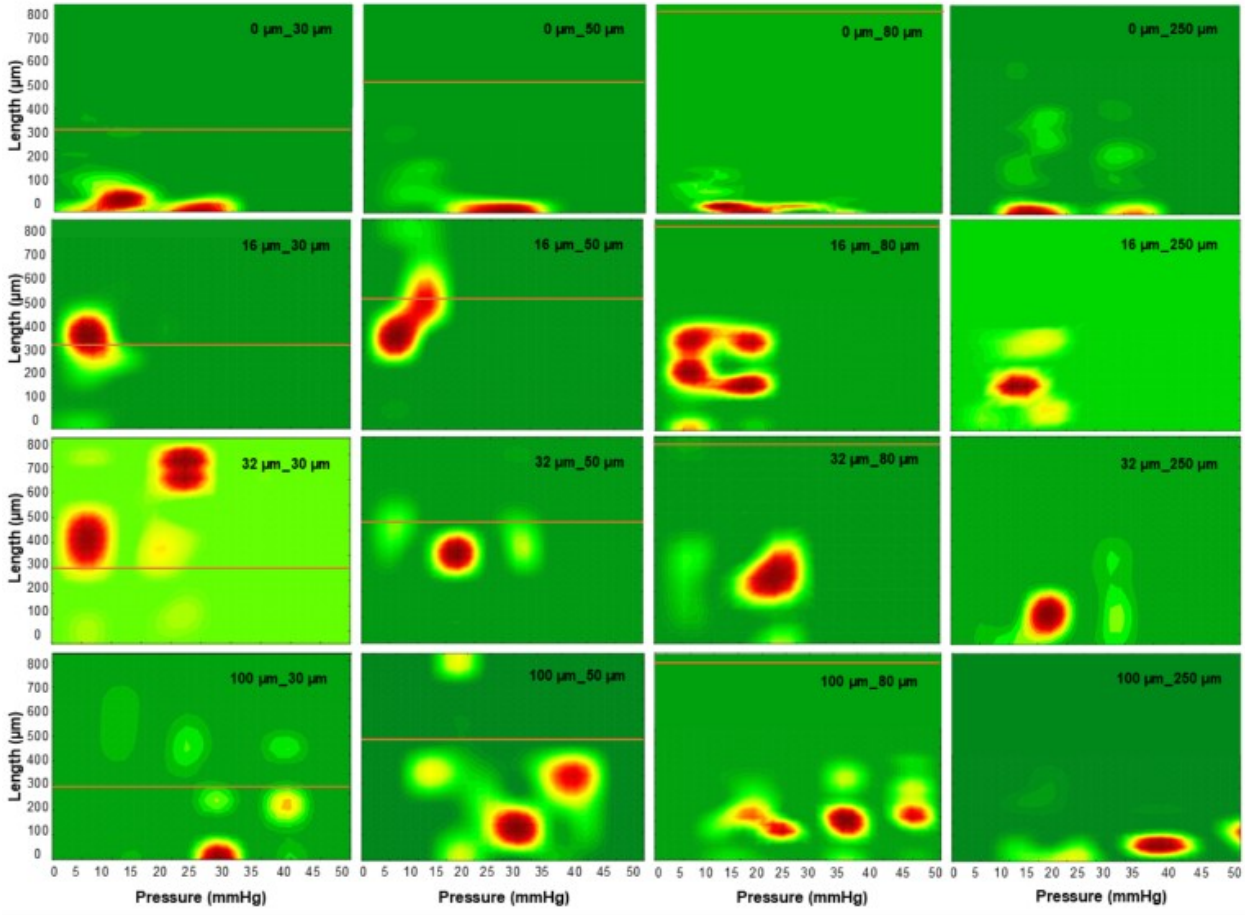

Figure 2.7. The distribution of the lengths of individual bubbles versus applied pressures for channels with widths of 30 µm, 50 µm, 80 µm, and 250 µm (columns from left to right), comprising 0 µm, 16 µm, 32 µm, and 100 µm perforations (rows from top to bottom). The red colour represents the highest number of observations, gradually transitioning to dark green, which represents no observations.

2.2.5. Conclusion

The characteristics of gas embolism include: (i) unpredictable occurrence, resulting from a poor understanding of its causes, particularly at the microscopic level; (ii) relative rarity (or underreporting); (iii) varied medical causation and responses; and (iv) a high incidence of mortality and morbidity. These factors make traditional experimental research extremely challenging and ethical clinical trials nearly impossible. Additionally, iatrogenic cases of gas embolism are inevitably increasing due to the rising use of pressured gases in invasive medical procedures, particularly, but not exclusively, in laparoscopic surgeries. The last important motivation for the present study, which simulates the iatrogenesis of gas emboli in abiotic microfluidic networks mimicking human microvasculature, is the predominantly physical nature of the initial stages of gas embolism.

The study of the iatrogenesis of gas embolism at the microscopic level has provided medically relevant insights: (i) in intact small blood vessels, the width of their walls modulates the regime of *in situ* microscopic gas embolism, ranging from frequent wall ruptures (below 25 μm) to constant gas emboli generation (below 50 μm) to no emboli formation (above 75 μm); (ii) prolonged exposure of tissues to pressured gases transforms them into 'gas reservoirs,' which extend the gas embolism; (iii) in small vessels such as venules and arterioles, the generation of gas emboli primarily occurs at lower pressures than those used in laparoscopic surgeries but results in a significant proportion of larger bubbles capable of triggering embolic events; and (iv) in contrast, larger vessels, especially those with surgical or accidental openings, exhibit a more even distribution of bubble sizes across the range of insufflation pressures but contain a considerably greater total volume of air within the microvasculature.

This study also serves as a framework for investigating medically relevant phenomena at the microscale by simulating them in microfluidic networks that mimic biological systems.

Author contributions

Karine Baassiri: conceptualization, methodology, validation, formal analysis, investigation, image analysis, writing (original draft, review and editing), visualization. Thomas Allen: image analysis. Dan V. Nicolau: conceptualization, methodology, validation, formal analysis, review and editing the original draft, visualization, supervision, project administration, funding acquisition.

Conflicts of interest

The authors declare no conflicts of interest.

Data availability

The data supporting this article have been included as part of the Supplementary Information.

Acknowledgements

This research was funded by the Canadian Natural Sciences and Engineering Research Council (NSERC), grant no. RGPIN- 2022-04053. We also Drs. Galyna Shul, Ayyappasamy Sudalaiyadum Perumal, and Mohammad Mahdi Mardanpour for their support, training, and professional expertise.

2.2.6. Supplementary Information

2.2.6.1.Matlab Script for Detection and Quantification of Gas Emboli

```
%% Load in files and analyzebubble_info30um_100mlh
clear;
close all;
%Save them in Matlab folder or add their folder to the path with this line:
addpath('C:\Users\Dell\Desktop\McGill\PhD Progress Track\Set 12 Hyperbaric and Perforations\Final Experiments\Perforation Paper\Data Analysis\Post Plasma Treatment\Frames\100um_250um_50mlh')
%Set files to read (1 to 1000)
   %Will read and analyze images #1 to filestoread
filesstart = 126;
filestoread = 126;
% Set threshhold value: (change based on data, or set inside loop to change value for each image)
thresh_val = 0.25;
low_thresh = 50;
%Call several files and store them in matrix
for i = filesstart:filestoread
```

```
    if i < 10
        im1 = imread(['000', num2str(i), '.png']);
    elseif i < 100
        im1 = imread(['00', num2str(i), '.png']);
    elseif i < 1000
        im1 = imread(['0', num2str(i), '.png']);
    else
        im1 = imread(['1000.png']);
    end
    im1 = rgb2gray(im1);
    im1 = im2double(im1);
    mask1 = imread('C:\Users\Dell\Desktop\McGill\PhD Progress Track\Set 12 Hyperbaric and
Perforations\Final Experiments\Perforation Paper\Data Analysis\Post Plasma
Treatment\Masks\100um_250um_50mlh.tif');
    mask1=mask1(:,:,1)
    mask = double(imbinarize(mask1));
        %Create a "binary image" called mask from the original image
    mask(mask==0) = NaN;
    %mask the image:
    imagestore{1,i} = im1;
    im2{1,i} = im1.*mask;
end
clear i
% Analyze and set threshholds, then compute the volume:
    % The pixel to micron conversion factor and height of channel in microns must be set
% Set the pixel to micron conversion factor - how many microns is one pixel
pix_conv = 5.182;
%pix_conv = 4.31778929188256;
    % the image is 800 x 450 pixels
    % the test channel is approx 23 pixels wide and approx 230 microns wide
    % therefore each pixel is equal to 10 microns
```

```
% Set the height of the channel in microns
    % i.e. the SU-8 fabrication depth
h = 40;
% Calculate the number of pixels in the mask
mask_pixels = sum(mask(:), 'omitnan');
fprintf('Total Pixels in Mask: %d\n', mask_pixels);
%for i = filesstart:filestoread
for i = filesstart:filestoread
    %threshhold
    im_temp = (im2{1,i});
    im_temp(im_temp>thresh_val) = NaN;
    im_temp(im_temp<=thresh_val) = 1;
    im_temp_thresh = uint8(im_temp);
    %im_temp_thresh = imfill(im_temp_thresh);
    %now you have an image of 1sUnrecognized function or variable 'export_fig'. and 0s
    im3{1,i} = im_temp_thresh;
    %obtain information
    [bubble_label_temp,num_bubbles]= bwlabel(im_temp_thresh,4); %identifies separate bubbles
as objects
    info_bubble_temp = (regionprops(bubble_label_temp,im_temp_thresh,'Area','Centroid')');
    num_bubbles2 = bwlabel(im_temp_thresh,4);
    %Get rid of the noise, set a small threshold
    a = cat(1,info_bubble_temp.Area);
    d = cat(1,info_bubble_temp.Centroid);
    b = find(a>low_thresh);
    if isempty(b)
        c(:,1:3) = 0;
    else
        c(:,1) = a(b);
        c(:,2:3) = d(b,1:2);
    end
```

```
    %redefine bubbles
    im_filt = zeros(size(mask));
    for j = 1:size(b,1)
        bubba = bubble_label_temp;
        bubba(bubba~=b(j)) = 0;
        im_filt = imadd(im_filt,bubba);
        clear bubba
    end
    %save in a matrix
    bubble_info{1,i} = c;
    %extract the volume
    area = cat(1,c(:,1))*(pix_conv^2);   %get area and convert to micron
    volume = area*h;
    pixel = cat(1,c(:,1));

    bubble_vol{1,i} = volume;
    bubble_info{1,i}(:,4) = volume;
    bubble_pixel{1, i} = pixel;
    % fprintf('   Area    CentroidX   CentroidY   Volume \n');
    %disp(bubble_info{1,i});
    % totalvol = sum(bubble_vol{1,1}(:,1));
    % fprintf('Total volume: %d\n', totalvol);
    totalpixels(i) = sum(bubble_pixel{1, i});
    %fprintf('well... i is %d\n', i);
    fprintf('Total Bubble Pixels for Image #%d: %d\n', i, totalpixels(i))
    %fprintf('Total Pixels in Mask: %d',);
    clear a  c d volume
    % Make and save each bubble figure
    clear rgbImage grayImage binaryImage rgbImage desiredColor redChannel greenChannel
blueChannel
    grayImage = (mat2gray(imagestore{1,i}))*255;
```

```
    binaryImage = logical(im_filt);
    rgbImage = cat(3, grayImage, grayImage, grayImage);
    desiredColor = [0.594 1 0]*255;
    redChannel = uint8(rgbImage(:, :, 1));
    greenChannel = uint8(rgbImage(:, :, 2));
    blueChannel = uint8(rgbImage(:, :, 3));
    redChannel(binaryImage) = desiredColor(1);
    greenChannel(binaryImage) = desiredColor(2);
    blueChannel(binaryImage) = desiredColor(3);
    rgbImage = cat(3, redChannel, greenChannel, blueChannel);
    %Illustrate by highlighting bubble
    imshow(rgbImage);
    export_fig(gcf, fullfile('C:\Users\Dell\Desktop\McGill\PhD Progress Track\Set 12 Hyperbaric and Perforations\Final Experiments\Perforation Paper\Data Analysis\Post Plasma Treatment\Marked Bubbles\100um_250um_50mlh', ['100um_250um_50mlh_' num2str(i, '%04d') '.png']));
end
array = bubble_info{1,i};
clear num_bubbles im_temp h i
```

2.2.6.2.Time Rates for Lethal Gas Infusion

The reported lethal gas volume has an average value of 4 mL/kg. For a 60 kg person, the lethal volume is calculated at 240 mL (4 mL/kg x 60 kg). During a laparoscopic procedure, the gas insufflation rate is from 4000 to 6000 mL/min, and the maintenance rate is between 200 and 400 mL/min.

i. The time to lethality using an average gas insufflation rate of 5000 mL/min is 240 mL / 5000 mL/min = 0.048 minutes, equivalent to 2.88 seconds.

ii. The time to lethality using an average maintenance rate of 300 mL/min is 0.8 minutes (240 mL / 300 mL/min), i.e., 48 seconds.

2.2.6.3.Selection of Insufflation Gases

The use of carbon dioxide as insufflation gas in laparoscopy is increasingly preferred for its considerably higher solubility in blood than air or nitrogen (approximately 12 times), thus decreasing the possible complications related to gas embolism[107].

On the other hand, with respect to the non-convective transfer of gases, while the diffusivity of carbon dioxide is slightly lower than that of air, its permeability is much higher (approximately 4.5 times higher) as demonstrated in Table 2.1.

Moreover, the higher solubility of carbon dioxide in artificial tissue would result in a higher mass transfer of gas in artificial blood, upon the application of pressure on the channel wall.

Finally, the permeability of carbon dioxide increases with applied pressure, whereas the permeability of air decreases[108].

To this end, the use of air is a conservative choice allowing the focus on the transfer of gas through the membrane delimiting the pressure cavity from the artificial blood vessel, rather than from the surrounding tissue.

2.2.6.4.Onset of Intravascular Bubble Formation in Microvasculature with Intact Separations

The onset of intravascular bubble formation in the 30 μm, 50 μm, 80 μm, and 250 μm channels occurred at pressures of 2.9 mmHg at 6.5 seconds, 8.6 mmHg at 7.8 seconds, 9.4 mmHg at 8.6 seconds, and 10.5 mmHg at 20.1 seconds, respectively.

This was determined based on two to three experimental observations for the same channel width. The pressure thresholds were calculated via the method below, and the timescales were determined based on the frame number from a total of 1,000 frames, equivalent to 142 seconds.

The applied pressures in the pressure chambers were calculated at the source and on the “vascular” walls, using the ideal gas law for constant temperatures and mole numbers.

Assuming that the gas transfer mechanism is solely based on gas diffusion, the initial and final volumes, denoted as V_0 and V_1 respectively, were measured from the microscopy recordings.

The applied pressure at the source was calculated using the expanded volume of the pressure chamber, while the applied pressure on the wall was estimated using the deformed interface between the pressure chamber and the vascular channel.

$$P_0V_0 = P_1V_1 \quad (1)$$

$$P_1 = \frac{P_0 V_0}{V_1} \quad (2)$$

P_0 is the initial pressure at atmospheric conditions, and P_1 represents the new calculated pressure.

2.2.6.5.Distribution of Individual Bubble Volumes in Microvasculature with Intact Separations

The investigation into individual bubble volumes, rather than the average or total volumes, revealed an unexpected and potentially critical pattern that challenges initial assumptions about the relationship between pressure and bubble formation during procedures like laparoscopic surgery.

While individual bubble volumes at low pressures are generally small, there are notable exceptions. Specifically, in the 30 µm channels, there were three instances of significantly large bubbles appearing at pressures of 2.95 mmHg, 6.78 mmHg, and 11.31 mmHg. The 50 µm channels exhibited maximum bubble volumes from the lowest levels of pressure application, between 8.62 mmHg to 11.57 mmHg. Similarly, the 80 µm and 250 µm channel diameters displayed the largest bubble volumes in the vicinity of 12.56 mmHg. This indicates that low insufflation pressures do not eliminate the risk of large bubble formation. The occurrence of these large bubbles appears to

be sporadic and unpredictable, which suggests a more complex interaction between pressure and bubble dynamics than previously understood.

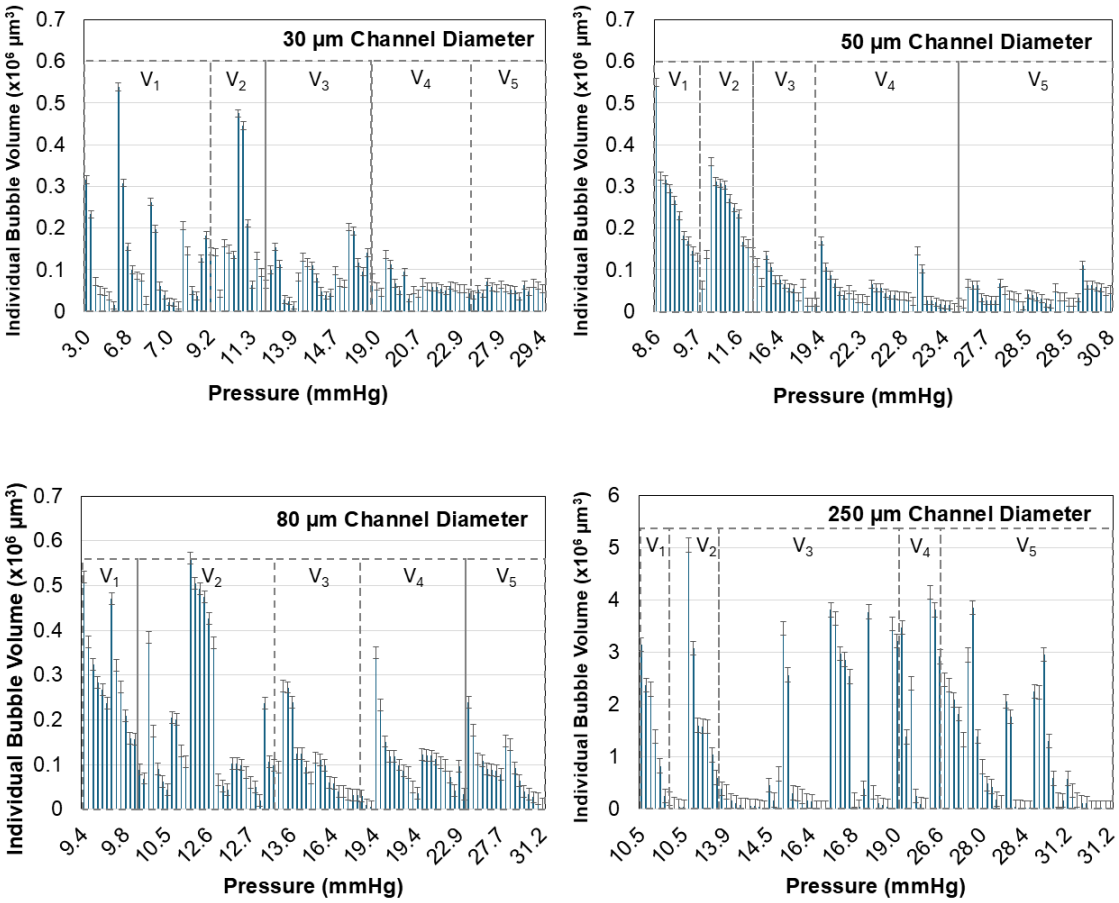

Figure 2.S1. The distribution of individual bubble volumes in 30 µm, 50 µm, 80 µm and 250 µm channel widths for increasing volumes of dyed water solutions of 0.05 mL, 0.1 mL, 0.15 mL, 0.2 mL, and 0.3 mL.

2.2.6.6.Calculation of Pressure Thresholds in Microvasculature with Ruptured Membranes

The pressure applied within compromised artificial blood vessels varied depending on channel width, perforation size, and gas insufflation rate. It was measured using a manometer and compared with calculated values obtained from the following equation.

Where ρ is the density of blood (1,060 kg/m3), u_L is the liquid phase velocity (20 µL/h, 50 µL/h, 110 µL/h, and 770 µL/h over the cross sectional area of the vascular channel), u_G is the gas phase velocity (10 to 100 mL/h over the cross sectional area of the perforation), Ca is the capillary number = blood viscosity 4.5 cP (taken as the average of the typical range of 3.5 to 5.5 cP) x blood velocity / surface tension of air-blood interface (taken as air-water interface at 0.072 N/m), H is the height of the perforation (50 µm), and W is the width of the nozzle (16, 32 and 100 µm).

The calculated pressure range, verified using a manometer, spanned from 4.54 mmHg to 42.74 mmHg, as summarized in the table below.

Table 2.S1. Calculated and measured pressure ranges in microvasculature with varying perforation sizes and channel widths.

Perforation Size (µm)	Channel Width (µm)	Pressure Range (mmHg)
16	30	4.54 – 14.35
16	50	5.00 – 15.81
16	80	5.04 – 15.94
16	250	5.41 – 17.10
32	30	6.42 – 20.29
32	50	7.07 – 22.36
32	80	7.13 – 22.54
32	250	7.65 – 24.18
100	30	11.34 – 35.87
100	50	12.50 – 39.54
100	80	12.60 – 39.84
100	250	13.52 – 42.74

2.2.6.7.Mechanism of Gas Transfer in Microvasculature with Intact Separations

After establishing the relationship between applied pressures and the formation of bubbles from ex-diffusion, the driving mechanism behind gas embolism was investigated by studying the correlation between excess gas volumes, i.e., the volume of air that emerges from the expanded pressure cavity and the reduced separation (calculated by subtracting the gas volumes in the expanded chamber from initial values at atmospheric conditions), and generated bubble volumes in the healthy vascular channels. As most formed emboli were Taylor bubbles, their volumes were obtained by assuming a uniform rectangular shape with a height of 40 µm.

As the source pressures in the chamber increased, the volumes of excess gases emerging from the reduced separation expanded progressively across all channel widths (Figure 2.S2.A). These excess gas volumes were subsequently correlated with the total bubble volumes in the 30 µm and 80 µm channels. The formation of bubbles was triggered at lower excess gas volumes, indicating lower applied pressures, for smaller channel widths. This trend was depicted in Figure 2.S2.B,

wherein the 30 µm channel widths exhibited an earlier onset, occurring at smaller excess gas volumes, compared to the 80 µm channel widths. With increasing pressure levels, the total volume of generated bubbles became larger for both channels, albeit remaining smaller than the volume of excess gases. For example, in the 80 µm channels, the total bubble volume generated was 31.6 x 10^4 μm^3 for excess gas volumes of 154.7 x 10^4 μm^3, as opposed to 90.9 x 10^4 μm^3 for excess gas volumes of 343.1 x 10^4 μm^3. Similar bubble volumes were also observed in the 30 µm channels, but at significantly lower pressure values. Furthermore, notable discrepancies existed in the maximum pressure tolerance of each channel, as depicted by the peak of each curve. The 30 µm channels displayed susceptibility to rupture at excess gas volumes greater than 17.6 x 10^4 μm^3, whereas the 80 µm channel widths were able to withstand a maximum volume of 41.1 x 10^4 μm^3. Beyond these thresholds, the vascular walls became increasingly vulnerable to rupture, even more so in the case of smaller channel widths. This observation reinforces the claim that veins are more prone to gas embolism-related incidents than arteries and are inherently more susceptible to ruptures, as the 30 µm channels were unable to endure the same elevated pressure ranges as the 80 µm channel widths (Figure 2.S2.B).

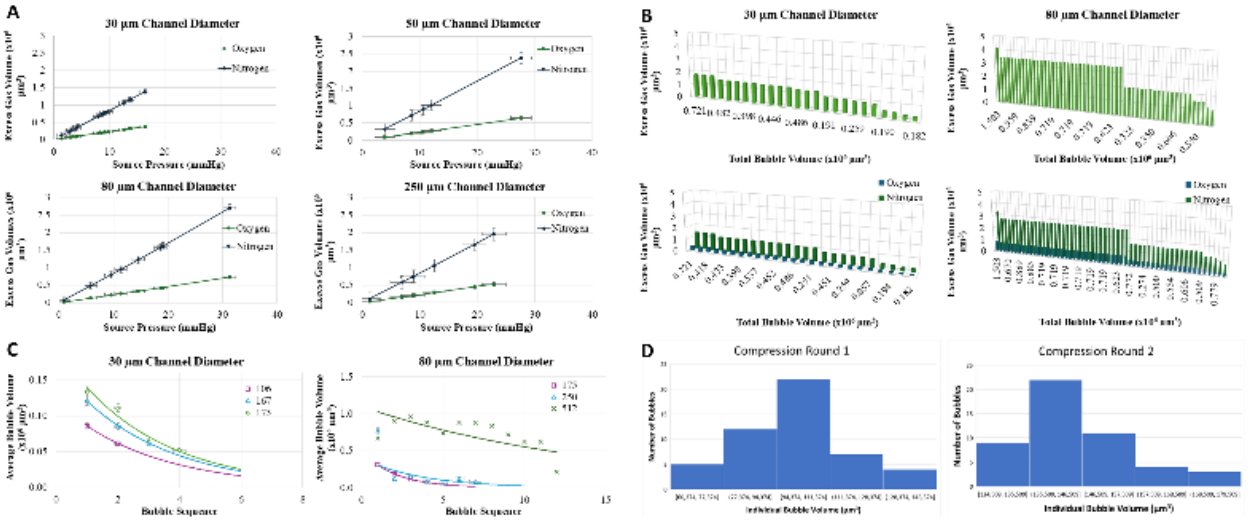

Figure 2.S2. Formation of bubbles from ex-diffusion at the interface between the pressure cavity and the "vascular" wall. **A.** Relationship between excess gas volumes and the source pressure in the pressure cavities, for all channel widths. **B.** Excess gas volumes, namely air in (a), and oxygen and nitrogen in (b), and total volumes of concurrently generated bubbles in each selected frame. The datapoints were fitted into a second-order polynomial equation. **C.** Effects of gas depletion on the average volume of continuously generated bubbles at specific wall pressures. **D.** Depletion of gases in relation with the declining individual bubble volume, at consecutive compression rounds.

A comparative analysis was conducted between empirical data and analytical calculations of intravascular bubble volumes. Assuming that the gas transfer mechanism is solely based on gas diffusion, the theoretical gas volumes in the vascular channel revealed that they are smaller than the calculated gas volumes in this experimental setup. This difference between theoretical and experimental results amounted to 27.9 x 10^4 μm^3 for the 30 µm channel, and 42.9 x 10^4 μm^3 for the 80 µm channel. The details of these calculations are explained below.

The partial pressures of oxygen and nitrogen, denoted as $P_{1,O2}$ and $P_{1,N2}$, were calculated using Dalton's law to estimate the theoretical volumes of oxygen and nitrogen that would diffuse into the vessel. Starting with Fick's first law of diffusion, the equation was simplified to its fundamental form while integrating Henry's law.

$$J = -D\frac{\partial C^2}{\partial x^2} \tag{3}$$

$$J = \frac{\dot{v}}{A} = \frac{D(P_1 - P_2)}{x} \tag{4}$$

$$\dot{v} = \frac{DA(P_1 - P_2)}{x} \tag{5}$$

Where J is the diffusion flux, D is the gas diffusion coefficient in the polymer, C is the gas concentration, x is the diffusion distance, $\dot{v}$ is the volumetric rate of gases diffusing over time, A is the surface area of the pressure chamber, and P_2 is the initial pressure in the vascular channel (760 mmHg).

Consequently, the application of varying pressure levels led to air entrapment with increasingly smaller volumes within the pressure cavity, as previously observed, resulting in reduced capacity to contain the same gas volumes. This phenomenon initiated the release and transfer of excess gases from pressurized regions to adjacent vascular channels with atmospheric conditions. This gas transfer mechanism, observed in the microfluidic network, offers insights into real gas transport processes in the human body due to two critical factors: (i) the similarity in gas permeability between PDMS and human tissues, and (ii) the ability of the polymer to replicate stress-induced responses of blood vessels[109-111]. These parallels underscore the physiological relevance of the experimental findings and their potential applications in understanding gas embolism behavior in human vascular systems.

In Figure 2.S2.C, a pattern was observed regarding the impact of gas depletion from the region between the pressure cavity and vascular channel on bubble formation. Once the maximum pressure that the channels could withstand without rupture was reached, gradual decompression of

the pressure cavity occurred because of diminishing volumes of excess gases within the chamber and its interface with the vascular channel. In other words, this process of gas depletion, primarily driven by ex-diffusion, led to the decompression of the pressure cavity, accompanied by the continuous formation of increasingly smaller gas bubbles. To gain a deeper understanding of gas embolism behavior under different gas transfer mechanisms—specifically, pressurization and depressurization cycles—the average volume of concurrently generated bubbles was quantified at a fixed volume of dyed water injection. This analysis was conducted to elucidate how gas emboli behave at various pressure levels. Subsequently, all gas bubbles generated within a selected span of 10 frames were grouped into sequential clusters, enabling a comparison of their average volumes at each pressure level. The largest pressure levels were associated with the highest range of volumes. For instance, the 30 μm channel width exhibited a decreasing trend in average bubble volumes after reaching steady state at pressures of 106.4 mmHg, 167.2 mmHg, and 190 mmHg. Similarly, the average bubble volumes in the 80 μm channel demonstrated a progressive decline at each applied pressure of 174.8 mmHg, 250.8 mmHg, and 509.2 mmHg. To further validate the observed decreasing pattern in generated bubble volumes, consecutive compression rounds were conducted for the 30 μm channel width, as depicted in Figure 2.S2.D. This iterative process reinforced the consistency in declining bubble volumes at fixed pressures, over multiple compression cycles.

In laparoscopy and real gas insufflation procedures, the behavior of gas bubbles under varying pressures is crucial for understanding and preventing gas embolism. These findings suggest that smaller blood vessels, like veins, are more susceptible to rupture and bubble formation at lower pressures, which directly correlates to the increased risk of gas embolism during laparoscopic surgeries[112-114]. As the pressure increases, bubble formation becomes more pronounced, especially in smaller channels, mirroring the potential dangers in smaller veins when insufflation pressures are not carefully controlled. Additionally, the gradual decompression observed in this study, where gas bubbles continue to form at progressively smaller volumes as pressures decrease, emphasizes the need for careful management of pressure cycles during laparoscopic procedures, despite their decline, to minimize the risk of embolism. The similarity between the material used in the study and human tissues suggests that the current experimental setup can provide valuable insights into the real-world implications of gas insufflation, underlining the importance of maintaining appropriate pressure levels to prevent complications associated with gas embolism.

2.2.7. Notes and References

1. S. Gordy and S. Rowell, "Vascular air embolism," *International journal of critical illness and injury science,* vol. 3, no. 1, p. 73, 2013.
2. S. Goldman, M. Solano-Altamirano, and K. Ledez, *Gas Bubble Dynamics in the Human Body*. Academic Press, 2017.
3. C. J. McCarthy, S. Behravesh, S. G. Naidu, and R. Oklu, "Air embolism: diagnosis, clinical management and outcomes," *Diagnostics,* vol. 7, no. 1, p. 5, 2017.
4. V. Červeňák *et al.*, "Cerebral air embolism: neurologic manifestations, prognosis, and outcome," (in eng), *Front Neurol,* vol. 15, p. 1417006, 2024, doi: 10.3389/fneur.2024.1417006.
5. A. M. Alexander, A. Sankari, and N. Martin, "Arterial gas embolism," in *StatPearls [Internet]*: StatPearls Publishing, 2024.
6. S. Fuentes, C. Grande-Moreillo, J. Margarit-Mallol, S. Flores-Villar, E. Solé-Heuberger, and A. Jaen-Manzanera, "Gas Embolism in Pediatric Minimally Invasive Surgery: Should It Be a Concern?," *Journal of Laparoendoscopic & Advanced Surgical Techniques,* vol. 33, no. 10, pp. 1011-1017, 2023.
7. R. E. Moon. "Arterial Gas Embolism." Merck Manual. https://www.merckmanuals.com/en-ca/professional/injuries-poisoning/injury-during-diving-or-work-in-compressed-air/arterial-gas-embolism (accessed 2023).
8. N. Heming, M. A. Melone, and D. Annane, "Update on the Management of Iatrogenic Gas Embolism," in *Annual Update in Intensive Care and Emergency Medicine 2020*, J.-L. Vincent Ed. Cham: Springer International Publishing, 2020, pp. 559-568.
9. S. Q. Liu, S. Z. Zhao, Z. W. Li, S. P. Lv, Y. Q. Liu, and Y. Li, "Monitoring of gas emboli during hysteroscopic surgery: A prospective study," *Journal of Ultrasound in Medicine,* Article vol. 36, no. 4, pp. 749-756, 2017, doi: 10.7863/ultra.16.03051.
10. K. Baassiri, M. M. Mardanpour, K. M. LeDez, N. W. Pollock, D. Popa, and D. V. Nicolau, "In Vitro Studies of Gas Embolism," in *Recent Advances in Hemodynamics and Blood Mimetics*: Elsevier, 2026.
11. C. M. Muth and E. S. Shank, "Gas embolism," *New England Journal of Medicine,* Review vol. 342, no. 7, pp. 476-482, 2000, doi: 10.1056/NEJM200002173420706.

12. P. Mandelstam, C. Sugawa, S. E. Silvis, O. T. Nebel, and G. Rogers, "Complications associated with esophagogastroduodenoscopy and with esophageal dilation," *Gastrointestinal Endoscopy,* Article vol. 23, no. 1, pp. 16-19, 1976, doi: 10.1016/S0016-5107(76)73568-5.
13. L. K. Afreen *et al.*, "Incidence of venous air embolism during endoscopic retrograde cholangiopancreatography," *Anesthesia & Analgesia,* vol. 127, no. 2, pp. 420-423, 2018.
14. M. Derouin, P. Couture, D. Boudreault, D. Girard, and D. Gravel, "Detection of gas embolism by transesophageal echocardiography during laparoscopic cholecystectomy," *Anesthesia & Analgesia,* vol. 82, no. 1, pp. 119-124, 1996.
15. E. Y. Park, J.-Y. Kwon, and K. J. Kim, "Carbon dioxide embolism during laparoscopic surgery," *Yonsei medical journal,* vol. 53, no. 3, pp. 459-466, 2012.
16. K. M. LeDez, "Air embolism and blunt chest trauma," *Canadian Journal of Anesthesia/Journal canadien d'anesthésie,* vol. 58, pp. 1140-1141, 2011.
17. D. Levett and I. Millar, "Bubble trouble: a review of diving physiology and disease," *Postgraduate medical journal,* vol. 84, no. 997, pp. 571-578, 2008.
18. P. L. Marsh *et al.*, "Iatrogenic air embolism: pathoanatomy, thromboinflammation, endotheliopathy, and therapies," *Frontiers in Immunology,* vol. 14, p. 1230049, 2023.
19. V. Červeňák *et al.*, "Cerebral air embolism: neurologic manifestations, prognosis, and outcome," *Frontiers in Neurology,* vol. 15, p. 1417006, 2024.
20. S. M. Auñón-Chancellor, J. M. Pattarini, S. Moll, and A. Sargsyan, "Venous thrombosis during spaceflight," *New England Journal of Medicine,* vol. 382, no. 1, pp. 89-90, 2020.
21. D. Hatling, A. Høgset, A. B. Guttormsen, and B. Müller, "Iatrogenic cerebral gas embolism–A systematic review of case reports," *Acta Anaesthesiologica Scandinavica,* vol. 63, no. 2, pp. 154-160, 2019.
22. Z. U. Rahman *et al.*, "Cardiac Arrest as a Consequence of Air Embolism: A Case Report and Literature Review," (in eng), *Case Rep Med,* vol. 2016, p. 8236845, 2016, doi: 10.1155/2016/8236845.
23. T. Wu *et al.*, "Two cases of fatal iatrogenic air embolism confirmed by autopsies," *Journal of Forensic and Legal Medicine,* vol. 82, p. 102209, 2021.
24. Y. Y. Phillips, "Primary blast injuries," *Annals of emergency medicine,* vol. 15, no. 12, pp. 1446-1450, 1986.

25. C. Horrocks, "Blast injuries: biophysics, pathophysiology and management principles," *BMJ Military Health,* vol. 147, no. 1, pp. 28-40, 2001.
26. A. M.-H. Ho and E. Ling, "Systemic air embolism after lung trauma," *The Journal of the American Society of Anesthesiologists,* vol. 90, no. 2, pp. 564-575, 1999.
27. K. M. LeDez, "Air embolism and blunt chest trauma," *Canadian Journal of Anesthesia/Journal canadien d'anesthésie,* vol. 58, no. 12, pp. 1140-1141, 2011.
28. Y. Hashimoto, T. Yamaki, T. Sakakibara, J. Matsui, and M. Matsui, "Cerebral air embolism caused by cardiopulmonary resuscitation after cardiopulmonary arrest on arrival," *Journal of Trauma and Acute Care Surgery,* vol. 48, no. 5, pp. 975-977, 2000.
29. L. M. Bralow and M. Piehl, "Barotrauma and Arterial Gas Embolism: A Diving Emergencies Simulation Case for Emergency Medicine Residents," (in eng), *MedEdPORTAL,* vol. 14, p. 10788, Dec 21 2018, doi: 10.15766/mep_2374-8265.10788.
30. D. Riley, M. Clark, and T. Wong, "World Trade Center Terror: Explosion Trauma—Blast, Burns, and Crush Injury," *Advanced Emergency Nursing Journal,* vol. 24, no. 2, pp. 47-59, 2002.
31. Y. Mushkat, D. Luxman, Z. Nachum, M. P. David, and Y. Melamed, "Gas embolism complicating obstetric or gynecologic procedures. Case reports and review of the literature," (in eng), *Eur J Obstet Gynecol Reprod Biol,* vol. 63, no. 1, pp. 97-103, Nov 1995, doi: 10.1016/0301-2115(95)02221-r.
32. T. M. Atkinson, G. D. Giraud, B. M. Togioka, D. B. Jones, and J. E. Cigarroa, "Cardiovascular and ventilatory consequences of laparoscopic surgery," *Circulation,* vol. 135, no. 7, pp. 700-710, 2017.
33. A. Verma and M. P. Singh, "Venous gas embolism in operative hysteroscopy: A devastating complication in a relatively simple surgery," *Journal of Anaesthesiology Clinical Pharmacology,* vol. 34, no. 1, pp. 103-106, 2018.
34. J. Bazin, T. Gillart, P. Rasson, N. Conio, L. Aigouy, and P. Schoeffler, "Haemodynamic conditions enhancing gas embolism after venous injury during laparoscopy: a study in pigs," *British journal of anaesthesia,* vol. 78, no. 5, pp. 570-575, 1997.
35. J. J. Maleszewski, C. K. Lai, V. Nair, and J. P. Veinot, "Anatomic considerations and examination of cardiovascular specimens (excluding devices)," *Cardiovascular pathology,* pp. 27-84, 2022.

36. K. R. Olson, "DESIGN AND PHYSIOLOGY OF ARTERIES AND VEINS | Physiology of Capacitance Vessels," in *Encyclopedia of Fish Physiology*, A. P. Farrell Ed. San Diego: Academic Press, 2011, pp. 1111-1118.
37. Q. Wu *et al.*, "Organ-on-a-chip: Recent breakthroughs and future prospects," *Biomedical engineering online,* vol. 19, pp. 1-19, 2020.
38. Y. Lu *et al.*, "Adhesion of silicone oil and emulsification: an in vitro assessment using a microfluidic device and 'Eye-on-a-Chip'," *Acta Ophthalmologica,* vol. 97, no. 3, pp. 313-318, 2019.
39. L. Si *et al.*, "A human-airway-on-a-chip for the rapid identification of candidate antiviral therapeutics and prophylactics," *Nature biomedical engineering,* vol. 5, no. 8, pp. 815-829, 2021.
40. M. Zhang *et al.*, "Biomimetic human disease model of SARS-CoV-2-induced lung injury and immune responses on organ chip system," *Advanced Science,* vol. 8, no. 3, p. 2002928, 2021.
41. D. Huh, B. D. Matthews, A. Mammoto, M. Montoya-Zavala, H. Y. Hsin, and D. E. Ingber, "Reconstituting organ-level lung functions on a chip," *Science,* vol. 328, no. 5986, pp. 1662-1668, 2010.
42. T. Cao *et al.*, "Biomimetic alveolus-on-a-chip for SARS-CoV-2 infection recapitulation," *Research,* 2022.
43. B. Müller *et al.*, "High-resolution tomographic imaging of microvessels," in *Developments in X-ray tomography VI*, 2008, vol. 7078: SPIE, pp. 89-98.
44. T.-Y. Tu and P. C.-P. Chao, "Continuous blood pressure measurement based on a neural network scheme applied with a cuffless sensor," *Microsystem Technologies,* vol. 24, pp. 4539-4549, 2018.
45. B. Alberts, A. Johnson, J. Lewis, M. Raff, K. Roberts, and P. Walter, "Blood vessels and endothelial cells," in *Molecular Biology of the Cell. 4th edition*: Garland Science, 2002.
46. E. Nader *et al.*, "Blood rheology: key parameters, impact on blood flow, role in sickle cell disease and effects of exercise," *Frontiers in physiology,* vol. 10, p. 1329, 2019.
47. L. Webb, "Mimicking Blood Rheology for More Accurate Modeling in Benchtop Research," *The Pegasus Review: UCF Undergraduate Research Journal,* vol. 12, no. 1, p. 6, 2020.
48. K. Brookshier and J. Tarbell, "Evaluation of a transparent blood analog fluid: aqueous xanthan gum/glycerin," *Biorheology,* vol. 30, no. 2, pp. 107-116, 1993.

49. T. E. Kornfield and E. A. Newman, "Measurement of retinal blood flow using fluorescently labeled red blood cells," *Eneuro,* vol. 2, no. 2, 2015.
50. E. L. Jablonski, B. M. Vogel, D. P. Cavanagh, and K. L. Beers, "Microfluidics in the Undergraduate Laboratory: Device Fabrication and an Experiment to Mimic Intravascular Gas Embolism," *Chemical Engineering Education,* vol. 44, no. 1, pp. 81-87, 2010.
51. A. B. Schroeder, E. T. Dobson, C. T. Rueden, P. Tomancak, F. Jug, and K. W. Eliceiri, "The ImageJ ecosystem: Open-source software for image visualization, processing, and analysis," *Protein Science,* vol. 30, no. 1, pp. 234-249, 2021.
52. J. G. Riess, "Fluorocarbon-based injectable gaseous microbubbles for diagnosis and therapy," *Current opinion in colloid & interface science,* vol. 8, no. 3, pp. 259-266, 2003.
53. V. Cottin, B. Delafosse, and J.-P. Viale, "Gas embolism during laparoscopy: a report of seven cases in patients with previous abdominal surgical history," *Surgical endoscopy,* vol. 10, pp. 166-169, 1996.
54. J. D. Waye, S. A. Yessayan, B. S. Lewis, and T. L. Fabry, "The technique of abdominal pressure in total colonoscopy," *Gastrointestinal endoscopy,* vol. 37, no. 2, pp. 147-151, 1991.
55. C. Henny and J. Hofland, "Laparoscopic surgery: pitfalls due to anesthesia, positioning, and pneumoperitoneum," *Surgical Endoscopy and Other Interventional Techniques,* vol. 19, pp. 1163-1171, 2005.
56. M. Perrin and A. Fletcher, "Laparoscopic abdominal surgery," *Continuing Education in Anaesthesia, Critical Care & Pain,* vol. 4, no. 4, pp. 107-110, 2004.
57. X. Yang *et al.*, "Gases for establishing pneumoperitoneum during laparoscopic abdominal surgery," *Cochrane Database of Systematic Reviews,* no. 3, 2022.
58. A. Bettiol *et al.*, "Erythrocyte oxidative stress and thrombosis," *Expert Reviews in Molecular Medicine,* vol. 24, p. e31, 2022.
59. L. O. Ferreira *et al.*, "Biochemical changes in cardiopulmonary bypass in cardiac surgery: New insights," *Journal of Personalized Medicine,* vol. 13, no. 10, p. 1506, 2023.
60. W. Fan, B. Gui, X. Zhou, L. Li, and H. Chen, "A narrative review on lung injury: mechanisms, biomarkers, and monitoring," *Critical Care,* vol. 28, no. 1, pp. 1-13, 2024.
61. K. Draper, R. Jefson, J. Jongeward, R, and M. McLeod, "Duration of postlaparoscopic pneumoperitoneum," *Surgical endoscopy,* vol. 11, pp. 809-811, 1997.

62. S. Jayaraman, A. Khakhar, H. Yang, D. Bainbridge, and D. Quan, "The association between central venous pressure, pneumoperitoneum, and venous carbon dioxide embolism in laparoscopic hepatectomy," *Surgical endoscopy,* vol. 23, pp. 2369-2373, 2009.
63. V. J. Orhurhu, C. C. Gao, and C. Ku, "Carbon dioxide embolism," 2019.
64. A. Haggerty and M. Nirmalan, "Capillary dynamics, interstitial fluid and the lymphatic system," *Anaesthesia & Intensive Care Medicine,* vol. 23, no. 2, pp. 130-137, 2022.
65. N. Radhakrishnan, "Chapter 5–The pathophysiology of varicose veins of the lower limb," *Genesis, Pathophysiology and Management of Venous and Lymphatic Disorders; Radhakrishnan, N., Ed,* pp. 95-137, 2022.
66. E. Y. Park, J.-Y. Kwon, and K. J. Kim, "Carbon dioxide embolism during laparoscopic surgery," *Yonsei medical journal,* vol. 53, no. 3, p. 459, 2012.
67. A. A. Kader and M. E. Saltveit, "Respiration and gas exchange," *Postharvest physiology and pathology of vegetables,* pp. 31-56, 2002.
68. M. A. Mirski, A. V. Lele, L. Fitzsimmons, T. J. Toung, and D. C. Warltier, "Diagnosis and treatment of vascular air embolism," *The Journal of the American Society of Anesthesiologists,* vol. 106, no. 1, pp. 164-177, 2007.
69. D. Fuard, T. Tzvetkova-Chevolleau, S. Decossas, P. Tracqui, and P. Schiavone, "Optimization of poly-di-methyl-siloxane (PDMS) substrates for studying cellular adhesion and motility," *Microelectronic Engineering,* vol. 85, no. 5-6, pp. 1289-1293, 2008.
70. R. Baudoin, G. Alberto, P. Paullier, C. Legallais, and E. Leclerc, "Parallelized microfluidic biochips in multi well plate applied to liver tissue engineering," *Sensors and Actuators B: Chemical,* vol. 173, pp. 919-926, 2012.
71. X. Q. Brown, K. Ookawa, and J. Y. Wong, "Evaluation of polydimethylsiloxane scaffolds with physiologically-relevant elastic moduli: interplay of substrate mechanics and surface chemistry effects on vascular smooth muscle cell response," *Biomaterials,* vol. 26, no. 16, pp. 3123-3129, 2005.
72. R. N. Palchesko, L. Zhang, Y. Sun, and A. W. Feinberg, "Development of polydimethylsiloxane substrates with tunable elastic modulus to study cell mechanobiology in muscle and nerve," *PloS one,* vol. 7, no. 12, p. e51499, 2012.
73. R. Akhtar, M. J. Sherratt, J. K. Cruickshank, and B. Derby, "Characterizing the elastic properties of tissues," *Materials Today,* vol. 14, no. 3, pp. 96-105, 2011.

74. M. Manzo and M. Bakaraju, "Novel thin polymeric magnetic membranes study for applications in the future biomedical devices," *AIP Advances,* vol. 12, no. 11, 2022.
75. K. L. Monson, W. Goldsmith, N. M. Barbaro, and G. T. Manley, "Axial mechanical properties of fresh human cerebral blood vessels," *J. Biomech. Eng.,* vol. 125, no. 2, pp. 288-294, 2003.
76. T. L. Poepping, H. N. Nikolov, M. L. Thorne, and D. W. Holdsworth, "A thin-walled carotid vessel phantom for Doppler ultrasound flow studies," *Ultrasound in medicine & biology,* vol. 30, no. 8, pp. 1067-1078, 2004.
77. L. Xu, H. Lee, D. Jetta, and K. W. Oh, "Vacuum-driven power-free microfluidics utilizing the gas solubility or permeability of polydimethylsiloxane (PDMS)," *Lab on a Chip,* vol. 15, no. 20, pp. 3962-3979, 2015.
78. S. Kanehashi, T. Sato, S. Sato, and K. Nagai, "Microstructure and gas diffusivity of poly (dimethylsiloxane) dense membrane using molecular dynamics (MD) simulation," *Transactions of the Materials Research Society of Japan,* vol. 37, no. 3, pp. 439-442, 2012.
79. A. S. Popel, "Theory of oxygen transport to tissue," *Critical reviews in biomedical engineering,* vol. 17, no. 3, p. 257, 1989.
80. A. Vadapalli, R. N. Pittman, and A. S. Popel, "Estimating oxygen transport resistance of the microvascular wall," *American Journal of Physiology-Heart and Circulatory Physiology,* vol. 279, no. 2, pp. H657-H671, 2000.
81. D. A. Markov, E. M. Lillie, S. P. Garbett, and L. J. McCawley, "Variation in diffusion of gases through PDMS due to plasma surface treatment and storage conditions," *Biomedical microdevices,* vol. 16, no. 1, pp. 91-96, 2014.
82. S. O. Woo, M. Oh, K. Nietfeld, B. Boehler, and Y. Choi, "Molecular diffusion analysis of dynamic blood flow and plasma separation driven by self-powered microfluidic devices," *Biomicrofluidics,* vol. 15, no. 3, 2021.
83. R. Ariati, F. Sales, A. Souza, R. A. Lima, and J. Ribeiro, "Polydimethylsiloxane composites characterization and its applications: A review," *Polymers,* vol. 13, no. 23, p. 4258, 2021.
84. T. Tsuzuki, Baassiri, K., Mahmoudi, Z., Nicolau, D.V., "Hydrophobic recovery of PDMS surfaces in contact with hydrophilic entities: relevance to biomedical devices," *Materials,* vol. in print, 2022.
85. F. Khan, K. Singh, and M. T. Friedman, "Artificial blood: the history and current perspectives of blood substitutes," *Discoveries,* vol. 8, no. 1, p. e104, 2020.

86. H. Minasyan, "Bactericidal Capacity of Erythrocytes in Human Cardiovascular System," *International Clinical Pathology Journal,* vol. 2, 07/22 2016, doi: 10.15406/icpjl.2016.02.00052.
87. M. Sawdon and E. Kirkman, "Capillary dynamics and the interstitial fluid–lymphatic system," *Anaesthesia & Intensive Care Medicine,* vol. 18, no. 6, pp. 309-315, 2017.
88. M. P. Goldman and R. A. Weiss, *Sclerotherapy: Treatment of Varicose and Telangiectatic Leg Veins (Expert Consult)*. Elsevier Health Sciences, 2016.
89. H. Minasyan, "Bactericidal capacity of erythrocytes in human cardiovascular system," *Int Clin Pathol J,* vol. 2, no. 5, p. 00052, 2016.
90. G. T. Feke, H. Tagawa, D. M. Deupree, D. G. Goger, J. Sebag, and J. Weiter, "Blood flow in the normal human retina," *Investigative ophthalmology & visual science,* vol. 30, no. 1, pp. 58-65, 1989.
91. E. L. Boulpaep, "Arteries and veins," *Medical physiology,* vol. 2, pp. 467-81, 2012.
92. N. D. Bouvy *et al.*, "Effects of carbon dioxide pneumoperitoneum, air pneumoperitoneum, and gasless laparoscopy on body weight and tumor growth," *Archives of Surgery,* vol. 133, no. 6, pp. 652-656, 1998.
93. B. Liu *et al.*, "Manipulation of micro-objects using acoustically oscillating bubbles based on the gas permeability of PDMS," (in eng), *Biomicrofluidics,* vol. 12, no. 3, p. 034111, May 2018, doi: 10.1063/1.5028419.
94. P. Ma *et al.*, "An integrated microfluidic device for studying controllable gas embolism induced cellular responses," *Talanta,* vol. 208, p. 120484, 2020.
95. J. Neudecker *et al.*, "The European Association for Endoscopic Surgery clinical practice guideline on the pneumoperitoneum for laparoscopic surgery," *Surgical endoscopy,* vol. 16, pp. 1121-1143, 2002.
96. S. Goldman, J. M. Solano-Altamirano, and K. M. LeDez, *Gas Bubble Dynamics in the Human Body* (Gas Bubble Dynamics in the Human Body). Academic Press, 2017, pp. 1-295.
97. B. S. Storm *et al.*, "Air Bubbles Activate Complement and Trigger Hemostasis and C3-Dependent Cytokine Release Ex Vivo in Human Whole Blood," *Journal of Immunology,* Article vol. 207, no. 11, pp. 2828-2840, 2021, doi: 10.4049/jimmunol.2100308.
98. J. R. Walker III, E. J. Hexdall, and H. M. Murphy-Lavoie, "Diving Gas Embolism," in *StatPearls [Internet]*: StatPearls Publishing, 2022.

99. P. Shah and M. A. Louis, "Physiology, Central Venous Pressure," in *StatPearls*. Treasure Island (FL): StatPearls Publishing Copyright © 2024, StatPearls Publishing LLC., 2024.
100. C. Gopalan and E. Kirk, "Chapter 8 - Blood pressure, hypertension, and exercise," in *Biology of Cardiovascular and Metabolic Diseases*, C. Gopalan and E. Kirk Eds.: Academic Press, 2022, pp. 141-156.
101. R. Chaudhry, J. H. Miao, and A. Rehman, "Physiology, cardiovascular," in *StatPearls [Internet]*: StatPearls Publishing, 2022.
102. W. Maue-Dickson, "Section II. Anatomy and physiology," *The Cleft Palate Journal,* vol. 14, no. 4, pp. 270-287, 1977.
103. J. Y. Lee and S. J. Lee, "Murray's law and the bifurcation angle in the arterial micro-circulation system and their application to the design of microfluidics," *Microfluidics and Nanofluidics,* Article vol. 8, no. 1, pp. 85-95, 2010, doi: 10.1007/s10404-009-0454-1.
104. T. F. Sherman, "On connecting large vessels to small," *Journal of General Physiology,* Article vol. 78, no. 4, pp. 431-453, 1981, doi: 10.1085/jgp.78.4.431.
105. S. Lorthois, F. Lauwers, and F. Cassot, "Tortuosity and other vessel attributes for arterioles and venules of the human cerebral cortex," *Microvascular research,* vol. 91, pp. 99-109, 2014.
106. M. M. Mardanpour, A. Sudalaiyadum Perumal, Z. Mahmoodi, G. Montiel Rubies, K. M. LeDez, and D. V. Nicolau, "In vitro investigation of gas embolism in microfluidic networks mimicking microvasculature," *Lab on a chip,* vol. in review, 2022.
107. V. J. Orhurhu, C. C. Gao, and C. Ku, "Carbon dioxide embolism," 2019.
108. T. C. Merkel, V. I. Bondar, K. Nagai, B. D. Freeman, and I. Pinnau, "Gas sorption, diffusion, and permeation in poly(dimethylsiloxane)," Journal of Polymer Science Part B: Polymer Physics, https://doi.org/10.1002/(SICI)1099-0488(20000201)38:3<415::AID-POLB8>3.0.CO;2-Z vol. 38, no. 3, pp. 415-434, 2000/02/01 2000, doi: https://doi.org/10.1002/(SICI)1099-0488(20000201)38:3<415::AID-POLB8>3.0.CO;2-Z.
109. M. Held, O. Kašpar, C. Edwards, and D. V. Nicolau, "Intracellular mechanisms of fungal space searching in microenvironments," Proceedings of the National Academy of Sciences, vol. 116, no. 27, pp. 13543-13552, 2019.
110. D. A. Markov, E. M. Lillie, S. P. Garbett, and L. J. McCawley, "Variation in diffusion of gases through PDMS due to plasma surface treatment and storage conditions," Biomedical microdevices, vol. 16, no. 1, pp. 91-96, 2014.

111. A. Vadapalli, R. N. Pittman, and A. S. Popel, "Estimating oxygen transport resistance of the microvascular wall," American Journal of Physiology-Heart and Circulatory Physiology, vol. 279, no. 2, pp. H657-H671, 2000.
112. P. L. Marsh et al., "Iatrogenic air embolism: pathoanatomy, thromboinflammation, endotheliopathy, and therapies," Frontiers in Immunology, vol. 14, p. 1230049, 2023.
113. W. D. Tucker, Y. Arora, and K. Mahajan, "Anatomy, blood vessels," 2017.
114. I. C. Gawthrope, M. Summers, D. J. Macey, and D. A. Playford, "An observation of venous gas emboli in divers and susceptibility to decompression sickness," Diving Hyperb Med, vol. 45, no. 1, pp. 25-28, 2015.

2.3. Additional Studies Related to Article 1

The impact of gas insufflation rates on bubble volumes in different artificial blood vessel widths and perforation sizes was analyzed in greater details, starting with an insufflation rate of 10 mL/h, reaching as high as 100 mL/h. The data is presented in a grid format in the figures below, with varying artificial blood vessel widths (30 µm, 50 µm, 80 µm, and 250 µm) in the columns and different perforation sizes (16 µm, 32 µm, and 100 µm) in the rows.

2.3.1. Impact of Reynolds Number

The channel width, and consequently the Reynolds number (Re), had a significant effect on bubble volumes in the vascular channels. Since larger channel widths were associated with faster blood flow, as in the case of real blood circulation in the human body, the Reynolds number was directly related to the flow rate and the viscosity of the synthetic blood used in these experiments. Table 2.A1 and Figure 2.A1 present the Reynolds number of the synthetic blood solution in each channel geometry versus the maximum bubble volume for different air injection rates.

Table 2.A1. Correlation between the Reynolds number of the synthetic blood solution and the maximum bubble volume for each gas insufflation rate.

Re (Synthetic Blood)	**Maximum Bubble Volume (µm^3)**					
	10 mL/h	**15 mL/h**	**25 mL/h**	**50 mL/h**	**75 mL/h**	**100 mL/h**
0.07	1.216E+05	5.547E+05	6.392E+05	4.588E+05	8.950E+05	8.950E+05
0.07	4.615E+05	5.347E+05	4.079E+05	8.303E+05	7.955E+05	7.955E+05
0.07	6.688E+05	5.667E+05	4.309E+05	4.253E+05	8.902E+05	7.404E+05
0.07	6.688E+05	8.218E+05	4.064E+05	6.560E+05	3.338E+05	4.897E+05
0.11	0E+00	1.551E+06	9.100E+05	1.514E+06	1.446E+06	1.065E+06
0.11	8.771E+05	1.146E+06	6.455E+05	6.338E+05	6.269E+05	1.317E+06
0.11	1.528E+06	8.448E+05	5.525E+05	5.872E+05	8.924E+05	1.267E+06

0.11	1.305E+06	1.490E+06	6.546E+05	7.209E+05	7.819E+05	7.735E+05
0.15	0E+00	1.383E+06	1.142E+06	1.286E+06	1.325E+06	1.230E+06
0.15	2.429E+06	1.196E+06	2.129E+06	9.655E+05	1.943E+06	8.238E+05
0.15	1.235E+06	8.696E+05	2.044E+06	2.057E+06	2.057E+06	1.941E+06
0.15	9.871E+05	1.024E+06	9.271E+05	1.246E+06	1.432E+06	1.205E+06
0.24	9.021E+05	7.440E+05	1.446E+06	1.292E+06	5.306E+05	1.031E+06
0.33	3.364E+06	3.633E+06	3.411E+06	3.457E+06	3.298E+06	3.348E+06
0.33	3.230E+06	3.109E+06	6.982E+06	3.570E+06	3.496E+06	6.944E+06
0.33	0E+00	2.622E+06	2.161E+06	4.011E+06	4.063E+06	3.768E+06
0.33	3.032E+06	3.205E+06	2.285E+06	2.246E+06	3.157E+06	2.772E+06

For the lowest Reynolds number tested (Re = 0.07), the maximum bubble volumes varied widely for different air injection rates. At a flow rate of 10 mL/h, the maximum bubble volume was relatively low, reaching 6.69 x 10^5 μm^3, but increased with higher flow rates, peaking at 75 mL/h and 100 mL/h, both resulting in maximum bubble volumes of 8.95 x 10^5 μm^3. This trend suggests that at very low Reynolds numbers, higher flow rates lead to larger bubbles due to the reduced stability in the fluid dynamics within the microchannels.

As the Reynolds number increased to 0.11, the maximum bubble volumes were generally higher than those at Re = 0.07. For instance, at 10 mL/h, the maximum bubble volume jumped to 1.53 x10^6 μm^3, significantly higher than any value observed at Re = 0.07. Whereas at 100 mL/h, the bubble volumes reached a maximum value of 1.32 x10^6 μm^3. This indicates that at slightly higher Reynolds numbers, the fluid flow leads to the formation of larger bubbles within the channel. However, higher air injection rates didn't necessarily lead to greater bubble volumes at these intermediate Reynolds numbers. When examining an even higher Reynolds number of 0.15, the trend of increasing maximum bubble volume with increasing blood flow rate continued. At this

Re, the maximum bubble volume reached up to 2.43 x10^6 µm³ at a flow rate of 10 mL/h – a substantial increase compared to lower Re values. Consequently, artificial blood vessels sustain larger bubbles as the Reynolds number increases, likely due to increased flow turbulence, but the volumes are not necessarily greater for larger air injection rates.

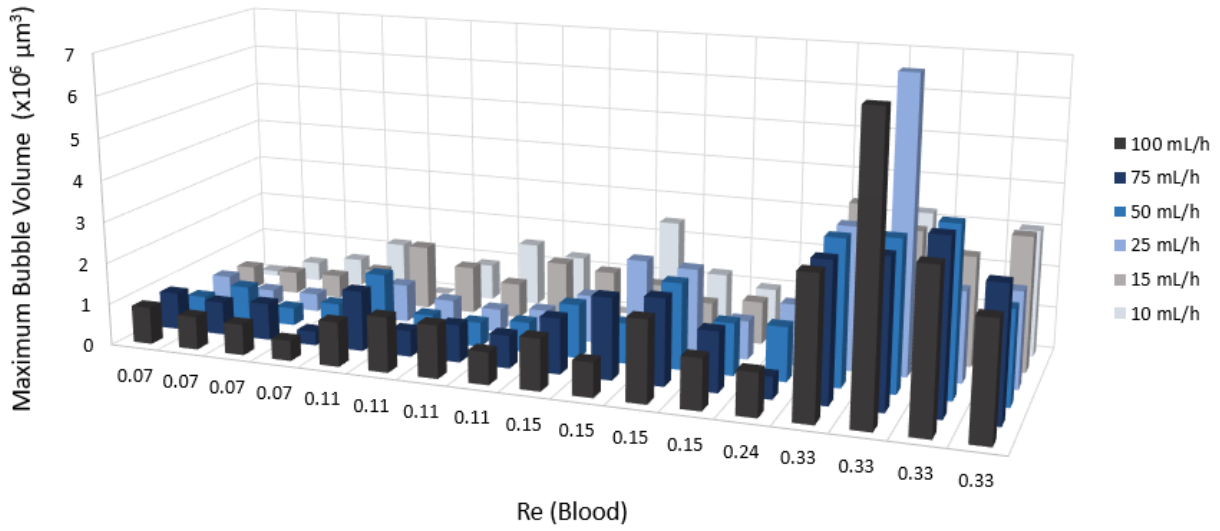

Figure 2.A1. Maximum bubble volumes at different Reynolds numbers of the synthetic blood solution for air injection rates between 10 mL/h and 100 mL/h.

At a Reynolds number of 0.24, the maximum bubble volumes exhibited further increases, but interestingly, there was a notable instance at 10 mL/h where the volume dropped to 9.02 x10^5 µm³, indicating some variability and potential instability at this intermediate Reynolds number. Nonetheless, the bubble volumes were observed to increase with the air injection rate, going from 7.44 x 10^5 µm³ at 15 mL/h to 1.03 x 10^6 µm³ at 100 mL/h. Finally, at the highest Reynolds number tested (Re = 0.33), the bubble volumes reached their maximum recorded values for all air injection rates, with volumes as high as 3.36 x 10^6 µm³, 3.63 x 10^6 µm³, 6.98 x 10^6 µm³, 4.01 x 10^6 µm³, 4.06 x 10^6 µm³, and 6.94 x 10^6 µm³ at the respective flow rates of 10 mL/h, 15 mL/h, 25 mL/h, 50 mL/h, 75 mL/h, and 100 mL/h. The trend across different flow rates at this Reynolds number resulted in the highest bubble volumes, especially as the air injection rate increased, suggesting that the flow conditions at this Reynolds number were most conducive to the formation and maintenance of large bubbles.

Consequently, the maximum bubble volumes generally increased with higher Reynolds numbers, though some variability was observed at intermediate Reynolds numbers, where larger air injection

rates did not always result in larger bubble volumes. Higher Reynolds numbers, indicative of higher flow rates, tended to promote the formation of larger bubbles within the microfluidic channels, especially as the air injection rate increased. This relationship highlights the critical role of fluid dynamics and channel geometry in the behavior of bubbles during intravascular bubble formation.

2.3.2. Impact of Gas Insufflation Rate

The impact of gas insufflation rates on bubble volumes in different channel widths and perforation sizes was analyzed, starting with an insufflation rate of 10 mL/h, reaching as high as 100 mL/h. The data is presented in a grid format in the figures below, with varying channel widths (30 μm, 50 μm, 80 μm, and 250 μm) in the columns and different perforation sizes (16 μm, 32 μm, and 100 μm) in the rows.

Low Insufflation Rates. At an insufflation rate of 10 mL/h, the smallest perforation size of 16 μm presented nearly negligible bubble volumes across the 30 μm, 50 μm, and 80 μm artificial blood vessel widths. However, in the 250 μm artificial blood vessel width, which is associated with the largest bubble volumes, there were only two instances of bubble formation as clusters with maximum volumes of 3.05×10^6 μm^3 and 3.36×10^6 μm^3, corresponding to bubble lengths of 12.7 μm and 14 μm, respectively.

As the perforation size increased to 32 μm, a noticeable rise in bubble volumes was observed in all artificial blood vessel widths, suggesting that larger perforations allow more gas to enter the artificial blood vessel, thereby facilitating bubble growth, especially as the artificial blood vessel widths increased. The rapid increase in bubble volume in the 30 μm, 50 μm and 80 μm artificial blood vessels indicate that the perforation size and artificial blood vessel width synergistically promote bubble formation. The bubble volumes were once again at their maximum in the 250 μm artificial blood vessel width, but there were more notable variations in the recorded volumes. While perforation size plays a role, the artificial blood vessel width significantly influences the final bubble size.

With the largest perforation size of 100 μm, the bubble volumes varied significantly across each artificial blood vessel width. In the narrowest artificial blood vessel (30 μm), the bubble volumes increased with time but exhibited fluctuations that became increasingly more significant when the

same experiments were performed in artificial blood vessels with larger widths. This was particularly evident in the larger artificial blood vessels, where the bubble volumes reached their maximum observed values of 9.87 x 10^5 μm^3 with a length of 4.11 µm in the 80 µm artificial blood vessels, and 3.03 x 10^6 μm^3 with a length of 12.62 µm in the 250 µm artificial blood vessels, with significant fluctuations indicating chaotic bubble behavior at this perforation size and flow rate.

Figure 2.A2A shows that smaller artificial blood vessels tend to produce smaller bubbles, and smaller perforations lead to more constant production of bubbles. Consequently, larger artificial blood vessels facilitate the formation of larger bubbles, but also with increased variability at higher perforation sizes. In Figure 2.A2B, the impact of different artificial blood vessel widths and perforation sizes on bubble volumes is presented for a higher gas insufflation rate of 15 mL/h. At this insufflation rate, the bubbles began to form in the 16 µm perforation rather than the 32 µm perforation for the 30 µm, 50 µm, and 80 µm artificial blood vessel widths, with larger bubble volumes appearing in all artificial blood vessel widths compared to the 10 mL/h rate. In the narrowest artificial blood vessel (30 µm), the bubble volumes remained at their lowest, compared to larger artificial blood vessel widths. However, the bubbles exhibited notable variability in the recorded volumes, especially in the 80 µm and 250 µm artificial blood vessels.

For the 32 µm perforation size, there was a marked increase in bubble volumes and, more dramatically, numbers, across all artificial blood vessel widths. The 50 µm artificial blood vessel showed a significant increase in bubbles compared to the 30 µm artificial blood vessel, highlighting the role of artificial blood vessel width in accommodating larger bubbles. The 80 µm and 250 µm artificial blood vessels exhibited substantial bubble volumes with considerable variability, suggesting that (i) larger artificial blood vessels facilitate the formation of greater bubble volumes, and (ii) higher perforations lead to less stable bubble formation at this higher insufflation rate.

For the largest perforation size of 100 µm, the bubble volumes displayed substantial increases across all artificial blood vessel widths. In the smallest artificial blood vessel (30 µm), bubble volumes increased in volume and chaotic behavior, but it remained more stable compared to larger artificial blood vessels. The 50 µm artificial blood vessel showed a significant rise in bubble volumes, while the 80 µm and 250 µm artificial blood vessels exhibited the highest bubble volumes with pronounced variability. This chaotic character indicates that at higher gas insufflation rates,

larger perforations and artificial blood vessels create dynamic flow conditions that significantly influence bubble size and stability.

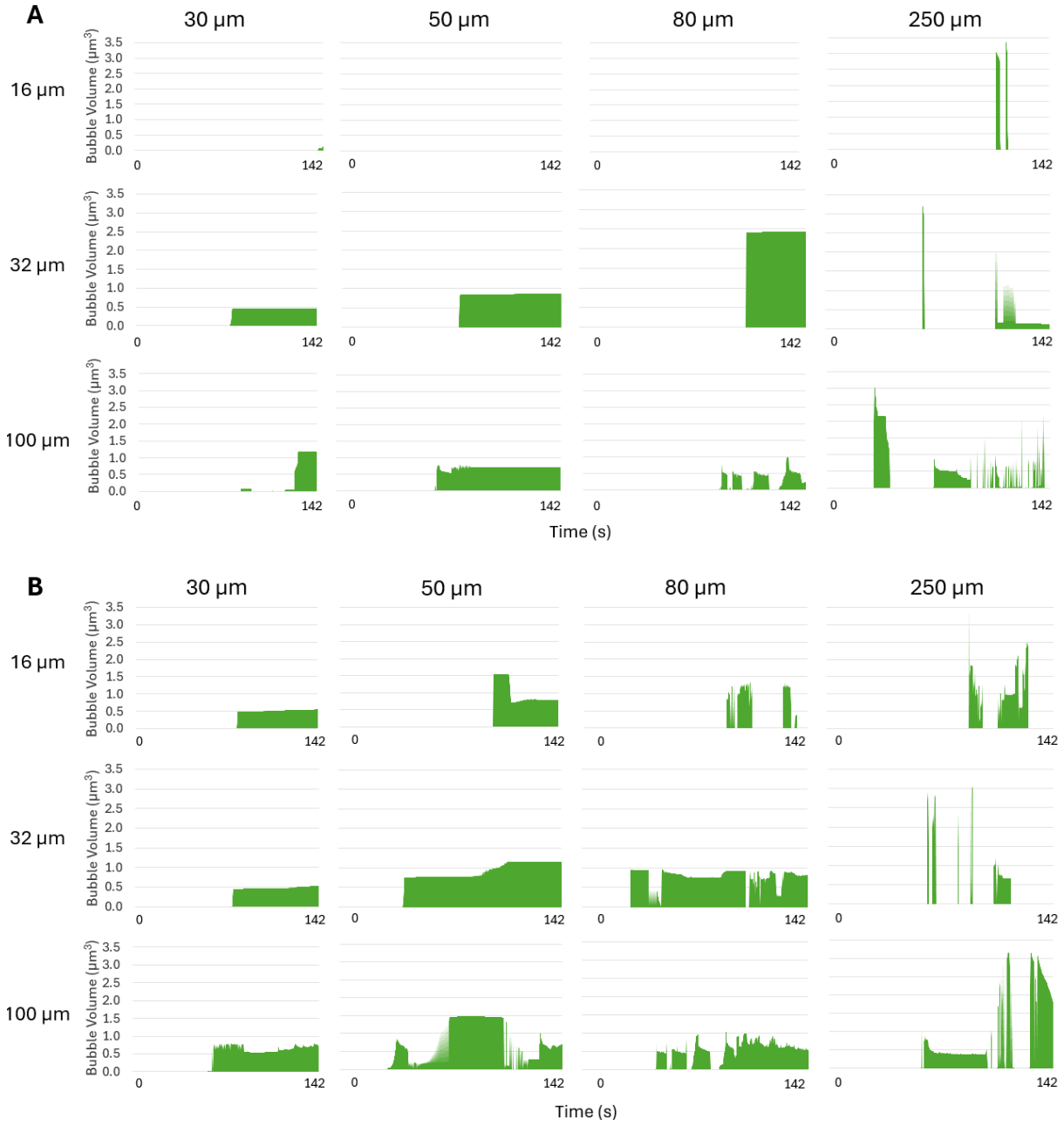

Figure 2.A2. Patterns of bubble formation in four artificial blood vessel widths, namely 30 µm, 50 µm, 80 µm, and 250 µm, with three perforation sizes, i.e., 16 µm, 32 µm, and 100 µm at gas insufflation rate of **(A)** 10 mL/h and **(B)** 15 mL/h. The bubble volumes are presented in units of x 10^6. The recording time is approximately 2 mins (0 to 142 seconds).

This shows once again that both artificial blood vessel width and perforation size significantly impact bubble volumes. Consequently, wider perforations generally lead to greater variability and larger artificial blood vessels lead to increased bubble volumes.

Medium Insufflation Rate. The impact of gas insufflation at 25 mL/h and 50 mL/h on bubble formation and volumes in artificial blood vessels with widths between 30 µm and 250 µm and perforations ranging from 16 µm to 100 µm is presented in Figure 2.A3.

At a medium-low insufflation rate of 25 mL/h, bubble formation dynamics became more pronounced across all perforation sizes and artificial blood vessel widths, demonstrating a clear impact of the increased gas flow. For the smallest perforation size (16 µm), bubble volumes exhibited a consistent rise compared to the lower insufflation rates. In the 30 µm artificial blood vessel, bubbles formed but remained relatively small and stable, maintaining low variability. However, as the vessel width increased to 50 µm, the bubble volumes increased significantly, showing that larger vessels are more capable of accommodating higher gas volumes even at modest perforation sizes. In the larger vessels (80 µm and 250 µm), bubble volumes grew more substantially, with fluctuations indicating less stable and more chaotic bubble formation. This suggests that the combined effect of vessel width and flow rate begins to amplify bubble dynamics, leading to larger and more irregular bubbles.

For the 32 µm perforation, the overall volume and variability of bubbles increased markedly across all artificial blood vessels. In the 30 µm artificial blood vessel, bubble volumes remained relatively small but showed more fluctuations than at lower flow rates. In the 50 µm vessel, there was a significant rise in bubble volumes, suggesting that intermediate vessel widths start to play a more critical role in enabling larger bubbles to form as insufflation rates rise. In the larger 80 µm and 250 µm artificial blood vessels, bubble volumes became more substantial and highly variable, reflecting the influence of both perforation size and vessel width on bubble dynamics at this medium flow rate. The variability in the 250 µm width was especially pronounced, indicating that larger vessels with moderate perforation sizes are prone to more chaotic bubble behavior at this insufflation rate.

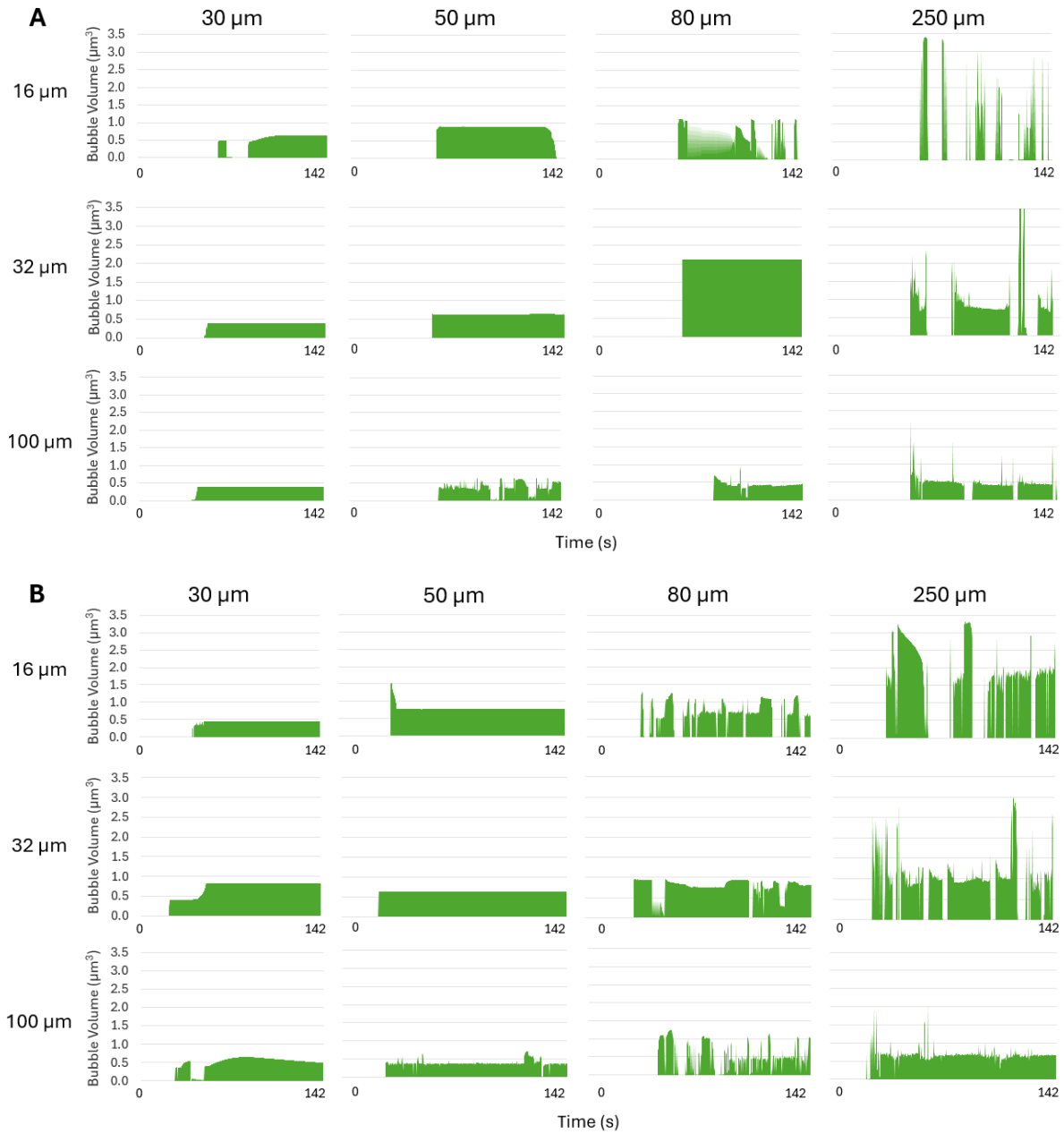

Figure 2.A3. Patterns of bubble formation in 30 µm, 50 µm, 80 µm, and 250 µm artificial blood vessels, with perforation sizes of 16 µm, 32 µm, and 100 µm at gas insufflation rate of **(A)** 25 mL/h and **(B)** 50 mL/h. The bubble volumes are presented in units of x 10^6. The recording time is approximately 2 mins (0 to 142 seconds).

At the largest perforation size (100 µm), bubble volumes across all vessel widths increased substantially, with larger artificial blood vessels showing a dramatic rise in both volume and variability. In the smallest artificial blood vessel (30 µm), the bubble volumes rose gradually but remained more stable than in larger vessels. In the 50 µm vessel, bubble volumes increased significantly and began to exhibit irregular fluctuations, indicating a shift towards more unstable

bubble formation. The 80 µm and 250 µm artificial blood vessels exhibited the largest bubble volumes, with pronounced fluctuations, indicating chaotic bubble formation at this flow rate. This chaotic behavior reflects the complex interaction between the gas insufflation rate, the large perforation size, and the wider vessel widths. In particular, the 250 µm vessel showed the most significant variations, with bubbles reaching maximum observed volumes but exhibiting considerable instability, likely due to dynamic flow conditions induced by the high insufflation rate and large perforation size.

At a medium-high gas insufflation rate of 50 mL/h, the artificial blood vessels with a 30 µm width and 16 µm perforation presented a steady increase in bubble volume over time, indicating a gradual accumulation of gas. Similarly, the 32 µm perforation also exhibited a steady increase, but at an earlier onset. The 100 µm perforation displayed a more erratic pattern with significant fluctuations in bubble volume, likely due to intermittent gas escape.

In the 50 µm width artificial blood vessel, the 16 µm perforation resulted in a rapid increase in bubble volume with the peak reached immediately at the onset of bubble formation. The 32 µm and 100 µm perforations had a sharp increase, followed by stabilization, with the largest perforation exhibiting high variability and frequent fluctuations, indicating irregular and substantial bubble formation events. For the 80 µm width artificial blood vessel, all perforation sizes exhibited significant fluctuations, especially for the largest perforation size, indicating unstable and irregular bubble formation, with higher peaks of bubble volumes in comparison with the smaller artificial blood vessel widths.

Similarly, in the 250 µm width artificial blood vessel, there was rapid initial bubble formation followed by extreme variability in bubble volumes, whereby larger perforation sizes amplified the chaotic character of the bubbles. Overall, the data suggest that smaller widths and perforations tend to result in more stable and gradual bubble formation, while larger widths and perforations lead to irregular and substantial bubble volumes.

High Insufflation Rates. Gas insufflation at a rate of 75 mL/h revealed a similar yet more pronounced pattern of bubble formation in comparison with the medium insufflation rates, as seen in Figure 2.A4A. For the artificial blood vessels with a 30 µm width, the 16 µm and 32 µm perforations showed a rapid and steady increase in bubble volume, similarly to the trend observed

at 50 mL/h but with larger volumes. The 100 μm perforations displayed more irregular and frequent fluctuations in bubble volumes throughout the frames.

In the 50 μm artificial blood vessels, the 16 μm perforation shows a steady increase in bubble volumes, which were larger than those recorded in the 30 μm widths. The 32 μm perforation resulted in a sharp initial increase, followed by a stable pattern. The 100 μm perforations exhibited higher variability with more frequent fluctuations in bubble volume, indicating irregular and significant bubble formation events. For the 80 μm artificial blood vessel, the generation of bubbles began in the 16 μm perforation with significant fluctuations in the reported volumes. The 32 μm perforation showed a rapid increase and subsequent variability, while the 100 μm perforation demonstrated frequent and substantial fluctuations in bubble volume, indicating unstable and irregular bubble formation. Finally, in the 250 μm artificial blood vessel, all perforation sizes demonstrated highly variable and irregular bubble formation patterns with significant spikes in bubble volumes. The data for the 75 mL/h insufflation rate show once again that smaller perforations lead to more stable and gradual bubble formation, while larger perforations lead to irregular bubble volumes that increase with the artificial blood vessel width.

The analysis of a larger gas insufflation at the rate of 100 mL/h in perforated artificial blood vessels revealed amplified patterns of bubble formation compared to lower insufflation rates (Figure 2.A4B). For artificial blood vessels with a 30 μm width, the 16 μm and 32 μm perforations showed a rapid yet steady increase in bubble volumes, suggesting consistent and significant bubble formation. While the 100 μm perforations revealed highly erratic patterns with substantial spikes, suggesting frequent and irregular bubble events. In the 50 μm width artificial blood vessel, the 16 μm perforation resulted in a steady increase in bubble volume, more pronounced than in the 30 μm artificial blood vessel. The 32 μm perforation showed an initial spike followed by stabilization. The 100 μm perforations exhibited once again high variability with frequent and substantial fluctuations in bubble volume, indicating significant and chaotic bubble formation events. For the 80 μm and 250 μm width artificial blood vessels, all perforation sizes exhibited frequent and substantial fluctuations in bubble volumes, indicating unstable bubble formation. This was more pronounced for the larger artificial blood vessel width with the maximum peaks observed for the 100 mL/h gas insufflation rate, in comparison with the lower values.

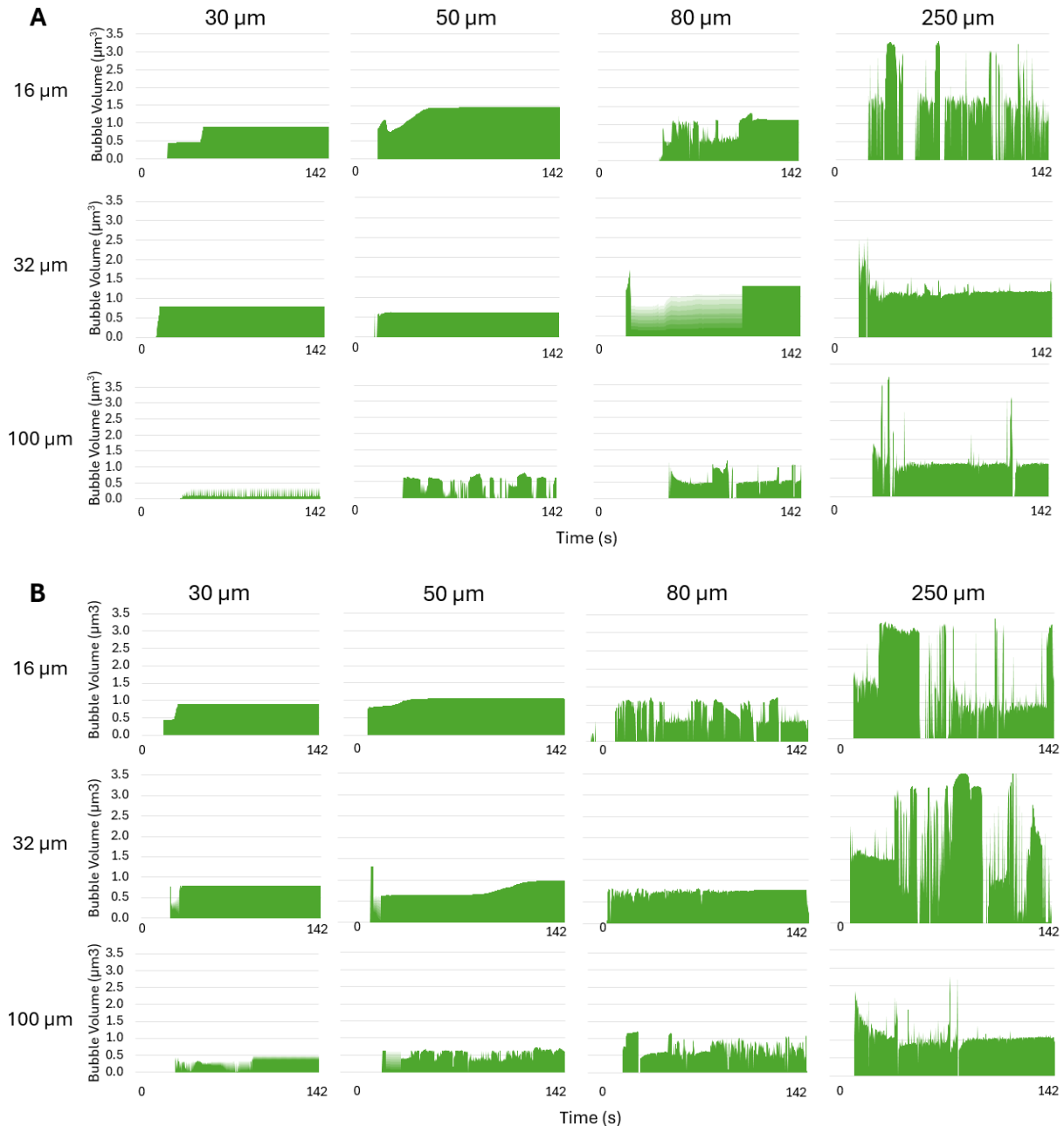

Figure 2.A4. Patterns of bubble formation in 30 µm, 50 µm, 80 µm, and 250 µm artificial blood vessels, with perforation sizes of 16 µm, 32 µm, and 100 µm at gas insufflation rate of **(A)** 75 mL/h and **(B)** 100 mL/h. The bubble volumes are presented in units of x 10^6. The recording time is approximately 2 mins (0 to 142 seconds).

Chapter 3. Impact of Biological Factors

3.1. Background of Second Article

This work, published in the *Biomimetics* journal, goes beyond merely exploring the genesis of gas embolism. It delves into the multifaceted role that hematological and anatomical variations play in the formation and progression of gas bubbles within the circulatory system. Specifically, the study examines how differences in blood viscosity and vascular geometry influence both the initiation and behavior of intravascular bubbles. To investigate these phenomena, the study utilizes microfluidic devices that incorporate bilateral pressure chambers to isolate unwanted variables and ensure a uniform pressure distribution along a larger region of interest, all the while providing precise control and monitoring of the input parameters under which bubbles are formed.

The blood viscosities in the experiment were simulated using carefully prepared mixtures of water, glycerin, and xanthan gum. These mixtures were designed to replicate the properties of blood in a range of clinical conditions: healthy individuals, as well as those with specific hematological disorders such as anemia, thrombocytopenia, or patients undergoing treatment with blood-thinning medications like heparin. The use of these different blood-mimicking solutions allowed for an in-depth analysis of how variations in blood composition impact the formation and progression of gas embolism under different physiological conditions. Additionally, the study validates and expands upon findings from Chapter 3, confirming that the relationship between gas bubble formation and the proximity of applied pressures is consistent. This consistency strengthens the theoretical framework around how external pressure and internal blood flow conditions contribute to embolism dynamics. One of the key advancements of this research is its demonstration that blood viscosity and the width of the microfluidic channels are closely correlated with key bubble generation parameters, including the number of nucleation sites and the frequency of bubble formation.

Furthermore, the study explores the characteristics of the bubbles that are generated, highlighting how viscosity and channel width influence bubble behavior, such as bubble volume and average velocity. These findings provide valuable insights into how variations in blood properties can alter embolism dynamics, potentially influencing clinical outcomes in individuals with different

hematological conditions or those undergoing anticoagulant therapy. The results from this research have significant implications for understanding and mitigating the risks associated with gas embolism in various medical contexts.

3.2. Article 2:

biomimetics

MDPI

Article

Understanding the Impact of Synthetic Hematocrit Levels and Biomimetic Channel Widths on Bubble Parameters in Vascular Systems on a Chip

Karine Baassiri[a], Dan V. Nicolau[a,*]

[a]Department of Bioengineering, Faculty of Engineering, McGill University, Montreal, Québec, H3A 0E9, Canada

*Corresponding author: dan.nicolau@mcgill.ca.

3.2.1. Abstract

Gas embolism is a rare but life-threatening process characterized by the presence of gas bubbles in the venous or arterial systems. These bubbles, if sufficiently large or numerous, can block the delivery of oxygen to critical organs, in particular the brain, and subsequently they can trigger a cascade of adverse biochemical reactions with severe medical outcomes. Despite its critical nature, gas embolism remains poorly understood, necessitating extensive investigation, particularly regarding its manifestations in the human body and its modulation by various biological conditions. However, given its elusive nature, as well as potential lethality, gas embolism is extremely difficult to study *in vivo*, and nearly impossible to be the subject of clinical trials. To this end, we developed a microfluidic de-vice designed to study in vitro the impact of blood properties and vascular geometries on the formation and evolution of gas bubbles. The system features a biomimetic vascular channel surrounded by two pressure chambers, which induce the genesis of bubbles under varying circumstances. The bubble parameters were correlated with different input parameters, i.e., channel widths, wall thicknesses, viscosities of the artificial blood, and pressure levels. Smaller channel widths and higher equivalent hematocrit concentrations in synthetic blood solutions increased the nucleation density and bubble generation frequencies. Small channel widths were also more prone to bubble formation, with implications for the vulnerability of vascular walls, leading to increased risks of damage or compromise to the integrity

of the blood vessels. Larger channel widths, along with higher equivalent hematocrit concentrations, translated into larger bubble volumes and decreased bubble velocities, leading to an increased risk of bubble immobilization within the blood vessels. This biomimetic approach provides insights into the impact of patient history and biological factors on the incidence and progression of gas embolism. Medical conditions, such as anemia, along with anatomical features related to age and sex—such as smaller blood vessels in women and children or larger vascular widths in adult men—affect the susceptibility to the initiation and progression of gas embolism, explored here in vitro through the development of a controlled, physiological-like environment. The analysis of the videos that recorded gas embolism events in vitro for systems where pressure is applied laterally on the microvasculature with thin walls, i.e., 50 μm or less, suggests that the mechanism of gas transfer for the pressure area to the blood is based on percolation, rather than diffusion. These findings highlight the importance of personalized approaches in the management and prevention of gas embolism.

3.2.2. Introduction

Vascular gas embolism, first reported in the late 19th century [1], is characterized by the presence of an abnormally high number or volume of gas bubbles in the venous or arterial circulation [2]. This process can lead to the partial or complete blockage of blood flow, and—consequently—the oxygen starvation of essential organs, especially the brain, followed by a wide range of circulatory, cardiovascular, and neurological complications, potentially causing death [3]. Gas bubbles enter or form in the vascular system due to abrupt pressure variations surrounding the human body [4], direct introduction during medical procedures [5], trauma to gas-containing organs [6], lung over-expansion injury [6], or leakage from the venous to the arterial circulation [7]. The reported incidence rates of gas embolism vary widely due to the lack of specificity in its signs and symptoms, leading to difficulty in achieving a clear and accurate diagnosis [8]. For instance, these rates were reported to range from 0.2% for significant gas embolism [9] to as high as 50% for venous gas embolism [10]. On the other hand, in medical settings, the occurrence of gas embolism was reported to be 2.65 cases out of 100,000 hospitalizations [11]. Whatever the case, the actual rate of gas embolism is progressively increasing due to the growing number of invasive medical procedures [12]. In severe cases of gas embolism, the mortality rates were reported as 16% at hospital discharge and 21% within the following year [13], with severe neurological sequelae

recorded as high as 35% [14]. The patient's medical history is currently the most indicative factor in determining not only the risk, but also the progression and behavior of gas embolism [8]. However, given its elusive nature, as well as potential lethality, gas embolism is extremely difficult to study *in vivo*, and nearly impossible to be the subject of clinical trials. Therefore, in vitro investigations of the genesis and pathophysiology of vascular gas embolism can provide insights into its fundamental origins and mechanisms, ultimately improving diagnostic techniques, preventive measures, and medical treatments.

Microfluidics-based biomimetic systems were a suitable platform [15–20] for replicating gas embolism, due to their ability to simulate a controlled microenvironment and provide real-time monitoring of disease initiation and progression. This approach enables the use of microfluidic devices as vascular systems on a chip, ranging from diagnostics to complex organoids-on-a-chip that can mimic real-life systems and organs, such as the lungs [21]. Moreover, polydimethylsiloxane-based channels offer the ability to mimic blood vessels and biological tissue [22], facilitating the study of gas bubble formation at the onset of different nucleation sites by simulating sudden pressure variations, both globally and locally. Hydrodynamic techniques have been extensively researched and utilized for the creation of gaseous bubbles in microfluidic channels containing liquid solutions [23]. Several research efforts investigated the behavior, evolution, and biological effects of artificially induced bubbles in microfluidic devices [16–20]. However, the origins of gas embolism in biomimetic systems, with real-time observation and imaging of bubble genesis, triggered by global and local pressure applications, were never attempted.

The present work replicates gas embolism in vitro to investigate its origins and evolution mechanisms, through the study and quantification of bubble generation. By introducing microfluidic devices as vascular systems on a chip, our research objectives were twofold: first, to use microfluidic platforms to replicate gas embolism by exposing a central vascular channel to side local pressures; and second, to distinguish microbubble characteristics, such as volume, frequency, and velocity, based on rheological properties (viscosity and flow rate of the synthetic blood solution) and biomimetic network geometries (channel widths and wall thicknesses). The goal of this study is to ultimately contribute to the development of better diagnostic, preventive, and therapeutic strategies for gas embolism with personalized approaches.

3.2.3. Materials and Methods

The origins of intravascular bubble formation were explored in a controllable environment, mimicking the stress-induced responses of human blood vessels, upon exposure to increasing levels of pressure, at the microscopic scale.

Device Design and Fabrication. The microfluidic system comprised a central channel with widths of 30 μm, or alternatively 40 μm, simulating small arterioles and venules. This central channel hosting the flow of synthetic blood was surrounded by two chambers comprising pressured air, which spanned the entire length of the channel, i.e., 6 mm, on both sides, at a separation of 50 μm, or alternatively 100 μm. Figure 3.1A outlines the dimensions and features of the microfluidic structure.

After designing device layouts and printing the respective photomasks, the microfluidic devices were fabricated following two processing steps: fabrication of master structures by standard SU-8 photolithography, followed by polymer replica molding through soft lithography, using polydimethylsiloxane (PDMS) [24–26], to obtain the final chips. The optimum fabrication conditions required to achieve high dimensional accuracy when replicating the designed structures were established as follows: a spin coating speed of 4000 rpm; soft baking conditions of 3 min at 65 °C followed by 6 min at 95 °C; 55 s of ultraviolet exposure; and hard baking conditions of 2 min at 65 °C then 7 min at 95 °C. After replication, the devices were cured and treated with oxygen plasma before being sealed onto clean glass slides.

Preparation of Working Fluid. The blood-mimicking solutions were prepared by mixing distilled water, glycerin, and Xanthan gum [27,28] on a hot plate at 35 °C to ensure optimal solubility and homogenization of the components. Simultaneously, the solution was subjected to continuous stirring using a magnetic stirrer at a consistent speed for 15 min. This ensured thorough dispersion of Xanthan gum, preventing clumping and facilitating the formation of a homogenous and stable solution. Two working fluids mimicked the rheological properties of anemic human blood, i.e., 20% hematocrit level, and healthy hu-man blood, i.e., 46% hematocrit level, in terms of viscosity (typically between 3.5 and 5.5 cP [29]) and surface tension (usually in the range of 53 to 58 mN/m [28]). Although PDMS channels allow direct visualization of blood flow, a fluorescent tracer, namely fluorescein sodium salt, was incorporated into the blood formulations at a volume of 1 mL

from a 2% stock solution for 50 mL of each working fluid. This guaranteed fast, easy, and high-resolution imaging of gas bubble formation and movement in microfluidic channels, without affecting the important characteristics of the blood-mimicking fluid.

Experimental Setup. The experimental setup (Figure 3.1B) consisted of an inverted con-focal microscope (Olympus IX83 fluorescence microscope, Olympus Corporation, Tokyo, Japan), two programmable syringe pumps, i.e., Pump 11 Elite Syringe Pumps, Harvard Apparatus (Holliston, MA, USA) pumping liquid, and a BD Plastipak™ (Franklin Lakes, NJ, USA) syringe pumping air. Using the first syringe pump, the working fluid was injected, from a reservoir at atmospheric conditions, into the main channel at flow rates similar to real blood flow, i.e., 20 μL/h and 35 μL/h for the 30 μm and 40 μm widths, respectively [30,31]. The second pump was used to exert varying levels of pressure on the main channel, by injecting 1 to 20 mL of air into the bilateral pressure chambers at 100 mL/h. To calibrate the pressure drop in the central channel with fluid flow, and the pressure achieved in the lateral pressure chambers, control experiments were run with the micro-fluidics systems assisted by manometers (Bidirectional Microfluidic Flow Sensor, Fluigent, Paris, France).

Image Acquisition and Analysis. The microfluidic devices were fixed on the micro-scope table, allowing high-speed imaging at sub-millimeter resolutions, using a 4X Upla-no magnifying objective. The still images and movies were acquired at a frame rate of 50 frames per second (fps) using a high-speed camera (C11440-42U30, Hamamatsu Photonics K.K., Shizuoka, Japan). All acquired data were analyzed using the software ImageJ V1.53 (FIJI) based on variations in the fluorescence intensity. The output parameters related to bubble generation in the microchannels—including the onset (frame number at which bubbles began to emerge), nucleation density (sites of bubble formation per mm), generation frequency (number of bubbles per frame), mean velocity (distance over which bubbles travel per frame), and bubble volume (width x length x height)—were correlated with channel width, equivalent hematocrit concentration, gas transport distance, and applied pressure.

Aside from the analysis of still images, the dynamics of the generation of bubbles, modulated by the applied pressure for 50 μm separation, were observed in systems comparing the effect of two viscosities, i.e., 20% and 46% hematocrit concentrations in channels with 30 μm widths, and the effect of two channel widths, i.e., 30 μm and 40 μm, for blood with 20% hematocrit concentrations.

Calculation of Applied Pressures on the Mimicked Blood Vessel. The local pressures applied sideways on the vascular channel were calculated based on the volume of injected air into the side pressure chambers. According to Boyle's law, the product of the pressure and volume (P_1V_1) at atmospheric conditions must be equal to the resulting pressure and volume after air injection (P_2V_2). The initial pressure was assumed as 760 mmHg, and the initial volume was the designed separation distance of 50 µm x the height of the channel based on the spin coating conditions 40 µm x the designed length of the channel 6000 µm. The compressed volume of the interface between the two pressure chambers and the vascular channel was calculated after measuring the new separation distance using ImageJ (FIJI). Finally, the applied pressure on the vascular walls was calculated as $P_2 = (P_1V_1)/V_2$. Control experiments compared the calculated pressures in the lateral chambers with those measured using a manometer, installed immediately after the air pump. This comparison showed that the calculations were accurate (measured pressure = 0.9724 calculated pressure in the chambers, $R^2 = 0.9983$).

The measurements and the estimation of the pressure drop in the fluid phase used a similar methodology. The pressure was measured at the exit from the fluid pump—the exit from the microfluidic system being at atmospheric pressure. Using the Hagen–Poiseuille equation, the pressure drop was then estimated for the full circuit and for the region of interest, i.e., the central channel guarded by pressure chambers for a 6 mm long distance.

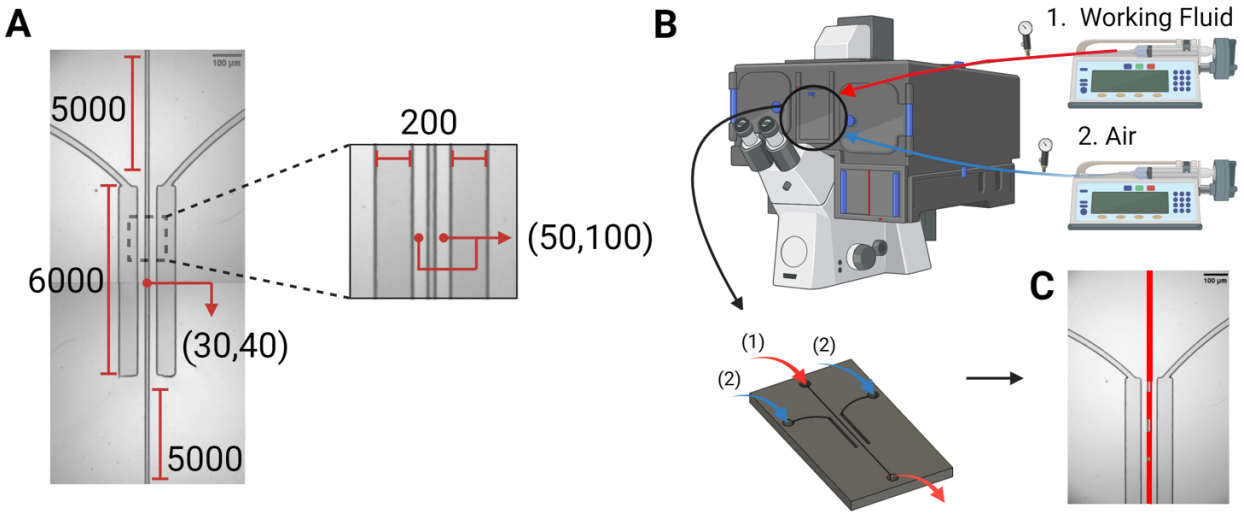

Figure 3.1. Device design and experimental setup. **(A)** The microfluidic device, i.e., the bilateral pressure chambers, consisted of a central vascular channel with a width of either 30 µm or 40 µm, surrounded by

200 μm wide pressure chambers on both sides. Dimensions are given in μm. **(B)** The microfluidic devices were placed in the microscope system, with inlets connected to two syringe pumps for the air stream (blue) and working fluids (red, taken from a reservoir at atmospheric conditions), and an outlet for draining the circulated working fluids (red, back into atmospheric conditions). **(C)** Patterns of bubble formation, resulting from pressure application on the vascular channel, via air injection into the side pressure chambers.

3.2.4. Results

Mimicry of the Microvasculature. Microfluidic devices were designed and fabricated as vascular systems on a chip made of PDMS, with bilateral pressure chambers, to mimic possible situations of gas embolism at the microscopic scale [24–26]. One possible natural system to be mimicked is the pulmonary alveolae, which has a total area in the range of 0.123 to 0.785 mm^2, leading to an average area of ~0.455 mm^2 that is exposed to gas transfer. By comparison, the central channel in the microfluidic devices, with a length of 6 mm and a height of 40 μm, presents an area for gas transfer (facing the parallel pressure chambers) of 0.48 mm^2. Another possible real system to be mimicked is the exposure of microvasculature to pressured gases during surgery, e.g., laparoscopy (the microvasculature is typically located within the organs being irrigated).

The devices were placed in the microscope system, with inlets connected to two syringe pumps for the air stream (blue) and working fluids (red). Two types of blood-equivalent solutions were injected into the channels at realistic flow rates, mimicking the circulatory system [27,28]. The rheological properties of the working fluid, widths of the vascular channel, and thicknesses of the vascular walls were evaluated in the central channel, which was undergoing uniform pressure variations along its entire length. This is particularly important because the onset of gas embolism is sudden and has never been observed and recorded in close to real-life scenarios, and it is, at least in the first instance, a predominantly physical phenomenon that requires precise control and observation of fluid behavior. The values of the pressure drop for these two types of fluids, in two channel widths, and for the full length of the microfluidic system, or the 6 mm length guarded by pressure chambers, respectively, are presented in Table 3.1.

Table 3.1. Calculation of pressure drops, using the Hagen–Poiseuille equation for fluid flow in a rectangular channel, for the region of interest (ROI), i.e., 6 mm, and the full length of the microfluidic channels.

Channel Width (μm)	Hematocrit Concentration (%)	Total Pressure Drop (mmHg)	ROI Pressure Drop (mmHg)
30	20	10.43	3.91
40	20	13.67	5.13
30	46	25.03	9.38

3.2.4.1.Selection of Materials and Fluids Mimicking the Biological System

Vascular Systems on a Chip. Polydimethylsiloxane (PDMS) was selected for fabricating the biomimetic devices, due to its biocompatibility, gas diffusivity, optical transparency, ease of replication, precise microfabrication [32], and inherent properties that are amenable to mimicking blood vessels [33,34]. More specifically, the Young's Modulus of PDMS is close to the measured values in human vessels, reported to fall within the range of 0.05 to 2 MPa [35], but possibly going up to 5 MPa [36]. By comparison, the Young's modulus for biological materials ranges from 0.05 to 2 MPa for the walls of the human veins [37], 0.04 to 2 MPa for abdominal aorta sections, 0.05 to 1.45 MPa for iliac arteries [38], and up to 5 MPa for cerebral arteries [36].

The diffusion coefficient of air in PDMS (10:1 mixing ratio) at 35 °C is between 3.21×10^{-5} cm^2/s [39] and 3.40×10^{-5} cm^2/s [40,41]. By comparison, there is a much larger variability in air diffusivity in human arteries, ranging from approximately 1×10^{-5} cm^2/s [42] to 1.39×10^{-5} cm^2/s [43]. However, in hamster retractor muscles comprising much finer blood vessels than human arteries, the diffusivity of air was reported as 2.42×10^{-5} cm^2/s at 37 °C [42]. Consequently, for the even finer blood vessels considered in this study, PDMS can reasonably be considered as a material that mimics the diffusional properties of blood vessel walls.

Synthetic Blood Solution. The working fluid must present rheological properties simi-lar to those of real blood, including dynamic viscosity, shear-thinning behavior, and refractive index. Accordingly, two blood-mimicking solutions were prepared from a base mixture of 60% distilled

water and 40% glycerin. Distilled water served as the primary solvent, while glycerin was incorporated to adjust the density and enhance the viscosity of the fluid. Xanthan gum, a high-molecular-weight polysaccharide, was subsequently added, at either 0.0075% or 0.04%, to emulate the non-Newtonian shear-thinning behavior of human blood at respective hematocrit concentrations of 20%, and 46%, representing mimicked blood from patients with anemia and normal individuals, respectively [44].

3.2.4.2.Proximity of the Application of Pressure

Initially, two separations between the pressured gas and the mimicked blood were evaluated and compared to determine the relationship between gas bubble formation and the proximity of applied pressures. It was found that bubble generation cannot occur for separations of 100 µm, irrespective of the injected air volume and flow rate (Figure 3.2). However, bubbles steadily emerged for the 50 µm separation, in both 30 µm and 40 µm channel widths, with different parameters related to bubble generation and dynamic behavior. This observation is consistent with earlier studies [19,45] investigating the gas diffusivity of PDMS that emphasized the significance of membrane thickness in diffusion-driven processes. These findings stated that for efficient gas diffusion, the thickness of PDMS membranes should ideally be around 50 µm, as thicker membranes were impeding pressure-driven processes. In an anatomical context, the majority of blood vessels are situated within the first 100 µm from airways [46,47], which makes our biomimetic microfluidic system relevant for the study of gas embolism *in vitro*.

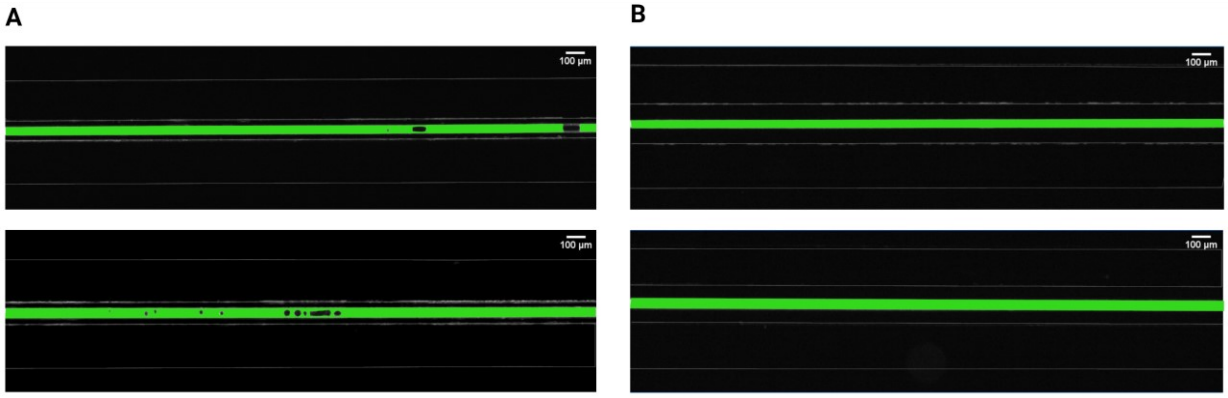

Figure 3.2. Comparison of intravascular bubble formation in 30 µm (first row) and 40 µm (second row) channels, surrounded by bilateral pressure chambers at distances of **(A)** 50 µm and **(B)** 100 µm. The injected air volume was maintained constant at 14 mL with a volumetric flow rate of 100 mL/h.

After setting the separation at 50 μm, the generation of bubbles in biomimetic vascular channels was evaluated against the equivalent hematocrit concentrations, and vascular channel widths, following uniform exposure to different pressure levels. These pressures were achieved and maintained via the introduction of two air streams in both pressure chambers, at total volumes of injected air ranging between 1 and 20 mL, thereby controlling the extent of compression on the polymer and the neighboring channel.

3.2.4.3.Characteristics of the Generation of Bubbles

Various output parameters modulating the formation of intravascular bubbles were studied, specifically two blood-mimicking solutions, i.e., anemia-like 20% [48], and nor-mal-like 46% equivalent hematocrit concentrations, and two geometries, namely channel widths of 30 μm and 40 μm. The observed output parameters of air bubbles consisted of the nucleation density, i.e., the locations of *in situ* bubble generation per mm and the generation frequency, i.e., the number of formed bubbles per second, following the application of pressure in the range of 760 mmHg to 1248.6 mmHg, due to air injections of 1 mL to 20 mL into the bilateral pressure chambers (results presented in Figures 3.3 and 3.4).

As intuitively expected, the intensity of bubble generation increased with the increase in gas pressure in the side channels (Figure 3.3A,B). However, less expected was that lower equivalent hematocrit concentrations, mimicking lower blood viscosities prevalent in anemic patients [48], and larger channel widths, resulted in a lower nucleation density. For the synthetic blood solution at 20% hematocrit level, local pressures of 1132.4 mmHg and 1193.2 mmHg led to the formation of bubbles with nucleation densities of 0.33 and 6, respectively. This is significantly smaller than for the synthetic blood solution at 46% hematocrit level, which is the value for healthy people, where the same level of pressure application generated bubbles with 0.17 and 14.33 nucleation densities, respectively, within the 30 μm channels.

When the channel width increased from 30 μm to 40 μm while using the same blood-mimicking solution at 20% equivalent hematocrit concentration, the nucleation density exhibited an upward trend for increasing volumes of air injection, but it remained smaller in comparison with the smaller channel width. At 1170.4 mmHg and 1208.4 mmHg, the bubbles emerged with nucleation densities of 1.33 and 8.33 for the 30 μm channel, in comparison with 0.83 and 3.17 for the 40 μm channel.

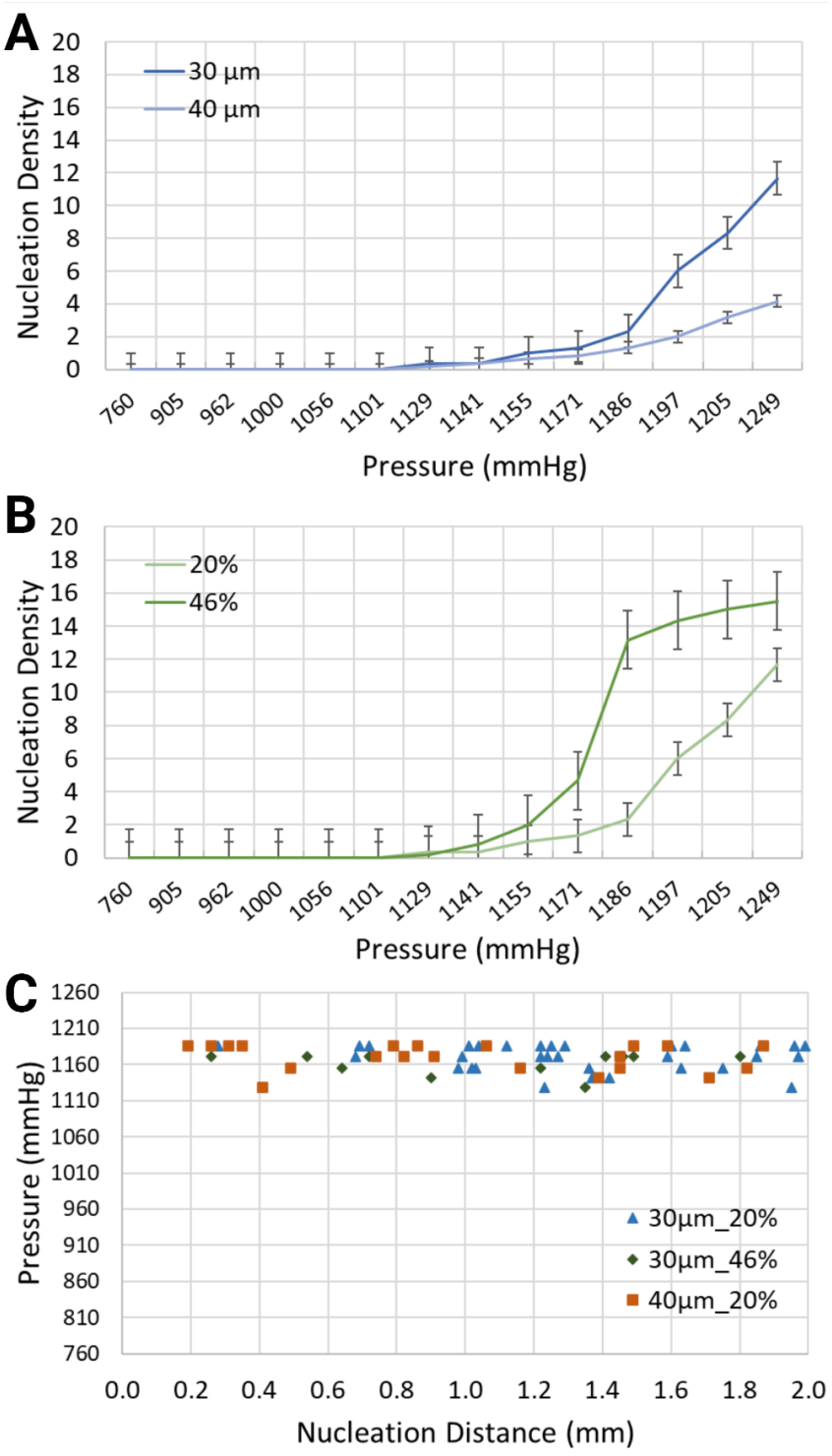

Figure 3.3. Nucleation density (nucleation sites/mm) for **(A)** two channel widths, i.e., 30 µm and 40 µm, containing a synthetic blood solution at 20% hematocrit level, and **(B)** the same channel width, i.e., 30 µm, containing two different synthetic blood solutions, at 20% and 46% hematocrit levels. **(C)** Location of nucleation sites with respect to the inlet of the synthetic blood solutions.

Regarding the spatial distribution of nucleation sites, Figure 3.3C depicts the distance between the inlet of the synthetic blood solution and the points of bubble formation. The distribution of bubbles was assessed along the visible 2 mm segment of the vascular channel. For the 30 μm channel width with the synthetic blood solution at 20% equivalent hematocrit concentration, nucleation site distances ranged from 0.28 mm to 1.99 mm. In the 40 μm channels with the same solution, distances spanned from 0.19 mm to 2.00 mm. Meanwhile, for the 30 μm channels with 46% hematocrit solution, nucleation sites were between 0.26 mm and 1.80 mm from the synthetic blood inlet. Notably, the location of nucleation sites was largely independent of the flow direction—whether upstream or downstream.

Similarly to the response of nucleation density to increased air pressure, the frequency of bubble generation also increased (Figure 3.4). Furthermore, the frequency of bubble generation increased noticeably for channels with smaller widths. This trend was further marginally amplified for the artificial blood with higher equivalent hematocrit concentration. Injected air volumes corresponding to pressures of 1185.6 mmHg and 1193.2 mmHg resulted in generation frequencies of 297.5 s^{-1} and 820 s^{-1} for the synthetic blood solution at 20% hematocrit level, and 976.25 s^{-1} and 1521 s^{-1} for the synthetic blood solution at 46% hematocrit level (30 μm channel width, Figure 3.4B). The same pressure levels led to respective frequencies of 80 s^{-1} and 162.5 s^{-1} in the 40 μm channels, holding a blood-mimicking solution at 20% equivalent hematocrit concentration (Figure 3.4A).

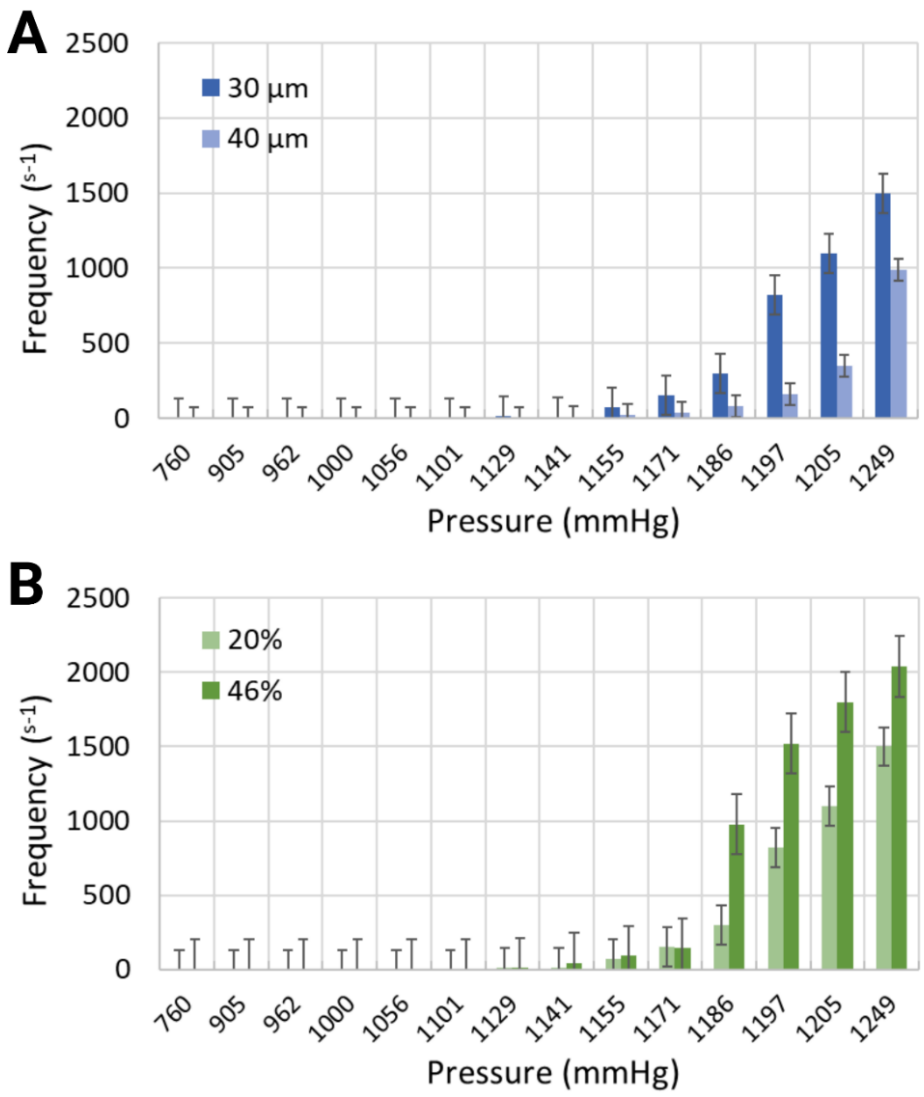

Figure 3.4. Generation frequency for **(A)** 30 µm and 40 µm channel widths containing the working fluid with 20% equivalent hematocrit concentration, and **(B)** 30 µm channel width containing two working fluids at 20% and 46% hematocrit concentrations.

3.2.4.4.Parameters of the Bubbles

Once the simulated gas embolism is initiated, the behavior of the generated bubbles varied depending on several input parameters. The intravascular bubbles were first evaluated for two different widths, i.e., 30 µm and 40 µm, containing a synthetic blood solution at 20% hematocrit level. The bubble characteristics were then assessed for the same channel width, namely 30 µm, containing 20% and 46% equivalent hematocrit concentrations.

The volume of the bubbles varied substantially, as modulated by the widths of the channels with the same synthetic blood solution, due to (i) simultaneous formation of small and large microbubbles, and (ii) recurring, yet stochastic, coalescence. The maximum bubble volumes were compared for each input parameter at different levels of compression, as presented in Figure 3.5A. In the 30 μm channels, the largest bubble volume was 150×10^3 μm^3, corresponding to a length of 125 μm for the 20% equivalent hematocrit concentration, and 640.65×10^3 μm^3 with a bubble length of 533.87 μm for the 46% equivalent hematocrit concentration, at the same injected air volume of 20 mL, resulting in the highest level of pressure application at 1248.6 mmHg. To put things in perspective, this volume translates in bubbles approximately 2.5 times, and 18 times longer, respectively, than the width of the mimicked blood vessel. However, the maximum bubble volume generated in the 40 μm channel width with a synthetic blood solution at 20% hematocrit level was determined at 773.28×10^3 μm^3, corresponding to a bubble length of 483.29 μm, for a pressure of 1185.6 mmHg (approximately 10 times longer than the vasculature width). As the volume of air injection increased, the bubble volume began to progressively decline until complete dissipation. This counterintuitive observation can be explained, as before by the authors of [15], by the chaotic character of the distribution of bubble sizes at lower pressures, when a smaller number of bubbles are produced, with few large ones, as opposed to the normal distribution at higher pressures, when many, but small, bubbles are present. Although the working fluid with a higher viscosity exhibited larger bubble volumes, the channel width had a more pronounced effect on bubble dimensions (Figure 3.5B). This effect was particularly evident at the pressure of 1185.6 mmHg in the 40 μm channel, where the bubble volume reached its maximum. The surge in bubble size observed in this case can be attributed to the peak of bubble coalescence, where multiple smaller bubbles fused to form a significantly larger single bubble. This suggests that higher pressures are not necessarily the most hazardous conditions for gas embolism. In fact, lower pressures can also pose significant risks, as they may lead to the stochastic formation of numerous small bubbles, with the occasional appearance of much larger bubbles due to coalescence. This dynamic behavior warrants further investigation in future studies.

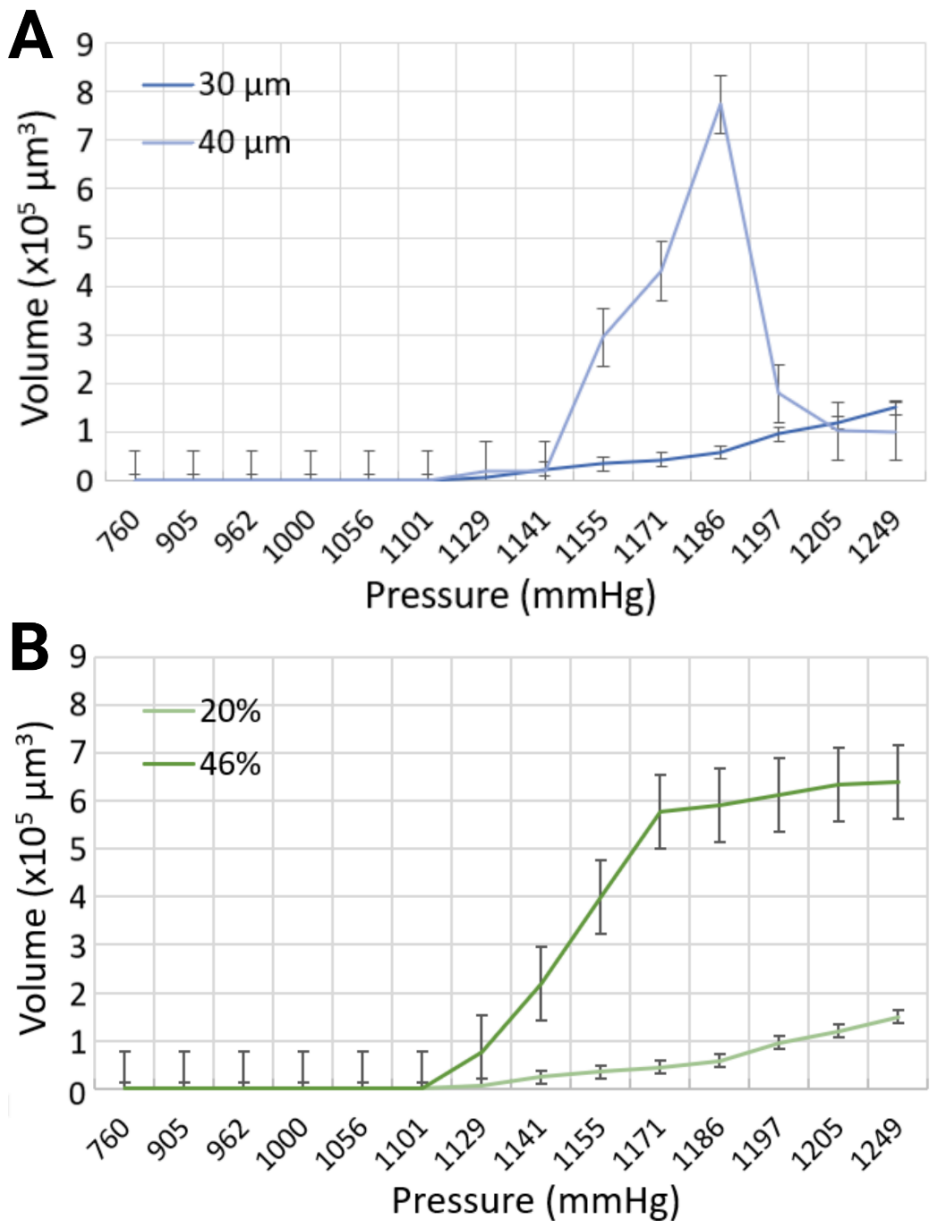

Figure 3.5. Comparison of maximum bubble volumes in **(A)** 30 µm and 40 µm channels with 20% blood-mimicking solution, and **(B)** 30 µm channel width with 20% and 46% blood-mimicking solutions.

The mean velocity of generated microbubbles in 30 µm channels was larger for the synthetic blood solution at 20% hematocrit level than for the synthetic blood solution at 46% hematocrit level (Figure 3.6). For local pressure levels of 1170.4 mmHg, 1185.6 mmHg, and 1193.2 mmHg, the average velocities were 32.26 mm/s, 41.02 mm/s, and 45.97 mm/s for the 20% equivalent hematocrit concentration, as opposed to 0.46 mm/s, 2.5 mm/s, and 4.73 mm/s for the 46%

equivalent hematocrit concentration. Working fluids with smaller viscosities are typically associated with reduced resistance to flow, thereby enabling bubble motion at higher speeds [49]. The 40 µm width channels, containing a synthetic blood solution at 20% hematocrit level, exhibited slightly slower bubble motion than smaller channel widths. The mean velocities were 15.42 mm/s, 40.15 mm/s, and 43.21 mm/s for the same applied pressures.

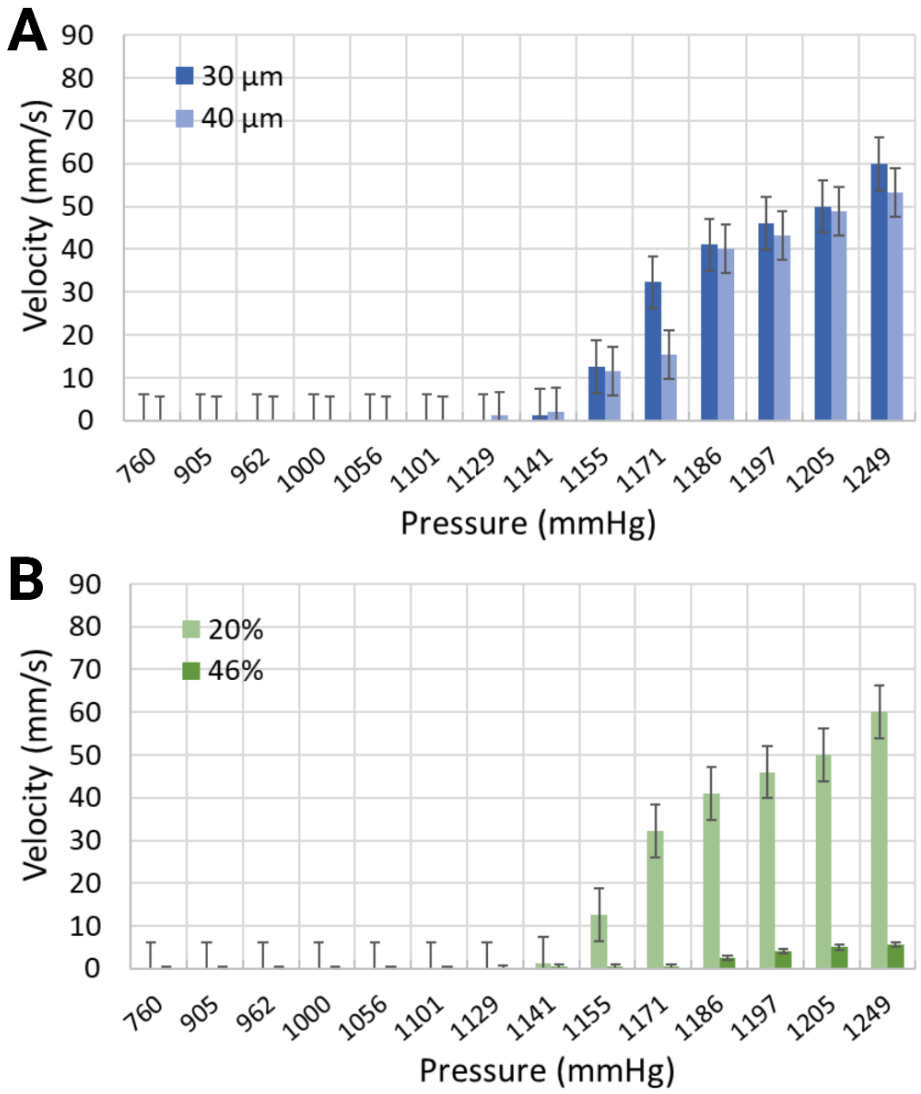

Figure 3.6. Mean velocity of the synthetic blood solutions in **(A)** two different channel widths with 20% equivalent hematocrit concentrations, and **(B)** the same channel width with 20% and 46% equivalent hematocrit concentrations.

3.2.4.5.Mechanism of Gas Embolism Modulated by Pressure, Width, and Blood Viscosity

The comparative dynamics of gas embolism, modulated by applied pressures ranging from a minimum of 960 mmHg to 1248.6 mmHg (200 mmHg to 488.6 mmHg above the atmospheric pressure of 760 mmHg), were studied and compared in microfluidic systems with 50 μm separations. These systems featured channel widths of 30 μm and 40 μm (for equivalent hematocrit concentrations of 20%), and blood concentrations of 20% and 46% (for channels with 30 μm widths). The dynamics of gas embolism mimicked in vitro can be summarized as follows:

Dynamics of Gas Embolism Modulated by Blood Viscosity. In channels with 30 μm widths and 20% equivalent hematocrit concentration, at 370 mmHg above normal atmospheric conditions, very few small, spherical bubbles formed at specific locations but were quickly washed away by the working fluid. A slight increase in pressure, e.g., 380–410 mmHg, resulted in substantial changes in bubble formation dynamics, with higher nucleation densities and larger bubbles that frequently coalesced, forming cylindrical Taylor bubbles that moved rapidly with the fluid. Further increases in pressure, up to 440 mmHg, led to the emergence of two distinct populations of bubbles: large, cylindrical bubbles filling the channels, and small, spherical ones not reaching the walls.

Conversely, in channels with 30 μm widths and 46% hematocrit concentration, the dynamics were more complex. At lower pressures, between 340 mmHg and 370 mmHg, more bubbles formed compared to the lower viscosity blood, but these bubbles grew slowly and were often static. As the pressure increased to 420–430 mmHg, the nucleation density rose, and the bubbles coalesced, forming long cylindrical bubbles that occupied the entire channel. Interestingly, although Taylor bubbles filled most of the observed vessel length, short sections filled with liquid were intermittently observed, with these liquid-filled regions still containing multiple active sites of bubble formation.

Dynamics of Gas Embolism Modulated by Vessel Width. The dynamics of gas embolism in vitro in channels with 30 μm widths and 20% hematocrit concentration was previewed above. At small pressures, i.e., 200 mmHg to 360 mmHg, only minor differences were observed compared to the dynamics in narrower channels. However, with a small increase in pressure, i.e., 400 mmHg to 420mm Hg, numerous long Taylor bubbles were observed. These bubbles collected all the smaller bubbles that formed in between, before they were fully grown, thus cascading into even longer

bubbles. At higher pressures, i.e., 445 mmHg, the flow transitioned to a fast and biphasic regime. In this state, the long bubbles developed chaotic shapes that did not fully occupy the channel width, allowing blood to flow along the sides.

Mechanism of Gas Embolism. The analysis of the videos that recorded gas embolism events in vitro for systems where pressure is applied laterally on the microvasculature with thin walls, i.e., 50 μm or less, suggests that the mechanism of gas transfer for the pressure area to the blood is based on percolation, rather than diffusion. Indeed, in all instances, that is, different blood viscosities and different blood vessel widths, the nucleation spots, once established, remain constantly fixed in the same position. The percolation rather than diffusion through PDMS further suggests that the microfluidics system developed here has more similarity to blood vessel tissue, which is inherently heterogenous, i.e., comprising cell 'islets' and interconnective matter.

3.2.5. Discussion

The experimental findings can provide insights into the formation and behavior of gas bubbles in biomimetic vascular models, advancing our understanding of gas embolism. By mimicking the structural and rheological properties of blood vessels and blood, respectively, these models can shed light onto key factors that influence bubble nucleation, growth, and movement in physiological contexts.

Mechanism of Gas Transport at the Microscale. In general, two mechanisms are known to be responsible for gas embolism: the direct injection of gas in the bloodstream, either intentional, e.g., for ultrasound imaging, or unintentional, e.g., incorrect catheterization; and gas absorption in the blood at high pressure, followed by sudden desorption due to rapid decompression, e.g., in decompression sickness. While these two alternative transport mechanisms are usually considered at the macroscale, they equally require validation at the microscale. For instance, in principle, a compression/decompression cycle of external pressure outside an individual alveolus, especially if sudden, e.g., explosions, airbag release, and forceful resuscitation, could lead to *in situ* desorption or to 'direct injection' if the thin alveolar walls are mechanically compromised. Moreover, the usage of pressured gas in modern medical practice, e.g., laparoscopy, could lead to the exposure of fine blood vessels to higher pressures and thus indirect gas transport in blood, or alternatively to blood vessel damage and thus direct injection. Indeed, it was recently reported [50]

that half of the young patients, on which laparoscopic appendectomy was performed, presented gas embolism, occurring during the dissection and ligation of the mesoappendix.

Considering the adsorption/desorption cycle, the difference in pressure in the fluid circuit is very small, i.e., a maximum of 10 mmHg (for the length of the microvasculature exposed to parallel pressure chambers, Table 3.1). Conversely, the visual analysis of the videos that recorded the gas embolism-like events in vitro for systems where pressure was applied laterally on the microvasculature with thin walls, i.e., 50 μm or less, suggests a different mechanism than the absorption/desorption mechanism, as the spatial distribution of the nucleation of the bubbles did not show any correlation with the—admittedly small—gradient of pressure along the fluid flow. Furthermore, the analysis of the nucleation suggests that the mechanism of gas transfer for the pressure area to the blood is based on percolation, rather than diffusion. Indeed, in all instances, that is, different blood viscosities and different blood vessels widths, the nucleation spots, once established, re-main constantly fixed in the same position. The percolation rather than diffusion through PDMS further suggests that the microfluidic system developed here has more similarity to blood vessels tissue, which is inherently heterogenous, i.e., comprising cell 'islets' and interconnective matter.

Proximity of Pressure Application. The observation that the generation of gas bubbles does not occur at a separation of 100 μm between the source of pressure and blood flow, but occurs readily at 50 μm, highlights the critical role of membrane thickness in gas transport through the walls of blood vessels, even under moderate pressure. These findings underscore the physiological relevance of mimicking the vascular dimensions closely tied to gas transport in the human body, where most blood vessels lie within a 100 μm range from the airways [46,47]. Such spatial constraints could influence embolism risks in clinical scenarios involving rapid pressure changes, such as decompression sickness or hyperbaric exposures, by altering the conditions under which gas bubbles form and propagate. The closer proximity of pressure sources to blood vessels (i.e., within 50 μm), overwhelmingly prevalent in lung tissues, can significantly increase the likelihood of bubble formation, thereby intensifying the risks of pulmonary embolism in environments with fluctuating pressures, such as airbags deployed in car accidents, strong CPR, and explosions.

Rheological and Geometric Factors. The present study demonstrated that blood viscosity and vascular geometry significantly impact the formation and behavior of intravascular microbubbles.

Higher hematocrit levels, associated with increased blood viscosity, were linked to greater nucleation densities, higher bubble frequencies, and larger bubbles. These findings suggest that increased viscosity exacerbates gas embolism risks by promoting conditions favorable for bubble formation and persistence. This observation is particularly relevant to men, who typically exhibit higher hematocrit levels than women [51], contributing to their greater susceptibility to gas embolism. On the other hand, a 20% equivalent hematocrit concentration, as seen in conditions like anemia, resulted in lower nucleation densities and smaller bubbles, reflecting the reduced blood viscosity, and therefore the decreased resistance to flow. The latter causes lower pressure drops in the synthetic blood solution, which, in turn, creates smaller pressure gradients than those generated in higher blood viscosities, as global pressures are applied in the vicinity of the vascular channel. While this may suggest a lower risk of embolism in anemic individuals under normal conditions, the altered flow dynamics and bubble behavior in low-viscosity environments could still pose unique risks under specific circumstances.

Furthermore, larger widths of blood vessels, e.g., arteries, facilitated larger bubble volumes, likely due to reduced flow resistance and increased energy availability for bubble nucleation and growth. This trend underscores the higher risk of gas embolism in the arterial system compared to the venous one, where smaller widths and slower flow rates limit bubble dynamics. However, smaller channel widths were found to be more vulnerable to bubble formation, due to increased nucleation densities. This vulnerability is consistent with findings in studies of decompression sickness, where researchers have reported that gas embolism is believed to originate in veins [52], where less energy is required for bubble nucleation to occur, due to blood circulation being at lower flow rates than in the arteries.

Dynamic Behavior of Bubbles. Bubble volume and velocity also varied significantly with changes in channel geometry and fluid properties. Smaller channels and lower viscosities allowed faster bubble movement, consistent with reduced resistance to flow. Conversely, higher viscosities, driven by increased hematocrit levels, produced slower-moving, larger bubbles due to enhanced coalescence and resistance. Such bubbles pose a greater obstruction risk, particularly in arterial systems, where the combination of low velocity and large vessel size exacerbates their impact on blood circulation.

One important qualification with respect to the present study is the absence of red blood cells in the current experimental setup. *In vivo*, red blood cells are believed to con-tribute to bubble lodging due to the formation of blood clots at the tail of the bubble [16–18]. The present study suggests that future research should incorporate these cells into the experimental setup to enhance the clinical relevance of these findings.

Clinical Relevance and Implications. The experimental conditions modeled in these biomimetic devices provide parallels to physiological conditions that can trigger and then precipitate gas embolism. The pronounced effects of higher hematocrit levels and larger vascular channels help explain sex-specific differences in embolism susceptibility, as well as the heightened severity of arterial gas embolism compared to venous embolism. Arterial embolisms are particularly severe because bubbles are more likely to lodge in critical pathways, obstructing blood flow and causing tissue damage. In contrast, venous embolisms often encounter the pulmonary bubble filter [53], which mitigates their progression.

By providing a controlled environment to simulate and study gas bubble formation and behavior, these biomimetic devices offer a powerful tool for exploring gas embolism mechanisms. They pave the way for targeted therapeutic interventions, such as modifying blood viscosity or designing medical protocols to minimize embolism risks under specific physiological or procedural conditions. Future studies incorporating red blood cells and clotting dynamics will further refine these findings and enhance their applicability to clinical scenarios.

3.2.6. Conclusions

The present study aims to contribute to the fundamental understanding of the genesis of vascular gas embolism for the mitigation of bubble formation, through the design and use of a novel microfluidic design monitoring the impact of local pressure applications. Although microfluidic devices are routinely used for diagnostics and high-throughput screening, they are emerging as invaluable tools for studies mimicking in vitro biological process at the microscale, such as—here—gas embolism, thereby advancing scientific and medical knowledge. The proposed biomimetic platforms allowed the simulation of a controllable environment, with the ability to fine-tune experimental conditions in order to dissect the underlying mechanisms governing intravascular bubble formation. Microscopic-level information can be obtained and analyzed in

increasingly complex vascular systems on a chip in order to derive adequate diagnostic, preventive, and therapeutic techniques while providing a better understanding of the medical implications of microbubbles on the vascular system. This approach can also be translated into design guidelines for surgical instruments and medical interventions, which can prevent the application of forces on human tissue that lead to gas embolism. Furthermore, the use of bilateral pressure chambers provides insights into the relationship between local pressure variations and the emergence of bubbles within vascular networks. Geometric variations and blood viscosities were proven to have a considerable impact on the genesis and evolution of intravascular microbubbles. The tendency of microbubbles to coalesce and form larger, slower-moving bubbles in thicker blood-mimicking solutions and larger channel widths was supported by empirical-based evidence from the current findings.

Author Contributions: Conceptualization, K.B. and D.V.N.; methodology, K.B.; validation, K.B.; formal analysis, K.B.; investigation, K.B. and D.V.N.; resources, D.V.N.; data curation, K.B.; writ-ing—original draft preparation, K.B.; writing—review and editing, K.B. and D.V.N.; visualization, K.B.; supervision, D.V.N.; project administration, D.V.N.; funding acquisition, D.V.N. All authors have read and agreed to the published version of the manuscript.

Funding: This research was funded by the Canadian Natural Sciences and Engineering Research Council (NSERC), under grant no. RGPIN-2022-04053.

Institutional Review Board Statement: Not applicable.

Informed Consent Statement: Not applicable.

Data Availability Statement: The raw data supporting the conclusions of this article will be made available by the authors on request.

Acknowledgments: We extend our gratitude to Galyna Shul and Ayyappasamy Sudalaiyadum Perumal for their support, training, and professional expertise.

Conflicts of Interest: The authors declare no conflicts of interest. The funders had no role in the design of the study; in the collection, analyses, or interpretation of data; in the writing of the manuscript; or in the decision to publish the results.

3.2.7. References

1. Mirski, M.A.; Lele, A.V.; Fitzsimmons, L.; Toung, T.J.K. Diagnosis and treatment of vascular air embolism. J. Am. Soc. Anesthesiol. 2007, 106, 164–177.
2. van Hulst, R.A.; Klein, J.; Lachmann, B. Gas embolism: Pathophysiology and treatment. Clin. Physiol. Funct. Imaging 2003, 23, 237–246.
3. Malik, N.; et al. Air embolism: Diagnosis and management. Futur. Cardiol. 2017, 13, 365–378.
4. Dick, A.P.; Massey, E.W. Neurologic presentation of decompression sickness and air embolism in sport divers. Neurology 1985, 35, 667.
5. Marsh, P.L.; et al. Iatrogenic air embolism: Pathoanatomy, thromboinflammation, endotheliopathy, and therapies. Front. Im-munol. 2023, 14, 1230049.
6. Muth, C.M.; Shank, E.S. Gas embolism. New Engl. J. Med. 2000, 342, 476–482.
7. Hakman, E.N.; Cowling, K.M. Paradoxical Embolism. StatPearls: Treasure Island, Florida. 2017.
8. Gordy, S.; Rowell, S. Vascular air embolism. Int. J. Crit. Illn. Inj. Sci. 2013, 3, 73–76.
9. Alexander, A.M.; Martin, N. Arterial Gas Embolism. StatPearls: Treasure Island, Florida. 2019.
10. Verma, A.; Singh, M.P. Venous gas embolism in operative hysteroscopy: A devastating complication in a relatively simple surgery. J. Anaesthesiol. Clin. Pharmacol. 2018, 34, 103–106.
11. McCarthy, C.J.; Behravesh. S.; Naidu, S.G.; Oklu, R. Air embolism: Diagnosis, clinical management and outcomes. Diagnostics 2017, 7, 5.
12. Kerrigan, M.J.; Cooper, J.S. Venous Gas Embolism. StatPearls: Treasure Island, Florida. 2018.
13. Cooper, J. Treatment of endoscopy associated cerebral gas embolism. Off. J. Am. Coll. Gastroenterol. ACG 2018, 113, 1742–1744.
14. Heming, N.; Melone, M.-A.; Annane, D. Update on the management of iatrogenic gas embolism. Annu. Update Intensive Care Emerg. Med. 2020, 2020, 559–568.
15. Mardanpour, M.M.; Perumal, A.S.; Mahmoodi, Z.; Baassiri, K.; Montiel-Rubies, G.; LeDez, K.M.; Nicolau, D.V. Investigation of air bubble behaviour after gas embolism events induced in a microfluidic network mimicking microvasculature. Lab Chip 2024, 24, 2518–2536.

16. Bento, D.; Lopes, S.; Maia, I.; Pereira, A. I.; Fernandes, C. S.; Miranda, J. M.; Lima, R. Blood Flow of Bubbles Moving in Micro-channels with Bifurcations. In VipIMAGE 2019: Proceedings of the VII ECCOMAS Thematic Conference on Computational Vision and Medical Image Processing, Porto, Portugal, 16–18 October 2019; Springer: Berlin/Heidelberg, Germany, 2019.
17. Bento, D.; Lopes, S.; Maia, I.; Lima, R.; Miranda, J. M. Bubbles moving in blood flow in a microchannel network: The effect on the local hematocrit. Micromachines 2020, 11, 344.
18. Bento, D.; Sousa, L.; Yaginuma, T.; Garcia, V.; Lima, R.; Miranda, J. M. Microbubble moving in blood flow in microchannels: Effect on the cell-free layer and cell local concentration. Biomed. Microdevices 2017, 19, 6.
19. Ma, P.; Wang, S.; Guan, R.; Hu, L.; Wang, X.; Ge, A.; Zhu, J.; Du, W.; Liu, B.F. An integrated microfluidic device for studying controllable gas embolism induced cellular responses. Talanta 2020, 208, 120484.
20. Li, Z.; Li, G.; Li, Y.; Chen, Y.; Li, J.; Chen, H. Flow field around bubbles on formation of air embolism in small vessels. Proc. Natl. Acad. Sci. USA 2021, 118, e2025406118.
21. Huh, D. A human breathing lung-on-a-chip. Ann. Am. Thorac. Soc. 2015, 12 (Suppl. S1), S42–S44.
22. Miranda, I.; Souza, A.; Sousa, P.; Ribeiro, J.; Castanheira, E. M.; Lima, R.; Minas, G. Properties and applications of PDMS for biomedical engineering: A review. J. Funct. Biomater. 2021, 13, 2.
23. Garstecki, P. Formation of droplets and bubbles in microfluidic systems. In Microfluidics Based Microsystems: Fundamentals and Applications; Springer: Berlin/Heidelberg, Germany, 2010; pp. 163–181.
24. Nilsson, D.P.; Holmgren, M.; Holmlund, P.; Wåhlin, A.; Eklund, A.; Dahlberg, T.; Wiklund, K.; Andersson, M. Patient-specific brain arteries molded as a flexible phantom model using 3D printed water-soluble resin. Sci. Rep. 2022, 12, 10172.
25. Kim, J.H.; Chhai, P.; Rhee, K. Development and characterization of viscoelastic polydimethylsiloxane phantoms for simulating arterial wall motion. Med. Eng. Phys. 2021, 91, 12–18.

26. Nomoni, M.; May, J.M.; Kyriacou, P.A. Novel polydimethylsiloxane (PDMS) pulsatile vascular tissue phantoms for the in-vitro investigation of light tissue interaction in photoplethysmography. Sensors 2020, 20, 4246.
27. Perrira, N.; Shuib, A. S.; Phang, S. W.; Muda, A. S. Experimental Investigation of Blood Mimicking Fluid Viscosity for Application in 3D-Printed Medical Simulator. J. Phys. Conf. Ser. 2022, 2222, 012016.
28. Webb, L. Mimicking Blood Rheology for More Accurate Modeling in Benchtop Research. Pegasus Rev. UCF Undergrad. Res. J. 2020, 12, 6.
29. Nader, E.; et al. Blood rheology: Key parameters, impact on blood flow, role in sickle cell disease and effects of exercise. Front. Physiol. 2019, 10, 1329.
30. Kornfield, T.E.; Newman, E.A. Measurement of retinal blood flow using fluorescently labeled red blood cells. eNeuro 2015, 2, 005-15.
31. Jablonski, E.L.; Vogel, B. M.; Cavanagh, D. P.; Beers, K. L. Microfluidics in the Undergraduate Laboratory: Device Fabrication and an Experiment to Mimic Intravascular Gas Embolism. Chem. Eng. Educ. 2010, 44, 81–87.
32. Bhattacharjee, N.; Urrios, A.; Kang, S.; Folch, A. The upcoming 3D-printing revolution in microfluidics. Lab a Chip 2016, 16, 1720–1742.
33. Fuard, D.; Tzvetkova-Chevolleau, T.; Decossas, S.; Tracqui, P.; Schiavone, P. Optimization of poly-di-methyl-siloxane (PDMS) substrates for studying cellular adhesion and motility. Microelectron. Eng. 2008, 85, 1289–1293.
34. Baudoin, R.; Alberto, G.; Paullier, P.; Legallais, C.; Leclerc, E. Parallelized microfluidic biochips in multi well plate applied to liver tissue engineering. Sens. Actuators B Chem. 2012, 173, 919–926.
35. Brown, X.Q.; Ookawa, K.; Wong, J.Y. Evaluation of polydimethylsiloxane scaffolds with physiologically-relevant elastic moduli: Interplay of substrate mechanics and surface chemistry effects on vascular smooth muscle cell response. Biomaterials 2005, 26, 3123–3129.
36. Palchesko, R.N.; Zhang, L.; Sun, Y.; Feinberg, A. W. Development of polydimethylsiloxane substrates with tunable elastic modulus to study cell mechanobiology in muscle and nerve. PLoS ONE 2012, 7, e51499.
37. Monson, K.L.; Goldsmith, W.; Barbaro, N. M.; Manley, G. T. Axial mechanical properties of fresh human cerebral blood vessels. J. Biomech. Eng. 2003, 125, 288–294.

38. Poepping, T.L.; Nikolov, H. N.; Thorne, M. L.; Holdsworth, D. W. A thin-walled carotid vessel phantom for Doppler ultrasound flow studies. Ultrasound Med. Biol. 2004, 30, 1067–1078.
39. Markov, D.A.; Lillie, E. M.; Garbett, S. P.; McCawley, L. J. Variation in diffusion of gases through PDMS due to plasma surface treatment and storage conditions. Biomed. Microdevices 2013, 16, 91–96.
40. Kanehashi, S.; Sato, T.; Sato, S.; Nagai, K. Microstructure and gas diffusivity of poly (dimethylsiloxane) dense membrane using molecular dynamics (MD) simulation. Trans. Mater. Res. Soc. Jpn. 2012, 37, 439–442.
41. Xu, L.; Lee, H.; Jetta, D.; Oh, K. W. Vacuum-driven power-free microfluidics utilizing the gas solubility or permeability of polydimethylsiloxane (PDMS). Lab Chip 2015, 15, 3962–3979.
42. Vadapalli, A.; Pittman, R.N.; Popel, A.S. Estimating oxygen transport resistance of the microvascular wall. Am. J. Physiol. Circ. Physiol. 2000, 279, H657–H671.
43. Popel, A.S.; Pittman, R.N.; Ellsworth, M.L. Rate of oxygen loss from arterioles is an order of magnitude higher than expected. Am. J. Physiol. Circ. Physiol. 1989, 256, H921–H924.
44. Brookshier, K.; Tarbell, J. Evaluation of a transparent blood analog fluid: Aqueous xanthan gum/glycerin. Biorheology 1993, 30, 107–116.
45. Liu, B.; Tian, B.; Yang, X.; Li, M.; Yang, J.; Li, D.; Oh, K. W. Manipulation of micro-objects using acoustically oscillating bubbles based on the gas permeability of PDMS. Biomicrofluidics 2018, 12, 034111.
46. Anderson, J.C.; Bernard, S. L.; Luchtel, D. L.; Babb, A. L.; Hlastala, M. P. Axial and radial distribution of the bronchial vasculature in sheep. Respir. Physiol. Neurobiol. 2002, 132, 329–339.
47. Laitinen, A.; Laitinen, L. A.; Moss, R.; Widdicombe, J. G. Organisation and structure of the tracheal and bronchial blood vessels in the dog. J. Anat. 1989, 165, 133.
48. Broberg Craig, S.; et al. Blood viscosity and its relationship to iron deficiency, symptoms, and exercise capacity in adults with cyanotic congenital heart disease. J. Am. Coll. Cardiol. 2006, 48, 356–365.
49. Zhang, C.; Weldetsadik, N. T.; Hayat, Z.; Fu, T.; Zhu, C.; Jiang, S.; Ma, Y. The effect of liquid viscosity on bubble formation dynamics in a flow-focusing device. Int. J. Multiph. Flow 2019, 117, 206–211.

50. Fuentes, S.; Grande-Moreillo, C.; Margarit-Mallol, J.; Flores-Villar, S.; Solé-Heuberger, E.; Jaen-Manzanera, A. Gas Embolism in Pediatric Minimally Invasive Surgery: Should It Be a Concern? J. Laparoendosc. Adv. Surg. Tech. 2023, 33, 1011–1017.
51. Billett, H.H. Hemoglobin and hematocrit. In Clinical Methods: The History, Physical, and Laboratory Examinations, 3rd ed.; Butter-worth, England. 1990.
52. Mitchell Simon, J. Decompression illness: A comprehensive overview. Diving Hyperb. Med. 2024, 54 (Suppl. S1), 1–53.
53. Butler, B.D.; Hills, B.A. The lung as a filter for microbubbles. J. Appl. Physiol. Respir. Environ. Exerc. Physiol. 1979, 47, 537–543.

Chapter 4. Simulation of Decompression Sickness

4.1. Background of Third Article

Decompression sickness (DCS), commonly known as "the bends," is a severe physiological condition that arises when dissolved gases, primarily nitrogen, come out of solution within bodily fluids and form bubbles due to a sudden drop in ambient pressure. While DCS has been extensively studied in the context of diving physiology, many of its fundamental mechanisms remain elusive due to the complex interplay of physical, biological, and environmental factors governing bubble nucleation and growth. Given that vascular gas embolism shares a similar underlying physical process with DCS—the formation of intravascular bubbles—studying DCS in controlled environments can provide crucial insights into embolism-related pathophysiology, risk factors, and potential mitigation strategies.

One of the primary challenges in understanding and mitigating DCS is the lack of real-time visualization and quantification of bubble dynamics inside the body. Traditional approaches rely on computational modeling, clinical observation, and large-scale hyperbaric experiments, which provide valuable but often indirect evidence of bubble behavior. To bridge this gap, this chapter employs a microfluidic-based approach to simulate decompression-induced gas embolism within a controlled, microscale hyperbaric system. By leveraging PDMS-based microfluidic devices that mimic human vascular bifurcations, this research aims to elucidate the role of heterogeneous nucleation, vascular geometry, and tissue supersaturation in bubble formation during decompression events.

A key aspect of this study is the distinction between tissue-derived and intravascular bubbles. Since PDMS is known to absorb and release gases, it serves as an analog for biological tissues that experience supersaturation during prolonged high-pressure exposure. By monitoring the emergence and behavior of bubbles from both the PDMS scaffold and the circulating synthetic blood, this research aims to differentiate between extravascular and intravascular gas embolism events. Notably, the delayed appearance of bubbles—particularly within 10 to 30 minutes post-decompression—aligns with clinical observations of DCS symptoms manifesting after surfacing from a dive or post-flight.

Findings from this study hold significant implications for both fundamental decompression research and practical safety protocols. Understanding the factors that contribute to larger and more numerous bubbles during prolonged high-pressure exposure can inform guidelines for safer ascent profiles, improved decompression schedules, and potential therapeutic interventions such as optimized hyperbaric oxygen treatment. Furthermore, by demonstrating the feasibility of using microfluidic models for studying DCS, this research paves the way for future investigations into the biomechanical and biochemical interactions underlying gas embolism-related disorders.

The status of this chapter is pending a final confirmation on the journal to which it will be submitted.

4.2. Article 3:

Mechanisms of Bubble Formation in a Microfluidic Diver Model Simulating Decompression Sickness in a Microscale Hyperbaric System

Karine Baassiri[a], Thomas Allen[a], Dan V. Nicolau*[a]

[a]McGill University, Faculty of Engineering, Department of Bioengineering, Montreal, Quebec, H3A 0C3, Canada
*Corresponding author: dan.nicolau@mcgill.ca

4.2.1. Abstract

Decompression sickness occurs when dissolved gases come out of solution, forming bubbles within the vascular system and tissues. This phenomenon typically results from rapid decompression following prolonged exposure to elevated pressures, as observed in activities such as diving, aviation, and space exploration. The sudden formation of bubbles and the challenges associated with real-time visualization highlight the need for *in vitro* studies to examine the parameters and conditions governing bubble formation and evolution. In this study, a microscale hyperbaric system was developed to provide a controlled environment for replicating multiple decompression scenarios by varying key factors, including the type of gases used, the duration of compression, and the pressure threshold. Compressed air and nitrogen were tested at 1 bar and 3 bars, with compression periods lasting 2 hours, 4 hours, 6 hours, and 12 hours. Three microfluidic channels, designed to mimic human vasculature based on Murray's law of bifurcation, were integrated into the system. These channels were subjected to either steady-state injection or pulsatile circulation of a synthetic blood solution at physiologically relevant flow rates. Bubble formation was observed and recorded, originating both from the polydimethylsiloxane-based scaffold, which represented human tissues, and from the synthetic blood solution, with the latter being the predominant source. Notably, bubble volumes were significantly larger when the hyperbaric system was rapidly decompressed from 3 bars to atmospheric pressure, particularly after 12 hours of compression. Additionally, longer compression periods were associated with an increase in both the size and number of bubbles within the vascular channels, with the majority appearing between 10 and 30 minutes after returning to standard atmospheric conditions. These findings provide valuable insights into the mechanisms underlying decompression sickness and

highlight critical safety measures needed to mitigate its risks. Furthermore, this study establishes a robust experimental platform for future research aimed at optimizing treatment protocols and improving preventive strategies for individuals exposed to high-pressure environments.

4.2.2. Introduction

Decompression sickness (DCS) is a type of decompression illness that occurs due to a sudden decrease in ambient pressure following exposure to high-pressure environments, leading to the formation of gas bubbles within the bloodstream and tissues[1]. These bubbles emerge through either heterogeneous nucleation or diffusion from supersaturated tissues, the latter acting as gas reservoirs when overburdened with the gas content[2]. These bubbles can cause musculoskeletal discomfort and mild symptoms if they are confined to the skin and joints, such as itching, joint pain, swelling, and fatigue[3]. However, their presence in blood vessels can have life-threatening consequences, including tissue ischemia, neurological dysfunction, paralysis, organ failure, and even cardiac arrest[4].

Inert gases, particularly nitrogen, play a vital role in the development and progression of DCS. These gases dissolve in biological tissue, under high-pressure conditions, at concentrations determined by their solubility[5]. The solubility varies depending on the nature of the gas, the composition of the tissue (the proportion of aqueous versus lipid components in particular), the temperature, and the partial pressure[6]. Since nitrogen is five times more soluble in fatty tissues than in blood components[7], its concentration becomes problematic upon sudden decompression at interfaces between the bloodstream and the surrounding tissues. If the rate of pressure reduction exceeds the rate of gas elimination, the dissolved gases will form bubbles by either emerging from solution, or diffusing into the blood vessels[8, 9]. The decompression theory delves into this phenomenon, exploring the complex interplay of factors that include gas solubility, partial pressure, diffusion, and bubble mechanics within living tissues[10].

While decompression sickness is relatively rare, occurring at an estimated 1.5 to 10 cases per 10,000 commercial dives[3], it poses substantial risks, especially for males[3, 11]. The Divers Alert Network (DAN) initiated "Project Dive Exploration" in 1999 to analyze the incidence rates, by collecting information on dive profiles and events. From 1998 to 2002, they documented 50,150 dives, out of which 28 required recompressions, translating to a rate of about 0.05%[12]. However,

these statistics were believed to include occurrences of the second type of decompression illness, arterial gas embolism (AGE). AGE refers to the direct entry of gas bubbles into the arterial system, often occurring as a result of pulmonary barotrauma, where ruptures in lung tissue cause gas leaks into the pulmonary vasculature[13]. This happens when divers ascend rapidly while holding their breath, triggering the expansion of breathing gases in their lungs[14]. If the expansion surpasses the lung capacity, pulmonary tissue continues to inflate until the tensile strength limit is reached[15, 16]. Subsequent pressure gradients between the trapped gases and the ambient pressure can then rupture tissues, releasing gas into exposed areas. If the damaged tissues intersect with alveolar capillaries, breathing gases mechanically enter the venous pulmonary circulation, eventually reaching the left side of the heart and circulating through the systemic arteries to the rest of the body, leading to a high risk of arterial gas embolism[17].

The gas bubbles are reported to initially form in the venous side of the systemic circulation, where the concentration of inert gases is at its highest[18]. These bubbles are usually eliminated in the lungs, acting as a natural bubble filter[19]. However, capillaries may be overwhelmed by the number and volume of bubbles, leading to their leakage from the venous to the arterial network[20]. Gradual decompression, achieved by slowing down the ascent rate, is recommended for scuba divers and aviation specialists, to mitigate the formation of gas bubbles[21]. This approach reduces the rate of pressure reduction, allowing for the safe exhalation of inert gases. Consequently, strict protocols and training procedures have been established to ensure the adherence of divers to safe ascent profiles, thereby minimizing nitrogen loading and bubble formation within the body[22].

If gas embolism is detected, hyperbaric oxygen therapy (HBOT) is the primary treatment technique[23]. This therapy involves breathing pure oxygen in a pressurized chamber, to reduce the size of nitrogen bubbles and promote their elimination. The use of electronic devices is strictly prohibited in the hyperbaric chambers, meaning that phones, cameras, microscopes, and other imaging tools can’t be used to monitor the efficiency of the treatment. Moreover, DCS research has been largely focused on monitoring macro environments with significant pressure variations, such as deep-sea diving[24], aviation activities[25], and aerospace exploration[26]. To this end, microscale hyperbaric systems offer a novel approach to understanding and exploring decompression illness in a controlled and miniaturized setting. These systems provide precise

control over pressure and decompression rates, enabling the replication of both conditions that induce DCS in real life, and treatment protocols during HBOT. The formation, evolution, and dissipation of bubbles can be investigated in real time, offering insights into the underlying mechanisms of gas embolism at the microscopic level. Microscale hyperbaric studies may even be used to optimize pre-dive conditioning protocols aimed at reducing nitrogen absorption and mitigating the risk of DCS.

4.2.3. Materials and Methods

The microscale hyperbaric system consists of six interconnected components designed to simulate a simplified diver model. The key components are: (i) a microfluidic device, made of polydimethylsiloxane (PDMS), mimicking human blood vessels as vascular systems on a chip; (ii) a synthetic blood solution, formulated with an equivalent hematocrit concentration of 46% to simulate human blood; (iii) a peristaltic pump, used to generate pulsatile blood flow, closely mimicking real physiological condition; (iv) a motor hat, providing a continuous power source to the pump; (v) a blood reservoir, serving as both the fluid intake for the pump and the outlet for the circulated blood from the microfluidic channels; and finally (vi) a clear pressure tank, housing all components within a controllable environment. The system also included an inverted confocal microscope for imaging, and the acquired data were analyzed using custom-developed Matlab code.

Chip Design and Fabrication. Three distinct microfluidic devices were designed at biologically relevant widths and geometries, adhering to Murray's law of bifurcation. According to this law, the cubed radius of a parent vessel is equal to the sum of the cubed radii of its daughter vessels[27, 28]. Murray's diameter model has been validated in various animal models, including small arteries in rat cardiovascular systems, with widths ranging between 50 μm and 500 μm[29, 30], and arterioles in swine hearts with widths that are smaller than 100 μm[30, 31]. The angle between all bifurcations, known as the bifurcation angle, was set at 60° to further mimic the natural branching patterns found in biological systems[30, 32]. The structure of the vascular channels in all three devices was detailed in Figure 4.1.

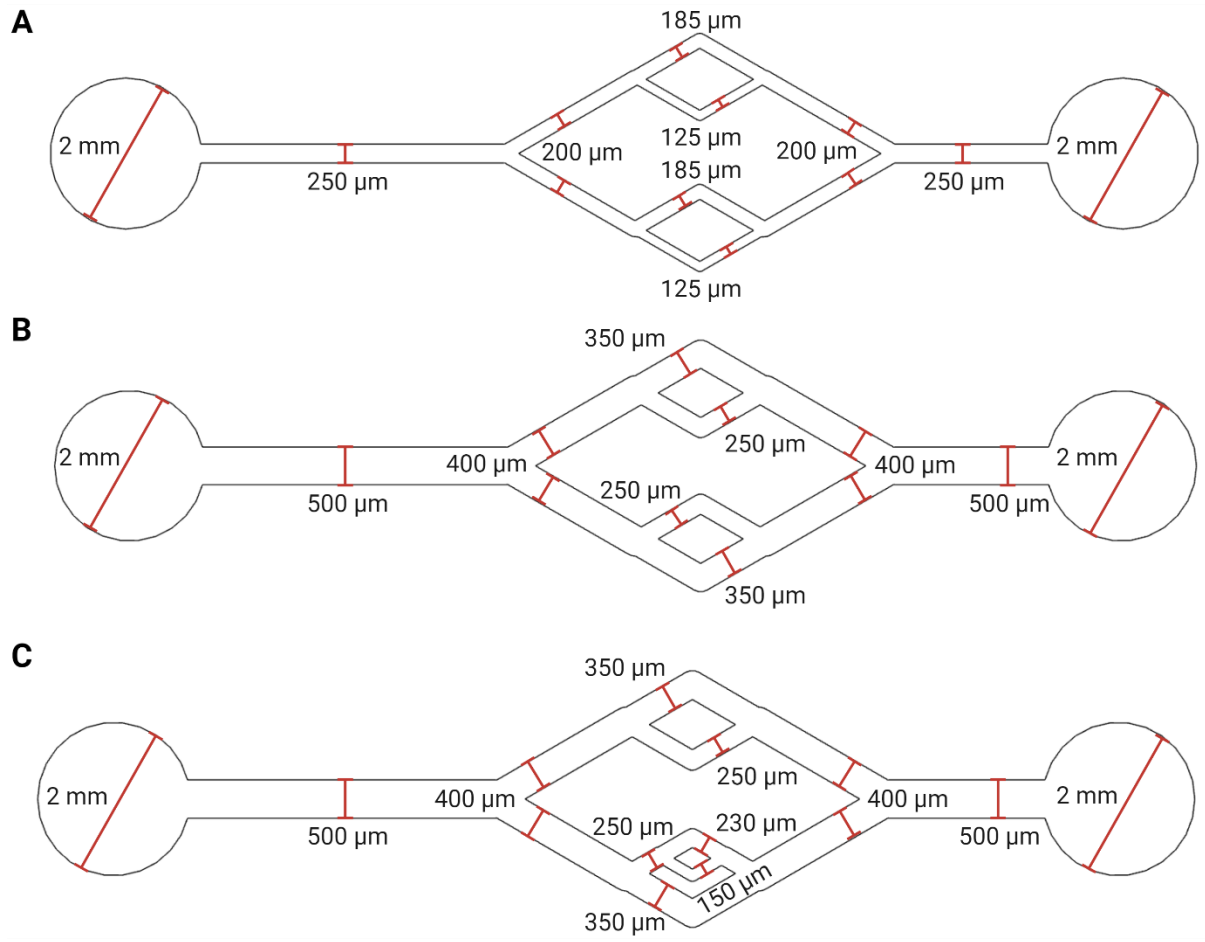

Figure 4.1. Design of three types of microfluidic devices with bifurcating networks. **A.** The first device comprises two generations of bifurcations. **B.** The second device presents two generations of bifurcations with larger channel widths than the first device. **C.** The structure of the third device includes three generations of bifurcations in the lower branching network. The bifurcation angle was set at 60° in each branching.

The devices were fabricated using standard SU8 photolithography, which involves transferring a pattern from a photomask to a photosensitive polymer on a substrate, typically a silicon wafer. SU8, a commonly used negative photoresist, was chosen due to its high resolution and mechanical stability[33], making it ideal for creating detailed microscale structures. During photolithography, the SU8 was spin-coated onto the silicon wafer and exposed to ultraviolet (UV) light through the designed photomask (Figure 4.1). After exposure, the unexposed regions of the SU8 were washed away, leaving behind the raised microstructures on the wafer. Following the photolithography process, soft lithography was employed to replicate these microstructures using polydimethylsiloxane (PDMS). PDMS was mixed at a ratio of 10:1 (base elastomer to curing

agent), ensuring the material's optimal properties for biomedical applications[34]. The mixture was degassed to remove any air bubbles and then poured over the silicon wafer containing the microscale patterns. The polymer was selected due to its (i) optical transparency[35] allowing direct observation of fluid flow in the microchannels, (ii) gas permeability simulating the natural environment of blood vessels[36] where gas exchange occurs, and (iii) mechanical properties, i.e., elasticity and flexibility[37], that make it suitable for replicating the behavior of blood vessels. The most crucial factor is the diffusion coefficient of gases in PDMS, namely 3.4 x 10^{-5} cm^2/s for oxygen[38, 39] and 4.1 x 10^{-5} cm^2/s for nitrogen[40] at 308 K, both of which are closely related to the values recorded in human blood vessels, i.e., 10^{-6} cm^2/s[41] and tissues in general, i.e., 1.1 x 10^{-4} to 4 x 10^{-8} cm^2/s[42]. After curing the PDMS overnight in an oven set at 65°C, the solidified PDMS replicas were carefully peeled off the silicon wafer. Inlet and outlet holes were punctured to insert tubing for the fluid flow through the microchannels. Plasma treatment was performed to bond the PDMS devices to clean glass coverslips. This step involved exposing the surfaces to oxygen plasma, which activates the PDMS and glass surfaces, creating strong covalent bonds upon contact[43]. The sealed devices provided a robust and leak-proof environment suitable for further experimental procedures.

Synthetic Circulatory System. A synthetic blood solution was prepared using a mixture of 60% distilled water, 40% glycerol and 0.04% xanthan gum, resulting in a 46% equivalent hematocrit concentration[44], which mimics the normal range for human blood[45]. This formulation has a dynamic viscosity (3.5 cP to 5.5 cP for normal blood[46]) and a surface tension (53 mN/m to 58 mN/m for normal blood[47]) that are comparable to those measured in real blood. Fluorescein sodium salt (Fischer Scientific) was also added to the solution to facilitate visualization and enable accurate bubble detection. The synthetic blood solution was stored in a custom-designed and 3D-printed blood reservoir, measuring 45 mm in length, 35 mm in width, and 22 mm in depth, with an extra 3 mm on each side for wall thickness, resulting in a total volume of 34.65 cm^3. This reservoir fed the working fluid to a peristaltic pump, specifically the SP100VO Variable-Flow OEM Peristaltic Pump from APT Instruments, which operated at 12V DC and 5 RPM, with a flow rate range of 0.09 to 13 mL/min. The peristaltic pump, chosen for its ability to simulate the pulsatile nature of blood flow, drew the synthetic blood solution from the reservoir and delivered it to the microfluidic device. After passing through the microfluidic channels, the fluid was re-routed into the reservoir, establishing a closed-loop system.

Power Source. A custom-built motor hat was mounted directly on top of the pump, powered by four lithium-ion 18650 batteries. These batteries, each boasting a measured capacity of at least 1500 mAh (at a nominal voltage of 3.6 V and a discharge rate of 0.5 A), were connected in series, yielding a combined voltage of 16.8 V. This output was then routed to a step-down converter, also known as a buck converter, which uses pulse width modulation[48] to lower the input voltage to a stable 7.19 V. This reduction in voltage was crucial for ensuring compatibility with the operational requirements of the pump and the realistic flow rates expected within the designed channel widths. The final flow rate was measured at 0.095 mL/min, aligning within the capabilities of the pump, with a consistent output voltage maintained throughout the battery discharge cycle. With a measured maximum power draw of 100 milliamps at 7.19 V, the pump configuration could maintain operation for a minimum of 15 hours, extending all the way up to 35 hours, contingent upon the conversion efficiency of the step-down converter. As a standard procedure during the experiments, the power source was recharged after every 24-hour usage cycle. This routine maintenance, coupled with periodic voltage checks, ensured stability in both voltage levels and flow rates throughout the experimental procedures, thereby validating the reliability of this setup.

Pressure Tank. A 2L clear vessel (CT series, SR-TEK Limited, UK), made from acrylic cylinder and stainless steel, was used to establish a controllable environment with a maximum pressure of 4 bars. The vessel featured a 6 mm inlet push-in fitting for the gas intake, allowing easy and secure connections to the gas sources, a pressure regulator for fine-tuning the internal pressure, and a relief valve to prevent over-pressurization and ensure operational safety. The gas intake was either from a compressed nitrogen tank or an air nozzle, introduced into the vessel at set pressures of 1 bar and 3 bars.

Data Acquisition and Processing. Still images were acquired using an inverted confocal microscope (Olympus IX83 fluorescence microscope, Olympus Corporation). The images underwent initial processing using ImageJ, a Java-based image processing program. Masks representing the filled channels were generated using GIMP and aligned with the processed images to discern regions exhibiting fluorescence (white), indicating filled channels, and areas devoid of fluorescence (green), signifying bubbles. For accurate bubble detection, a threshold was established using a Matlab script (SI). The pixel conversion factor was factored in to correspond to the 1.25X magnifying objective used during imaging. Bubble volumes were subsequently

calculated using this code, based on the channel height, i.e., 40 µm[49], multiplied by the area per pixel, which was estimated using the conversion factor.

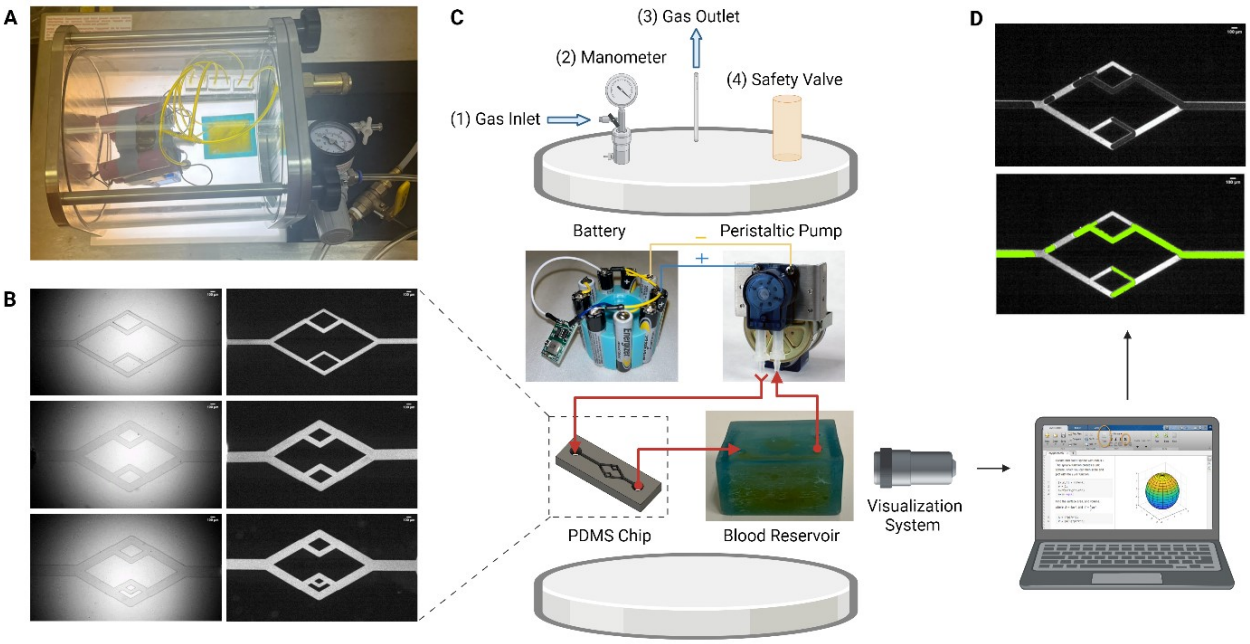

Figure 4.2. Experimental setup of the microscale hyperbaric system. **A.** Photograph of the pressure tank containing the closed system with synthetic blood circulating in the microfluidic channels. **B.** Brightfield and fluorescence microscope images of the three types of devices. The scale bar is set at 100 µm. **C.** Different components of the system placed within the pressure tank, including the batteries as the power source, the peristaltic pump, the blood reservoir, and the PDMS chip. **D.** Acquired images were sent for processing and bubble detection using a custom-developed Matlab code.

4.2.4. Results and Discussion

The microfluidic devices were subjected to various compression and decompression cycles in a clear pressure vessel, to determine the risk and severity of decompression sickness under different global conditions. Two types of experiments were conducted, *Tissue Compression* and *Diver Model Compression*, both of which were evaluated under steady-state and pulsatile flow conditions. In the steady-state system, the channels were filled with the working fluid and sealed, while in pulsatile flow, the fluid was continuously circulated in the channels in a closed-loop system. This comprehensive approach allowed for the assessment of the origins of bubble formation, the volume of generated bubbles from each origin, and the impact of DCS under different flow dynamics.

4.2.4.1.Tissue Compression

The tissue scaffold was initially examined to understand the contribution of tissue supersaturation to bubble formation during DCS. PDMS-based devices were used to simulate human tissues undergoing compression at 1 bar and 3 bars, for periods of 2 hours, 4 hours, 6 hours, and 12 hours. These devices became saturated with air, acting as gas reservoirs, with varying capacities depending on the gas solubility, compression duration, and pressure level. To achieve this, the devices with empty channels were placed in the pressure vessel and subjected to sudden pressure drops. Once the pressure returned to atmospheric conditions, the channels were filled with the working fluid to observe bubble formation under either a steady one-time injection, or a pulsatile closed-loop circulation. The volumes of generated bubbles were calculated using the Matlab script immediately after decompression, then 10 minutes and 30 minutes post-return to standard temperature and pressure conditions.

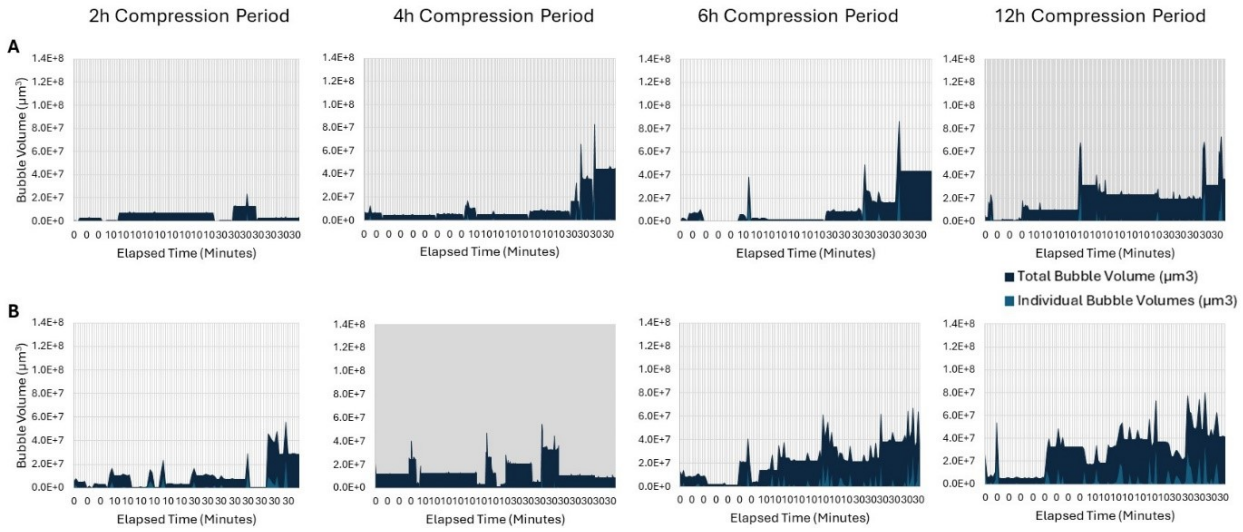

Figure 4.3. Individual and total bubble volumes after sudden tissue decompression in the steady state system at **A.** 1 bar and **B.** 3 bars across all microfluidic devices.

In the steady state systems shown in Figure 4.3, both the individual and total bubble volumes increased as the compression period was extended from 2 hours to 12 hours. Individual bubble volumes reached maximum values of 1.06 x 10^7 µm^3, 3.87 x 10^7 µm^3, 4.29 x 10^7 µm^3 and 3.65 x 10^7 µm^3 after 30 minutes of decompression from 1 bar for 2 hours, 4 hours, 6 hours and 12 hours, respectively. While the largest total bubble volumes were 1.25 x 10^7 µm^3, 4.41 x 10^7 µm^3, 4.33 x 10^7 µm^3 and 4.45 x 10^7 µm^3 after 30 minutes of decompression from 1 bar with the respective

compression durations of 2 hours, 4 hours, 6 hours and 12 hours. As for the varying compression periods at 3 bars, the 2-hour, 4-hour, 6-hour and 12-hour durations were associated with maximum individual bubble volumes of 2.72 x 10^7 µm^3, 2.08 x 10^7 µm^3, 3.34 x 10^7 µm^3 and 3.90 x 10^7 µm^3, and maximum total bubble volumes of 3.57 x 10^7 µm^3, 3.47 x 10^7 µm^3, 3.84 x 10^7 µm^3 and 4.75 x 10^7 µm^3, respectively.

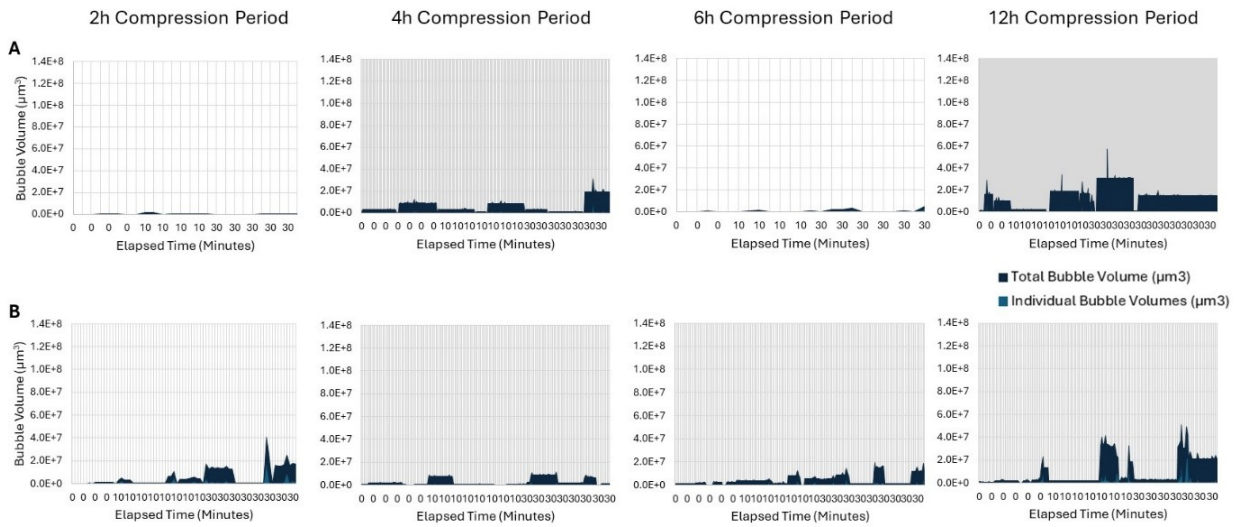

Figure 4.4. Individual and total bubble volumes after sudden tissue decompression in the system with pulsatile flow at **A.** 1 bar and **B.** 3 bars across all microfluidic devices.

For transient systems with pulsatile blood flow (Figure 4.4), a similar trend was observed for the individual and total bubble volumes as the compression pressure and periods increased. At 30 minutes post-decompression from 1 bar, the maximum volumes were identified as 1.24 x 10^7 µm^3, 2.35 x 10^6 µm^3 and 2.65 x 10^7 µm^3 for individual bubbles, and 1.90 x 10^7 µm^3, 2.35 x 10^6 µm^3 and 3.09 x 10^7 µm^3 for total bubbles after 4-hour, 6-hour and 12-hour compression periods, respectively. However, the devices that underwent compression for 2 hours exhibited maximum individual and total bubble volumes at 10 minutes post-decompression, with the respective values being 6.22 x 10^5 µm^3 and 1.08 x 10^6 µm^3. As for compression at 3 bars, the largest bubbles were all determined at 30 minutes following decompression with individual bubble volumes of 2.00 x 10^7 µm^3, 2.76 x 10^6 µm^3, 7.22 x 10^6 µm^3 and 2.22 x 10^7 µm^3, and total bubble volumes of 2.06 x 10^7 µm^3, 8.93 x 10^6 µm^3, 1.43 x 10^7 µm^3 and 3.18 x 10^7 µm^3 for compression periods of 2 hours, 4 hours, 6 hours and 12 hours, respectively.

The study of different input parameters in this microscale hyperbaric system resulted in three major findings. First, longer compression periods were associated with larger bubble volumes. This could be due to the PDMS scaffolds having more time to build a greater gas reservoir at each pressure level, leading to a larger concentration of gases diffusing into the vascular channels. Second, the risk of developing the largest and most lethal bubbles was at its peak 10 and 30 minutes after decompression, indicating a time-dependent mechanism for bubble growth and aggregation. This suggests that the symptoms of decompression sickness may continue to worsen over time, as sudden removal from high pressures appears to have lasting effects on the system. Finally, higher pressures were not directly correlated with more prominent bubble formation, especially in terms of volume. Compression at 1 bar appeared to generate numerous small bubbles, but a few emerged with significantly larger volumes than the maximum volumes generated after compression at 3 bars. This chaotic distribution will be further examined in subsequent experiments.

Impact of Channel Geometry. The relationship between intravascular bubble volume and the width of the artificial blood vessel in bifurcating networks is depicted in Figure 4.5. Total bubble volumes were compared across each microfluidic device at 1 bar and 3 bars, using compressed air, with compression periods extending between 2 hours and 12 hours. In the first device with the smallest channel widths, the maximum bubble volumes recorded under steady state conditions were 1.73×10^7 μm^3 at 1 bar and 2.38×10^7 μm^3 at 3 bars, both occurring after 12 hours of compression. In pulsatile flow conditions, the largest bubble volumes observed were 2.26×10^4 μm^3 at 1 bar after 6 hours of compression and 1.77×10^7 μm^3 at 3 bars after 12 hours of compression. These maximums values were reached 30 minutes after device 1 was returned to atmospheric conditions.

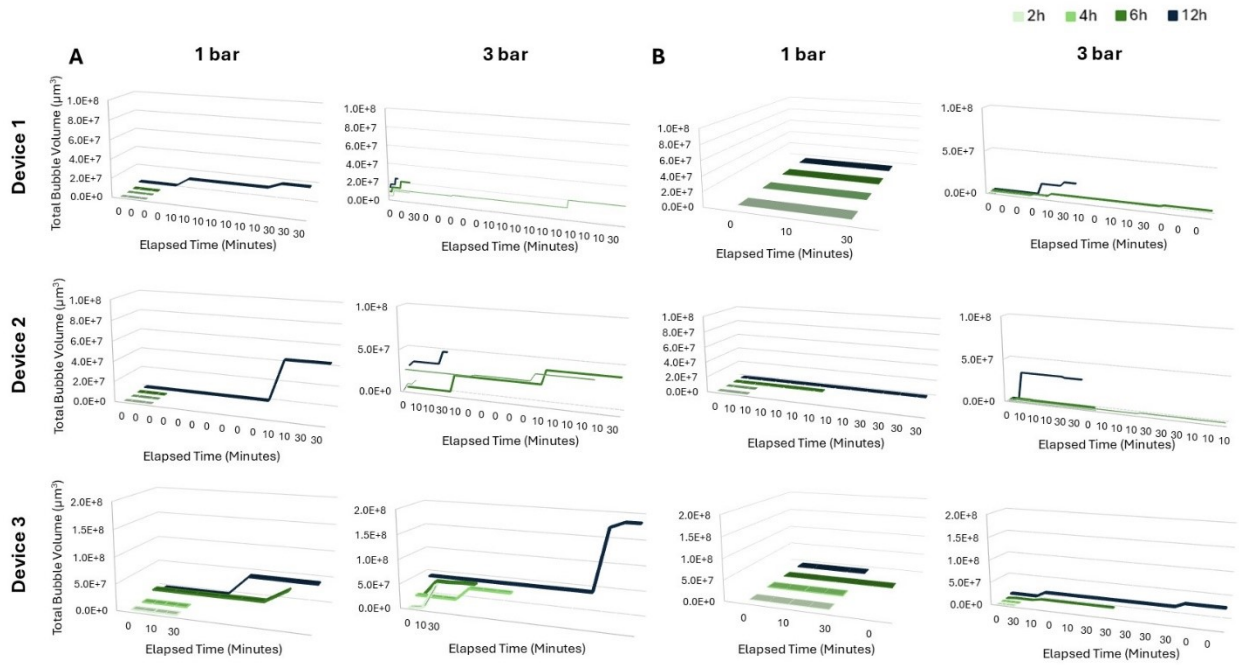

Figure 4.5. Total bubble volumes after sudden tissue decompression in all microfluidic devices at **A.** steady state and **B.** pulsatile flow for pressure levels of 1 bar and 3 bars.

For the second device, featuring slightly larger channel widths, steady state conditions resulted in maximum total bubble volumes of 4.36 x 10^7 µm^3 at 1 bar and 4.69 x 10^7 µm^3 at 3 bars, both after 12 hours of compression. Under pulsatile flow, the maximum bubble volumes were 2.04 x 10^5 µm^3 at 1 bar after 6 hours of compression and 3.18 x10^7 µm^3 at 3 bars after 12 hours of compression. These maximum values were all reached 30 minutes after sudden decompression, with one instance happening earlier, at 10 minutes after decompression. The bubble volumes in the second device were significantly larger than those recorded for the smaller channel widths in the first device, confirming a direct correlation between channel width and bubble volume.

In the third device with even larger channel widths, bubbles volumes continued to increase. At 1 bar of compression, steady-state conditions produced maximum bubble volumes of 4.45 × 10^7 µm³, while pulsatile flow generated maximum volumes of 4.98 × 10^5 µm³. When the pressure was increased to 3 bars, bubble volumes reached 4.13 × 10^7 µm³ under steady-state conditions and 2.08 × 10^7 µm³ in pulsatile flow. All of these maximum values were observed after 12 hours of compression and 30 minutes post-decompression. Interestingly, bubble volumes recorded for 1 bar compression in the third device were higher than those in the second device, while the opposite trend was observed for compression at 3 bars. This suggests that bifurcating channels may

influence bubble behavior differently at varying pressures. However, the relationship between larger channel width and increased bubble volumes was consistent, aligning with clinical statistics that suggest arterial gas embolism—typically associated with larger vessels—is more severe than venous gas embolism. Additionally, higher pressures and longer compression periods consistently resulted in larger bubble volumes across all devices and flow conditions, even though higher pressures may sometimes lead to distinct dynamics due to the interaction of bifurcating geometries. As for the role of flow conditions, pulsatile flow generally produced smaller bubble volumes compared to steady-state conditions at the same pressures, likely because pulsatile flow disrupts bubble stability, thereby reducing the likelihood of sustained growth.

4.2.4.2.Diver Model Compression

The role of tissues as gas reservoirs was established through the prominent formation of bubbles within the PDMS channels, which exhibited a direct correlation with the pressure level, compression duration, and flow condition. In this section, decompression sickness was simulated in a more realistic setting by placing the entire synthetic circulatory system, including the microfluidic device, inside the pressure vessel. This setup was designed to represent a simplified diver model, subjected to the same pressure variations as in the previous experiments.

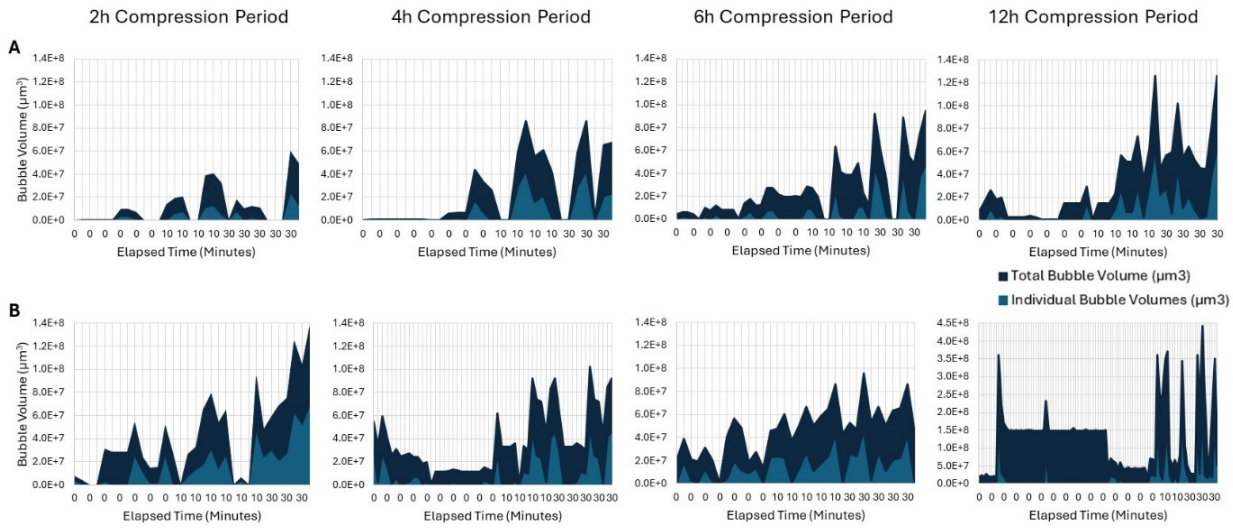

Figure 4.6. Individual and total bubble volumes after sudden system decompression in the steady state system at A. 1 bar and B. 3 bars across all microfluidic devices.

At 1 bar, the steady state system resulted in maximum individual and total bubble volumes of 2.32 x 10^7 μm^3 and 3.64 x 10^7 μm^3 after 2 hours of compression, 4.30 x 10^7 μm^3 and 4.42 x 10^7 μm^3 after 4 hours of compression, 4.73 x 10^7 μm^3 and 4.81 x 10^7 μm^3 after 6 hours of compression, and 6.31 x 10^7 μm^3 for both after 12 hours of compression (Figure 4.6A). As for the compression at 3 bars, the maximums for individual and total bubble volumes were 6.81 x 10^7 μm^3 for both at 2 hours, 5.12 x 10^7 μm^3 for both at 4 hours, 4.65 x 10^7 μm^3 and 4.95 x 10^7 μm^3 at 6 hours, and 2.09 x 10^8 μm^3 and 2.44 x 10^7 μm^3 at 12 hours (Figure 4.6B). These volumes were all reported after 30 minutes of returning the system to atmospheric pressure, as observed in the *Tissue Compression* experiments. However, there was a wide difference in the scale of calculated bubble volumes, whereby the sudden decompression of the circulatory system with the tissue scaffold led to much larger bubbles under each tested condition. The additional volumes of individual bubbles were 1.26 x 10^7 μm^3 at 1 bar and 4.09 x 10^7 μm^3 at 3 bars after 2 hours, 0.43 x 10^7 μm^3 at 1 bar and 3.04 x 10^7 μm^3 at 3 bars after 4 hours, 0.44 x 10^7 μm^3 at 1 bar and 1.31 x 10^7 μm^3 at 3 bars after 6 hours, and 2.66 x 10^7 μm^3 at 1 bar and 17.00 x 10^7 μm^3 at 3 bars after 12 hours. As for the total bubble volumes, the 2-hour, 4-hour, 6-hour and 12-hour compression periods resulted in residual values of 2.39 x 10^7 μm^3 at 1 bar and 3.24 x 10^7 μm^3 at 3 bar, 0.01 x 10^7 μm^3 at 1 bar and 1.65 x 10^7 μm^3 at 3 bar, 0.48 x 10^7 μm^3 at 1 bar and 1.11 x 10^7 μm^3 at 3 bar, and 1.86 x 10^7 μm^3 at 1 bar and 2.31 x 10^7 μm^3 at 3 bar, respectively.

The increase in pressure levels and compression periods were once again associated with larger bubble volumes, whereby the maximums appeared 30 minutes after sudden decompression rather than immediately at the onset. This delay in bubble formation highlights the lasting effects of high-pressure exposure on the system, with significant bubble growth occurring during the post-decompression period. Furthermore, it is evident that the supersaturation of tissues is not the only and more prominent factor contributing to decompression sickness. The significant difference in calculated bubble volumes between compressed tissues and compressed systems highlights the impact of nucleation in the manifestation and progression of DCS. While supersaturation causes dissolved gases to exceed their solubility limit and begin forming bubbles, nucleation significantly contributes to this process by triggering the emergence of bubbles from the synthetic blood solution on specific nucleation sites.

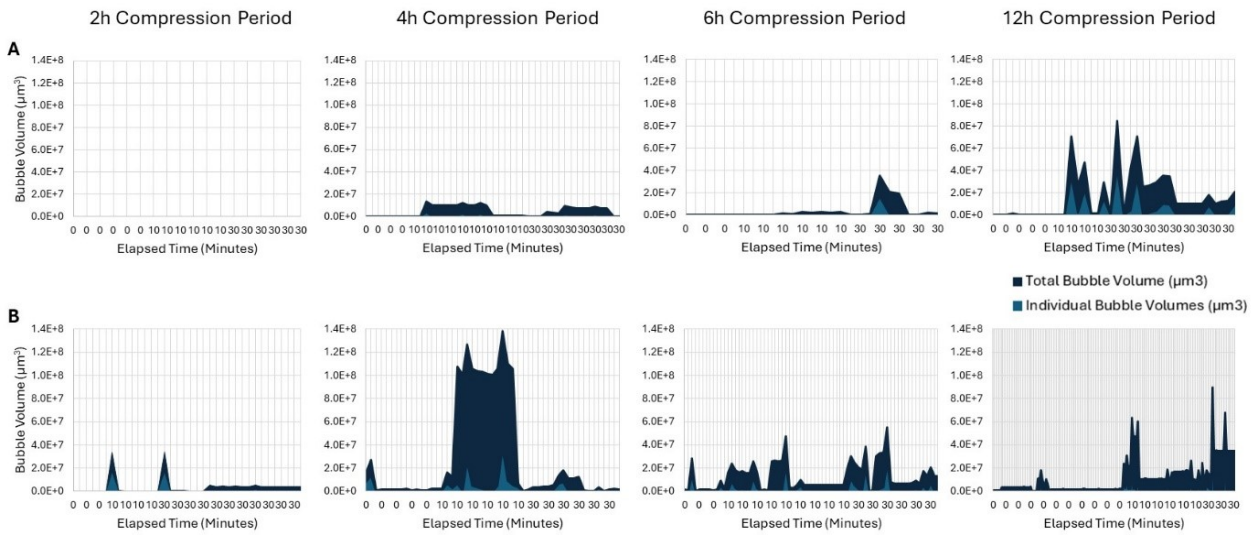

Figure 4.7. Individual and total bubble volumes after sudden system decompression in the system with pulsatile flow at **A.** 1 bar and **B.** 3 bars across all microfluidic devices.

The channels with pulsatile flow resulted in smaller bubble volumes than the steady state system at each compression period, highlighting the impact of dynamic blood flow on bubble formation. However, not all generated bubbles were larger than those observed with the *Tissue Compression* experiments. At 1 bar, the differences in recorded maximums were -5.04 x 10^5 µm^3 and -9.62 x 10^5 µm^3 for individual and total bubbles after 2 hours, -0.85 x 10^7 µm^3 and -0.95 x 10^7 µm^3 for individual and total bubbles after 4 hours, 1.42 x 10^7 µm^3 and 1.65 x 10^7 µm^3 for individual and total bubbles after 6 hours, and 1.56 x 10^7 µm^3 and 1.12 x 10^7 µm^3 for individual and total bubbles after 12 hours. As for compression at 3 bars, the residual volumes of individual and total bubbles were -0.29 x 10^7 µm^3 and -0.35 x 10^7 µm^3 after 2 hours, 3.47 x 10^7 µm^3 and 9.21 x 10^7 µm^3 after 4 hours, 1.74 x 10^7 µm^3 and 1.61 x 10^7 µm^3 after 6 hours, and 2.28 x 10^7 µm^3 and 1.32 x 10^7 µm^3 after 12 hours, respectively. All the peaks for the *Diver Model Compression* experiments were determined after 30 minutes of sudden decompression, except the maximum volumes for the 4-hour compression, which occurred after 10 minutes. These findings show the chaotic distribution of bubbles at low pressures and short compression durations in both types of systems. The maximum bubbles eventually became larger in the *Diver Model Compression* than in the *Tissue Compression* experiments, but this occurred faster in the 3-bar compression (4 hours) than the 1-bar compression (6 hours).

Impact of Channel Geometry. In Figure 4.8, the first and smallest microfluidic device was evaluated in terms of total bubble volumes, in comparison with *Tissue Decompression*, for air compression at 1 bar and 3 bars. Under steady state conditions, the maximum volumes were identified at 2.24 x 10^7 μm^3 with a residual volume of 0.51 x 10^7 μm^3 at 1 bar and 1.94 x 10^8 μm^3 with a residual volume of 0.44 x 10^7 μm^3 at 3 bars. While systems with pulsatile flow yielded maximum bubble volumes of 1.14 x 10^7 μm^3 with a residual of -1.12 x 10^7 μm^3 at 1 bar and 1.90 x 10^7 μm^3 with a residual of -0.13 x 10^7 μm^3 at 3 bars. For the second device, which had slightly larger channel widths, the maximum bubble volumes in steady state and pulsatile flow systems were 5.37 x 10^7 μm^3 and 3.96 x 10^5 μm^3 at 1 bar, and 2.44 x 10^8 μm^3 and 1.01 x 10^8 μm^3 at 3 bars. The residual bubble volumes for steady state and pulsatile flow were 1.01 x 10^7 μm^3 and 1.92 x 10^5 μm^3 at 1 bar, and 19.71 x 10^7 μm^3 and 6.92 x 10^7 μm^3 at 3 bars. In the third device, which feaured the largest widths of artificial blood vessels, the bubble volumes recorded for steady state and transient systems were 4.23 x 10^7 μm^3 and 2.92 x 10^5 μm^3 at 1 bar, and 1.84 x 10^8 μm^3 and 2.53 x 10^7 μm^3 at 3 bars. The residual volumes for these conditions were -0.22 x 10^7 μm^3 and -2.06 x 10^5 μm^3 at 1 bar, and 14.27 x 10^7 μm^3 and 0.45 x 10^7 μm^3 at 3 bars.

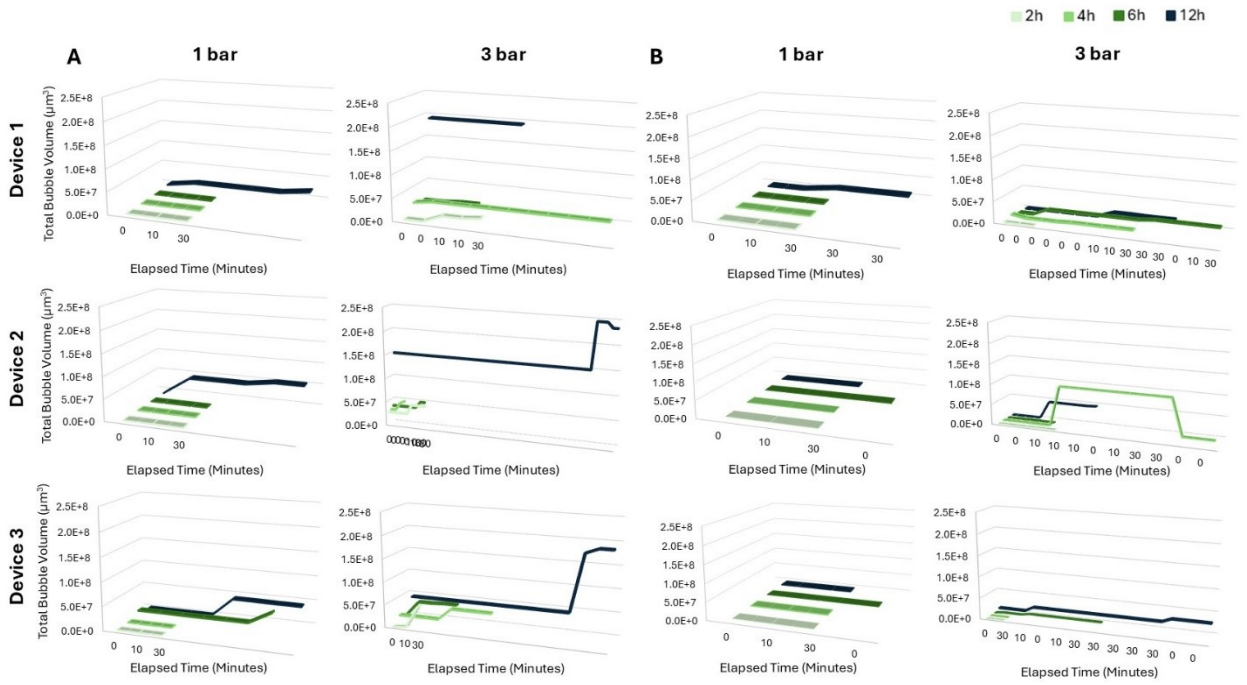

Figure 4.8. Total bubble volumes after sudden system decompression in all microfluidic devices at A. steady state and B. pulsatile flow for pressure levels of 1 bar and 3 bars.

Based on these results, several key findings can be derived regarding intravascular bubble formation in microfluidic devices under varying conditions of gas compression, pressure level, and flow state. First, higher pressures consistently resulted in larger bubble volumes compared to lower pressures across all devices and conditions. This trend indicates that increased pressure enhances the dissolution of gases in tissues, which are then released as bubbles upon sudden decompression. Specifically, at 3 bars, the recorded bubble volumes were significantly higher than those at 1 bar, emphasizing the impact of pressure on gas solubility and bubble dynamics.

Second, steady state conditions typically resulted in larger maximum bubble volumes than pulsatile flow conditions. This suggests that continuous flow provides a more stable environment for bubble formation, while pulsatile flow, characterized by variable pressure fluctuations, tends to reduce bubble growth. Under steady state conditions, bubble volumes reached their peak more consistently, whereas pulsatile flow led to lower maximum volumes, indicating that dynamic flow conditions are less conducive to bubble growth.

Third, the analysis of residual bubble volumes revealed significant variations. Positive residual values indicated sustained bubble formation, while negative or very low values pointed to stabilization or reduction in bubble formation. Residual volumes were generally lower under pulsatile flow, implying better bubble clearance or stabilization in these conditions. This supports the hypothesis that pulsatile flow could help mitigate excessive bubble accumulation and reduce the risk of embolism.

Finally, the size and design of the microfluidic devices had a notable effect on bubble volumes. Larger devices with more complex geometries, such as bifurcating networks, exhibited higher maximum bubble volumes. This is likely due to the increased surface area and more intricate flow dynamics within these devices, which promote nucleation and bubble growth. The data from the third device, which incorporated an additional bifurcation, demonstrated particularly high bubble volumes, illustrating how design intricacies can significantly influence bubble formation.

4.2.5. Conclusion

The present study identifies key factors that influence bubble volumes in microfluidic devices, offering valuable insights into the mechanisms of decompression sickness and the optimization strategies of decompression protocols. Channel geometry, pressure levels, and flow conditions

were found to have a significant impact on bubble formation and growth following sudden decompression. Notably, larger bubble volumes were consistently observed in vessels with larger widths, reflecting the heightened severity of arterial gas embolism compared to venous embolism. Higher pressure and prolonged compression durations further exacerbated bubble formation, suggesting that increased pressures promote greater gas dissolution in tissues, leading to larger bubbles upon decompression and an increased risk of vascular blockages and tissue ischemia. Additionally, steady state conditions resulted in larger bubble volumes than pulsatile flow, indicating that continuous flow supports bubble stability and growth, while pulsatile flow may reduce bubble formation. This suggests that regulating flow conditions could be an effective strategy for mitigating the risk of embolism during decompression or medical procedures.

While tissue supersaturation was indeed a critical factor in bubble formation, it is not the sole contributor to DCS. The study emphasizes the role of nucleation in compressed blood solutions, where heterogeneous nucleation accelerates bubble formation and exacerbates the severity of this medical condition. Furthermore, bubbles grew more rapidly during extended compression periods, even after return to atmospheric pressure. This delayed bubble growth highlights the significance of compression intensity and duration in bubble dynamics, reinforcing the notion that DCS may have lasting implications that go well beyond the immediate decompression event.

4.2.6. Supplementary Information

The Matlab script is shown below.

```
%% Load in files and analyze:
clear;
close all;


%Save them in MATLAB folder or add their folder to the path with this line:
addpath('/home/McGill/PhD/Hyperbaric/Results/20240202/N2_3BAR/Device1/')
%Then call files but use the following if they are images:
%(change image name, image must exist in loaded folder)
% im1 = imread('image_001.tif');
% mask1 = imread(['mask_001.tif']);
```

```
% If .jpg files are used, they must be converted to single channel
   % not necessary for tif files
%Or, to call several files and store them in matrix use this:
for i = 1%:3
   %im1 = imread([['microdluid_channel_00',num2str(i),'.tif']);
   %mask1 = imread('microdluid_channel_mask.tif');
   im1 = double(imread('D1_6h_30min.tif'));
   mask1 = imread('MASK_D1_6h_30min.tif');
   mask1=mask1(:,:,1);
   % shifting the image over the mask if necessary
   % im_s = im1;
    % setting all pixel values in the image under a specified threshold to zero
   % This is basically getting rid of any noise in the image
   % im_s(im_s<1600) = 0;
   % Finding the coordinates where the image is above the threshold
    % This should include the entire channel, but not the noise
    % This way, the lowest and highest points of the channel can be derived
   % im_s_coord = find(im_s>0);
    % Deriving the lowest point in the channel to center the mask
   % [im_x, im_y] = ind2sub(size(im_s), im_s_coord);
   % im_lowest_y = min(im_y);
   % im_lowest_x = im_x(im_y == im_lowest_y);
   shiftX = 0;
   shiftY = 0;
   shiftedImage = imtranslate(im1, [shiftX, shiftY]);

   %mask1 = imread('2h_30mins_Compression_mask.tif');
   mask = double(imbinarize(mask1));
    % Create a "binary image" called mask from the original image
   mask(mask==0) = NaN;
```

```
    %mask the image:
    im2{1,i} = im1.*mask;
end
clear i
%Add an extra loop for multiple image sets

% Analyze and set thresholds, then compute the volume:
    % The pixel to micron conversion factor and height of channel in microns must be set

% Set threshold value:
thresh_val = 120;
low_thresh = 20;

% Set the pixel to micron conversion factor - how many microns are in one pixel
pix_conv = 5.182;

% Set the height of the channel in microns, i.e., the SU-8 fabrication depth
h = 40;

% mask = imread('12pos91_NucMask06.tiff');
% im = imread('12pos91_NucMask07.tiff');

for i = 1

    %threshhold
    im_temp = (im2{1,i});
    im_temp(im_temp>thresh_val) = NaN;
    im_temp(im_temp<=thresh_val) = 1;
    im_temp_thresh = uint8(im_temp);
    %im_temp_thresh = imfill(im_temp_thresh);
```

```
%now we have an image of 1s and 0s
im3{1,i} = im_temp_thresh;

%obtain information
[bubble_label_temp,num_bubbles]= bwlabel(im_temp_thresh,4); %identifies separate bubbles as objects
info_bubble_temp = (regionprops(bubble_label_temp,im_temp_thresh,'Area','Centroid')');

%Get rid of the noise, set a small threshold
a = cat(1,info_bubble_temp.Area);
d = cat(1,info_bubble_temp.Centroid);
b = find(a>low_thresh);
c(:,1) = a(b);
c(:,2:3) = d(b,1:2);

%redefine bubbles
im_filt = zeros(size(mask));
for j = 1:size(b,1)

   bubba = bubble_label_temp;
   bubba(bubba~=b(j)) = 0;
   im_filt = imadd(im_filt,bubba);
   clear bubba

end

%save in a matrix
bubble_info{1,i}s = c;

%extract the volume
area = cat(1,c(:,1))*(pix_conv^2)   %get area and convert to micron
```

```
    volume = area*h
    bubble_vol{1,i} = volume;
    bubble_info{1,i}(:,4) = volume;
    fprintf('   Area    CentroidX   CentroidY  Volume \n');
    disp(bubble_info{1,i});
    clear a  c d volume
end
array = bubble_info{1,i};

clear num_bubbles im_temp h i

%% Colour in the bubble

% figure(1)
% imshow(mat2gray(im1));
grayImage = (mat2gray(im1))*255;
binaryImage = logical(im_filt);
rgbImage = cat(3, grayImage, grayImage, grayImage);
desiredColor = [0.594 1 0]*255;
redChannel = uint8(rgbImage(:, :, 1));
greenChannel = uint8(rgbImage(:, :, 2));
blueChannel = uint8(rgbImage(:, :, 3));

redChannel(binaryImage) = desiredColor(1);
greenChannel(binaryImage) = desiredColor(2);
blueChannel(binaryImage) = desiredColor(3);
rgbImage = cat(3, redChannel, greenChannel, blueChannel);

%Illustrate by highlighting bubble
imshow(rgbImage)
```

4.2.7. References

1. Moon, R.E., R.D. Vann, and P.B. Bennett, The physiology of decompression illness. Scientific American, 1995. 273(2): p. 70-77.
2. Papadopoulou, V., et al., A critical review of physiological bubble formation in hyperbaric decompression. Advances in colloid and interface science, 2013. 191: p. 22-30.
3. Cooper, J.S. and K.C. Hanson, Decompression sickness, in StatPearls [Internet]. 2023, StatPearls Publishing.
4. Mitchell, S.J., Decompression illness: a comprehensive overview. Diving and Hyperbaric Medicine, 2024. 54(1Suppl): p. 1.
5. Brown, J. and M.J. Antuqano, Altitude-induced decompression sickness. 2010, United States. Office of Aviation Medicine.
6. Hills, B., Effect of decompression per se on nitrogen elimination. Journal of Applied Physiology, 1978. 45(6): p. 916-921.
7. Gabler-Smith, M.K., A.J. Westgate, and H.N. Koopman, Microvessel density, lipid chemistry and N 2 solubility in human and pig adipose tissue. Undersea & Hyperbaric Medicine, 2020. 47(1).
8. Vann, R.D., The Physiological Basis of Decompression: 38th Workshop: Papers and Discussions. 1989: Undersea and Hyperbaric Medical Society.
9. ACKLES, K., Blood-bubble interaction in decompression sickness(proceedings of a symposium). 1973.
10. Wienke, B., Decompression theory. Nuclear Weapons Technology/Stimulation And Computing: Los Alamos National Laboratory: NM, 2000. 87545.
11. Freiberger, J.J., et al., Consensus factors used by experts in the diagnosis of decompression illness. Aviation, space, and environmental medicine, 2004. 75(12): p. 1023-1028.
12. Thalmann, E., Decompression illness: what is it and what is the treatment. Alert Diver, DAN: Divers Alert Network, 2004.
13. Alexander, A.M. and N. Martin, Arterial gas embolism. 2019.
14. Buzzacott, P., et al., Section 4 THE DIVING INCIDENT REPORTING SYSTEM (DIRS). 2020, Divers Alert Network.

15. Melamed, Y., A. Shupak, and H. Bitterman, Medical problems associated with underwater diving. New England Journal of Medicine, 1992. 326(1): p. 30-35.
16. Bove, A.A., Diving medicine. American journal of respiratory and critical care medicine, 2014. 189(12): p. 1479-1486.
17. Schaefer, K.E., et al., Mechanisms in development of interstitial emphysema and air embolism on decompression from depth. Journal of applied physiology, 1958. 13(1): p. 15-29.
18. Mukherji, S.K., Emergent Neuroimaging: A Patient-Focused Approach. Neuroimaging Clinics, 2018. 28(3): p. xv.
19. Butler, B. and B. Hills, The lung as a filter for microbubbles. Journal of Applied Physiology, 1979. 47(3): p. 537-543.
20. Marsh, P.L., et al., Iatrogenic air embolism: pathoanatomy, thromboinflammation, endotheliopathy, and therapies. Frontiers in Immunology, 2023. 14: p. 1230049.
21. Bennett, P.B., et al. What ascent profile for the prevention of decompression sickness? I–Recent research on the Hill/Haldane ascent controversy. in Proceedings of the 28th Annual Scientific Meeting of the European Underwater and Biomedical Society. 2002.
22. Carturan, D., et al., Ascent rate, age, maximal oxygen uptake, adiposity, and circulating venous bubbles after diving. Journal of applied physiology, 2002. 93(4): p. 1349-1356.
23. Lam, G., et al., Hyperbaric oxygen therapy: exploring the clinical evidence. Advances in skin & wound care, 2017. 30(4): p. 181-190.
24. Hall, J., The risks of scuba diving: a focus on Decompression Illness. Hawai'i Journal of Medicine & Public Health, 2014. 73(11 Suppl 2): p. 13.
25. Jersey, S.L., et al., Neurological altitude decompression sickness among U-2 pilots: 2002–2009. Aviation, space, and environmental medicine, 2011. 82(7): p. 673-682.
26. Conkin, J., Evidence-based approach to the analysis of serious decompression sickness with application to EVA astronauts. 2001: National Aeronautics and Space Administration, Lyndon B. Johnson Space Center.
27. Painter, P.R., P. Edén, and H.-U. Bengtsson, Pulsatile blood flow, shear force, energy dissipation and Murray's Law. Theoretical Biology and Medical Modelling, 2006. 3: p. 1-10.
28. Murray, C.D., The physiological principle of minimum work: The vascular system and the cost of blood volume. Proceedings of the National Academy of Sciences, 1926. 12(3): p. 207-214.

29. Zamir, M., S. Wrigley, and B. Langille, Arterial bifurcations in the cardiovascular system of a rat. The Journal of general physiology, 1983. 81(3): p. 325-335.
30. Huo, Y., et al., Which width and angle rule provides optimal flow patterns in a coronary bifurcation? Journal of biomechanics, 2012. 45(7): p. 1273-1279.
31. Kaimovitz, B., et al., Diameter asymmetry of porcine coronary arterial trees: structural and functional implications. American Journal of Physiology-Heart and Circulatory Physiology, 2008. 294(2): p. H714-H723.
32. Kamenskiy, A.V., et al., Three-dimensional geometry of the human carotid artery. 2012.
33. Hammacher, J., et al., Stress engineering and mechanical properties of SU-8-layers for mechanical applications. Microsystem Technologies, 2008. 14: p. 1515-1523.
34. Miranda, I., et al., Properties and applications of PDMS for biomedical engineering: A review. Journal of functional biomaterials, 2021. 13(1): p. 2.
35. Stankova, N., et al., Optical properties of polydimethylsiloxane (PDMS) during nanosecond laser processing. Applied Surface Science, 2016. 374: p. 96-103.
36. Weber, J., et al., Development of an in vitro blood vessel model using autologous endothelial cells generated from footprint-free hiPSCs to analyze interactions of the endothelium with blood cell components and vascular implants. Cells, 2023. 12(9): p. 1217.
37. Nilsson, D.P., et al., Patient-specific brain arteries molded as a flexible phantom model using 3D printed water-soluble resin. Scientific Reports, 2022. 12(1): p. 10172.
38. Markov, D.A., et al., Variation in diffusion of gases through PDMS due to plasma surface treatment and storage conditions. Biomedical microdevices, 2014. 16: p. 91-96.
39. Held, M., et al., Intracellular mechanisms of fungal space searching in microenvironments. Proceedings of the National Academy of Sciences, 2019. 116(27): p. 13543-13552.
40. Markov, D.A., et al., Variation in diffusion of gases through PDMS due to plasma surface treatment and storage conditions. Biomedical microdevices, 2014. 16(1): p. 91-96.
41. Vadapalli, A., R.N. Pittman, and A.S. Popel, Estimating oxygen transport resistance of the microvascular wall. American Journal of Physiology-Heart and Circulatory Physiology, 2000. 279(2): p. H657-H671.
42. Popel, A.S., Theory of oxygen transport to tissue. Critical reviews in biomedical engineering, 1989. 17(3): p. 257.

43. Zhou, J., et al., Surface modification for PDMS-based microfluidic devices. Electrophoresis, 2012. 33(1): p. 89-104.
44. Brookshier, K. and J. Tarbell, Evaluation of a transparent blood analog fluid: aqueous xanthan gum/glycerin. Biorheology, 1993. 30(2): p. 107-116.
45. Billett, H.H., Hemoglobin and hematocrit. Clinical Methods: The History, Physical, and Laboratory Examinations. 3rd edition, 1990.
46. Nader, E., et al., Blood rheology: key parameters, impact on blood flow, role in sickle cell disease and effects of exercise. Frontiers in physiology, 2019. 10: p. 1329.
47. Webb, L., Mimicking Blood Rheology for More Accurate Modeling in Benchtop Research. The Pegasus Review: UCF Undergraduate Research Journal, 2020. 12(1): p. 6.
48. Inanlou, R., et al., A buck converter based on dual mode asynchronous pulse width modulator. AEU-International Journal of Electronics and Communications, 2020. 114: p. 152998.
49. Griffin, J., H. Hassan, and E. Spooner, Spin Coating: Complete Guide to Theory and Techniques. Ossila. Available online: https://www.ossila. com/en-eu/pages/spin-coating (accessed on 15 September 2022), 2022.

Chapter 5. Comprehensive Discussion

Vascular gas embolism is classified as a rare medical condition across multiple research papers and medical reports[385-387]. The incidence rates vary widely depending on the nature of the emboli and the detection methods used[387]. In medical settings, its occurrence has been estimated to range from 0.005%, and goes up to 50% for cases involving laparoscopy, endoscopy, colonoscopy, central venous catheterization, hemodialysis, and surgical interventions[388-390]. However, these rates underestimate the true incidence as many cases often go unnoticed or undiagnosed. This is largely attributed to the available diagnostic tools lacking the sensitivity required for early detection, and insufficient awareness amongst healthcare professionals regarding the condition's subtle clinical manifestations[391].

In recent years, the rise in minimally invasive procedures has significantly contributed to the risk of gas embolism, leading to an increase in reported cases with subsequent medical complications. The use of gas insufflation techniques surged by approximately 462% from 2000 to 2018 for laparoscopy alone[392], highlighting the pressing need to understand and mitigate the risks associated with gas embolism, particularly given that mortality rates associated with severe cases of venous gas embolism can reach 30% to 80%[393]. The morbidity rates can be even higher, as patients who survive embolic events often suffer from long-term neurological deficits due to ischemic injury.

While thromboembolism has received extensive research focus over the years due to its high prevalence in cardiovascular pathology, emerging evidence suggests that gas embolism may contribute to thromboembolic events via biochemical pathways that promote white and red clot formation[394]. The intersection between gas embolism and thrombogenesis remains an understudied yet crucial aspect of embolic pathophysiology. Additionally, the economic burdens and financial liabilities of gas embolism are substantial. A simple PubMed search for 'Venous Air' yields more than 2,000 peer-reviewed studies, showing an increase in scientific interest in this condition. Data from insurance companies in three U.S. states indicate that hospital costs related to air embolism claims have a median payment of $325,000, with settlements ranging from $25,800 to $4,120,200[395, 396]. These figures do not account for additional hospital settlements

for severe outcomes, such as brain injury or death, due to intravenous air embolism, with payouts reportedly ranging between $750,000 and $2,500,000[395, 396].

This thesis provides a rigorous, fact-based examination of emboli formation and behavior, as well as their impact on the vascular system, to address these gaps in knowledge. Microfluidic devices, ranging from linear channels to complex bifurcated networks, were designed to replicate vascular conditions and investigate embolic formation under controlled conditions. While initial models featured abiotic channels, future iterations can incorporate more intricate geometries with endothelial cell coatings and active hydrophobic spots to enhance physiological relevance. This approach offers valuable insights into (i) gas insufflation during medical procedures in patients with different health profiles and (ii) the parameters contributing to decompression sickness. Key biological and environmental factors—including channel width, wall thickness, perforation size, hematocrit concentration, gas type, compression duration, and gas pressure—were analyzed to determine their influence on bubble formation dynamics.

Beyond elucidating the fundamental physics of gas embolism, the findings of this thesis hold significant clinical implications. By demonstrating how gas bubbles form and coalesce, this research lays the groundwork for refining surgical tool designs, improving procedural protocols, and developing targeted interventions aimed at reducing the risks associated with gas embolism. As this condition becomes increasingly prevalent in surgical and critical care settings, a deeper understanding of its pathophysiology is paramount to minimizing its clinical impact and enhancing patient safety.

5.1.Key Findings

The most significant contribution of this thesis is the use of microfluidic devices to investigate pathological conditions *in vitro*. Gas embolism is a physical process with an unpredictable occurrence, presenting a sudden and challenging nature that makes it difficult to study *in vivo*.

Although recent studies have investigated bubble dynamics in microfluidic channels, as detailed in the comprehensive review from Chapter 1, most of the existing research efforts focus on bubble generation using flow-focusing devices, operating based on hydrodynamic principles, i.e., by mixing two or more fluid streams to induce bubble formation. There are three primary hydrodynamics-based techniques utilized for this purpose[397, 398]. The first involves a

compressed air stream that supersaturates the working liquid with air, followed by a rapid pressure release through an expansion nozzle. The second technique relies on a narrow passage within the main channel that constricts the continuous fluid, while the discontinuous fluid is dispensed from a nozzle positioned upstream of the constriction under low offset pressures or mechanical vibration. The third method utilizes cavitation through the application of power ultrasound, which creates bubbles at points of extreme rarefaction within standing ultrasonic waves. Among the most prominent systems studied in the literature, one microscale model employed a Y-junction microchannel at biologically-relevant length scales to investigate gas bubble formation using a water-air mixture[399]. The findings revealed that the likelihood of bubble division was higher when bubble size was relatively large in comparison with the channel length and when flowing through a liquid with a higher Reynolds number. Another study examined flow patterns and fluorescence intensity profiles of air bubbles versus liquid slugs in various microfluidic structures, analyzing their behavior under increasing air-to-liquid ratios[400]. The results indicated that at lower air-to-liquid ratios, the size distribution of air bubbles was chaotic. It was observed that longer bubbles with lower velocity formed in narrower channels, resistance to flow increased with higher hematocrit concentrations, and the propensity for gas embolism-like events heightened in honeycomb architectures with acute bifurcation angles, such as 30°. A separate investigation utilized microfluidics to demonstrate that short-term exposure to bubbles (less than 15 minutes) generally did not result in endothelial cell death[401]. However, bubble contact significantly increased intracellular calcium levels in the affected cells, with calcium signals being propagated via small nucleotides and gap junctions between adjacent cells during the bubble expansion process.

Despite these insights, none of these studies directly addressed the genesis of gas embolism or the origins of bubble formation under conditions closely resembling real-life settings. A crucial question remained unanswered: Can gas embolism be accurately simulated in vascular systems on a chip to establish correlations between intravascular bubble parameters and biological or environmental factors? To bridge this gap, this study aimed to replicate the microvasculature by designing channels that corresponded to the dimensions of arterioles and venules. A synthetic blood solution was also introduced, consisting of distilled water as the primary solvent, glycerine for density and viscosity adjustments, and xanthan gum for non-Newtonian shear-thinning behavior. By varying the concentration of xanthan gum, two solutions were created with

rheological properties that closely resemble those of real blood[402]. One solution mimicked a hematocrit level of 46%, representing healthy individuals, while the other simulated a hematocrit level of 20%, indicative of conditions such as anemia or thrombocytopenia, which can result from liver diseases, infections, cancers, alcohol consumption, and medications like heparin.

Furthermore, an artificial tissue model was developed using PDMS at a mixing ratio of 10:1, which resulted in a measured incremental elastic modulus of approximately 580 kPa, making it suitable for mimicking the tunica intima of blood vessels within the lower modulus range of 0.2 to 0.6 MPa[403]. Comparative analyses were conducted on the modulus and diffusion coefficients of oxygen and nitrogen in PDMS versus vascular walls to ensure appropriate modeling. Additional considerations included surface wettability, as natural blood vessels exhibit both hydrophobic and hydrophilic characteristics, with the luminal side being predominantly hydrophilic[404]. Although PDMS is inherently hydrophobic, its surface can be modified to become hydrophilic through exposure to ultraviolet or oxygen plasma treatment. Another key aspect investigated was the ability to replicate the heterogeneity of intravascular routes. Since nucleation sites in blood vessels are primarily associated with lipid islets and active hydrophobic spots[405], this heterogeneity was simulated using atomic force microscopy scans[406]. Topography and lateral force measurements of hydrophilized PDMS surfaces embedded with hydrophilic beads demonstrated the capability of surface functionalization to mimic the heterogeneous inner walls of blood vessels, thereby providing a more physiologically relevant model for studying gas embolism.

Origins of Bubble Formation. In Article 1 from Chapter 2, the origins of bubble formation were linked to the presence of excess gases through a series of controlled experiments. These experiments included standard devices, devices that had undergone degasification for 24 and 48 hours, and devices that were immersed in nitrogen. The complete absence of bubbles in degasified devices, irrespective of applied pressure, and the persistent presence of bubbles in nitrogen-immersed devices, even in the absence of pressure, provided compelling evidence that intravascular bubble formation is driven by supersaturation of the surrounding tissues rather than just mechanical forces. This distinction had not been clearly established in prior research, which often attributed bubble formation primarily to pressure changes[387] rather than the fundamental role of gas saturation levels.

This chapter also revealed the impact of induced pressure on bubble formation. Our findings showed a direct correlation between increased pressures and larger bubble volumes across all channel widths, as demonstrated in Chapters 2 and 3. This aligns with prior studies[407] that suggest a pressure-dependent mechanism for gas embolism formation. However, our research expands upon this by illustrating that higher insufflation rates, which are associated with elevated pressures, significantly influence the prominence and distribution of bubbles, particularly in larger vessels. The literature previously discussed the role of rapid pressure changes in bubble formation[408], but the influence of controlled, sustained insufflation rates on microvascular bubble dynamics has not been previously characterized in this manner.

Further supporting these observations, Chapter 4 demonstrated that compression at 3 bars consistently produced larger bubbles across all experimental settings compared to compression at 1 bar. While this was anticipated based on existing theoretical models, an unexpected finding emerged regarding lower pressure thresholds. Contrary to the assumption that lower pressures are inherently safer[407, 409], our experiments revealed dynamic behavior at low to medium pressure ranges. Specifically, while bubbles formed at smaller volumes under these conditions, there were always small populations of bubbles exhibiting significantly larger volumes. This discovery is medically significant because it challenges the conventional wisdom that operating at lower pressures is a guaranteed method for preventing bubble formation in high-risk or critical patients. Many clinical protocols assume that minimizing pressure fluctuations and using lower insufflation pressures will mitigate the risk of gas embolism, yet our findings suggest that even at seemingly safe pressure levels, unpredictable and potentially hazardous bubbles can still form.

Patient-specific factors, such as microvascular integrity, blood composition, and pre-existing medical conditions, influence the risk of gas embolism. Therefore, gas management procedures must be tailored to the patient's profile. Our findings demonstrate that bubble formation is not merely a function of pressure but also of tissue gas saturation states, offering a novel perspective with direct implications for surgical procedures, hyperbaric medicine, and critical care practices. These results necessitate a reassessment of clinical guidelines for procedures involving gas insufflation, decompression, and mechanical ventilation.

Width of Vascular Channels. A common finding from Chapters 2, 3, and 4 was the relationship between vascular geometry and bubble formation characteristics. In particular, the width of

artificial blood vessels in microfluidic models directly influences how bubbles coalesce and behave. Smaller vessel widths, typically less than 50 μm, were found to generate bubbles at lower pressures, suggesting heightened sensitivity to pressure changes. This observation aligns well with the common understanding that smaller vessels in the body are more prone to localized embolism formation, particularly during decompression sickness[410]. In fact, veins exhibit three key characteristics that create favorable conditions for bubble nucleation and stabilization: they contain the highest concentration of inert gases; they experience the lowest pressures and thus the highest pressure gradients; and they maintain higher flow velocities, leading to increased capillary numbers.

Conversely, larger channels were found to produce more numerous and chaotic bubbles under similar conditions, but they also facilitate the growth and expansion of bubbles due to increased space for coalescence. The relationship between channel size and bubble formation was further supported by additional studies related to Article 1, which demonstrated that maximum bubble volumes generally increased with the Reynolds number, a measure that scales with the channel width. Since larger channels are associated with a regime dominated by inertial forces, they exhibited higher Reynolds numbers but lower capillary numbers.

The impact of pressure distribution across different channel widths further illustrates the clinical relevance of these findings. In smaller vessels, confinement limits the growth of the bubble while larger vessels allow for greater expansion due to uniform pressure distribution. This distinction is particularly significant in understanding why arterial gas embolism tends to be more severe than venous gas embolism[387]. While arterial emboli are typically considered more dangerous due to their role in supplying oxygen and nutrients to tissues and organs, this study suggests an additional factor that larger volumes of emboli at reduced velocities in arterial systems may contribute to higher risks of bubble immobilization and vascular occlusion.

Devices with bifurcations also demonstrated a correlation between increased channel width and bubble volume. Larger bifurcated systems consistently exhibited greater bubble volumes under similar pressure conditions. This finding aligns with clinical observations that patients with larger or more compliant blood vessels—such as those suffering from vascular diseases like aneurysms—may experience more complex and unpredictable bubble dynamics. These insights have significant implications for patient-specific risk assessments and the development of tailored interventions to

minimize embolism risks. By accounting for individual variations in vascular geometry, clinicians may improve the precision of embolism prevention and treatment strategies, ultimately reducing the likelihood of severe complications associated with gas embolism.

Proximity of Pressure Application. The thickness of vascular walls plays a crucial role in modulating the propensity for bubble formation, as it directly dictates the proximity of pressure application. Channels with thinner walls, such as 25 μm, exhibited earlier onset and greater bubble volumes compared to thicker walls, such as 75 μm, even when exposed to identical pressure levels. Notably, the absence of bubble formation in channels with 100 μm separations underscores the protective effect of thicker vascular walls, which likely results from their ability to withstand pressure fluctuations and limit the availability of nucleation sites. This observation aligns with prior studies on the gas permeability of PDMS [411], which emphasized membrane thickness as a critical factor in diffusion-driven processes. Research has demonstrated that for efficient gas diffusion, PDMS membranes should ideally be around 50 μm, as thicker membranes tend to impede pressure-driven processes. These findings further correlate with anatomical studies showing that most blood vessels are located within the first 100 μm from airways and nutrients[412, 413], supporting the relevance of gas exchange dynamics in microfluidic models.

Even in emboli-prone channels with smaller separations, bubble formation remained prominent regardless of vessel width, indicating that wall thickness and channel width independently contribute to bubble dynamics. While this does not necessarily imply that thinner-walled blood vessels are inherently more susceptible to bubble formation, it does suggest that the closer the pressure source is to the vessel, the greater the likelihood of intravascular bubble formation. This has direct implications for laparoscopic procedures, where the insertion of a Veress needle in close proximity to blood vessels—even without direct puncture—may induce bubble formation due to localized pressure disturbances. Similarly, clinical conditions associated with vascular wall thinning, such as atherosclerosis, aneurysms, or vascular trauma, may heighten susceptibility to gas embolism, making these findings particularly relevant for surgical planning, patient-specific risk assessments, and the development of safer insufflation techniques

Compromised Vascular Walls. Artificial blood vessels with compromised integrity, particularly those with perforations, exhibited significantly larger bubble volumes upon gas insufflation, as demonstrated in Article 1. These perforations were designed to simulate ruptured vessels caused

by Veress needle insertion or preexisting vulnerabilities in high-risk patient populations, such as the elderly, obese individuals, or those with a history of cardiovascular and pulmonary diseases.

The unexpected observation, however, was the increased variability in bubble volumes as the perforation size grew, leading to unpredictable and potentially severe outcomes. Larger perforations consistently resulted in the sporadic formation of oversized bubbles, elevating the risk of vascular obstruction. Conversely, smaller perforations produced more consistent bubble generation. This apparent consistency did not equate to a lower risk, as even small but sustained embolization events can have cumulative and severe consequences. At the highest insufflation rates, wider perforations facilitated earlier and more erratic bubble formation, with larger vessels hosting greater bubble volumes. These findings indicate that higher gas insufflation rates in the presence of vessel perforations create dynamic flow conditions that significantly influence bubble size, stability, and overall embolization risk.

Another alarming insight from this study is that these bubble dynamics were observed within a two-minute timeframe—far shorter than a typical 30-to-60-minute laparoscopic procedure. This finding suggests that even brief gas exposure in a perforated vessel can result in substantial embolization, raising serious concerns about silent gas uptake during surgery. For instance, a perforated blood vessel with a diameter of just 2.5 mm and a fissure of 0.1 mm was found to accumulate approximately 0.2 mL of gas during an insufflation event. Though seemingly minor, this volume can be clinically significant, particularly if undetected, as microbubbles may coalesce into larger emboli or enter critical circulatory pathways, leading to delayed but severe post-operative complications. Furthermore, vessel perforations have been shown to significantly increase fatality risks[414]. When gas bubbles enter the bloodstream, they can exacerbate the situation by obstructing blood flow, triggering embolism, and causing a cascade of harmful effects, such as ischemia. The combination of vessel perforation and gas bubbles amplifies the damage by increasing mechanical stress and pressure on the affected vessels, potentially leading to severe complications, including shock or organ failure.

These findings underscore the urgent need for improved intraoperative monitoring, revised insufflation protocols, and preventative measures to mitigate the risks associated with undetected vascular perforations.

Equivalent Hematocrit Concentration. Two critical biological variables, examined in Chapter 3, were blood viscosity and surface tension, both of which play a major role in intravascular bubble formation. These factors were studied through hematocrit levels, which represent the concentration of red blood cells in the blood. The findings demonstrated that higher hematocrit levels were associated with increased blood viscosity and lower surface tension, both of which promoted conditions favorable for bubble generation. This is particularly important because higher viscosities slowed bubble movement, increasing the likelihood of bubble coalescence. In turn, this heightened the risk of bubble immobilization within microvascular networks, where restricted flow can lead to vascular occlusion, tissue ischemia, and potential organ dysfunction.

The clinical implications of these findings are substantial, as hematocrit levels vary widely among patients due to factors such as underlying medical conditions, age, sex, and anatomical differences. For instance, anemia—characterized by a reduced RBC concentration—results in lower blood viscosity[415], which could lead to different bubble dynamics compared to individuals with normal or elevated hematocrit levels. This underscores the necessity of accounting for patient-specific factors when assessing embolism risks in medical procedures involving gas insufflation or rapid pressure changes.

The impact of elevated hematocrit levels, such as those seen in patients with polycythemia or certain cardiovascular diseases, can be determined based on the trend that was observed in the two synthetic blood solutions from Chapter 3. These individuals exhibit thicker blood with a greater tendency to trap bubbles, increasing the risk of embolism-related complications. This highlights the potential for personalized medicine to mitigate gas embolism risks by adjusting procedural parameters based on individual patient hematocrit levels. For instance, tailored strategies—such as modifying gas insufflation pressures, optimizing fluid management, or using anticoagulants to regulate blood viscosity—could help minimize bubble formation during surgical interventions.

Flow Conditions. Flow conditions play a crucial role in determining the behavior of bubbles, particularly their stability and growth, which are key factors in the formation of gas embolism. The type of flow—whether pulsatile, or steady-state—has a direct impact on bubble dynamics, influencing not only the volume of the emboli but also their likelihood of forming and persisting. Microfluidic devices are typically associated with laminar flow due to the small scale of the channels, where inertial effects are minimal.

According to Chapter 4, steady-state flow conditions promote the growth of larger gas bubbles, as they facilitate stable nucleation and continuous bubble expansion. Steady flow allows bubbles to accumulate gas in a relatively predictable and consistent manner, leading to larger emboli as they experience less disruption from fluctuating flow patterns.

In contrast, pulsatile flow—mimicking the pulsations of the human heart—creates fluctuating shear forces. These fluctuations can cause instability in bubbles, impeding their growth and increasing the likelihood of bubble fragmentation. The alternating pressure cycles in pulsatile flow can disrupt the delicate balance needed for continuous nucleation and gas accumulation, resulting in smaller and less stable emboli.

In the context of vascular gas embolism, this modulation could be beneficial. By inducing pulsatile flow, practitioners may reduce the likelihood of large emboli forming, potentially minimizing the risk of catastrophic events.

Compression Parameters. The findings related to decompression sickness in Chapter 4 align with established knowledge but add valuable granularity to the understanding of how bubbles form during rapid pressure changes. The duration of compression plays a critical role in determining the size of gas bubbles that form during decompression. Longer compression periods are associated with larger bubbles. This is because the local tissue network has more time to build a larger reservoir of dissolved gas, primarily nitrogen, under high-pressure conditions. The longer the compression, the more gas can dissolve into tissues, forming larger gas reservoirs. When pressure is subsequently reduced too quickly, the dissolved gas comes out of solution and forms bubbles. This reinforces the understanding that tissue supersaturation, where tissues hold an excessive amount of dissolved gas, contributes significantly to the onset of decompression sickness.

Nitrogen, being far more soluble in tissues than in blood, plays a key role in decompression sickness. As per Henry's law, the solubility of a gas in a liquid is proportional to the partial pressure of the gas. Under high-pressure conditions, nitrogen is much more likely to dissolve in tissues compared to other gases, such as oxygen or air[416]. This higher solubility causes a stronger concentration gradient between the tissues and blood vessels. When pressure is rapidly reduced, nitrogen comes out of solution more quickly, forming larger bubbles. Since nitrogen has this higher affinity for dissolution in tissues compared to blood, alternative gas mixtures may offer a safer solution for high-pressure environments. Helium, for example, is less soluble in tissues than

nitrogen and diffuses more quickly[417], reducing the concentration gradient between tissues and blood vessels during decompression. This results in a lower likelihood of large bubble formation. In fact, studies have shown that helium-based mixtures, such as Heliox (a mixture of helium and oxygen), can be beneficial in reducing the risk of DCS during deep-sea diving, as they promote faster off-gassing and reduce the supersaturation of nitrogen[418].

In addition to the immediate effects of decompression, the results from Chapter 4 shed light on the timing of bubble formation, showing that bubbles can continue to nucleate and grow even after decompression has ceased. This delayed onset of bubble formation is critical to understanding the full timeline of decompression sickness. It suggests that the symptoms of DCS may not manifest immediately after decompression but may develop over hours, potentially even up to 48 hours after the exposure to pressure changes. This delayed effect underlines the importance of conservative decompression protocols. Since bubbles may continue to grow and cause harm long after the decompression phase, it becomes crucial to monitor individuals for an extended period after pressure changes.

5.2.Unanswered Questions and Limitations

Despite the strides made in understanding gas embolism, several critical questions and limitations remain unaddressed. A significant knowledge gap pertains to the long-term biological effects of intravascular bubbles and the mechanisms driving their persistence or clearance across larger sections of the microvasculature. While the current studies focus on the physics of bubble formation and short-term behaviors in small sections of the artificial blood vessels, their impact on surrounding tissues over time—particularly in sensitive regions such as the brain, heart, or spinal cord—has not been thoroughly explored. For instance, the biological mechanisms underlying bubble immobilization, such as the aggregation of blood cells or clot formation, could critically contribute to vessel blockages caused by emboli. This results in ischemia, inflammation, or immune activation, with potentially severe consequences for organ function in the human body. Investigating these long-term, global outcomes is vital for understanding the chronic implications of gas embolism and decompression sickness.

Similarly, the process of bubble dissipation remains unexplored. Understanding how the body naturally clears bubbles or how therapeutic interventions like hyperbaric oxygen therapy facilitate

their absorption is essential for improving treatment strategies. Although this would be a large-scale project, spanning over multiple years with the collaboration of numerous disciplines, it remains an important avenue in gas embolism research.

Another limitation is the patient-specific factors that influence the pathophysiology of gas embolism. While the impact of variables like blood viscosity, vascular width, and wall thickness have been partially elucidated, their evolution with age, comorbidities, genetic predispositions, or vascular health remains unclear. Diseases such as diabetes and atherosclerosis, which alter vascular and rheological properties, may significantly affect bubble formation and propagation, yet they were not explicitly addressed. Additionally, the influence of vascular wall properties, including elasticity and rigidity, warrants deeper investigation in patients with varying health profiles and medical histories.

Lastly, the static and transient flow conditions used in our experimental models do not accurately replicate the dynamic nature of blood flow *in vivo*, where pulsatile motion, shear stress fluctuations, and complex branching geometries are predominant. This oversimplification limits the ability to predict bubble behavior under real-world physiological conditions, calling for more comprehensive models to enhance clinical relevance.

5.3.Future Work

Building on the insights gained, future research must address these limitations through targeted investigations. One promising avenue is to prioritize patient-specific modeling to better understand individual risks of gas embolism formation and its clinical complications. Incorporating biological variables such as age, gender, genetic predisposition, and comorbidities into predictive frameworks could lead to tailored prevention and treatment strategies. Computational models that integrate genomic and biophysical data may allow personalized interventions to mitigate embolism risks, particularly in vulnerable populations.

Additionally, bubble lodging, growth and clearance mechanisms require further investigation. Studies examining the role of immune cells, vascular endothelial responses, and therapeutic strategies like hyperbaric oxygen therapy could uncover new pathways to enhance bubble dissipation. This research may also explore pharmaceutical interventions that modify gas solubility or inhibit bubble coalescence, offering adjunct treatments to existing therapies.

Addressing the limitations of static flow conditions, future research must incorporate dynamic blood flow parameters into experimental designs. Simulations of pulsatile flow, pressure fluctuations, and branching vascular geometries will create more realistic models, enabling a better understanding of bubble behaviors *in vivo*. This would provide insights applicable to surgical settings, diving decompression, and aerospace medicine.

On the technological front, leveraging deep-learning algorithms to analyze bubble dynamics could revolutionize embolism prediction. Training these algorithms on extensive experimental datasets could yield predictive tools capable of real-time decision-making, allowing clinicians to modify procedures to minimize embolism risks.

Lastly, efforts should focus on translating experimental findings into clinical applications. *In vivo* validation of microfluidic models, combined with the development of risk-based clinical guidelines, would ensure that the discoveries from this research improve real-world patient outcomes. For instance, enhanced detection techniques could inform safer surgical protocols, while insights into decompression sickness could refine safety standards for high-risk activities like diving or space exploration.

By addressing these unanswered questions and advancing experimental methodologies, future research can provide a comprehensive framework for understanding and mitigating the risks of gas embolism and decompression sickness, ultimately enhancing patient safety and treatment outcomes.

Chapter 6. Conclusion

Vascular gas embolism, though rare, presents serious threats to patient health, particularly in iatrogenic conditions. The formation and lodging of gas bubbles within the vascular system can lead to life-threatening complications, revealing the importance of understanding their origins, behavior, and physiological consequences to enhance patient safety. However, despite its severe implications, gas embolism remains poorly understood, with limited research efforts exploring its underlying mechanisms and clinical management.

This work significantly advances our understanding of gas embolism by providing experimental-based insights through real-time imaging and reproducible observations, effectively bridging the gap between theoretical models and real-world applications. By mimicking physiological microvascular environments *in vitro*, this research offers unprecedented control over key input parameters, allowing for more accurate and reliable studies of embolism dynamics.

The research begins by investigating the fundamental process of gas bubble formation, primarily driven by pressure variations within the vascular network, in chapter 2. Using microfluidic devices, the study simulates gas insufflation in blood vessels, allowing for precise observation of bubble dynamics under different pressure regimes. By varying channel widths, wall thicknesses, and pressure levels, the experiments reveal crucial relationships between bubble size and vascular geometry, highlighting how increased pressure and larger vessel widths raise the risk of embolism.

In the same chapter, the focus is also placed on compromised vascular systems, examining the risks associated with gas insufflation near damaged blood vessels. By introducing perforations of varying sizes in the vascular channels, the study simulates conditions where vessel integrity is compromised. The findings reveal a strong correlation between perforation size, channel width, and gas flow rate, with larger perforations and higher gas flow rates resulting in more chaotic and voluminous bubble formation. This underscores the need for stringent safety protocols during medical procedures involving gas introduction, particularly for patients with vascular damage.

Building on this, the third chapter explores how blood properties and vascular geometries affect bubble formation and evolution. By incorporating synthetic blood solutions with varying viscosities based on equivalent hematocrit concentrations, the study simulates patient-specific

factors that influence gas embolism risk. The results highlight the role of larger channels with thicker blood-mimicking solutions in increasing bubble immobilization, underscoring the need for personalized approaches to embolism prevention based on blood properties and vessel sizes.

The fourth chapter addresses decompression sickness, a condition where rapid pressure changes cause dissolved gases to form bubbles within the body. A microscale hyperbaric system was developed to simulate different decompression scenarios using air and nitrogen. The study provides critical insights into bubble formation during decompression, with higher pressures and longer compression periods leading to larger and more numerous bubbles, especially in larger artificial blood vessels. These findings are particularly relevant for the prevention of decompression sickness in high-risk activities such as diving.

Collectively, the findings presented in this thesis offer a comprehensive investigation into the formation and behavior of gas bubbles within the vascular system, shedding light on the mechanisms driving gas embolism and decompression sickness. The insights gained from these experiments highlight the urgent need for improved detection and prevention methods, as well as the development of targeted safety protocols for both medical and environmental applications.

Reference Master

1. Gordy, S. and S. Rowell, *Vascular air embolism.* Int J Crit Illn Inj Sci, 2013. **3**(1): p. 73-6.
2. Goldman, S., J.M. Solano-Altamirano, and K.M. LeDez, *Gas Bubble Dynamics in the Human Body*. Gas Bubble Dynamics in the Human Body. 2017: Academic Press. 1-295.
3. Yu, X., et al., *Bubble-induced endothelial microparticles promote endothelial dysfunction.* PloS one, 2017. **12**(1): p. e0168881.
4. Dardeau, M.R., et al., *The incidence of decompression illness in 10 years of scientific diving.* Diving Hyperb Med, 2012. **42**(4): p. 195-200.
5. Bessereau, J., et al., *Long-term outcome of iatrogenic gas embolism.* Intensive care medicine, 2010. **36**: p. 1180-1187.
6. Freund, M.C., et al., *Systemic air embolism during percutaneous core needle biopsy of the lung: frequency and risk factors.* BMC pulmonary medicine, 2012. **12**(1): p. 1-12.
7. Mandelstam, P., et al., *Complications associated with esophagogastroduodenoscopy and with esophageal dilation.* Gastrointestinal Endoscopy, 1976. **23**(1): p. 16-19.
8. Verma, A. and M.P. Singh, *Venous gas embolism in operative hysteroscopy: A devastating complication in a relatively simple surgery.* Journal of Anaesthesiology Clinical Pharmacology, 2018. **34**(1): p. 103-106.
9. Fuentes, S., et al., *Gas Embolism in Pediatric Minimally Invasive Surgery: Should It Be a Concern?* Journal of Laparoendoscopic & Advanced Surgical Techniques, 2023.
10. van Hulst, R.A., J. Klein, and B. Lachmann, *Gas embolism: pathophysiology and treatment.* Clin Physiol Funct Imaging, 2003. **23**(5): p. 237-46.
11. Moon, R.E., *Hyperbaric oxygen treatment for decompression sickness.* Undersea Hyperb Med, 2014. **41**(2): p. 151-7.
12. Vesely, T.M., *Air embolism during insertion of central venous catheters.* Journal of Vascular and Interventional Radiology, 2001. **12**(11): p. 1291-1295.
13. Shaikh, N. and F. Ummunisa, *Acute management of vascular air embolism.* Journal of Emergencies, Trauma and Shock, 2009. **2**(3): p. 180.
14. Hatling, D., et al., *Iatrogenic cerebral gas embolism–A systematic review of case reports.* Acta Anaesthesiologica Scandinavica, 2019. **63**(2): p. 154-160.

15. Bazin, J., et al., *Haemodynamic conditions enhancing gas embolism after venous injury during laparoscopy: a study in pigs.* British journal of anaesthesia, 1997. **78**(5): p. 570-575.
16. Brull, S.J. and R.C. Prielipp, *Vascular air embolism: A silent hazard to patient safety.* Journal of critical care, 2017. **42**: p. 255-263.
17. Ross, C., et al., *Acute Management of High-Risk and Intermediate-Risk Pulmonary Embolism in Children: A Review.* Chest.
18. Roy, P.-M., D. Douillet, and A. Penaloza, *Contemporary management of acute pulmonary embolism.* Trends in cardiovascular medicine, 2021.
19. Papadopoulou, V., et al., *A critical review of physiological bubble formation in hyperbaric decompression.* Advances in colloid and interface science, 2013. **191**: p. 22-30.
20. Medby, C., A.O. Brubakk, and H.E. Myrvold, *Iatrogen gassemboli.* Tidsskrift for Den norske legeforening, 2001.
21. Walker III, J.R., E.J. Hexdall, and H.M. Murphy-Lavoie, *Diving Gas Embolism*, in *StatPearls [Internet]*. 2022, StatPearls Publishing.
22. Rosengartenis, L., *How much air in an IV line is too much?*
23. Rybárová, V., et al., *GAS EMBOLISM: A REVIEW, INSIGHTS INTO THE ETIOPATHOLOGY, AND FORENSIC IMPLICATIONS.* ROMANIAN JOURNAL OF LEGAL MEDICINE, 2020. **28**(3): p. 229-235.
24. McCarthy, C.J., et al., *Air embolism: practical tips for prevention and treatment.* Journal of Clinical Medicine, 2016. **5**(11): p. 93.
25. Feil, M. and P.P.S. Authority, *Reducing risk of air embolism associated with central venous access devices.* Situations, 2012. **56**(18): p. 24.
26. Irwin, B. and S. Ray, *Patent foramen ovale--assessment and treatment.* Cardiovasc Ther, 2012. **30**(3): p. e128-35.
27. Zhao, E., et al., *Influence of the Valsalva maneuver on cardiac hemodynamics and right to left shunt in patients with patent foramen ovale.* Sci Rep, 2017. **7**: p. 44280.
28. Eldridge, M.W., et al., *Exercise-induced intrapulmonary arteriovenous shunting in healthy humans.* Journal of Applied Physiology, 2004. **97**(3): p. 797-805.
29. Goldman, S., M. Solano-Altamirano, and K. Ledez, *Gas Bubble Dynamics in the Human Body*. 2017: Academic Press.

30. Pearson, E., *Emergency Medical Responder. 3rd Can Ed*. 2010, Pearson.
31. Takahara, K. and S. Suzuki, *In situ water radiolysis in a scanning electron microscope and observation of micro-and nanobubbles formation.* Journal of Applied Physics, 2021. **130**(2).
32. Brown, W.R., et al., *Longer Duration of Cardiopulmonary Bypass Is Associated With Greater Numbers of Cerebral Microemboli.* Stroke, 2000. **31**(3): p. 707-713.
33. Kadri, O.E., et al., *In vivo measurement of blood clot mechanics from computational fluid dynamics based on intravital microscopy images.* Computers in biology and medicine, 2019. **106**: p. 1-11.
34. David, M., et al., *The effect of the substrate temperature on extended defects created by hydrogen implantation in germanium.* Journal of Applied Physics, 2007. **102**(9).
35. Nordmark, H., et al., *Transmission electron microscopy study of hydrogen defect formation at extended defects in hydrogen plasma treated multicrystalline silicon.* Journal of Applied Physics, 2009. **105**(3).
36. Hantgan, R.R., R.G. Taylor, and J.C. Lewis, *Platelets interact with fibrin only after activation.* 1985.
37. Tosi, L., G. Rigoli, and A. Beltramello, *Fibrocartilaginous embolism of the spinal cord: a clinical and pathogenetic reconsideration.* Journal of Neurology, Neurosurgery & Psychiatry, 1996. **60**(1): p. 55-60.
38. Stanton, P.E., et al., *White clot syndrome.* Southern Medical Journal, 1988. **81**(5): p. 616-620.
39. Storm, B.S., et al., *Air Bubbles Activate Complement and Trigger Hemostasis and C3-Dependent Cytokine Release Ex Vivo in Human Whole Blood.* Journal of Immunology, 2021. **207**(11): p. 2828-2840.
40. Auñón-Chancellor, S.M., et al., *Venous thrombosis during spaceflight.* New England Journal of Medicine, 2020. **382**(1): p. 89-90.
41. Bollinger, B., et al., *Dual-frequency ultrasound detection of stationary microbubbles in tissue.* Undersea Hyperb Med, 2009. **36**(2): p. 127-36.
42. Newhouse, V. and P.M. Shankar, *Bubble size measurements using the nonlinear mixing of two frequencies.* The Journal of the Acoustical Society of America, 1984. **75**(5): p. 1473-1477.

43. Nishi, R., *The scattering and absorption of sound waves by a gas bubble in a viscous liquid.* Acta Acustica united with Acustica, 1975. **33**(2): p. 65-74.
44. Wilbur, J.C., et al., *Signals consistent with microbubbles detected in legs of normal human subjects after exercise.* Journal of Applied Physiology, 2010. **108**(2): p. 240-244.
45. Pollock, N.W., *Use of ultrasound in decompression research.* Diving and Hyperbaric Medicine, 2007. **37**(2): p. 68-72.
46. LeDez, K.M., *Air embolism and blunt chest trauma.* Canadian Journal of Anesthesia/Journal canadien d'anesthésie, 2011. **58**(12): p. 1140-1141.
47. Ho, A.M.-H. and E. Ling, *Systemic air embolism after lung trauma.* The Journal of the American Society of Anesthesiologists, 1999. **90**(2): p. 564-575.
48. Horrocks, C., *Blast injuries: biophysics, pathophysiology and management principles.* BMJ Military Health, 2001. **147**(1): p. 28-40.
49. Phillips, Y.Y., *Primary blast injuries.* Annals of emergency medicine, 1986. **15**(12): p. 1446-1450.
50. Riley, D., M. Clark, and T. Wong, *World Trade Center Terror: Explosion Trauma—Blast, Burns, and Crush Injury.* Advanced Emergency Nursing Journal, 2002. **24**(2): p. 47-59.
51. Muth, C.M. and E.S. Shank, *Gas embolism.* New England Journal of Medicine, 2000. **342**(7): p. 476-482.
52. Klein, J., et al., *A systematic review of the semi-sitting position in neurosurgical patients with patent foramen ovale: how frequent is paradoxical embolism?* World neurosurgery, 2018. **115**: p. 196-200.
53. Wu, T., et al., *Two cases of fatal iatrogenic air embolism confirmed by autopsies.* Journal of Forensic and Legal Medicine, 2021. **82**: p. 102209.
54. Platz, E., *Tangential gunshot wound to the chest causing venous air embolism: a case report and review.* The Journal of emergency medicine, 2011. **41**(2): p. e25-e29.
55. Orhurhu, V.J., C.C. Gao, and C. Ku, *Carbon dioxide embolism.* 2019.
56. Kennedy-Little, D. and T. Sharman, *Pulmonary barotrauma.* 2020.
57. Cipel, L. and M.T. Gyepes, *"Contrast buttle": a sign indicating perforation of the digestive tract.* American Journal of Roentgenology, 1979. **133**(1): p. 97-101.
58. Vaezeafshar, R., et al., *Barosinusitis: Comprehensive review and proposed new classification system.* Allergy Rhinol (Providence), 2017. **8**(3): p. 109-117.

59. *Divers Alert Network Annual Diving Reports*, in *DAN Annual Diving Report 2018 Edition: A Report on 2016 Diving Fatalities, Injuries, and Incidents*, P. Buzzacott and P.J. Denoble, Editors. 2018, Divers Alert Network © 2018 Divers Alert Network.: Durham (NC).
60. Melamed, Y., A. Shupak, and H. Bitterman, *Medical problems associated with underwater diving.* N Engl J Med, 1992. **326**(1): p. 30-5.
61. Bove, A.A., *Diving medicine.* Am J Respir Crit Care Med, 2014. **189**(12): p. 1479-86.
62. Schaffer, K.E., et al., *Mechanisms in development of interstitial emphysema and air embolism on decompression from depth.* J Appl Physiol, 1958. **13**(1): p. 15-29.
63. Mirski, M.A., et al., *Diagnosis and treatment of vascular air embolism.* The Journal of the American Society of Anesthesiologists, 2007. **106**(1): p. 164-177.
64. Durant, T.M., J. Long, and M.J. Oppenheimer, *Pulmonary (venous) air embolism.* American heart journal, 1947. **33**(3): p. 269-281.
65. Feil, M., *Preventing central line air embolism.* AJN The American Journal of Nursing, 2015. **115**(6): p. 64-69.
66. Colley, P.S. and A.A. Artru, *Bunegin-Albin catheter improves air retrieval and resuscitation from lethal venous air embolism in upright dogs.* Anesthesia & Analgesia, 1989. **68**(3): p. 298-301.
67. Ericsson, J.A., J.D. Gottlieb, and R.B. Sweet, *Closed-chest cardiac massage in the treatment of venous air embolism.* New England Journal of Medicine, 1964. **270**(25): p. 1353-1354.
68. Eoh, E.J., B. Derrick, and R. Moon, *Cerebral arterial gas embolism during upper endoscopy.* A&A Practice, 2015. **5**(6): p. 93-94.
69. Moon, R.E., *Bubbles in the brain: what to do for arterial gas embolism?* Critical care medicine, 2005. **33**(4): p. 909-910.
70. Sackmann, E.K., A.L. Fulton, and D.J. Beebe, *The present and future role of microfluidics in biomedical research.* Nature, 2014. **507**(7491): p. 181-189.
71. Dittrich, P.S. and A. Manz, *Lab-on-a-chip: microfluidics in drug discovery.* Nature reviews Drug discovery, 2006. **5**(3): p. 210-218.
72. Kızılkurtlu, A.A., et al., *Lung on a chip for drug screening and design.* Current Pharmaceutical Design, 2018. **24**(45): p. 5386-5396.

73. Shrestha, J., et al., *Lung-on-a-chip: the future of respiratory disease models and pharmacological studies.* Critical Reviews in Biotechnology, 2020. **40**(2): p. 213-230.
74. Leiby, K.L., M.S.B. Raredon, and L.E. Niklason, *Bioengineering the blood-gas barrier.* Comprehensive Physiology, 2020. **10**(2): p. 415-452.
75. Jimenez-Valdes, R.J., et al., *Where We Stand: Lung Organotypic Living Systems That Emulate Human-Relevant Host–Environment/Pathogen Interactions.* Frontiers in Bioengineering and Biotechnology, 2020. **8**.
76. Li, K., et al., *Biomimetic human lung-on-a-chip for modeling disease investigation.* Biomicrofluidics, 2019. **13**(3).
77. Huh, D., et al., *Microfabrication of human organs-on-chips.* Nature Protocols, 2013. **8**(11): p. 2135-2157.
78. Aziz, A.U.R., et al., *The Role of Microfluidics for Organ on Chip Simulations.* Bioengineering (Basel), 2017. **4**(2).
79. Arieli, R., *Nanobubbles form at active hydrophobic spots on the luminal aspect of blood vessels: consequences for decompression illness in diving and possible implications for autoimmune disease—an overview.* Frontiers in Physiology, 2017. **8**: p. 591.
80. Bhattacharjee, N., et al., *The upcoming 3D-printing revolution in microfluidics.* Lab on a Chip, 2016. **16**(10): p. 1720-1742.
81. Fuard, D., et al., *Optimization of poly-di-methyl-siloxane (PDMS) substrates for studying cellular adhesion and motility.* Microelectronic Engineering, 2008. **85**(5-6): p. 1289-1293.
82. Baudoin, R., et al., *Parallelized microfluidic biochips in multi well plate applied to liver tissue engineering.* Sensors and Actuators B: Chemical, 2012. **173**: p. 919-926.
83. Nguyen and, T., et al., *A method for matching the refractive index and kinematic viscosity of a blood analog for flow visualization in hydraulic cardiovascular models.* J. Biomech. Eng., 2004. **126**(4): p. 529-535.
84. Filipponi, L., et al., *Microbeads on microposts: An inverted architecture for bead microarrays.* Biosensors and Bioelectronics, 2009. **24**(7): p. 1850-1857.
85. Vasina, E.N., et al., *The BAD project: data mining, database and prediction of protein adsorption on surfaces.* Lab on a Chip, 2009. **9**(7): p. 891-900.
86. Mongrain, R., et al., *Effects of diffusion coefficients and struts apposition using numerical simulations for drug eluting coronary stents.* 2007.

87. Wagner, C.E., et al., *Quantifying the consistency and rheology of liquid foods using fractional calculus.* Food Hydrocolloids, 2017. **69**: p. 242-254.
88. Wagner, C.E., et al., *A rheological study of the association and dynamics of MUC5AC gels.* Biomacromolecules, 2017. **18**(11): p. 3654-3664.
89. Brown, X.Q., K. Ookawa, and J.Y. Wong, *Evaluation of polydimethylsiloxane scaffolds with physiologically-relevant elastic moduli: interplay of substrate mechanics and surface chemistry effects on vascular smooth muscle cell response.* Biomaterials, 2005. **26**(16): p. 3123-3129.
90. Palchesko, R.N., et al., *Development of polydimethylsiloxane substrates with tunable elastic modulus to study cell mechanobiology in muscle and nerve.* PloS one, 2012. **7**(12): p. e51499.
91. Monson, K.L., et al., *Axial mechanical properties of fresh human cerebral blood vessels.* J. Biomech. Eng., 2003. **125**(2): p. 288-294.
92. Poepping, T.L., et al., *A thin-walled carotid vessel phantom for Doppler ultrasound flow studies.* Ultrasound in medicine & biology, 2004. **30**(8): p. 1067-1078.
93. Held, M., et al., *Intracellular mechanisms of fungal space searching in microenvironments.* Proceedings of the National Academy of Sciences, 2019. **116**(27): p. 13543-13552.
94. Markov, D.A., et al., *Variation in diffusion of gases through PDMS due to plasma surface treatment and storage conditions.* Biomedical microdevices, 2014. **16**(1): p. 91-96.
95. Vadapalli, A., R.N. Pittman, and A.S. Popel, *Estimating oxygen transport resistance of the microvascular wall.* American Journal of Physiology-Heart and Circulatory Physiology, 2000. **279**(2): p. H657-H671.
96. Popel, A.S., *Theory of oxygen transport to tissue.* Critical reviews in biomedical engineering, 1989. **17**(3): p. 257.
97. Müller, B., et al. *High-resolution tomographic imaging of microvessels*. in *Proceedings of SPIE - The International Society for Optical Engineering*. 2008.
98. Popel, A.S. and P.C. Johnson, *Microcirculation and Hemorheology.* Annu Rev Fluid Mech, 2005. **37**: p. 43-69.
99. Chen, Z. and J.B. Lee, *Biocompatibility of SU-8 and Its Biomedical Device Applications.* Micromachines (Basel), 2021. **12**(7).

100. Mack, C.A. and J.E. Connors. *Fundamental differences between positive-and negative-tone imaging*. in *Optical/Laser Microlithography V*. 1992. SPIE.
101. Geissler, M. and Y. Xia, *Patterning: Principles and some new developments.* Advanced Materials, 2004. **16**(15): p. 1249-1269.
102. Chen, Y., *Nanofabrication by electron beam lithography and its applications: A review.* Microelectronic Engineering, 2015. **135**: p. 57-72.
103. Bi, R., et al., *In vivo label-free functional photoacoustic monitoring of ischemic reperfusion.* Journal of biophotonics, 2019. **12**(7): p. e201800454.
104. Yang, J., Y.E. Pak, and T.-R. Lee, *Predicting bifurcation angle effect on blood flow in the microvasculature.* Microvascular research, 2016. **108**: p. 22-28.
105. Arieli, R. and A. Marmur, *Evolution of bubbles from gas micronuclei formed on the luminal aspect of ovine large blood vessels.* Respiratory physiology & neurobiology, 2013. **188**(1): p. 49-55.
106. Clancy, K.F.A., et al., *Protein microarray spots are modulated by patterning method, surface chemistry and processing conditions.* Biosensors and Bioelectronics, 2019. **130**: p. 397-407.
107. Arieli, R., *Nanobubbles form at active hydrophobic spots on the luminal aspect of blood vessels: Consequences for decompression illness in diving and possible implications for autoimmune disease-An overview.* Frontiers in Physiology, 2017. **8**(AUG).
108. Tsuzuki, T., Baassiri, K., Mahmoudi, Z., Nicolau, D.V., *Hydrophobic recovery of PDMS surfaces in contact with hydrophilic entities: relevance to biomedical devices.* Materials, 2022.
109. Kašpar, O., et al., *Confinement of water droplets on rectangular micro/nano-arrayed surfaces.* Lab on a Chip, 2016. **16**(13): p. 2487-2493.
110. Filipponi, L., et al., *Protein patterning by microcontact printing using pyramidal PDMS stamps.* Biomedical Microdevices, 2016. **18**(1): p. 1-7.
111. Ivanova, E.P., et al., *Polymer microstructures fabricated via laser ablation used for multianalyte protein microassay.* Langmuir, 2002. **18**(24): p. 9539-9546.
112. Nicolau, D.V., et al., *Protein immobilisation on micro/nanostructures fabricated by laser microablation.* Biosensors and Bioelectronics, 2010. **26**(4): p. 1337-1345.

113. Dobroiu, S., et al., *Laser-assisted structuring of metal-polymer bilayers for protein patterning.* Microelectronic Engineering, 2010. **87**(5-8): p. 1190-1194.
114. Kašpar, O., et al., *Confinement of water droplets on rectangular micro/nano-arrayed surfaces.* Lab on a Chip, 2016. **16**(13): p. 2487-2493.
115. Filipponi, L., et al., *Protein patterning by microcontact printing using pyramidal PDMS stamps.* Biomedical microdevices, 2016. **18**: p. 1-7.
116. Dobroiu, S., et al., *Laser-assisted structuring of metal–polymer bilayers for protein patterning.* Microelectronic engineering, 2010. **87**(5-8): p. 1190-1194.
117. Brookshier, K. and J. Tarbell, *Evaluation of a transparent blood analog fluid: aqueous xanthan gum/glycerin.* Biorheology, 1993. **30**(2): p. 107-116.
118. Sattari, A., P. Hanafizadeh, and M. Hoorfar, *Multiphase flow in microfluidics: From droplets and bubbles to the encapsulated structures.* Advances in Colloid and Interface Science, 2020. **282**: p. 102208.
119. Zhang, W., et al., *Bubble breakup in microchannels: A review.* Chemical Engineering Journal, 2024: p. 149868.
120. Thorsen, T., et al., *Dynamic pattern formation in a vesicle-generating microfluidic device.* Physical review letters, 2001. **86**(18): p. 4163.
121. Zimmerman, W.B., et al., *Microbubble generation.* Recent patents on engineering, 2008. **2**(1): p. 1-8.
122. Burns, S., S. Yiacoumi, and C. Tsouris, *Microbubble generation for environmental and industrial separations.* Separation and purification technology, 1997. **11**(3): p. 221-232.
123. Vion, P., *Pressurised water pressure-reducing nozzle for generating microbubbles in a flotation plant*. 2007, Google Patents.
124. Takahashi, T., T. Okumura, and K. Kubo, *Microbubble generating device and hair washing device utilizing the same*. 2010, Google Patents.
125. Garstecki, P., A. Gańán-Calvo, and G. Whitesides, *Formation of bubbles and droplets in microfluidic systems.* Bulletin of the Polish Academy of Sciences: Technical Sciences, 2005. **53**(4).
126. Zimmerman, W.B., *Microfluidics: history, theory and applications*. Vol. 466. 2006: Springer Science & Business Media.

127. Noguchi, Y. and S. Chuang, *Method and system for generating microbubble-contained liquid and microbubble generator to be assembled in the system*. 2011, Google Patents.
128. Lorenceau, E., et al., *A high rate flow-focusing foam generator.* Physics of fluids, 2006. **18**(9): p. 097103.
129. Tesař, V., C.-H. Hung, and W.B. Zimmerman, *No-moving-part hybrid-synthetic jet actuator.* Sensors and Actuators A: Physical, 2006. **125**(2): p. 159-169.
130. Tesař, V., *Pressure-driven microfluidics*. 2007: Artech House Norwood.
131. Zhang, X., *Novel aerator studies on yeast growth.* University of Sheffield, MSc in Environmental and Energy Engineering dissertation, 2007.
132. Varma, A., *Microbubble generation for the enhanced air lift recovery of oil from oil sands.* University of Sheffield, MSc in Environmental and Energy Engineering dissertation, 2007.
133. Makuta, T., et al., *Generation of micro gas bubbles of uniform width in an ultrasonic field.* Journal of Fluid Mechanics, 2006. **548**: p. 113-131.
134. Jablonski, E.L., et al., *Microfluidics in the Undergraduate Laboratory: Device Fabrication and an Experiment to Mimic Intravascular Gas Embolism.* Chemical Engineering Education, 2010. **44**(1): p. 81-87.
135. Jia, L., Z. Li, and Q. Wei, *Bubble generation and growth mechanism in PMMA microfluidic chip.* AIP Advances, 2022. **12**(5): p. 055106.
136. Baassiri, K. and D. Nicolau, *Investigating the Mechanism of Intravascular Bubble Formation in Designed Arrays of Vascularized Systems on a Chip.*
137. Baum, O., et al., *Laser-assisted formation of micropores and nanobubbles in sclera promote stable normalization of intraocular pressure.* Laser Physics Letters, 2017. **14**(6): p. 065601.
138. Sobol, E., et al., *Laser-induced micropore formation and modification of cartilage structure in osteoarthritis healing.* Journal of Biomedical Optics, 2017. **22**: p. 091515.
139. Bull, J.L., et al. *A microfluidic model of microbubble lodging in small arteriole bifurcations*. in *2005 3rd IEEE/EMBS Special Topic Conference on Microtechnology in Medicine and Biology*. 2005. IEEE.
140. Bento, D., et al., *Microbubble moving in blood flow in microchannels: Effect on the cell-free layer and cell local concentration.* Biomedical microdevices, 2017. **19**(1): p. 1-10.

141. Bento, D., et al. *Blood Flow of Bubbles Moving in Microchannels with Bifurcations*. in *ECCOMAS Thematic Conference on Computational Vision and Medical Image Processing*. 2019. Springer.
142. Bento, D., et al., *Bubbles moving in blood flow in a microchannel network: The effect on the local hematocrit.* Micromachines, 2020. **11**(4): p. 344.
143. Li, Z., et al., *Flow field around bubbles on formation of air embolism in small vessels.* Proceedings of the National Academy of Sciences, 2021. **118**(26): p. e2025406118.
144. Mardanpour, M.M., et al., *Investigation of air bubble behavior after gas embolism events induced in a microfluidic network mimicking microvasculature.* Lab on a Chip, 2024.
145. Mardanpour, M.M., et al., *In Vitro Investigation of Gas Embolism in Microfluidic Networks Mimicking Microvasculature.* 2022.
146. Hosseinpour Shafaghi, A., et al., *On cavitation inception and cavitating flow patterns in a multi-orifice microfluidic device with a functional surface.* Physics of fluids, 2021. **33**(3).
147. Li, M., et al., *Study of Venturi tube geometry on the hydrodynamic cavitation for the generation of microbubbles.* Minerals Engineering, 2019. **132**: p. 268-274.
148. Moholkar, V.S. and A.B. Pandit, *Modeling of hydrodynamic cavitation reactors: a unified approach.* Chemical Engineering Science, 2001. **56**(21): p. 6295-6302.
149. Hanwright, J., et al., *Influence of surfactant on gas bubble stability.* Langmuir, 2005. **21**(11): p. 4912-4920.
150. Vega, E.J. and J.M. Montanero, *Influence of a surfactant on bubble bursting.* Experimental Thermal and Fluid Science, 2024. **151**: p. 111097.
151. Eckmann, D.M., J. Zhang, and P.S. Ayyaswamy, *Hydrodynamics and interfacial surfactant transport in vascular gas embolism.* Journal of Heat Transfer, 2021. **143**(10): p. 100802.
152. Karthikesh, M.S. and X. Yang, *The effect of ultrasound cavitation on endothelial cells.* Experimental Biology and Medicine, 2021. **246**(7): p. 758-770.
153. Eckmann, D.M., S.C. Armstead, and F. Mardini, *Surfactants reduce platelet–bubble and platelet–platelet binding induced by in vitro air embolism.* The Journal of the American Society of Anesthesiologists, 2005. **103**(6): p. 1204-1210.
154. Cabrales, P., *Perfluorocarbon Emulsions.* Alternatives to Blood Transfusion in Transfusion Medicine, 2010: p. 380-388.

155. Krafft, M.P. and J.G. Riess, *Therapeutic oxygen delivery by perfluorocarbon-based colloids.* Advances in colloid and interface science, 2021. **294**: p. 102407.
156. Spiess, B.D., *Perfluorocarbon emulsions as a promising technology: a review of tissue and vascular gas dynamics.* Journal of Applied Physiology, 2009. **106**(4): p. 1444-1452.
157. Mayer, D. and K.B. Ferenz, *Perfluorocarbons for the treatment of decompression illness: how to bridge the gap between theory and practice.* European Journal of Applied Physiology, 2019. **119**(11-12): p. 2421-2433.
158. Branger, A.B. and D.M. Eckmann, *Theoretical and experimental intravascular gas embolism absorption dynamics.* Journal of Applied Physiology, 1999. **87**(4): p. 1287-1295.
159. Branger, A.B. and D.M. Eckmann, *Accelerated arteriolar gas embolism reabsorption by an exogenous surfactant.* The Journal of the American Society of Anesthesiologists, 2002. **96**(4): p. 971-979.
160. Eckmann, D.M. and S.L. Diamond, *Surfactants attenuate gas embolism-induced thrombin production.* The Journal of the American Society of Anesthesiologists, 2004. **100**(1): p. 77-84.
161. Eckmann, D.M., S. Kobayashi, and M. Li, *Microvascular embolization following polidocanol microfoam sclerosant administration.* Dermatologic surgery, 2005. **31**(6): p. 636-643.
162. Eckmann, D.M., et al., *Gas Embolism and Surfactant-Based Intervention: Implications for Long-Duration Space-Based Activity.* Annals of the New York Academy of Sciences, 2006. **1077**(1): p. 256-269.
163. Torres, L.N., B.D. Spiess, and I.P. Torres Filho, *Effects of perfluorocarbon emulsions on microvascular blood flow and oxygen transport in a model of severe arterial gas embolism.* journal of surgical research, 2014. **187**(1): p. 324-333.
164. Ingram, D.A., M.B. Forman, and J.J. Murray, *Activation of complement by Fluosol attributable to the pluronic detergent micelle structure.* Journal of cardiovascular pharmacology, 1993. **22**(3): p. 456-461.
165. Spiess, B.D., et al., *Protection from venous air embolism with fluorocarbon emulsion FC-43.* Journal of Surgical Research, 1986. **41**(4): p. 439-444.
166. Briceno, J.C., et al., *Oxygen transport and consumption during experimental cardiopulmonary bypass using oxyfluor.* ASAIO journal, 1999. **45**(4): p. 322-327.

167. Ma, P., et al., *An integrated microfluidic device for studying controllable gas embolism induced cellular responses.* Talanta, 2020. **208**: p. 120484.
168. Liu, B., et al., *Manipulation of micro-objects using acoustically oscillating bubbles based on the gas permeability of PDMS.* Biomicrofluidics, 2018. **12**(3): p. 034111.
169. S. Gordy and S. Rowell, "Vascular air embolism," *International journal of critical illness and injury science,* vol. 3, no. 1, p. 73, 2013.
170. S. Goldman, M. Solano-Altamirano, and K. Ledez, *Gas Bubble Dynamics in the Human Body*. Academic Press, 2017.
171. C. J. McCarthy, S. Behravesh, S. G. Naidu, and R. Oklu, "Air embolism: diagnosis, clinical management and outcomes," *Diagnostics,* vol. 7, no. 1, p. 5, 2017.
172. V. Červeňák *et al.*, "Cerebral air embolism: neurologic manifestations, prognosis, and outcome," (in eng), *Front Neurol,* vol. 15, p. 1417006, 2024, doi: 10.3389/fneur.2024.1417006.
173. A. M. Alexander, A. Sankari, and N. Martin, "Arterial gas embolism," in *StatPearls [Internet]*: StatPearls Publishing, 2024.
174. S. Fuentes, C. Grande-Moreillo, J. Margarit-Mallol, S. Flores-Villar, E. Solé-Heuberger, and A. Jaen-Manzanera, "Gas Embolism in Pediatric Minimally Invasive Surgery: Should It Be a Concern?," *Journal of Laparoendoscopic & Advanced Surgical Techniques,* vol. 33, no. 10, pp. 1011-1017, 2023.
175. R. E. Moon. "Arterial Gas Embolism." Merck Manual. https://www.merckmanuals.com/en-ca/professional/injuries-poisoning/injury-during-diving-or-work-in-compressed-air/arterial-gas-embolism (accessed 2023).
176. N. Heming, M. A. Melone, and D. Annane, "Update on the Management of Iatrogenic Gas Embolism," in *Annual Update in Intensive Care and Emergency Medicine 2020*, J.-L. Vincent Ed. Cham: Springer International Publishing, 2020, pp. 559-568.
177. S. Q. Liu, S. Z. Zhao, Z. W. Li, S. P. Lv, Y. Q. Liu, and Y. Li, "Monitoring of gas emboli during hysteroscopic surgery: A prospective study," *Journal of Ultrasound in Medicine,* Article vol. 36, no. 4, pp. 749-756, 2017, doi: 10.7863/ultra.16.03051.
178. K. Baassiri, M. M. Mardanpour, K. M. LeDez, N. W. Pollock, D. Popa, and D. V. Nicolau, "In Vitro Studies of Gas Embolism," in *Recent Advances in Hemodynamics and Blood Mimetics*: Elsevier, 2026.

179. C. M. Muth and E. S. Shank, "Gas embolism," *New England Journal of Medicine,* Review vol. 342, no. 7, pp. 476-482, 2000, doi: 10.1056/NEJM200002173420706.
180. P. Mandelstam, C. Sugawa, S. E. Silvis, O. T. Nebel, and G. Rogers, "Complications associated with esophagogastroduodenoscopy and with esophageal dilation," *Gastrointestinal Endoscopy,* Article vol. 23, no. 1, pp. 16-19, 1976, doi: 10.1016/S0016-5107(76)73568-5.
181. L. K. Afreen *et al.*, "Incidence of venous air embolism during endoscopic retrograde cholangiopancreatography," *Anesthesia & Analgesia,* vol. 127, no. 2, pp. 420-423, 2018.
182. M. Derouin, P. Couture, D. Boudreault, D. Girard, and D. Gravel, "Detection of gas embolism by transesophageal echocardiography during laparoscopic cholecystectomy," *Anesthesia & Analgesia,* vol. 82, no. 1, pp. 119-124, 1996.
183. E. Y. Park, J.-Y. Kwon, and K. J. Kim, "Carbon dioxide embolism during laparoscopic surgery," *Yonsei medical journal,* vol. 53, no. 3, pp. 459-466, 2012.
184. K. M. LeDez, "Air embolism and blunt chest trauma," *Canadian Journal of Anesthesia/Journal canadien d'anesthésie,* vol. 58, pp. 1140-1141, 2011.
185. D. Levett and I. Millar, "Bubble trouble: a review of diving physiology and disease," *Postgraduate medical journal,* vol. 84, no. 997, pp. 571-578, 2008.
186. P. L. Marsh *et al.*, "Iatrogenic air embolism: pathoanatomy, thromboinflammation, endotheliopathy, and therapies," *Frontiers in Immunology,* vol. 14, p. 1230049, 2023.
187. V. Červeňák *et al.*, "Cerebral air embolism: neurologic manifestations, prognosis, and outcome," *Frontiers in Neurology,* vol. 15, p. 1417006, 2024.
188. S. M. Auñón-Chancellor, J. M. Pattarini, S. Moll, and A. Sargsyan, "Venous thrombosis during spaceflight," *New England Journal of Medicine,* vol. 382, no. 1, pp. 89-90, 2020.
189. D. Hatling, A. Høgset, A. B. Guttormsen, and B. Müller, "Iatrogenic cerebral gas embolism–A systematic review of case reports," *Acta Anaesthesiologica Scandinavica,* vol. 63, no. 2, pp. 154-160, 2019.
190. Z. U. Rahman *et al.*, "Cardiac Arrest as a Consequence of Air Embolism: A Case Report and Literature Review," (in eng), *Case Rep Med,* vol. 2016, p. 8236845, 2016, doi: 10.1155/2016/8236845.
191. T. Wu *et al.*, "Two cases of fatal iatrogenic air embolism confirmed by autopsies," *Journal of Forensic and Legal Medicine,* vol. 82, p. 102209, 2021.

192. Y. Y. Phillips, "Primary blast injuries," *Annals of emergency medicine,* vol. 15, no. 12, pp. 1446-1450, 1986.
193. C. Horrocks, "Blast injuries: biophysics, pathophysiology and management principles," *BMJ Military Health,* vol. 147, no. 1, pp. 28-40, 2001.
194. A. M.-H. Ho and E. Ling, "Systemic air embolism after lung trauma," *The Journal of the American Society of Anesthesiologists,* vol. 90, no. 2, pp. 564-575, 1999.
195. K. M. LeDez, "Air embolism and blunt chest trauma," *Canadian Journal of Anesthesia/Journal canadien d'anesthésie,* vol. 58, no. 12, pp. 1140-1141, 2011.
196. Y. Hashimoto, T. Yamaki, T. Sakakibara, J. Matsui, and M. Matsui, "Cerebral air embolism caused by cardiopulmonary resuscitation after cardiopulmonary arrest on arrival," *Journal of Trauma and Acute Care Surgery,* vol. 48, no. 5, pp. 975-977, 2000.
197. L. M. Bralow and M. Piehl, "Barotrauma and Arterial Gas Embolism: A Diving Emergencies Simulation Case for Emergency Medicine Residents," (in eng), *MedEdPORTAL,* vol. 14, p. 10788, Dec 21 2018, doi: 10.15766/mep_2374-8265.10788.
198. D. Riley, M. Clark, and T. Wong, "World Trade Center Terror: Explosion Trauma—Blast, Burns, and Crush Injury," *Advanced Emergency Nursing Journal,* vol. 24, no. 2, pp. 47-59, 2002.
199. Y. Mushkat, D. Luxman, Z. Nachum, M. P. David, and Y. Melamed, "Gas embolism complicating obstetric or gynecologic procedures. Case reports and review of the literature," (in eng), *Eur J Obstet Gynecol Reprod Biol,* vol. 63, no. 1, pp. 97-103, Nov 1995, doi: 10.1016/0301-2115(95)02221-r.
200. T. M. Atkinson, G. D. Giraud, B. M. Togioka, D. B. Jones, and J. E. Cigarroa, "Cardiovascular and ventilatory consequences of laparoscopic surgery," *Circulation,* vol. 135, no. 7, pp. 700-710, 2017.
201. A. Verma and M. P. Singh, "Venous gas embolism in operative hysteroscopy: A devastating complication in a relatively simple surgery," *Journal of Anaesthesiology Clinical Pharmacology,* vol. 34, no. 1, pp. 103-106, 2018.
202. J. Bazin, T. Gillart, P. Rasson, N. Conio, L. Aigouy, and P. Schoeffler, "Haemodynamic conditions enhancing gas embolism after venous injury during laparoscopy: a study in pigs," *British journal of anaesthesia,* vol. 78, no. 5, pp. 570-575, 1997.

203. J. J. Maleszewski, C. K. Lai, V. Nair, and J. P. Veinot, "Anatomic considerations and examination of cardiovascular specimens (excluding devices)," *Cardiovascular pathology,* pp. 27-84, 2022.
204. K. R. Olson, "DESIGN AND PHYSIOLOGY OF ARTERIES AND VEINS | Physiology of Capacitance Vessels," in *Encyclopedia of Fish Physiology*, A. P. Farrell Ed. San Diego: Academic Press, 2011, pp. 1111-1118.
205. Q. Wu *et al.*, "Organ-on-a-chip: Recent breakthroughs and future prospects," *Biomedical engineering online,* vol. 19, pp. 1-19, 2020.
206. Y. Lu *et al.*, "Adhesion of silicone oil and emulsification: an in vitro assessment using a microfluidic device and 'Eye-on-a-Chip'," *Acta Ophthalmologica,* vol. 97, no. 3, pp. 313-318, 2019.
207. L. Si *et al.*, "A human-airway-on-a-chip for the rapid identification of candidate antiviral therapeutics and prophylactics," *Nature biomedical engineering,* vol. 5, no. 8, pp. 815-829, 2021.
208. M. Zhang *et al.*, "Biomimetic human disease model of SARS-CoV-2-induced lung injury and immune responses on organ chip system," *Advanced Science,* vol. 8, no. 3, p. 2002928, 2021.
209. D. Huh, B. D. Matthews, A. Mammoto, M. Montoya-Zavala, H. Y. Hsin, and D. E. Ingber, "Reconstituting organ-level lung functions on a chip," *Science,* vol. 328, no. 5986, pp. 1662-1668, 2010.
210. T. Cao *et al.*, "Biomimetic alveolus-on-a-chip for SARS-CoV-2 infection recapitulation," *Research,* 2022.
211. B. Müller *et al.*, "High-resolution tomographic imaging of microvessels," in *Developments in X-ray tomography VI*, 2008, vol. 7078: SPIE, pp. 89-98.
212. T.-Y. Tu and P. C.-P. Chao, "Continuous blood pressure measurement based on a neural network scheme applied with a cuffless sensor," *Microsystem Technologies,* vol. 24, pp. 4539-4549, 2018.
213. B. Alberts, A. Johnson, J. Lewis, M. Raff, K. Roberts, and P. Walter, "Blood vessels and endothelial cells," in *Molecular Biology of the Cell. 4th edition*: Garland Science, 2002.
214. E. Nader *et al.*, "Blood rheology: key parameters, impact on blood flow, role in sickle cell disease and effects of exercise," *Frontiers in physiology,* vol. 10, p. 1329, 2019.

215. L. Webb, "Mimicking Blood Rheology for More Accurate Modeling in Benchtop Research," *The Pegasus Review: UCF Undergraduate Research Journal,* vol. 12, no. 1, p. 6, 2020.
216. K. Brookshier and J. Tarbell, "Evaluation of a transparent blood analog fluid: aqueous xanthan gum/glycerin," *Biorheology,* vol. 30, no. 2, pp. 107-116, 1993.
217. T. E. Kornfield and E. A. Newman, "Measurement of retinal blood flow using fluorescently labeled red blood cells," *Eneuro,* vol. 2, no. 2, 2015.
218. E. L. Jablonski, B. M. Vogel, D. P. Cavanagh, and K. L. Beers, "Microfluidics in the Undergraduate Laboratory: Device Fabrication and an Experiment to Mimic Intravascular Gas Embolism," *Chemical Engineering Education,* vol. 44, no. 1, pp. 81-87, 2010.
219. A. B. Schroeder, E. T. Dobson, C. T. Rueden, P. Tomancak, F. Jug, and K. W. Eliceiri, "The ImageJ ecosystem: Open-source software for image visualization, processing, and analysis," *Protein Science,* vol. 30, no. 1, pp. 234-249, 2021.
220. J. G. Riess, "Fluorocarbon-based injectable gaseous microbubbles for diagnosis and therapy," *Current opinion in colloid & interface science,* vol. 8, no. 3, pp. 259-266, 2003.
221. V. Cottin, B. Delafosse, and J.-P. Viale, "Gas embolism during laparoscopy: a report of seven cases in patients with previous abdominal surgical history," *Surgical endoscopy,* vol. 10, pp. 166-169, 1996.
222. J. D. Waye, S. A. Yessayan, B. S. Lewis, and T. L. Fabry, "The technique of abdominal pressure in total colonoscopy," *Gastrointestinal endoscopy,* vol. 37, no. 2, pp. 147-151, 1991.
223. C. Henny and J. Hofland, "Laparoscopic surgery: pitfalls due to anesthesia, positioning, and pneumoperitoneum," *Surgical Endoscopy and Other Interventional Techniques,* vol. 19, pp. 1163-1171, 2005.
224. M. Perrin and A. Fletcher, "Laparoscopic abdominal surgery," *Continuing Education in Anaesthesia, Critical Care & Pain,* vol. 4, no. 4, pp. 107-110, 2004.
225. X. Yang *et al.*, "Gases for establishing pneumoperitoneum during laparoscopic abdominal surgery," *Cochrane Database of Systematic Reviews,* no. 3, 2022.
226. A. Bettiol *et al.*, "Erythrocyte oxidative stress and thrombosis," *Expert Reviews in Molecular Medicine,* vol. 24, p. e31, 2022.

227. L. O. Ferreira *et al.*, "Biochemical changes in cardiopulmonary bypass in cardiac surgery: New insights," *Journal of Personalized Medicine,* vol. 13, no. 10, p. 1506, 2023.
228. W. Fan, B. Gui, X. Zhou, L. Li, and H. Chen, "A narrative review on lung injury: mechanisms, biomarkers, and monitoring," *Critical Care,* vol. 28, no. 1, pp. 1-13, 2024.
229. K. Draper, R. Jefson, J. Jongeward, R, and M. McLeod, "Duration of postlaparoscopic pneumoperitoneum," *Surgical endoscopy,* vol. 11, pp. 809-811, 1997.
230. S. Jayaraman, A. Khakhar, H. Yang, D. Bainbridge, and D. Quan, "The association between central venous pressure, pneumoperitoneum, and venous carbon dioxide embolism in laparoscopic hepatectomy," *Surgical endoscopy,* vol. 23, pp. 2369-2373, 2009.
231. V. J. Orhurhu, C. C. Gao, and C. Ku, "Carbon dioxide embolism," 2019.
232. A. Haggerty and M. Nirmalan, "Capillary dynamics, interstitial fluid and the lymphatic system," *Anaesthesia & Intensive Care Medicine,* vol. 23, no. 2, pp. 130-137, 2022.
233. N. Radhakrishnan, "Chapter 5–The pathophysiology of varicose veins of the lower limb," *Genesis, Pathophysiology and Management of Venous and Lymphatic Disorders; Radhakrishnan, N., Ed,* pp. 95-137, 2022.
234. E. Y. Park, J.-Y. Kwon, and K. J. Kim, "Carbon dioxide embolism during laparoscopic surgery," *Yonsei medical journal,* vol. 53, no. 3, p. 459, 2012.
235. A. A. Kader and M. E. Saltveit, "Respiration and gas exchange," *Postharvest physiology and pathology of vegetables,* pp. 31-56, 2002.
236. M. A. Mirski, A. V. Lele, L. Fitzsimmons, T. J. Toung, and D. C. Warltier, "Diagnosis and treatment of vascular air embolism," *The Journal of the American Society of Anesthesiologists,* vol. 106, no. 1, pp. 164-177, 2007.
237. D. Fuard, T. Tzvetkova-Chevolleau, S. Decossas, P. Tracqui, and P. Schiavone, "Optimization of poly-di-methyl-siloxane (PDMS) substrates for studying cellular adhesion and motility," *Microelectronic Engineering,* vol. 85, no. 5-6, pp. 1289-1293, 2008.
238. R. Baudoin, G. Alberto, P. Paullier, C. Legallais, and E. Leclerc, "Parallelized microfluidic biochips in multi well plate applied to liver tissue engineering," *Sensors and Actuators B: Chemical,* vol. 173, pp. 919-926, 2012.

239. X. Q. Brown, K. Ookawa, and J. Y. Wong, "Evaluation of polydimethylsiloxane scaffolds with physiologically-relevant elastic moduli: interplay of substrate mechanics and surface chemistry effects on vascular smooth muscle cell response," *Biomaterials,* vol. 26, no. 16, pp. 3123-3129, 2005.
240. R. N. Palchesko, L. Zhang, Y. Sun, and A. W. Feinberg, "Development of polydimethylsiloxane substrates with tunable elastic modulus to study cell mechanobiology in muscle and nerve," *PloS one,* vol. 7, no. 12, p. e51499, 2012.
241. R. Akhtar, M. J. Sherratt, J. K. Cruickshank, and B. Derby, "Characterizing the elastic properties of tissues," *Materials Today,* vol. 14, no. 3, pp. 96-105, 2011.
242. M. Manzo and M. Bakaraju, "Novel thin polymeric magnetic membranes study for applications in the future biomedical devices," *AIP Advances,* vol. 12, no. 11, 2022.
243. K. L. Monson, W. Goldsmith, N. M. Barbaro, and G. T. Manley, "Axial mechanical properties of fresh human cerebral blood vessels," *J. Biomech. Eng.,* vol. 125, no. 2, pp. 288-294, 2003.
244. T. L. Poepping, H. N. Nikolov, M. L. Thorne, and D. W. Holdsworth, "A thin-walled carotid vessel phantom for Doppler ultrasound flow studies," *Ultrasound in medicine & biology,* vol. 30, no. 8, pp. 1067-1078, 2004.
245. L. Xu, H. Lee, D. Jetta, and K. W. Oh, "Vacuum-driven power-free microfluidics utilizing the gas solubility or permeability of polydimethylsiloxane (PDMS)," *Lab on a Chip,* vol. 15, no. 20, pp. 3962-3979, 2015.
246. S. Kanehashi, T. Sato, S. Sato, and K. Nagai, "Microstructure and gas diffusivity of poly (dimethylsiloxane) dense membrane using molecular dynamics (MD) simulation," *Transactions of the Materials Research Society of Japan,* vol. 37, no. 3, pp. 439-442, 2012.
247. A. S. Popel, "Theory of oxygen transport to tissue," *Critical reviews in biomedical engineering,* vol. 17, no. 3, p. 257, 1989.
248. A. Vadapalli, R. N. Pittman, and A. S. Popel, "Estimating oxygen transport resistance of the microvascular wall," *American Journal of Physiology-Heart and Circulatory Physiology,* vol. 279, no. 2, pp. H657-H671, 2000.
249. D. A. Markov, E. M. Lillie, S. P. Garbett, and L. J. McCawley, "Variation in diffusion of gases through PDMS due to plasma surface treatment and storage conditions," *Biomedical microdevices,* vol. 16, no. 1, pp. 91-96, 2014.

250. S. O. Woo, M. Oh, K. Nietfeld, B. Boehler, and Y. Choi, "Molecular diffusion analysis of dynamic blood flow and plasma separation driven by self-powered microfluidic devices," *Biomicrofluidics,* vol. 15, no. 3, 2021.
251. R. Ariati, F. Sales, A. Souza, R. A. Lima, and J. Ribeiro, "Polydimethylsiloxane composites characterization and its applications: A review," *Polymers,* vol. 13, no. 23, p. 4258, 2021.
252. T. Tsuzuki, Baassiri, K., Mahmoudi, Z., Nicolau, D.V., "Hydrophobic recovery of PDMS surfaces in contact with hydrophilic entities: relevance to biomedical devices," *Materials,* vol. in print, 2022.
253. F. Khan, K. Singh, and M. T. Friedman, "Artificial blood: the history and current perspectives of blood substitutes," *Discoveries,* vol. 8, no. 1, p. e104, 2020.
254. H. Minasyan, "Bactericidal Capacity of Erythrocytes in Human Cardiovascular System," *International Clinical Pathology Journal,* vol. 2, 07/22 2016, doi: 10.15406/icpjl.2016.02.00052.
255. M. Sawdon and E. Kirkman, "Capillary dynamics and the interstitial fluid–lymphatic system," *Anaesthesia & Intensive Care Medicine,* vol. 18, no. 6, pp. 309-315, 2017.
256. M. P. Goldman and R. A. Weiss, *Sclerotherapy: Treatment of Varicose and Telangiectatic Leg Veins (Expert Consult)*. Elsevier Health Sciences, 2016.
257. H. Minasyan, "Bactericidal capacity of erythrocytes in human cardiovascular system," *Int Clin Pathol J,* vol. 2, no. 5, p. 00052, 2016.
258. G. T. Feke, H. Tagawa, D. M. Deupree, D. G. Goger, J. Sebag, and J. Weiter, "Blood flow in the normal human retina," *Investigative ophthalmology & visual science,* vol. 30, no. 1, pp. 58-65, 1989.
259. E. L. Boulpaep, "Arteries and veins," *Medical physiology,* vol. 2, pp. 467-81, 2012.
260. N. D. Bouvy *et al.*, "Effects of carbon dioxide pneumoperitoneum, air pneumoperitoneum, and gasless laparoscopy on body weight and tumor growth," *Archives of Surgery,* vol. 133, no. 6, pp. 652-656, 1998.
261. B. Liu *et al.*, "Manipulation of micro-objects using acoustically oscillating bubbles based on the gas permeability of PDMS," (in eng), *Biomicrofluidics,* vol. 12, no. 3, p. 034111, May 2018, doi: 10.1063/1.5028419.
262. P. Ma *et al.*, "An integrated microfluidic device for studying controllable gas embolism induced cellular responses," *Talanta,* vol. 208, p. 120484, 2020.

263. J. Neudecker *et al.*, "The European Association for Endoscopic Surgery clinical practice guideline on the pneumoperitoneum for laparoscopic surgery," *Surgical endoscopy,* vol. 16, pp. 1121-1143, 2002.

264. S. Goldman, J. M. Solano-Altamirano, and K. M. LeDez, *Gas Bubble Dynamics in the Human Body* (Gas Bubble Dynamics in the Human Body). Academic Press, 2017, pp. 1-295.

265. B. S. Storm *et al.*, "Air Bubbles Activate Complement and Trigger Hemostasis and C3-Dependent Cytokine Release Ex Vivo in Human Whole Blood," *Journal of Immunology,* Article vol. 207, no. 11, pp. 2828-2840, 2021, doi: 10.4049/jimmunol.2100308.

266. J. R. Walker III, E. J. Hexdall, and H. M. Murphy-Lavoie, "Diving Gas Embolism," in *StatPearls [Internet]*: StatPearls Publishing, 2022.

267. P. Shah and M. A. Louis, "Physiology, Central Venous Pressure," in *StatPearls*. Treasure Island (FL): StatPearls Publishing Copyright © 2024, StatPearls Publishing LLC., 2024.

268. C. Gopalan and E. Kirk, "Chapter 8 - Blood pressure, hypertension, and exercise," in *Biology of Cardiovascular and Metabolic Diseases*, C. Gopalan and E. Kirk Eds.: Academic Press, 2022, pp. 141-156.

269. R. Chaudhry, J. H. Miao, and A. Rehman, "Physiology, cardiovascular," in *StatPearls [Internet]*: StatPearls Publishing, 2022.

270. W. Maue-Dickson, "Section II. Anatomy and physiology," *The Cleft Palate Journal,* vol. 14, no. 4, pp. 270-287, 1977.

271. J. Y. Lee and S. J. Lee, "Murray's law and the bifurcation angle in the arterial micro-circulation system and their application to the design of microfluidics," *Microfluidics and Nanofluidics,* Article vol. 8, no. 1, pp. 85-95, 2010, doi: 10.1007/s10404-009-0454-1.

272. T. F. Sherman, "On connecting large vessels to small," *Journal of General Physiology,* Article vol. 78, no. 4, pp. 431-453, 1981, doi: 10.1085/jgp.78.4.431.

273. S. Lorthois, F. Lauwers, and F. Cassot, "Tortuosity and other vessel attributes for arterioles and venules of the human cerebral cortex," *Microvascular research,* vol. 91, pp. 99-109, 2014.

274. M. M. Mardanpour, A. Sudalaiyadum Perumal, Z. Mahmoodi, G. Montiel Rubies, K. M. LeDez, and D. V. Nicolau, "In vitro investigation of gas embolism in microfluidic networks mimicking microvasculature," *Lab on a chip,* vol. in review, 2022.

275. V. J. Orhurhu, C. C. Gao, and C. Ku, "Carbon dioxide embolism," 2019.
276. T. C. Merkel, V. I. Bondar, K. Nagai, B. D. Freeman, and I. Pinnau, "Gas sorption, diffusion, and permeation in poly(dimethylsiloxane)," Journal of Polymer Science Part B: Polymer Physics, https://doi.org/10.1002/(SICI)1099-0488(20000201)38:3<415::AID-POLB8>3.0.CO;2-Z vol. 38, no. 3, pp. 415-434, 2000/02/01 2000, doi: https://doi.org/10.1002/(SICI)1099-0488(20000201)38:3<415::AID-POLB8>3.0.CO;2-Z.
277. M. Held, O. Kašpar, C. Edwards, and D. V. Nicolau, "Intracellular mechanisms of fungal space searching in microenvironments," Proceedings of the National Academy of Sciences, vol. 116, no. 27, pp. 13543-13552, 2019.
278. D. A. Markov, E. M. Lillie, S. P. Garbett, and L. J. McCawley, "Variation in diffusion of gases through PDMS due to plasma surface treatment and storage conditions," Biomedical microdevices, vol. 16, no. 1, pp. 91-96, 2014.
279. A. Vadapalli, R. N. Pittman, and A. S. Popel, "Estimating oxygen transport resistance of the microvascular wall," American Journal of Physiology-Heart and Circulatory Physiology, vol. 279, no. 2, pp. H657-H671, 2000.
280. P. L. Marsh et al., "Iatrogenic air embolism: pathoanatomy, thromboinflammation, endotheliopathy, and therapies," Frontiers in Immunology, vol. 14, p. 1230049, 2023.
281. W. D. Tucker, Y. Arora, and K. Mahajan, "Anatomy, blood vessels," 2017.
282. I. C. Gawthrope, M. Summers, D. J. Macey, and D. A. Playford, "An observation of venous gas emboli in divers and susceptibility to decompression sickness," Diving Hyperb Med, vol. 45, no. 1, pp. 25-28, 2015.
283. Mirski, M.A.; Lele, A.V.; Fitzsimmons, L.; Toung, T.J.K. Diagnosis and treatment of vascular air embolism. J. Am. Soc. Anesthesiol. 2007, 106, 164–177.
284. van Hulst, R.A.; Klein, J.; Lachmann, B. Gas embolism: Pathophysiology and treatment. Clin. Physiol. Funct. Imaging 2003, 23, 237–246.
285. Malik, N.; et al. Air embolism: Diagnosis and management. Futur. Cardiol. 2017, 13, 365–378.
286. Dick, A.P.; Massey, E.W. Neurologic presentation of decompression sickness and air embolism in sport divers. Neurology 1985, 35, 667.
287. Marsh, P.L.; et al. Iatrogenic air embolism: Pathoanatomy, thromboinflammation, endotheliopathy, and therapies. Front. Im-munol. 2023, 14, 1230049.

288. Muth, C.M.; Shank, E.S. Gas embolism. New Engl. J. Med. 2000, 342, 476–482.
289. Hakman, E.N.; Cowling, K.M. Paradoxical Embolism. StatPearls: Treasure Island, Florida. 2017.
290. Gordy, S.; Rowell, S. Vascular air embolism. Int. J. Crit. Illn. Inj. Sci. 2013, 3, 73–76.
291. Alexander, A.M.; Martin, N. Arterial Gas Embolism. StatPearls: Treasure Island, Florida. 2019.
292. Verma, A.; Singh, M.P. Venous gas embolism in operative hysteroscopy: A devastating complication in a relatively simple surgery. J. Anaesthesiol. Clin. Pharmacol. 2018, 34, 103–106.
293. McCarthy, C.J.; Behravesh. S.; Naidu, S.G.; Oklu, R. Air embolism: Diagnosis, clinical management and outcomes. Diagnostics 2017, 7, 5.
294. Kerrigan, M.J.; Cooper, J.S. Venous Gas Embolism. StatPearls: Treasure Island, Florida. 2018.
295. Cooper, J. Treatment of endoscopy associated cerebral gas embolism. Off. J. Am. Coll. Gastroenterol. ACG 2018, 113, 1742–1744.
296. Heming, N.; Melone, M.-A.; Annane, D. Update on the management of iatrogenic gas embolism. Annu. Update Intensive Care Emerg. Med. 2020, 2020, 559–568.
297. Mardanpour, M.M.; Perumal, A.S.; Mahmoodi, Z.; Baassiri, K.; Montiel-Rubies, G.; LeDez, K.M.; Nicolau, D.V. Investigation of air bubble behaviour after gas embolism events induced in a microfluidic network mimicking microvasculature. Lab Chip 2024, 24, 2518–2536.
298. Bento, D.; Lopes, S.; Maia, I.; Pereira, A. I.; Fernandes, C. S.; Miranda, J. M.; Lima, R. Blood Flow of Bubbles Moving in Micro-channels with Bifurcations. In VipIMAGE 2019: Proceedings of the VII ECCOMAS Thematic Conference on Computational Vision and Medical Image Processing, Porto, Portugal, 16–18 October 2019; Springer: Berlin/Heidelberg, Germany, 2019.
299. Bento, D.; Lopes, S.; Maia, I.; Lima, R.; Miranda, J. M. Bubbles moving in blood flow in a microchannel network: The effect on the local hematocrit. Micromachines 2020, 11, 344.
300. Bento, D.; Sousa, L.; Yaginuma, T.; Garcia, V.; Lima, R.; Miranda, J. M. Microbubble moving in blood flow in microchannels: Effect on the cell-free layer and cell local concentration. Biomed. Microdevices 2017, 19, 6.

301. Ma, P.; Wang, S.; Guan, R.; Hu, L.; Wang, X.; Ge, A.; Zhu, J.; Du, W.; Liu, B.F. An integrated microfluidic device for studying controllable gas embolism induced cellular responses. Talanta 2020, 208, 120484.
302. Li, Z.; Li, G.; Li, Y.; Chen, Y.; Li, J.; Chen, H. Flow field around bubbles on formation of air embolism in small vessels. Proc. Natl. Acad. Sci. USA 2021, 118, e2025406118.
303. Huh, D. A human breathing lung-on-a-chip. Ann. Am. Thorac. Soc. 2015, 12 (Suppl. S1), S42–S44.
304. Miranda, I.; Souza, A.; Sousa, P.; Ribeiro, J.; Castanheira, E. M.; Lima, R.; Minas, G. Properties and applications of PDMS for biomedical engineering: A review. J. Funct. Biomater. 2021, 13, 2.
305. Garstecki, P. Formation of droplets and bubbles in microfluidic systems. In Microfluidics Based Microsystems: Fundamentals and Applications; Springer: Berlin/Heidelberg, Germany, 2010; pp. 163–181.
306. Nilsson, D.P.; Holmgren, M.; Holmlund, P.; Wåhlin, A.; Eklund, A.; Dahlberg, T.; Wiklund, K.; Andersson, M. Patient-specific brain arteries molded as a flexible phantom model using 3D printed water-soluble resin. Sci. Rep. 2022, 12, 10172.
307. Kim, J.H.; Chhai, P.; Rhee, K. Development and characterization of viscoelastic polydimethylsiloxane phantoms for simulating arterial wall motion. Med. Eng. Phys. 2021, 91, 12–18.
308. Nomoni, M.; May, J.M.; Kyriacou, P.A. Novel polydimethylsiloxane (PDMS) pulsatile vascular tissue phantoms for the in-vitro investigation of light tissue interaction in photoplethysmography. Sensors 2020, 20, 4246.
309. Perrira, N.; Shuib, A. S.; Phang, S. W.; Muda, A. S. Experimental Investigation of Blood Mimicking Fluid Viscosity for Application in 3D-Printed Medical Simulator. J. Phys. Conf. Ser. 2022, 2222, 012016.
310. Webb, L. Mimicking Blood Rheology for More Accurate Modeling in Benchtop Research. Pegasus Rev. UCF Undergrad. Res. J. 2020, 12, 6.
311. Nader, E.; et al. Blood rheology: Key parameters, impact on blood flow, role in sickle cell disease and effects of exercise. Front. Physiol. 2019, 10, 1329.
312. Kornfield, T.E.; Newman, E.A. Measurement of retinal blood flow using fluorescently labeled red blood cells. eNeuro 2015, 2, 005-15.

313. Jablonski, E.L.; Vogel, B. M.; Cavanagh, D. P.; Beers, K. L. Microfluidics in the Undergraduate Laboratory: Device Fabrication and an Experiment to Mimic Intravascular Gas Embolism. Chem. Eng. Educ. 2010, 44, 81–87.
314. Bhattacharjee, N.; Urrios, A.; Kang, S.; Folch, A. The upcoming 3D-printing revolution in microfluidics. Lab a Chip 2016, 16, 1720–1742.
315. Fuard, D.; Tzvetkova-Chevolleau, T.; Decossas, S.; Tracqui, P.; Schiavone, P. Optimization of poly-di-methyl-siloxane (PDMS) substrates for studying cellular adhesion and motility. Microelectron. Eng. 2008, 85, 1289–1293.
316. Baudoin, R.; Alberto, G.; Paullier, P.; Legallais, C.; Leclerc, E. Parallelized microfluidic biochips in multi well plate applied to liver tissue engineering. Sens. Actuators B Chem. 2012, 173, 919–926.
317. Brown, X.Q.; Ookawa, K.; Wong, J.Y. Evaluation of polydimethylsiloxane scaffolds with physiologically-relevant elastic moduli: Interplay of substrate mechanics and surface chemistry effects on vascular smooth muscle cell response. Biomaterials 2005, 26, 3123–3129.
318. Palchesko, R.N.; Zhang, L.; Sun, Y.; Feinberg, A. W. Development of polydimethylsiloxane substrates with tunable elastic modulus to study cell mechanobiology in muscle and nerve. PLoS ONE 2012, 7, e51499.
319. Monson, K.L.; Goldsmith, W.; Barbaro, N. M.; Manley, G. T. Axial mechanical properties of fresh human cerebral blood vessels. J. Biomech. Eng. 2003, 125, 288–294.
320. Poepping, T.L.; Nikolov, H. N.; Thorne, M. L.; Holdsworth, D. W. A thin-walled carotid vessel phantom for Doppler ultrasound flow studies. Ultrasound Med. Biol. 2004, 30, 1067–1078.
321. Markov, D.A.; Lillie, E. M.; Garbett, S. P.; McCawley, L. J. Variation in diffusion of gases through PDMS due to plasma surface treatment and storage conditions. Biomed. Microdevices 2013, 16, 91–96.
322. Kanehashi, S.; Sato, T.; Sato, S.; Nagai, K. Microstructure and gas diffusivity of poly (dimethylsiloxane) dense membrane using molecular dynamics (MD) simulation. Trans. Mater. Res. Soc. Jpn. 2012, 37, 439–442.

323. Xu, L.; Lee, H.; Jetta, D.; Oh, K. W. Vacuum-driven power-free microfluidics utilizing the gas solubility or permeability of polydimethylsiloxane (PDMS). Lab Chip 2015, 15, 3962–3979.
324. Vadapalli, A.; Pittman, R.N.; Popel, A.S. Estimating oxygen transport resistance of the microvascular wall. Am. J. Physiol. Circ. Physiol. 2000, 279, H657–H671.
325. Popel, A.S.; Pittman, R.N.; Ellsworth, M.L. Rate of oxygen loss from arterioles is an order of magnitude higher than expected. Am. J. Physiol. Circ. Physiol. 1989, 256, H921–H924.
326. Brookshier, K.; Tarbell, J. Evaluation of a transparent blood analog fluid: Aqueous xanthan gum/glycerin. Biorheology 1993, 30, 107–116.
327. Liu, B.; Tian, B.; Yang, X.; Li, M.; Yang, J.; Li, D.; Oh, K. W. Manipulation of micro-objects using acoustically oscillating bubbles based on the gas permeability of PDMS. Biomicrofluidics 2018, 12, 034111.
328. Anderson, J.C.; Bernard, S. L.; Luchtel, D. L.; Babb, A. L.; Hlastala, M. P. Axial and radial distribution of the bronchial vasculature in sheep. Respir. Physiol. Neurobiol. 2002, 132, 329–339.
329. Laitinen, A.; Laitinen, L. A.; Moss, R.; Widdicombe, J. G. Organisation and structure of the tracheal and bronchial blood vessels in the dog. J. Anat. 1989, 165, 133.
330. Broberg Craig, S.; et al. Blood viscosity and its relationship to iron deficiency, symptoms, and exercise capacity in adults with cyanotic congenital heart disease. J. Am. Coll. Cardiol. 2006, 48, 356–365.
331. Zhang, C.; Weldetsadik, N. T.; Hayat, Z.; Fu, T.; Zhu, C.; Jiang, S.; Ma, Y. The effect of liquid viscosity on bubble formation dynamics in a flow-focusing device. Int. J. Multiph. Flow 2019, 117, 206–211.
332. Fuentes, S.; Grande-Moreillo, C.; Margarit-Mallol, J.; Flores-Villar, S.; Solé-Heuberger, E.; Jaen-Manzanera, A. Gas Embolism in Pediatric Minimally Invasive
333. Billett, H.H. Hemoglobin and hematocrit. In Clinical Methods: The History, Physical, and Laboratory Examinations, 3rd ed.; Butter-worth, England. 1990.
334. Mitchell Simon, J. Decompression illness: A comprehensive overview. Diving Hyperb. Med. 2024, 54 (Suppl. S1), 1–53.
335. Butler, B.D.; Hills, B.A. The lung as a filter for microbubbles. J. Appl. Physiol. Respir. Environ. Exerc. Physiol. 1979, 47, 537–543.

336. Moon, R.E., R.D. Vann, and P.B. Bennett, The physiology of decompression illness. Scientific American, 1995. 273(2): p. 70-77.
337. Papadopoulou, V., et al., A critical review of physiological bubble formation in hyperbaric decompression. Advances in colloid and interface science, 2013. 191: p. 22-30.
338. Cooper, J.S. and K.C. Hanson, Decompression sickness, in StatPearls [Internet]. 2023, StatPearls Publishing.
339. Mitchell, S.J., Decompression illness: a comprehensive overview. Diving and Hyperbaric Medicine, 2024. 54(1Suppl): p. 1.
340. Brown, J. and M.J. Antuqano, Altitude-induced decompression sickness. 2010, United States. Office of Aviation Medicine.
341. Hills, B., Effect of decompression per se on nitrogen elimination. Journal of Applied Physiology, 1978. 45(6): p. 916-921.
342. Gabler-Smith, M.K., A.J. Westgate, and H.N. Koopman, Microvessel density, lipid chemistry and N 2 solubility in human and pig adipose tissue. Undersea & Hyperbaric Medicine, 2020. 47(1).
343. Vann, R.D., The Physiological Basis of Decompression: 38th Workshop: Papers and Discussions. 1989: Undersea and Hyperbaric Medical Society.
344. ACKLES, K., Blood-bubble interaction in decompression sickness(proceedings of a symposium). 1973.
345. Wienke, B., Decompression theory. Nuclear Weapons Technology/Stimulation And Computing: Los Alamos National Laboratory: NM, 2000. 87545.
346. Freiberger, J.J., et al., Consensus factors used by experts in the diagnosis of decompression illness. Aviation, space, and environmental medicine, 2004. 75(12): p. 1023-1028.
347. Thalmann, E., Decompression illness: what is it and what is the treatment. Alert Diver, DAN: Divers Alert Network, 2004.
348. Alexander, A.M. and N. Martin, Arterial gas embolism. 2019.
349. Buzzacott, P., et al., Section 4 THE DIVING INCIDENT REPORTING SYSTEM (DIRS). 2020, Divers Alert Network.
350. Melamed, Y., A. Shupak, and H. Bitterman, Medical problems associated with underwater diving. New England Journal of Medicine, 1992. 326(1): p. 30-35.

351. Bove, A.A., Diving medicine. American journal of respiratory and critical care medicine, 2014. 189(12): p. 1479-1486.
352. Schaefer, K.E., et al., Mechanisms in development of interstitial emphysema and air embolism on decompression from depth. Journal of applied physiology, 1958. 13(1): p. 15-29.
353. Mukherji, S.K., Emergent Neuroimaging: A Patient-Focused Approach. Neuroimaging Clinics, 2018. 28(3): p. xv.
354. Butler, B. and B. Hills, The lung as a filter for microbubbles. Journal of Applied Physiology, 1979. 47(3): p. 537-543.
355. Marsh, P.L., et al., Iatrogenic air embolism: pathoanatomy, thromboinflammation, endotheliopathy, and therapies. Frontiers in Immunology, 2023. 14: p. 1230049.
356. Bennett, P.B., et al. What ascent profile for the prevention of decompression sickness? I–Recent research on the Hill/Haldane ascent controversy. in Proceedings of the 28th Annual Scientific Meeting of the European Underwater and Biomedical Society. 2002.
357. Carturan, D., et al., Ascent rate, age, maximal oxygen uptake, adiposity, and circulating venous bubbles after diving. Journal of applied physiology, 2002. 93(4): p. 1349-1356.
358. Lam, G., et al., Hyperbaric oxygen therapy: exploring the clinical evidence. Advances in skin & wound care, 2017. 30(4): p. 181-190.
359. Hall, J., The risks of scuba diving: a focus on Decompression Illness. Hawai'i Journal of Medicine & Public Health, 2014. 73(11 Suppl 2): p. 13.
360. Jersey, S.L., et al., Neurological altitude decompression sickness among U-2 pilots: 2002–2009. Aviation, space, and environmental medicine, 2011. 82(7): p. 673-682.
361. Conkin, J., Evidence-based approach to the analysis of serious decompression sickness with application to EVA astronauts. 2001: National Aeronautics and Space Administration, Lyndon B. Johnson Space Center.
362. Painter, P.R., P. Edén, and H.-U. Bengtsson, Pulsatile blood flow, shear force, energy dissipation and Murray's Law. Theoretical Biology and Medical Modelling, 2006. 3: p. 1-10.
363. Murray, C.D., The physiological principle of minimum work: I. The vascular system and the cost of blood volume. Proceedings of the National Academy of Sciences, 1926. 12(3): p. 207-214.

364. Zamir, M., S. Wrigley, and B. Langille, Arterial bifurcations in the cardiovascular system of a rat. The Journal of general physiology, 1983. 81(3): p. 325-335.
365. Huo, Y., et al., Which width and angle rule provides optimal flow patterns in a coronary bifurcation? Journal of biomechanics, 2012. 45(7): p. 1273-1279.
366. Kaimovitz, B., et al., Diameter asymmetry of porcine coronary arterial trees: structural and functional implications. American Journal of Physiology-Heart and Circulatory Physiology, 2008. 294(2): p. H714-H723.
367. Kamenskiy, A.V., et al., Three-dimensional geometry of the human carotid artery. 2012.
368. Hammacher, J., et al., Stress engineering and mechanical properties of SU-8-layers for mechanical applications. Microsystem Technologies, 2008. 14: p. 1515-1523.
369. Miranda, I., et al., Properties and applications of PDMS for biomedical engineering: A review. Journal of functional biomaterials, 2021. 13(1): p. 2.
370. Stankova, N., et al., Optical properties of polydimethylsiloxane (PDMS) during nanosecond laser processing. Applied Surface Science, 2016. 374: p. 96-103.
371. Weber, J., et al., Development of an in vitro blood vessel model using autologous endothelial cells generated from footprint-free hiPSCs to analyze interactions of the endothelium with blood cell components and vascular implants. Cells, 2023. 12(9): p. 1217.
372. Nilsson, D.P., et al., Patient-specific brain arteries molded as a flexible phantom model using 3D printed water-soluble resin. Scientific Reports, 2022. 12(1): p. 10172.
373. Markov, D.A., et al., Variation in diffusion of gases through PDMS due to plasma surface treatment and storage conditions. Biomedical microdevices, 2014. 16: p. 91-96.
374. Held, M., et al., Intracellular mechanisms of fungal space searching in microenvironments. Proceedings of the National Academy of Sciences, 2019. 116(27): p. 13543-13552.
375. Markov, D.A., et al., Variation in diffusion of gases through PDMS due to plasma surface treatment and storage conditions. Biomedical microdevices, 2014. 16(1): p. 91-96.
376. Vadapalli, A., R.N. Pittman, and A.S. Popel, Estimating oxygen transport resistance of the microvascular wall. American Journal of Physiology-Heart and Circulatory Physiology, 2000. 279(2): p. H657-H671.
377. Popel, A.S., Theory of oxygen transport to tissue. Critical reviews in biomedical engineering, 1989. 17(3): p. 257.

378. Zhou, J., et al., Surface modification for PDMS-based microfluidic devices. Electrophoresis, 2012. 33(1): p. 89-104.
379. Brookshier, K. and J. Tarbell, Evaluation of a transparent blood analog fluid: aqueous xanthan gum/glycerin. Biorheology, 1993. 30(2): p. 107-116.
380. Billett, H.H., Hemoglobin and hematocrit. Clinical Methods: The History, Physical, and Laboratory Examinations. 3rd edition, 1990.
381. Nader, E., et al., Blood rheology: key parameters, impact on blood flow, role in sickle cell disease and effects of exercise. Frontiers in physiology, 2019. 10: p. 1329.
382. Webb, L., Mimicking Blood Rheology for More Accurate Modeling in Benchtop Research. The Pegasus Review: UCF Undergraduate Research Journal, 2020. 12(1): p. 6.
383. Inanlou, R., et al., A buck converter based on dual mode asynchronous pulse width modulator. AEU-International Journal of Electronics and Communications, 2020. 114: p. 152998.
384. Griffin, J., H. Hassan, and E. Spooner, Spin Coating: Complete Guide to Theory and Techniques. Ossila. Available online: https://www.ossila. com/en-eu/pages/spin-coating (accessed on 15 September 2022), 2022.
385. Gordy, S., and Rowell, S. Vascular air embolism. International Journal of Critical Illness and Injury Science. 2013 Jan;3(1):73-6.
386. de Miguel Díez, J., and J. de la Torre Fernández. "Arterial Gas Embolism: A Rare Complication of Core Needle Biopsy in the Diagnosis of Solitary Pulmonary Nodule." Archivos de Bronconeumologia 55.9 (2019): 492-493.
387. Alexander, Ajit M., Abdulghani Sankari, and Nathan Martin. "Arterial gas embolism." StatPearls [Internet]. StatPearls Publishing, 2024.
388. Verma, Amit, and Madhu Pandey Singh. "Venous gas embolism in operative hysteroscopy: A devastating complication in a relatively simple surgery." *Journal of Anaesthesiology Clinical Pharmacology* 34.1 (2018): 103-106.
389. Imasogie, Ngozi, et al. "Probable gas embolism during operative hysteroscopy caused by products of combustion." *Canadian Journal of Anesthesia* 49.10 (2002): 1044.
390. Sabsovich, Ilya, et al. "Air embolism during operative hysteroscopy: TEE-guided resuscitation." *Journal of Clinical Anesthesia* 24.6 (2012): 480-486.

391. McCarthy, Colin J., et al. "Air embolism: practical tips for prevention and treatment." *Journal of Clinical Medicine* 5.11 (2016): 93.
392. St John, Ace, et al. "The rise of minimally invasive surgery: 16 year analysis of the progressive replacement of open surgery with laparoscopy." *JSLS: Journal of the Society of Laparoscopic & Robotic Surgeons* 24.4 (2020): e2020-00076.
393. Kerrigan, M. J., and J. S. Cooper. "Venous Gas Embolism.[Updated 2021 Oct 9]." *StatPearls [Internet]. Treasure Island (FL): StatPearls Publishing* (2022).
394. Marsh, Phillip L., et al. "Iatrogenic air embolism: pathoanatomy, thromboinflammation, endotheliopathy, and therapies." Frontiers in immunology 14 (2023): 1230049.
395. Bhanaker SM, Liau DW et al: Liability Related to Peripheral Venous and Arterial Catheterization: A Closed Claims Analysis - Anesth Analg 2009; 109:124-9.
396. Chubb and Frenkel & Co. Inc. - https://www.qps-nv.be/wp-content/uploads/2016/12/ClearLineIV.pdf.
397. Deng, Boxin, Karin Schroën, and Jolet de Ruiter. "Dynamics of bubble formation in spontaneous microfluidic devices: Controlling dynamic adsorption via liquid phase properties." *Journal of Colloid and Interface Science* 622 (2022): 218-227.
398. Garstecki, Piotr, A. M. Gańán-Calvo, and G. M. Whitesides. "Formation of bubbles and droplets in microfluidic systems." *Bulletin of the Polish Academy of Sciences: Technical* Sciences 53.4 (2005).
399. Jablonski, E.L., et al., Microfluidics in the Undergraduate Laboratory: Device Fabrication and an Experiment to Mimic Intravascular Gas Embolism. Chemical Engineering Education, 2010. 44(1): p. 81-87.
400. Mardanpour, M.M., et al., In Vitro Investigation of Gas Embolism in Microfluidic Networks Mimicking Microvasculature. 2022.
401. Ma, P., et al., An integrated microfluidic device for studying controllable gas embolism induced cellular responses. Talanta, 2020. 208: p. 120484.
402. Brookshier, K. and J. Tarbell, *Evaluation of a transparent blood analog fluid: aqueous xanthan gum/glycerin.* Biorheology, 1993. **30**(2): p. 107-116.
403. Ebrahimi, Ali P. "Mechanical properties of normal and diseased cerebrovascular system." *Journal of vascular and interventional neurology* 2.2 (2009): 155.

404. Yayapour, Noushin, and Håkan Nygren. "Interactions between whole blood and hydrophilic or hydrophobic glass surfaces: kinetics of cell adhesion." *Colloids and Surfaces B: Biointerfaces* 15.2 (1999): 127-138.

405. Arieli, R., *Nanobubbles form at active hydrophobic spots on the luminal aspect of blood vessels: consequences for decompression illness in diving and possible implications for autoimmune disease—an overview.* Frontiers in Physiology, 2017. **8**: p. 591.

406. Tsuzuki, T., Baassiri, K., Mahmoudi, Z., Nicolau, D.V., *Hydrophobic recovery of PDMS surfaces in contact with hydrophilic entities: relevance to biomedical devices.* Materials, 2022.

407. Luo, Wenchen, et al. "Low Pneumoperitoneum pressure reduces gas embolism during laparoscopic liver resection: A randomized controlled trial." (2024): 588-597.

408. Cooper, Jeffrey S., and Kenneth C. Hanson. "Decompression sickness." *StatPearls [Internet]*. StatPearls Publishing, 2023.

409. Reijnders-Boerboom, Gabby TJA, et al. "Low intra-abdominal pressure in laparoscopic surgery: a systematic review and meta-analysis." *International Journal of Surgery* 109.5 (2023): 1400-1411.

410. Hugon, J. "Decompression models: review, relevance and validation capabilities." *Undersea & Hyperbaric Medicine* 41.6 (2014).

411. Firpo, G., et al. "Permeability thickness dependence of polydimethylsiloxane (PDMS) membranes." *Journal of Membrane Science* 481 (2015): 1-8.

412. Baish, James W., et al. "Scaling rules for diffusive drug delivery in tumor and normal tissues." *Proceedings of the National Academy of Sciences* 108.5 (2011): 1799-1803.

413. Hislop, Alison A. "Airway and blood vessel interaction during lung development." *Journal of anatomy* 201.4 (2002): 325-334.

414. Denby, Kara, et al. "Understanding large vessel perforation requiring treatment with covered stent implantation: A case series." *Catheterization and Cardiovascular Interventions* 103.4 (2024): 570-579.

415. Dintenfass, Leopold. *Blood viscosity*. Springer Science & Business Media, 1985.

416. Gabler-Smith, Molly K., Andrew J. Westgate, and Heather N. Koopman. "Microvessel density, lipid chemistry and N 2 solubility in human and pig adipose tissue." *Undersea & Hyperbaric Medicine* 47.1 (2020).

417. Hawkins, James A., and Charles W. Shilling. "Helium solubility in blood at increased pressures." *Journal of Biological Chemistry* 113.3 (1936): 649-653.

418. Hyldegaard, Ole, Dikla Kerem, and Y. Melamed. "Effect of isobaric breathing gas shifts from air to heliox mixtures on resolution of air bubbles in lipid and aqueous tissues of recompressed rats." *European journal of applied physiology* 111 (2011): 2183-2193.